

## REPORT DOCUMENTATION P/

AD-A271 422

188

Public reporting burden for this collection of information is estimated to average 1 hour per gathering and maintaining the data needed, and completing and reviewing the collection of information, including suggestions for reducing this burden, to Washington Headquarters, Suite 1204, Arlington, VA 22202-4302, and to the Office of Management and

ing data sources  
ier aspect of this  
1215 Jefferson  
03

1. AGENCY USE ONLY (Leave blank)

2. REPORT DATE

6 Oct. 1993

3. REPORT TYPE AND DATES COVERED

final; 01 May 91 - 30 April 92

4. TITLE AND SUBTITLE

Surface Science at The Solid Liquid Interface

5. FUNDING NUMBERS

G N00014-91-J-1688

6. AUTHOR(S)

Thomas E. Furtak

7. PERFORMING ORGANIZATION NAME(S) AND ADDRESS(ES)

Colorado School of Mines  
Department of Physics  
Golden, CO 80401

8. PERFORMING ORGANIZATION  
REPORT NUMBER

Report Number 1

9. SPONSORING / MONITORING AGENCY NAME(S) AND ADDRESS(ES)

Office of Naval Research  
Code 1511.MAW  
800 North Quincy Street  
Arlington, VA 22217-5000

10. SPONSORING / MONITORING  
AGENCY REPORT NUMBER

11. SUPPLEMENTARY NOTES

DTIC  
SELECTE  
OCT 19 1993  
S B D

12a. DISTRIBUTION / AVAILABILITY STATEMENT

No limitation on distribution

DISTRIBUTION STATEMENT A

Approved for public release;  
Distribution Unlimited

12b. DISTRIBUTION CODE

13. ABSTRACT (Maximum 200 words)

This report contains a summary of the Topical Conference on Surface Science at the Electrolyte - Solid Interface, held in conjunction with the 38th. National Symposium of the American Vacuum Society on Nov. 11-12, 1991 in Seattle Washington.

93-24532

93 10 10 005



2719)

14. SUBJECT TERMS

Electrochemistry, Surface Science

15. NUMBER OF PAGES

86

16. PRICE CODE

17. SECURITY CLASSIFICATION  
OF REPORT

Unclassified

18. SECURITY CLASSIFICATION  
OF THIS PAGE

Unclassified

19. SECURITY CLASSIFICATION  
OF ABSTRACT

Unclassified

20. LIMITATION OF ABSTRACT

# **SURFACE SCIENCE AT THE SOLID-LIQUID INTERFACE**

## **A TOPICAL CONFERENCE COORDINATED WITH THE NATIONAL SYMPOSIUM OF THE AMERICAN VACUUM SOCIETY**

THE TWO-DAY TOPICAL CONFERENCE ON THE PHYSICS AND CHEMISTRY OF SURFACES UNDER WATER WILL BE HELD AT THE 38TH NATIONAL SYMPOSIUM OF THE AMERICAN VACUUM SOCIETY, MONDAY AND TUESDAY, NOVEMBER 11 AND 12, 1991, AT THE CONVENTION CENTER IN SEATTLE WASHINGTON. THIS EVENT IS SPONSORED BY THE AMERICAN VACUUM SOCIETY THROUGH THE APPLIED SURFACE SCIENCE DIVISION.

TUTORIAL PRESENTATIONS WILL BE ORGANIZED AROUND CENTRAL THEMES WHICH BRIDGE THE DISCIPLINES OF VACUUM SURFACE SCIENCE, ELECTROCHEMISTRY AND AQUEOUS INTERFACE CHEMISTRY. IN ADDITION, CONTRIBUTIONS WILL BE SOLICITED IN THE FOLLOWING MAJOR AREAS:

- \* X-RAY PROBES OF THE WATER-SOLID INTERFACE
- \* INTERFACIAL OPTICAL METHODS, NONLINEAR, RAMAN, INFRARED
- \* SCANNING PROBE TECHNIQUES
- \* DUAL ENVIRONMENT METHODS INVOLVING TRANSFER TO VACUUM
- \* NOVEL EXPERIMENTAL APPROACHES
- \* UHV STUDIES OF WATER ADSORPTION
- \* MODELING OF THE WATER-SOLID INTERFACE
- \* THEORY OF CHARGED SOLID SURFACES

A POSTER SESSION IS PLANNED FOR MONDAY EVENING WITH POSTERS ON DISPLAY THROUGHOUT THE DAY TUESDAY. APPROXIMATELY 10-12 CONTRIBUTIONS WILL BE SELECTED FOR ORAL PRESENTATIONS. THE PROCEEDINGS WILL NOT BE SEPARATELY PUBLISHED, BUT AUTHORS ARE ENCOURAGED TO SUBMIT PAPERS TO A COLLECTED SECTION OF THE JOURNAL OF THE AMERICAN VACUUM SOCIETY.

A CALL FOR PAPERS HAS BEEN ISSUED IN EARLY MARCH. THE DEADLINE FOR SUBMITTING ABSTRACTS FOR ORAL PRESENTATIONS IS MAY 15, 1991. ABSTRACTS FOR POSTER PRESENTATIONS WILL BE ACCEPTED UNTIL AUGUST 16, 1991.

FOR MORE INFORMATION, CONTACT: T. E. FURTAK, PHYSICS DEPARTMENT, COLORADO SCHOOL OF MINES, GOLDEN, CO 80401 (303)-273-3843; C. KOVAL, CHEMISTRY DEPARTMENT, UNIVERSITY OF COLORADO, BOULDER, CO 80309 (303)-492-5564; OR A. BEVOLO, AMES LABORATORY, AMES, IA 50011 (515)-294-5414.

## Topical Conference

# Surface Science at the Solid-Liquid Interface

held November 11-12, 1991 in Seattle, WA

Following a somewhat new direction, the AVS sponsored a Topical Conference at the Seattle National Symposium entitled "*Surface Science at the Solid-Liquid Interface*". The event was organized by Prof. Tom Furtak [Colorado School of Mines] with the backing of the Applied Surface Science, the Surface Science, and the Nanometer Scale Science and Technology Divisions. Funding was provided by the Office of Naval Research as well as by the AVS 1991 Program Committee.

The problems encountered in liquid-solid interfacial science are similar but more complicated than those with which most UHV surface scientists are familiar. However, in the last few years several important new experimental methods have been developed through which a closer link can now be made between the two environments. These include force measurements both perpendicular and parallel to the interface in experiments involving two flat surfaces with water or other liquids in between. Prof. Jacob Israelachvili [Univ. California, Santa Barbara] described this type of work which has demonstrated that structural packing of the liquid molecules has an important influence on the force. This was also identified in a talk by Prof. John Porter [Univ. California, Berkeley], who has discovered similar phenomena through electron tunneling measurements.

Some remarkable progress involving surface structure characterization under water was presented by Prof. Mike Weaver [Purdue] (STM) and by Prof. Andy Gewirth [Univ. Illinois] (AFM). Through these techniques it is now possible to follow atomic scale processes, such as foreign metal deposition and surface reconstruction, which are driven by changes in the interfacial potential difference.

X-ray techniques are also making a big impact on under-water surface

characterization. This was explained by Dr. Ben Ocko [Brookhaven] who has followed a variety of potential driven surface reconstructions involving the same structures as are seen in UHV (where the controlled variable is the sample temperature).

Direct connections between UHV surface science and the liquid-solid interface were promoted through the talks given by Prof. Pat Thiel [Iowa State] and by Dr. Fred Wagner [General Motors], who discussed adsorption of water and co-adsorption (leading to liquid interface analogues) respectively.

There were a wide variety of contributed presentations as well as posters covering optical spectroscopy, semiconductor-liquid and insulator-liquid interfaces as well as more tunneling.

All of the sessions were well attended, at times stretching the capacity of the 300-seat auditorium. The interactions after the presentations as well as during the poster session were marked by the enthusiasm which is a characteristic of AVS symposia. Although this represents a non-traditional topic for the Society, it is clear from the demonstrated interest that the participation of vacuum surface scientists in the work of helping understand this interesting environment is an idea whose time has come.

DTIC QUALITY INSPECTED 1

<b>Accession For</b>	
NTIS GRA&I	<input checked="checked" type="checkbox"/>
DTIC TAB	<input type="checkbox"/>
Unannounced	<input type="checkbox"/>
Justification	
By	
Distribution/	
Availability Codes	
Dist	Avail and/or Special
A-1	

# Surface Science at the Solid-Liquid Interface

sponsored by  
Applied Surface Science Division  
Surface Science Division

financially supported by  
Office of Naval Research

Monday Morning  
Liquids and Liquid Molecules at Interfaces

- 8:30 J. Israelachvili, University of California, Santa Barbara  
*"Interfacial Forces"*
- 9:10 M. Watanabe, A. M. Brodsky, W. P. Reinhardt, University of Pennsylvania  
*"Phase Transitions of Water Layers between Charged Plates"*
- 9:30 J. Porter, University of California, Berkeley  
*"Applications of Metal/Liquid/Metal Tunnel Junction Devices to the Study of Liquids at Interfaces"*
- 10:10 **Break**
- 10:30 P. A. Thiel, Iowa State University  
*"Water Adsorption in UHV"*
- 11:10 D. L. Blanchard, D. R. Baer, Pacific Northwest Laboratory  
*"A Study of the Interaction of Co, Mn, and Water with Calcite"*
- 11:30 M. Kwini, J. P. Cowin, M. Iedema, Pacific Northwest Laboratory  
*"Femtosecond Solvation Dynamics of Ions in UHV Multilayer Solvent Models"*
- 11:50 **Lunch**

# Surface Science at the Solid-Liquid Interface

## Monday Afternoon Photon Spectroscopies and Phenomena

- 2:00 **M. J. Weaver, S. -C. Chang, X. Gao, X. Jiang**, Purdue University  
*"Infrared Spectroscopy and Scanning Tunneling Microscopy as Atomic-Level Structural Probes at Ordered Metal-Solution Interfaces: Comparisons with Metal-UHV Systems"*
- 2:40 **A. E. Russel, W. E. O'Grady**, Naval Research Laboratory  
*"In Situ Far-Infrared Studies of the Structure of Water at Ag(111)"*
- 3:00 **L. A. Barnes, M. R. Philpott, B. Liu, H. Seki**, IBM Almaden  
*"Adsorption of Sulphate on Metal Electrodes"*
- 3:20 **K. Murakoshi, K. Uosaki**, Hokkaido University  
*"Photon Emission at Metal/Solution Interface: Observation and Mechanism"*
- 3:40 **L. -K. Chau, G. E. Collins, K. W. Nebesny, P. A. Lee, N. R. Armstrong**, University of Arizona; **B. A. Parkinson**, Colorado State University  
*"Photoelectrochemical Processes of Dye Molecules Deposited as Ordered Monolayers on SnS<sub>2</sub> and Other Layered Semiconductors"*
- 4:00 **R. M. Corn**, University of Wisconsin, Madison  
*"Adsorption, Orientation and Order at the Solid-Liquid Interface as Studied by Optical Second Harmonic Generation"*
- 4:40 **K. A. Friedrich, E. K. L. Wong, G. L. Richmond**, University of Oregon  
*"A Comparative Second Harmonic Study of Cu(111) in UHV and Solution"*
- 5:00 **Poster Session: Room 4C**

## Posters

TC1-P

Monday

Afternoon, November 11

Room 4C

<u>Poster</u>	<u>Abs. #</u>	<u>Presenter</u>	<u>Title</u>
1	0275	A. G. Schrott	Valence States of Chromium During Electrochemical Polarization of Al/Cr Alloys: <i>In Situ</i> XANES Results
2	0293	D. R. Yaniv	In-Situ Modification and Characterization of Iron and Stainless Steel Surfaces Utilizing Scanning Tunneling Microscopy
3	0325	J. C. Thompson	Dielectric Constant of Liquid NH <sub>3</sub> in Contact with Ag
4	0408	Barbara Bonner	Real Time Sampling Electronics for Double Modulation Experiments with FTIR Interferometers
5	0410	Tom Furtak	Optical Second Harmonic Electroreflectance Spectroscopy from Ag(111)
6	0411	Doug Frank	Direct Imaging of Electrochemically Deposited Monolayers by means of Auger Electrons
7	0412	H. Sambe	Auger and X-Ray Photoelectron Spectra for Anodic and Air-Formed Oxide Film on Aluminum: Evidence for Negative Space Charge near the Metal-Oxide Interface
8	0534	Curtis Shannon	Chemisorption of Nitriles on Pt(111) Electrode Surfaces
9	0537	R. A. Bradley	Observation of Electronic Structure at the Metal/Electrolyte and Metal/Vacuum Interface by Second Harmonic Generation

<u>Poster</u>	<u>Abs. #</u>	<u>Presenter</u>	<u>Title</u>
10	0538	Kuilong Wang	Electrochemical Properties of Ni(111) in Alkaline Media
11	0717	G. M. Brown	AFM-STM Investigation of Titanium Electrodes in the Active, Passive, and Active-Passive Transition Potential Regions
12	0758	P. Fenter	An <i>Ex-Situ</i> Glancing Incidence X-Ray Diffraction Study of Self-Assembled Monolayers on the Au(111) and Ag(111) Surfaces
13	0760	Eric Stuve	Coadsorption of Hydrofluoric Acid with Water and Oxygen on Ag(110): Adlayer Solution Chemistry
14	0788	C. F. Windisch, Jr.	Electrochemical and Surface Studies of the Effects of P and S on the Corrosion of Fe and Ni
15	0830	M. A. George	Oxidation of Gold(111) Thin Films Investigated by Scanning Tunneling Microscopy
16	0942	Dan Schwartz	Resonance-Modified Photoelectrochemical Charge Transfer
17	1000	Martin Helfand	XPS Studies of Passive Film Formation on Transition Metal-Phosphorus Metallic Glasses in Acidic Aqueous Electrolytes
18	1002	T. R. Dillingham	X-Ray Photoelectron Spectroscopy Analysis of Borate Substituted Polyaniline Thin Films
19	1050	Karl Robinson	In-Situ X-Ray Scattering from Au and Pt Single Crystal Electrodes



# Surface Science at the Solid-Liquid Interface

## Tuesday Morning Structural Studies of the Solid Surface

- 8:30 **A. A. Gewirth**, University of Illinois  
*"Atomic Force Microscopy of Electrochemical Processes at the Solid-Liquid Interface"*
- 9:10 **D. G. Frank, T. Golden, O. M. R. Chyan, A. T. Hubbard**, University of Cincinnati  
*"Direct Imaging of Electrochemically Deposited Monolayers by Means of Auger Electrons"*
- 9:30 **N. J. Tao, S. M. Lindsay**, Arizona State University  
*"Scanning Tunneling Microscopy (STM) Study of the  $22 \times \sqrt{3}$  on Au(111) Under Aqueous Solutions Under Potential Control"*
- 9:50 **M. P. Green, K. J. Hanson**, AT&T Bell Labs  
*"Cu UPD on Au(111) in Sulfate Electrolyte"*
- 10:10 **D. J. Trevor, C. D. E. Chidsey, P. L. Trevor**, AT&T Bell Labs; **I. Oppenheim, K. Sieradzki**, Johns Hopkins University  
*"In Situ Scanning Tunneling Microscopy of Corrosion of Silver/Gold Alloys"*
- 10:30 **B. M. Ocko**, Brookhaven National Laboratory  
*"Electrochemically Induced Reconstructions at Single Crystal Gold Electrodes: An In Situ X-ray Scattering Study"*
- 11:10 **W. E. O'Grady, E. McCafferty, P. M. Natishan, A. E. Russell**, Naval Research Laboratory; **K. I. Pandya**, Brookhaven National Laboratory; **D. E. Ramaker**, George Washington University  
*"The Uptake of Cl by a Passivated Al Electrode as Indicated by X-ray Absorption Spectroscopy"*
- 11:30 **M. F. Toney, J. G. Gordon, G. L. Borges, D. G. Wiesler, O. R. Melroy**, IBM Almaden; **D. Yee, L. B. Sorensen**, University of Washington  
*"In Situ Surface X-ray Scattering of Electrochemically Deposited Metal Monolayers"*
- 11:50 **Lunch**

# Surface Science at the Solid-Liquid Interface

## Tuesday Afternoon Surface Science and Electrochemistry

- 2:00 **F. T. Wagner, T. E. Moylan**, General Motors Research Laboratories  
*"Relationships Between Electrochemical Interfaces and Vacuum Analogues"*
- 2:40 **C. Benndorf, C. Mundt**, University of Hamburg  
*"H<sub>2</sub>O Adsorption on Ni(221): Evidence for a Step Induced Influence on the Adsorption Geometry"*
- 3:00 **N. Kizhakevariam, E. M. Stuve**, University of Washington  
*"Adsorption of Water on Chemically Modified Pt(100)"*
- 3:20 **A. J. Bard, D. O. Wipf, P. Unwin, D. Pierce, F. Shou**, University of Texas  
*"Investigations of the Solid-Liquid Interface by Scanning Electrochemical Microscopy"*
- 4:00 **L. -W. H. Leung, G. Gregg, D. W. Goodman**, Texas A&M University  
*"A Combined Electrochemical and Ultrahigh Vacuum Study of Ultra-Thin Films of Cu and Ag on Pt(111)"*
- 4:20 **R. L. Borup, D. E. Sauer, E. M. Stuve**, University of Washington  
*"Electrodeposition of Lead on Pt(111) Studied Ex Situ with Combined Ultrahigh Vacuum and Electrochemical Methods"*
- 4:40 **I. Villegas, J. L. Stickney**, University of Georgia  
*"GaAs Deposition on the (100) and (110) Planes of Gold by Electrochemical Atomic Layer Epitaxy: A LEED and Auger Electron Spectroscopy Study"*
- 5:00 **Closing**

# Interfacial forces

Jacob Israelachvili

Department of Chemical & Nuclear Engineering, and Materials Department, University of California, Santa Barbara, California 93106

(Received 16 September 1991; accepted 25 November 1991)

The past few years have witnessed tremendous advances in experimental and theoretical techniques for probing both the static and dynamic properties of surfaces at the angstrom level. Here we review how these advances have furthered our fundamental understanding of adhesion—particularly those processes that contribute to energy dissipation during adhesion and separation (loading–unloading cycles), and friction—particularly how the dynamic (e.g., viscous and rheological) properties of liquids in ultrathin films differ from the bulk liquid properties, and how this affects the friction forces of lubricated contacts. The emphasis will be on “ideal” surfaces and interfaces, i.e., surfaces that are molecularly smooth, and interfacial films that are no more than a few molecular layers thick.

## I. INTERFACIAL ADHESION

Under ideal conditions the adhesion energy is considered to be a well-defined thermodynamic quantity. It is normally denoted by  $\gamma$  or  $W$ , and it gives the work done on bringing two surfaces together or the work needed to separate two surfaces from contact. Under ideal, equilibrium conditions these two quantities are the same, but under most realistic conditions they are not: the work needed to separate two surfaces is always greater than that originally gained on bringing them together. An understanding of the molecular mechanisms underlying this phenomenon is essential for understanding many adhesion phenomena, energy dissipation during loading–unloading cycles, contact angle hysteresis, and—ultimately—the molecular mechanisms associated with many frictional processes. We start by describing both the theoretical and experimental basis of adhesion hysteresis, and how it arises even between perfectly smooth and chemically homogeneous surfaces.

## II. INTERFACIAL FRICTION

The static and dynamic properties of ordinary liquids, when confined within a very thin film between two surfaces, can be very different from those of the bulk liquids. Films thinner than 10 molecular diameters can become much more viscous, and those below 4 molecular diameters can undergo a phase transition into a liquid-crystalline or solidlike phase. Such “liquid” films can support finite loads and shear stresses. These modified properties depend intimately on the geometry of the liquid molecules, and how these molecules can fit in between the two (atomically) corrugated solid surfaces. The friction or shear forces of such molecularly thin liquid films are here described in the light of recent experimental and theoretical (computer simulation) studies.

## III. ADHESION

### A. Reversible and irreversible adhesion (adhesion hysteresis)

Most real processes involving adhesion are hysteretic or energy dissipating even though they are usually described

in terms of (ideally) reversible thermodynamic functions such as surface energy, adhesion free energy, reversible work of adhesion, etc. For example, the energy change, or work done, on separating two surfaces from adhesive contact is generally not fully recoverable by bringing the two surfaces back into contact again. This may be referred to as *adhesion hysteresis*, and expressed as

$$\begin{array}{ccc} W_R & > & W_A \\ \text{receding} & & \text{advancing} \\ (\text{separating}) & & (\text{approaching}) \end{array}$$

or

$$\Delta W = (W_R - W_A) > 0, \quad (1)$$

where  $W_R$  and  $W_A$  are the adhesion energies for receding (separating) and advancing (approaching) two solid surfaces, respectively. Adhesion hysteresis is responsible for such phenomena as “rolling” friction<sup>1</sup> and “elastoplastic” adhesive contacts<sup>2</sup> during loading–unloading and adhesion–decohesion cycles.

Hysteresis effects are also commonly observed in wetting/dewetting phenomena.<sup>3</sup> For example, when a liquid spreads and then retracts from a surface the advancing contact angle  $\theta_A$  is generally larger than the receding angle  $\theta_R$  [cf. Fig. 1(A)]. Since the contact angle  $\theta$  is related to the liquid-vapor surface tension  $\gamma$  and the solid–liquid adhesion energy  $W$  by the Dupré equation [Fig. 1(B)]

$$(1 + \cos \theta)\gamma_L = W, \quad (2)$$

we may conclude that *wetting hysteresis* or *contact angle hysteresis* ( $\theta_A > \theta_R$ ) actually implies adhesion energy hysteresis  $W_R > W_A$  as given by Eq. (1).

In all the above cases at least one of the surfaces is always a solid. In the case of solid–solid contacts, the hysteresis has generally been attributed to viscoelastic bulk deformations of the contacting materials or to plastic deformations of locally contacting asperities.<sup>1,2</sup> In the case of solid–liquid contacts, hysteresis has usually been attributed to surface roughness or to chemical heterogeneity<sup>3</sup> as illustrated in Figs. 1(C) and 1(D), though there have also

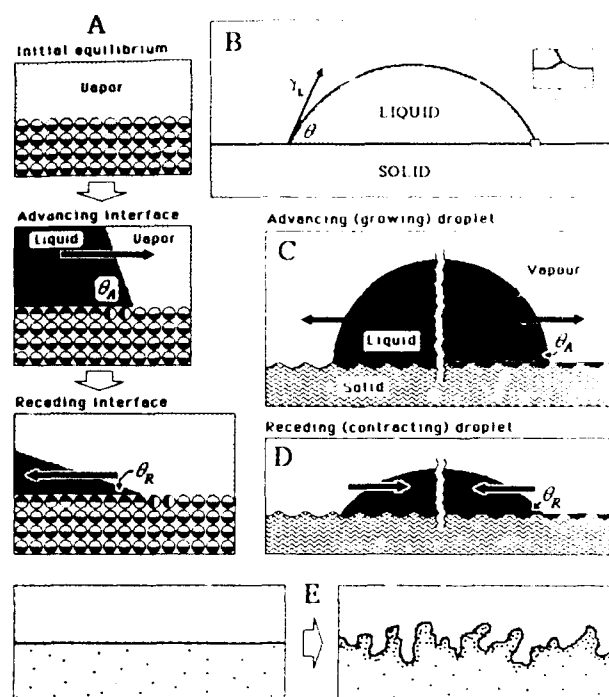


FIG. 1. Examples of wetting and contact-angle hysteresis. (A) Solid surface in equilibrium with vapor. On wetting the surface, the *advancing* contact angle  $\theta_A$  is observed; on dewetting it decreases to the *receding* angle  $\theta_R$ . This is an example of adhesion hysteresis during wetting/dewetting that is analogous to that occurring during the loading/unloading of two solid surfaces. (B) Liquid droplet resting on a flat solid surface. This is not a true equilibrium situation: at the three-phase contact boundary the normal liquid stress  $\gamma_L \sin \theta$  is balanced by high local stresses on the solid which induce elastic or plastic deformations (inset) and/or chemical rearrangements to relax these stresses. (C) and (D) Contact angle hysteresis is usually explained by the inherent roughness (left side) or chemical heterogeneity (right side) of surfaces. (E) Interdiffusion, interdigitation, molecular reorientations, and exchange processes at an interface may induce roughness and chemical heterogeneity even though initially both surfaces are perfectly smooth and homogeneous. Such surface restructuring effects can occur both on the macroscopic, microscopic and molecular scales. Here we will mainly be concerned with effects occurring at the molecular level.

been reports of significant hysteresis on molecularly smooth and chemically homogeneous surfaces.<sup>4</sup>

Here we shall focus on two other, less studied but equally important, mechanisms that can give rise to hysteresis. These may be conveniently referred to as (i) *mechanical hysteresis*, arising from intrinsic mechanical irreversibility of many adhesion/decohesion processes [see Fig. 1(B) *inset*, and Fig. 2], and (ii) *chemical hysteresis*, arising from the intrinsic chemical irreversibility at the contacting surfaces associated with the necessarily finite time it takes to go through any adhesion/decohesion or wetting/dewetting process [Fig. 1(E)]. Henceforth we shall use the term *approach/separation* to refer quite generally to any cyclic process, such as adhesion/decohesion, loading/unloading, advancing/receding and wetting/dewetting cycles.

Because of natural constraints of *finite time* and the *finite elasticity* of materials most approach/separation cycles are thermodynamically irreversible, and therefore en-

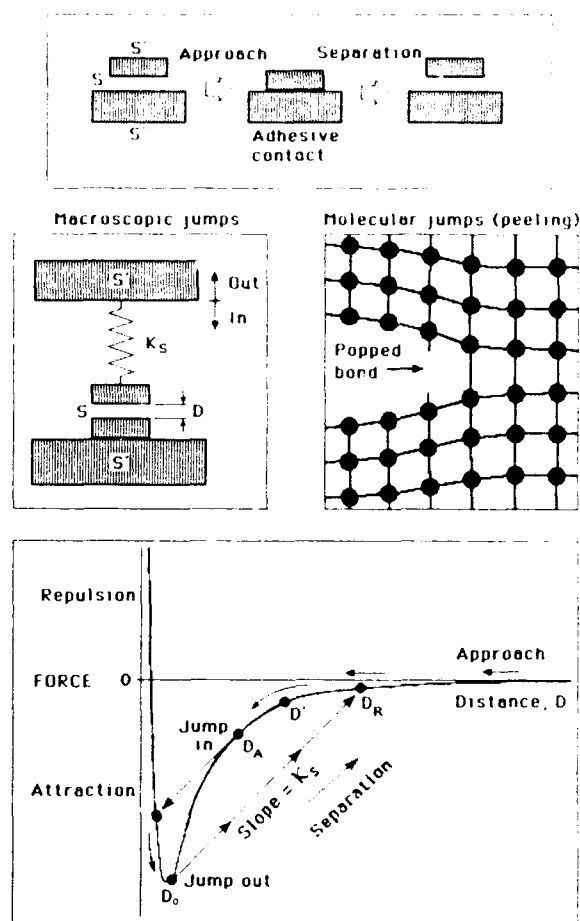


FIG. 2. Origin of mechanical adhesion hysteresis during the approach and separation of two solid surfaces. Top: In all realistic situations the force between two solid surfaces is never measured at the surfaces themselves  $S$  but at some other point, say  $S'$ , to which the force is elastically transmitted via the backing material supporting the surfaces. Center (left): "Magnet" analogy of two approaching surfaces, where the lower is fixed and where the other is supported at the end of a spring of stiffness  $K_s$ . Bottom: Force-distance curve for two surfaces interacting via an attractive van der Waals-type force law, showing the path taken by the upper surface on approach and separation. On approach, an instability occurs at  $D \approx D_A$ , where the surfaces spontaneously jump into "contact" at  $D \approx D_A$ . On separation, another instability occurs where the surfaces jump apart from  $\sim D_0$  to  $D_R$ . Center (right): On the molecular or atomic level, the separation of two surfaces is accompanied by the spontaneous popping of bonds, which is analogous to the jump apart of two macroscopic surfaces.

ergy dissipating. By thermodynamic irreversibility we simply mean that one cannot go through the approach/separation cycle via a continuous series of equilibrium states because some of these are connected via spontaneous—and therefore thermodynamically irreversible—instabilities or transitions. During such transitions there is an absence of *mechanical* and/or *chemical* equilibrium. In many cases the two will be intimately related and occur at the same time (and there is usually also an absence of *thermal* equilibrium), but the above distinction is nevertheless a useful one since there appears to be two fairly distinct molecular processes that give rise to them. These will now be considered in turn.

## B. Mechanical hysteresis

Consider two solid surfaces a distance  $D$  apart (Fig. 2) interacting with each other via an attractive potential and a hard-wall repulsion at some cutoff separation  $D_0$ . Let the materials of the surfaces have a bulk elastic modulus  $K$ , so that depending on the system geometry the surfaces may be considered to be supported by a simple spring of effective "spring constant"  $K_S$ .<sup>5</sup> When the surfaces are brought towards each other a mechanical instability occurs at some finite separation  $D_A$  from which the two surfaces jump spontaneously into contact (cf. lower part of Fig. 2). This instability occurs when the gradient of the attractive force  $dF/dD$  exceeds  $K_S$ .<sup>5</sup> Likewise, on separation from adhesive contact, there will be a spontaneous jump apart from  $D_0$  to  $D_R$ . Separation jumps are generally greater than approaching jumps.

Such spontaneous jumps occur at both the macroscopic and atomic levels. For example, they occur when two macroscopic surfaces are brought together in surface forces experiments;<sup>6</sup> they occur when scanning tunneling microscope (STM) or atomic force microscope (AFM) tips approach a flat surface,<sup>5,7</sup> and they occur when individual bonds are broken (or "popped") during fracture and crack propagation in solids.<sup>8</sup> But such mechanical instabilities will not occur if the attractive forces are weak or if the backing material supporting the surfaces is very rigid (high  $K$  or  $K_S$ ). However, in many practical cases these conditions are not met and the adhesion/decohesion cycle is inherently hysteretic regardless of how smooth the surfaces, of how perfectly elastic the materials, and of how slowly one surface is made to approach the other (via the supporting material).

Thus, the adhesion energy on separation from contact will generally be greater than that on approach, and the process is unavoidably energy dissipative. It is important to note that this irreversibility does not mean that the surfaces must become damaged or even changed in any way, or that the molecular configuration is different at the end from what it was at the beginning of the cycle. Energy can always be dissipated in the form of heat whenever two surfaces or molecules impact each other.

## C. Chemical hysteresis

When two surfaces come into contact the molecules at the interfaces relax and/or rearrange to a new equilibrium configuration that is different from that when the surfaces were isolated [Fig. 1(E)]. These rearrangements may involve simple positional and orientational changes of the surface molecules, as occurs when the molecules of two homopolymer surfaces slowly intermix by diffusion<sup>9</sup> or reptation.<sup>10</sup> In more complex situations, new molecular groups that were previously buried below the surfaces may appear and intermix at the interface. This commonly occurs with surfaces whose molecules have both polar and nonpolar groups, for example, copolymer surfaces,<sup>11</sup> surfactant surfaces,<sup>12,13</sup> and protein surfaces.<sup>14</sup> All these effects act to enhance the adhesion or cohesion of the contacting surfaces.

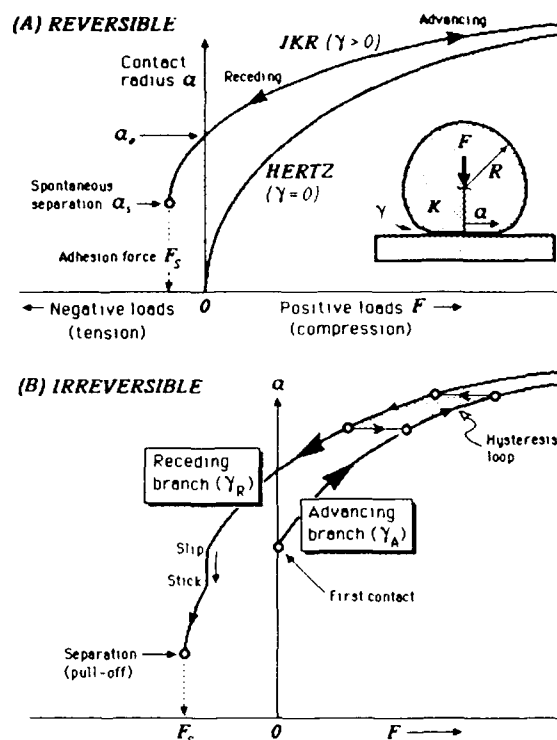


FIG. 3. (A) Reversible contact radius vs load curve of nonadhesive Hertzian contact and adhesive JKR contact under ideal conditions. No hysteresis. (B) Irreversible  $a$ - $F$  curves and the hysteresis loops they give rise to during an advancing-receding cycle (also commonly referred to as compression-decompression, loading-unloading, and bonding-debonding cycles). Hysteretic adhesion cycles are often discontinuous—the advancing or receding curves displaying small instability jumps. This may be referred to as stick-slip adhesion, and is illustrated in the lower figure.

What distinguishes chemical hysteresis from mechanical hysteresis is that during chemical hysteresis the chemical groups at the surfaces are different on separation from on approach. However, as with mechanical hysteresis, if the cycle were to be carried out infinitely slowly it *should* be reversible.

## D. Adhesive contacts of elastic materials: The Johnson-Kendall-Roberts (JKR) theory

Modern theories of the adhesion mechanics of two contacting solid surfaces are based on the JKR theory.<sup>15,16</sup> In the JKR theory two spheres of radii  $R_1$  and  $R_2$ , bulk elastic moduli  $K$ , and surface energy  $\gamma$  per unit area, will flatten when in contact. The contact area will increase under an external load or force  $F$ , such that at mechanical equilibrium the contact radius  $a$  is given by (cf. Fig. 3)

$$a^3 = \frac{R}{K} [F + 6\pi R\gamma + \sqrt{12\pi R\gamma F + (6\pi R\gamma)^2}], \quad (3)$$

where  $R = R_1 R_2 / (R_1 + R_2)$ . Another important result of the JKR theory gives the adhesion force or "pull off" force

$$F_s = -3\pi R\gamma_s, \quad (4)$$

where, by definition, the surface energy  $\gamma_s$  is related to the reversible work of adhesion  $W$ , by  $W = 2\gamma_s$ . Note that according to the JKR theory a finite elastic modulus  $K$

while having an effect on the load-area curve, has no effect on the adhesion force—an interesting and unexpected result that has nevertheless been verified experimentally.<sup>15,17</sup>

Equation (3) is the basic equation of the JKR theory and provides a suitable framework for measuring the adhesion energies of contacting solids and for studying the effects of surface conditions and time on adhesion energy hysteresis. This can be done in two ways: first, by measuring how  $a$  varies with load (cf. Fig. 3) and comparing this with Eq. (3), and second, by measuring the pull off force and comparing this with Eq. (4). We proceed to describe the results of such experiments. Of course, the JKR theory has been tested before, both for adhering and nonadhering surfaces,<sup>15,17,18</sup> but space does not allow all these experiments to be reviewed here. For nonadhering surfaces,  $\gamma = 0$ , and Eq. (3) reduces to the "Hertzian" limit:  $a^3 = RF/K$ . The inverse cubic dependence of  $a$  on  $F$  was verified by Horn *et al.*<sup>18</sup> for two microscopic, molecularly smooth curved surfaces of mica immersed in aqueous salt solution, where  $\gamma = 0$ . Moreover, the measured  $a$ - $F$  curves were found to be reversible (nonhysteretic) for increasing and decreasing loads. In contrast, for adhering mica surfaces in air ( $\gamma > 0$ ) there was a significant hysteresis in the  $a$ - $F$  curves.

#### E. Direct measurements of adhesion forces and adhesion hysteresis using the surface forces apparatus (SFA) technique

In our studies we have chosen to measure these effects using molecularly smooth mica surfaces onto which well-characterized surfactant monolayers were adsorbed, either by adsorption from solution (sometimes referred to as "self-assembly") or by the Langmuir-Blodgett deposition technique. Different types of surfactants and deposition techniques were used to provide surface-adsorbed monolayers with a wide variety of structural properties (Fig. 4). Further, by varying the surface coverage and temperature the surface layers could be in the solid crystalline, solid amorphous (glassy), liquid crystalline, or liquid states.

The surface forces apparatus technique<sup>18,19</sup> was used for measuring the adhesion or pull off forces  $F_S$ , as well as the loading-unloading  $a$ - $F$  curves for various surface combinations (cf. Fig. 5) under different experimental conditions. The pull-off method allows a measurement only of  $\gamma_R$ , while the  $a$ - $F$  curves give both  $\gamma_A$  and  $\gamma_R$ . We may note that if all these processes were occurring at thermodynamic equilibrium, then  $\gamma_A$  and  $\gamma_R$  should be the same and equal to the well-known literature values of hydrocarbon surfaces, viz.  $\gamma = 23$ – $31$  mJ/m<sup>2</sup>.<sup>20</sup> Note, too, that the phase state of hydrocarbon chains has little effect on  $\gamma$ , as can be ascertained from the similar values for liquid hexadecane ( $27$  mN m<sup>-1</sup>) and solid paraffin wax ( $25$ – $30$  mN m<sup>-1</sup>) at the same temperature of  $25^\circ\text{C}$ .<sup>20</sup> Thus, we would expect the equilibrium values of  $\gamma$  to fall within the range:  $23$ – $31$  mJ/m<sup>2</sup>.

All measurements were carried out after the monolayers had been allowed to equilibrate with an atmosphere of pure, dry nitrogen gas.

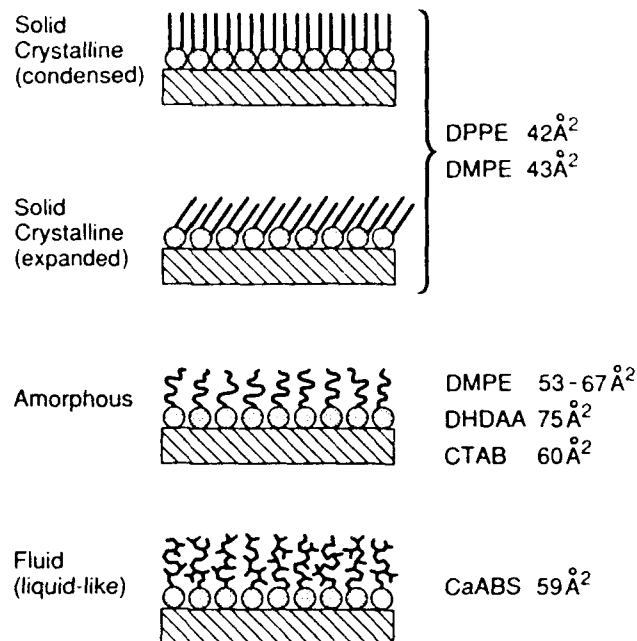


FIG. 4. Likely chain configurations (schematic) of the surface monolayers used in this study. The first two phase states are crystalline solid, the third is solid amorphous or glassy, and the last is liquidlike or gellike. Other possible phase states include various liquid-crystalline states, but these may occur only during shear motion or sliding. (Note that for a surface layer to be in the solid crystalline state each hydrocarbon chain must occupy an area close to the close-packed area of about  $20\text{\AA}^2$  per chain). The full names and structures of the surfactants used are: DPPE (di-palmitoyl-phosphatidyl-ethanolamine, a double 16-carbon saturated hydrocarbon chain surfactant that forms a close-packed crystalline layer when deposited at a surface area of  $42\text{\AA}^2$  per molecule), DMPE (di-myristoyl-phosphatidyl-ethanolamine, like DPPE but with 14 carbons per chain), DHDA (di-hexadecyl-dimethyl-ammonium-acetate, a double 16-carbon saturated chain surfactant that forms a loosely packed amorphous layer because its bulky headgroup prevents the molecular area from being less than about  $75\text{\AA}^2$ ), CTAB (cetyl-dimethyl-ammonium-bromide, a single 16-carbon saturated chain surfactant), CaABS (calcium-alkyl-benzene-sulphonate, a double randomly branched chained surfactant whose chains are in a highly fluidlike or liquid state at room temperature). The value next to each surfactant gives its molecular area in the monolayer as determined during the deposition.

Figure 6 shows the measured  $a$ - $F$  curves obtained for a variety of surface-surface combinations. Both the advancing (open circles) and receding (black circles) points were fitted to Eq. (3). These fits are shown by the continuous solid lines in Fig. 6, and the corresponding fitted values of  $\gamma_A$  and  $\gamma_R$  are also shown.

As already mentioned, under ideal (thermodynamically reversible) conditions  $\gamma$  should be the same regardless of whether one is going up or down the JKR curve, as was shown in Fig. 3(A). This was found to be the case for two solid crystalline monolayers [Fig. 6(A)] and almost so for two fluid monolayers [Fig. 6(B)]. The greatest hysteresis was found for two amorphous monolayers [Fig. 6(C)]. However, no hysteresis was measured when an amorphous or a fluid monolayer was brought together with a solid crystalline monolayer [Fig. 6(D)]. Additionally, in all cases where  $\gamma_R$  was also determined from the measured pull-off force, it was found to be the same as the value

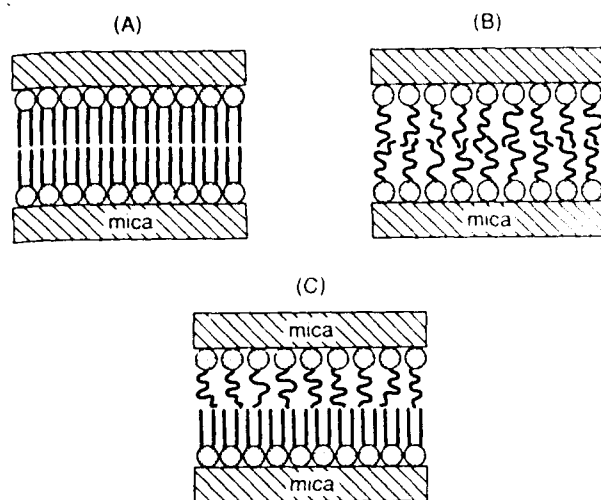


FIG. 5. Schematics of likely chain interdigitations occurring after two surfaces have been brought into contact. (A) Both surfaces in the solid crystalline state—no interdigitation. (B) Both surfaces amorphous or fluid—interdigitation (entanglements) and disentanglements occur slowly for two amorphous surfaces and rapidly for two fluid surfaces. If the surfaces are separated sufficiently quickly, the effective molecular areas being separated from each other will be greater than the "apparent" area, and the receding adhesion will be greater than the advancing adhesion. (C) One surface solid crystalline, the other amorphous or fluid—no interdigitation.

determined independently from the receding branch of the  $a$ - $F$  curve (see legend to Fig. 6).

Our results therefore provide a convincing test of the validity and inherent consistency of the two basic JKR equations, Eqs. (3) and (4). They also show that experimental pull-off forces should, in general, be higher than

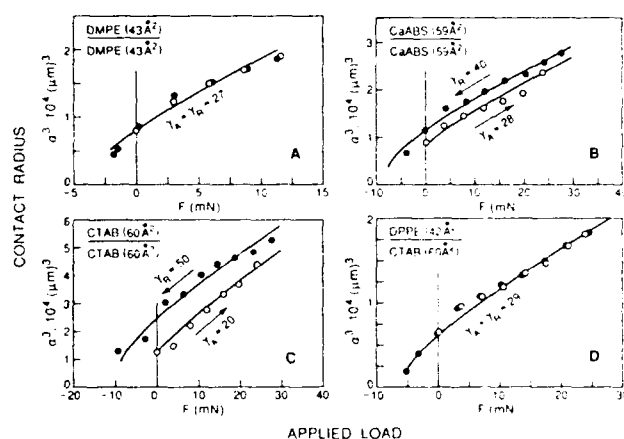


FIG. 6. Measured advancing and receding  $a$ - $F$  curves at 25 °C for four surface combinations. The solid lines are based on fitting the advancing and receding branches to the JKR theory, Eq. (3), from which the indicated values of  $\gamma_A$  and  $\gamma_R$  were determined. At the end of each cycle the pull-off force was measured. For the four cases shown here the following adhesion energy values were obtained based on Eq. (4): (A) crystalline on crystalline:  $\gamma_R = 28$  mJ/m<sup>2</sup>, (B) fluid on fluid:  $\gamma_R = 36$  mJ/m<sup>2</sup>, (C) amorphous on amorphous:  $\gamma_R = 44$ – $76$  mJ/m<sup>2</sup>, (D) amorphous on crystalline:  $\gamma_R = 32$  mJ/m<sup>2</sup>. The equilibrium (literature) values for  $\gamma$  are in the range 23–31 mJ/m<sup>2</sup>.

given by the JKR theory, Eq. (3), unless the system is truly close to equilibrium conditions.

The data presented so far strongly suggests that chain interdiffusion, interdigitation or some other molecular-scale rearrangement occurs after two amorphous or fluid surfaces are brought into contact, which enhances their adhesion during separation. The observation that two solid-crystalline or a crystalline and an amorphous surface do not exhibit hysteresis is consistent with this scenario, since only one surface needs to be frozen to prevent interdigitation from occurring with the other. All this is illustrated schematically in Fig. 5. The much reduced hysteresis between two fluidlike monolayers probably arises from the rapidity with which the molecules at these surfaces can disentangle (equilibrate) even as the two surfaces are being separated (peeled apart).

It appears, therefore, that the ability of molecules or molecular groups to interdiffuse, interdigitate, and/or reorient at surfaces, and especially the relaxation times of these processes, determine the extent of adhesion hysteresis (chemical hysteresis). Little or no hysteresis arises between frozen, rigid surfaces since no rearrangements occur during the time course of a typical loading-unloading cycle. Liquidlike surfaces are likewise not hysteretic, but now because the molecular rearrangements can occur faster than the loading-unloading rates. Amorphous surfaces, being somewhat in between these two extremes are particularly prone to being hysteretic because their molecular relaxation times can be comparable to loading-unloading times (presumably the time for the bifurcation front to traverse some molecular scale length).

If this interpretation is correct it shows that very significant hysteresis effects can arise purely from surface effects, which would be in addition to any contribution from bulk viscoelastic effects. The former involves molecular interdigitations that need not go much deeper than a few angstroms from an interface. Some further experiments support the above picture.

### E. Effects of contact time and temperature on adhesion hysteresis

The adhesion energy as determined from the pull-off force generally increased with the contact time for all the surfaces studied. This is shown in Fig. 7 for two amorphous monolayers of CTAB (defined in Fig. 4) for which the effect was most pronounced. Notice how the hysteresis (as manifested by the changing adhesion with time after the surfaces have been brought into contact) increases the more the monolayer goes into the amorphous, glassy state (15 °C) and disappears once it is heated to well above its chain-melting temperature (35 °C).

Similarly, the rate at which two surfaces were loaded or unloaded also affects their adhesion energy. Again, for two amorphous CTAB surfaces, Fig. 8 shows that on slowing down the loading/unloading rate, the hysteresis loop becomes narrower as both the advancing and receding energies  $\gamma_A$  and  $\gamma_R$  approach the equilibrium value.

One should note that decreasing the unloading or peel-off rate may sometimes act to increase the adhesion, since

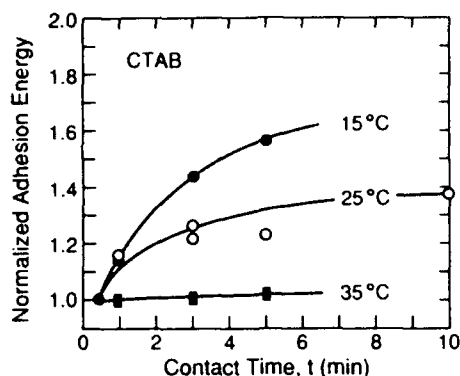


FIG. 7. Effect of contact time on the normalized adhesion energy of two amorphous (CTAB) monolayers with increasing temperature (at 35°C CTAB is in the liquid state). After separation, the adhesion energy returns to its original low value at  $t \approx 0$ .

by decreasing the peeling rate one also allows the surfaces to remain longer in contact. In Fig. 8, the surfaces were first allowed to remain in contact for longer than was needed for the interdigitation processes to be complete (as ascertained from the contact time measurements of Fig. 7).

#### G. Effects of capillary condensation on adhesion hysteresis

Figure 9 shows that when liquid hydrocarbon vapor is introduced into the chamber and allowed to capillary condense around the contact zone, all hysteresis effects disappear. This again shows that by fluidizing the monolayers they can now equilibrate sufficiently fast to be considered always at equilibrium (like a true liquid). Such effects may be expected to occur with other surfaces as well, so long as the vapor condenses as a liquid that also wets the surfaces.

"Stick-slip adhesion" (cf. Fig. 3) on loading but particularly on unloading (peeling) was often found to occur with most of the hysteretic monolayers studied, but this too disappeared when organic vapors were introduced, rendering all loading-unloading cycles totally smooth.

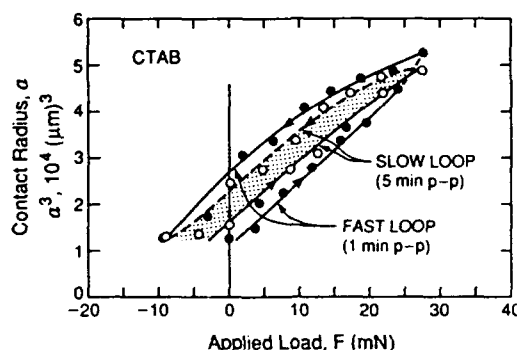


FIG. 8. Effect of advancing/receding rates on  $a$ - $F$  curves for two amorphous CTAB monolayers at 25°C. By fitting the data points to Eq. (3) the following values were obtained. For the fast loop (1 min between data points):  $\gamma_A = 20 \text{ mJ/m}^2$ ,  $\gamma_R = 50 \text{ mJ/m}^2$ . For the slow loop (5 min between points):  $\gamma_A = 24 \text{ mJ/m}^2$ ,  $\gamma_R = 44 \text{ mJ/m}^2$ .

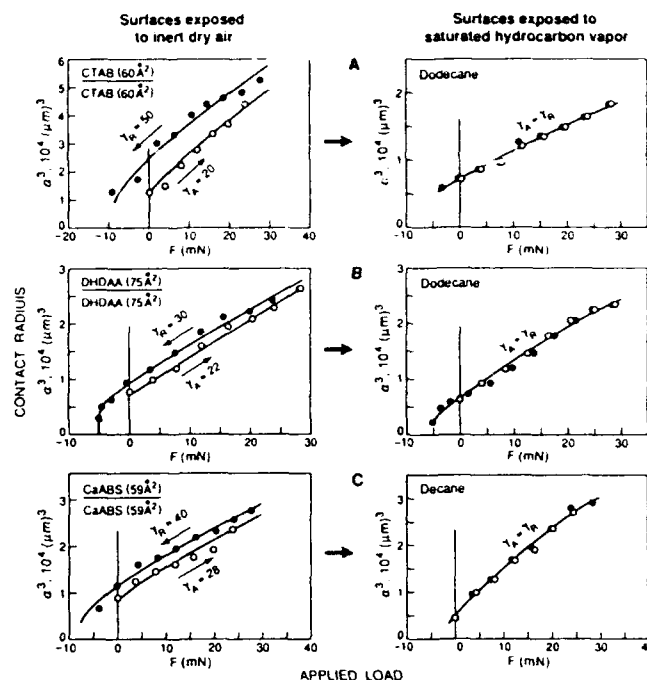


FIG. 9. Disappearance of adhesion hysteresis on exposure of monolayers to various organic vapors. The adhesion energies as measured by the pull-off forces were between 18 and 21 mJ/m² for the three systems shown.

#### H. Summary of molecular origin of adhesion hysteresis

The above results show that the adhesion of two molecularly smooth and chemically homogeneous surfaces can be hysteretic due to structural and chemical changes occurring at the molecular (or even ångström) level. Adhesion hysteresis increases with (i) the ability of the molecular groups at the surfaces to reorient and interdiffuse across the contact interface, which is often determined by the phase state of the surface molecules (i.e., whether the surface layers are in the solid crystalline, solid amorphous or glassy, liquid crystalline, or liquid state), (ii) the time two surfaces remain in contact and the externally applied load during this time, and (iii) the rate of approach and separation (or peeling) of the surfaces.

For the molecularly smooth surfaces studied here, it appears that chemical hysteresis is far more important than mechanical hysteresis. The results also question traditional explanations of hysteresis based purely on the static surface roughness and chemical heterogeneity of surfaces (cf. Fig. 1), and focuses more on the dynamics of these effects.

### IV. INTERFACIAL FRICTION

#### A. Introduction: The properties of liquids in very thin films

When a liquid is confined between two surfaces or within any narrow space whose dimensions are less than 5 to 10 molecular diameters, both the static (equilibrium) and dynamic properties of the liquid, such as its compressibility and viscosity, can no longer be described even qual-



itatively in terms of the bulk properties.<sup>17</sup> The molecules confined within such molecularly thin liquid films become ordered into layers ("out-of-plane" ordering), and they can also have lateral order within each layer ("in-plane" ordering). Such films may be thought of as being more solidlike than liquidlike.

It is now well-established<sup>17,21-23</sup> that the short-range forces between two solid surfaces across molecularly thin films exhibit exponentially decaying oscillations, varying between attraction and repulsion with a periodicity equal to some molecular dimension of the solvent molecules. Such films can therefore sustain a finite normal stress, and the adhesion between two surfaces across a film is "quantized," depending on the number of layers between the surfaces<sup>22,23</sup> and whose magnitude depends also on the "twist" angle between the two surface lattices.<sup>21</sup> The structuring of molecules in thin films and the oscillatory force law this gives rise to are now reasonably well understood, both experimentally and theoretically, at least for simple liquids.<sup>6,21-24</sup>

Work has also recently been done on the dynamic, e.g., viscous or shear, forces associated with molecularly thin films. Both experiments<sup>25-27</sup> and theory<sup>28-30</sup> indicate that even when two surfaces are in steady state sliding they still prefer to remain in one of their stable or "quantized" potential energy minima, i.e., a sheared film of liquid can retain its basic layered structure, though the time scales of molecular hops and the in-plane ordering are modified. Thus, even during motion the film does not regain its totally liquidlike state. Indeed, such films exhibit yield points before they begin to flow. They can therefore sustain a finite shear stress, in addition to a finite normal stress. The value of the yield stress depends on the number of layers comprising the film and represents another quantized property of molecularly thin films.

The dynamic properties of a liquid film undergoing shear are very complex. Depending on whether the film is more liquidlike or solidlike, the motion will be smooth or of the "stick-slip" type—the latter exhibiting yield points and/or periodic "serrations" characteristics of the stress-strain behavior of ductile solids. During sliding, transitions can occur between  $n$  solidlike layers and  $(n-1)$  layers or  $(n+1)$  layers, and the details of the motion depend critically on the externally applied load, the temperature, the sliding velocity, the twist angle, and the sliding direction relative to the surface lattices.

## B. Molecular events within a thin interfacial film during shear

Here we briefly review recent results on the shear properties of simple molecules in thin films and how these are related to changes in their molecular configurations. These have been studied using a sliding attachment for use with the surface forces apparatus technique (Fig. 10). Figure 11 shows typical results for the friction measured as a function of time (after commencement of sliding) between two mica surfaces separated by  $n = 3$  molecular layers of the inert liquid OMCTS (defined in Fig. 11), and how the

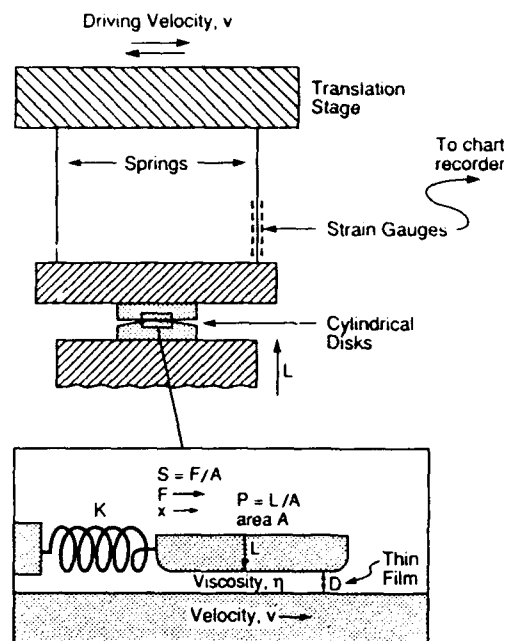


FIG. 10. Schematic drawing of the sliding attachment for use with the surface forces apparatus (Ref. 25).

stick-slip friction increases to higher values in a quantized way then the number of layers falls from  $n = 3$  to  $n = 2$  and then to  $n = 1$ .

With the much added insights provided by recent computer simulations of such systems<sup>28-30</sup> a number of distinct regimes can be identified during the stick-slip sliding that is characteristic of such films, shown in Figs. 12(a) to 12(d).

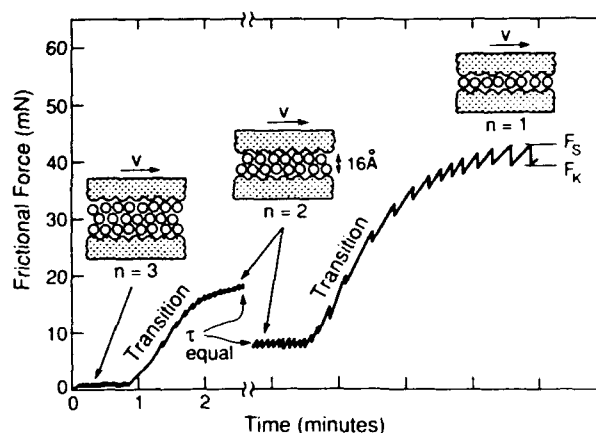


FIG. 11. Measured change in friction during interlayer transitions of the silicone liquid octamethylcyclotetrasiloxane (OMCTS, an inert liquid whose quasi spherical molecules have a diameter of 8 Å) (Ref. 26). In this system, the shear stress (friction force/contact area) was found to be constant so long as the number of layers  $n$  remained constant. Qualitatively similar results have been obtained with cyclohexane (Ref. 25). The shear stresses are only weakly dependent on the sliding velocity  $v$ . However, for sliding velocities above some critical value  $v_c$ , the stick slip disappears and the sliding is now smooth or "steady" at the kinetic value  $F_k$ .

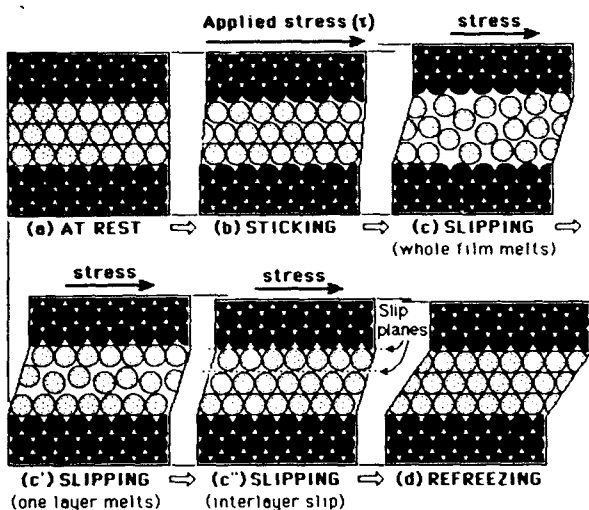


FIG. 12. Schematic illustration of molecular rearrangements occurring in a molecularly thin film of spherical or simple chain molecules between two solid crystalline surfaces during shear. Note that, depending on the system, a number of different molecular configurations within the film are possible during slipping and sliding, shown here as stages (c)—total disorder, (c')—partial disorder, and (c'')—order persists even during sliding with slip occurring at a single slip plane. The configurations of branched-chained molecules is much less ordered (more entangled) and remains amorphous during sliding, leading to smoother sliding with reduced friction and little or no stick slip.

### 1. Surfaces at rest—Figure 12(a)

With no externally applied shear force, solvent-surface interactions induce the liquid molecules in the film to adopt solidlike ordering. Thus at rest the surfaces are stuck to each other through the film.

### 2. Sticking regime (frozen, solidlike film)—Fig. 12(b)

A progressively increasing lateral shear stress  $\tau$ , is applied. This causes a small increase in the lateral displacement and film thickness, but only by a small fraction of the lattice spacing or molecular dimension. In this regime the film retains its solidlike “frozen” state—all the strains are elastic and reversible, and the surfaces remain effectively stuck to each other.

### 3. Slipping and sliding regimes (melted, liquidlike film)—Fig. 12(c), 12(c'), 12(c'')

When the applied shear stress has reached a certain critical value, the film suddenly melts (known as “shear melting”) and the two surfaces begin to slip rapidly past each other once the “static shear stress” ( $\tau_s$ ) or “static friction force” ( $F_s$ ) has been reached (in the language of materials science the “upper yield point” has been reached).

If the applied stress  $\tau$ , is kept at a constant value the upper surface will continue to slide indefinitely. Even if the shear stress is reduced below  $\tau_s$ , steady-state sliding will continue so long as it remains above some critical value, variously referred to as the dynamic or kinetic shear stress

( $\tau_k$ ), the kinetic friction force ( $F_k$ ), or the lower yield point. The experimental observation that the static and dynamic stresses are different suggests that during steady-state sliding the configuration of the molecules within the film is almost certainly different from that during the slip.

Experiments with linear chain (alkane) molecules<sup>26</sup> show that the film thickness remains quantized during sliding, so that the structure of such films is probably more like that of a nematic liquid crystal where the liquid molecules have become shear aligned in some direction enabling shear motion to occur while retaining some order within the film.

Computer simulations for simple spherical molecules<sup>29</sup> indicate that during the slip, the film thickness  $D$  is roughly 15% higher (i.e., the film density falls), and the order parameter drops from 0.85 to about 0.25. Both of these are consistent with a disorganized liquidlike state for the whole film during the slip, as illustrated schematically in Fig. 12(c). At this stage, we can only speculate on other possible configurations of molecules in the sliding regime. This probably depends on the shapes of the molecules (e.g., whether spherical or linear or branched), on the atomic structure of the surfaces, on the sliding velocity, etc. Figure 12(c), 12(c'), and 12(c'') show three possible sliding modes wherein the molecules within the shearing film either totally melt, or where movement occurs only within one or two layers that have melted while the others remain frozen, or where slip occurs between two or more totally frozen layers. Other sliding modes, for example, involving the movement of dislocations or disclinations are also possible, and it is unlikely that one single mechanism applies in all cases.

Clearly, it would be very interesting to establish whether shearing films should be considered more like quasi-ordered liquids or like quasi-disordered solids.

### 4. Freezing transitions—Fig. 12(d)

The slipping or sliding regime ends once the applied shear stress falls below  $\tau_k$ , when the film freezes and the surfaces become stuck once again. Depending on the structure of the surfaces and the liquid molecules, freezing can commensurate immediately after the slip or only after a certain “lag” time or “nucleation” time has elapsed, but once initiated the whole film freezes very rapidly. If the molecules in the film can freeze quickly, the slip is immediately followed by a stick; and if the externally applied stress is maintained the system will go into a continuous stick-slip cycle. This type of sliding usually occurs with simple, spherical liquid molecules that can quickly reorder from from one type of structure (liquid) to another (solid) within the film. On the other hand, if the liquid molecules are irregularly shaped they will not be able to order easily into a more solidlike structure, or their reordering time will be slow. Under such conditions the film will remain in the liquid state: there will be no stick slip and the surfaces will continue to slide smoothly. Experiments with irregularly shaped liquids such as branched alkanes show that the reordering times can be very long—many seconds—once the molecules are confined within a  $\sim 10$  Å film between

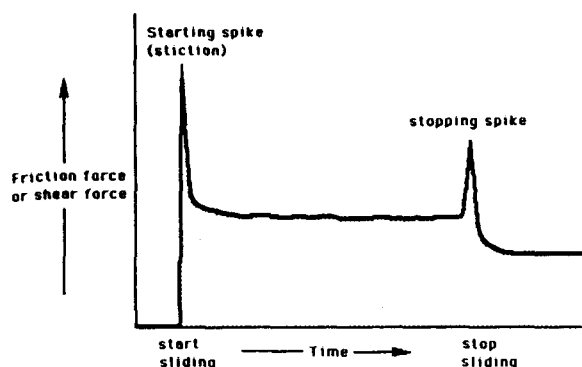


FIG. 13. Stiction is the high starting frictional force experienced by two moving surfaces which causes them to jerk forward rather than accelerate smoothly from rest. It is a major cause of surface damage and erosion. The figure shows a "stiction spike" or "starting spike" as well as a "stopping spike." The latter occurs when two sliding surfaces are brought to rest over a finite time during which the molecules in the film can freeze and stick before the surfaces stop moving.

two compressed surfaces.<sup>26</sup> This time may be compared with typical diffusion reorientational times of  $\sim 10^{-9}$  s for short-chain molecules in the bulk liquid.

However, unless the liquid molecules are highly fluid-like or very irregular in shape,<sup>26,27</sup> there will always be a single stick-slip "spike" on starting. This is known as "stiction" (Fig. 13), and it can be a serious cause of damage when two surfaces start moving from rest.

### C. Variation of friction forces with sliding velocity

A novel interpretation of the well known phenomenon of decreasing coefficient of friction with increasing sliding velocity has been proposed by Thompson and Robbins<sup>29</sup> based on their computer simulation which essentially reproduced the above scenario. This postulates that it is not the friction that changes with sliding speed  $v$ , but rather the time various parts of the system spend in the sticking and sliding modes. In other words, at any instant during sliding, the friction at any local region is always  $F_S$  or  $F_K$ , corresponding to the "static" or "kinetic" values. The measured frictional force, however, is the sum of all these discrete values averaged over the whole contact area. Since as  $v$  increases each local region spends more time in the sliding regime ( $F_K$ ) and less in the sticking regime ( $F_S$ ) the overall friction coefficient falls. Above a certain critical velocity  $v_c$  the stick slip totally disappears and sliding proceeds at the kinetic value.

### D. Shearing experiments with different types of liquids

The above scenario is already quite complicated, and yet this is the situation for the simplest type of experimental system. The factors that appear to determine the critical velocity  $v_c$  depend on the type of liquid between the surfaces (as well as on the surface lattice structure). Small spherical molecules such as cyclohexane and OMCTS have been found to have very high  $v_c$  which indicates that these

TABLE I. Tribological characteristics of some liquids and polymer melts in molecularly thin films between two shearing mica surfaces. Note that a low friction coefficient is generally associated with a high bulk viscosity.

Liquid (dry)	Short-range force	Type of sliding	Friction coefficient	Bulk viscosity (cP)
<b>Spherical molecules<sup>a</sup></b>				
Cyclohexane ( $\sigma = 5 \text{ \AA}$ )	Adhesive	Stick slip	$>1$ (quantized)	0.6
OMCTS ( $\sigma = 9 \text{ \AA}$ )	Adhesive	Stick slip	$>1$ (quantized)	2.3
<b>Chain molecules<sup>a</sup></b>				
Octane	Adhesive	Stick slip	1.5	0.5
Tetradecane	Adhesive	Stick slip	1.0	2.3
Octadecane (branched)	Repulsive	(Stick slip)	0.35	5.5
PDMS ( $M = 3700$ , melt)	Repulsive	Smooth	0.42	50
PBD ( $M = 3500$ , branched)	Repulsive	Smooth	0.03	800
<b>Water</b>				
Water (KCl solution)	Repulsive	Smooth	0.01–0.03	1
Hydrocarbon liquids (wet)	Adhesive <sup>b</sup>	Smooth	0.03	$\sim 1$

<sup>a</sup>PDMS: Polydimethylsiloxane, PBD: Polybutadiene, OMCTS: Octamethylcyclotetrasiloxane.

<sup>b</sup>The strong adhesion between two hydrophilic mica surfaces in wet hydrocarbon liquid is due to capillary forces, i.e., to the resolved Laplace pressure within the condensed water annulus bridging the two surfaces. The direct force between the two surfaces across the liquid (water) is actually repulsive.

molecules can rearrange relatively quickly in thin films. Chain molecules and especially branched chain molecules have been found to have much lower  $v_c$  which is to be expected, and such liquids tend to slide smoothly rather than in a stick-slip fashion. However, the values of  $v_c$  also depend on number of liquid layers comprising the film, the structure and relative orientation of the two surface lattices, the externally applied load, and of course on the stiffness of the spring (and in practice of the material of the surfaces). With more asymmetric molecules, such as branched isoparaffins and polymer melts, no regular spikes or stick-slip behavior occurs at any speed since these molecules can never order themselves sufficiently to "solidify." Example of such liquids are perfluoropolyethers and polydimethylsiloxanes (PDMS).

The shear properties of seven different types of organic and polymeric liquids are listed in Table I, together with the type of sliding observed, the friction coefficient, and the bulk viscosity of the liquids (given for reference purposes). From the data of Table I (top part) it appears that there is a direct correlation between the shapes of molecules and their coefficient of friction. Small spherical or chain molecules have high friction with stick slip because they can pack into ordered solidlike layers, whereas longer chained and branched molecules give low friction and smoother sliding.

It is interesting to note that the friction coefficient gen-

erally decreases as the bulk viscosity of the liquids *increases*. This is because the factors that are conducive to low friction are generally conducive to high viscosity. Thus, molecules with side groups such as branched alkanes and polymer melts usually have higher bulk viscosities than their linear homologues for obvious reasons. However, in thin films the linear molecules have the higher shear stresses. It is probably for this reason that branched liquid molecules are better lubricants—being more disordered in thin films because of this branching. In this respect it is important to note that if an “effective” viscosity were to be calculated for the liquids of Table I, the values would be  $10^6$  to 100 times the bulk viscosities ( $10^6$  for cyclohexane, 100 for polybutadienes, PBD). This indicates that the bulk viscosity plays no direct role in determining the frictional forces in such ultrathin films, at least at low shear rates. However, the bulk viscosity should give an indication of the *lowest* possible viscosity that might be attained in such films. Based on this hypothesis we may surmise that friction coefficients as low as  $10^{-4}$ – $10^{-3}$  might be attainable with the right system.

The only exception to the above correlations is water, which has been found to exhibit both low viscosity and low friction,<sup>31</sup> yet water is essentially a small spherical molecule. In addition, the presence of water can drastically lower the friction and eliminate the stick slip of hydrocarbon liquids when the sliding surfaces are hydrophilic. On the other hand, we have noted that with certain (hydrophobic) surfactant-coated monolayer surfaces and polymer melts the presence of water can act very differently, e.g., enhancing stick slip. However, the results with other surfaces are too few and too preliminary to allow us to draw any general conclusions about the tribological role of water at this stage.

### E. Summary and conclusions on interfacial friction

The static and dynamic properties of molecularly thin films between two solid surfaces cannot be described in terms of parameters or mechanisms applicable to bulk liquids or solids. Such ultrathin films (typically less than 10–40 Å thick) can support both normal and shear stresses, their effective viscosities can be  $10^6$  times the bulk values, molecular relaxations may take  $10^{10}$  times longer (seconds, compared to nanoseconds), and their melting points can be almost totally unrelated to the bulk values. Our results show that during normal sliding the films may undergo many freezing–melting cycles per second (solid–liquid transitions)—a mechanism that manifests itself macroscopically as the commonly observed phenomenon of stick slip.

Most interestingly, experiments on a variety of simple liquids, linear chained hydrocarbons and branched chained polymer melts show that there is a direct correlation between the shapes of molecules and their effectiveness as lubricants (at least at low shear rates). Small spherical or simple chain molecules exhibit high friction with stick slip because they can pack into well-ordered solidlike layers. In contrast, irregularly shaped molecules such as longer chained hydrocarbons or branched polymer liquids remain

in an entangled, disordered, fluidlike state even in very thin films and these give low friction and smoother sliding. It is probably for this reason that irregularly shaped branched chain molecules are usually better lubricants. These findings also lead to the seemingly paradoxical conclusion that molecular entanglements which lead to a *high* viscosity in bulk liquids are conducive to *low* friction when the liquids are confined within a thin film. An understanding of these complex phenomena at the molecular level may help in the processing of better lubricants, more durable surfaces, and better materials.

### ACKNOWLEDGMENTS

I thank the Department of Energy for financial support under Department of Energy (DOE) Grant No. DE-FG03-87ER45331, though this support does not constitute an endorsement by DOE of the views expressed in this article.

This article was presented at the 38th National Symposium of the American Vacuum Society Topical Conference, Surface Science at the Solid–Liquid Interface (TC1).

<sup>1</sup>F. P. Bowden, D. Tabor, *Friction and Lubrication* (Methuen, London, 1967).

<sup>2</sup>J. A. Greenwood, and K. L. Johnson, *Philos. Mag.* **A 43**, 697 (1981); F. Michel, and M. E. R. Shanahan, *C. R. Acad. Sci. Paris* **310** II, 17 (1990); D. Maugis, *J. Mater. Sci.* **20**, 3041 (1985).

<sup>3</sup>C. A. Miller, and P. Neogi, *Interfacial Phenomena* (Decker, New York, 1985).

<sup>4</sup>A. M. Schwartz, *J. Colloid Interface Sci.* **75**, 404 (1980).

<sup>5</sup>U. Landman, W. D. Luedtke, N. A. Burnham, and R. J. Colton, *Science* **248**, 454 (1990); J. B. Pethica, and A. B. Sutton, *J. Vac. Sci. Technol. A* **6**, 2490 (1980).

<sup>6</sup>R. G. Horn and J. N. Israelachvili, *J. Chem. Phys.* **75**, 1400 (1981).

<sup>7</sup>A. L. Weisenhorn, P. K. Hansma, T. R. Albrecht, and C. F. Quate, *Appl. Phys. Lett.* **54**, 26 (1989); P. K. Hansma, V. B. Elings, O. Marti, and C. E. Bracker, *Science* **243**, 1586 (1988).

<sup>8</sup>B. R. Lawn, and T. R. Wilshaw, *Fracture of Brittle Solids* (Cambridge Univ., London, 1975); M. Sahimi, and J. G. Goddard, *Phys. Rev. B* **33**, 7848 (1986).

<sup>9</sup>M. D. Ellul, and A. N. Gent, *J. Polym. Sci.: Polym. Phys.* **22**, 1953 (1984); **23**, 1823 (1985); M. E. R. Shanahan, P. Schreck, and J. Schultz, *C. R. Acad. Sci. Paris* **306** II, 1325 (1988); A. Okawa, B. Sc. thesis, Dept. Materials Science, University of Utah, 1983; F. J. Holly, and M. J. Refojo, *J. Biomed. Mater. Res.* **9**, 315 (1975).

<sup>10</sup>J. Klein, *J. Chem. Soc. Faraday Trans. 1* **79**, 99 (1983); *Makromol. Chem. Macromol. Symp.* **1**, 125 (1986).

<sup>11</sup>H. Yasuda, A. K. Sharma, and T. Yasuda, *J. Polym. Sci., Polym. Phys.* **19**, 1285 (1981).

<sup>12</sup>I. Langmuir, *Science* **87**, 493 (1938); S. R. Wasserman, Y.-T. Tao, G. M. Whitesides, *Langmuir* **5**, 1074 (1985).

<sup>13</sup>Y. L. Chen, M. L. Gee, C. A. Helm, J. N. Israelachvili, and P. M. McGuiggan, *J. Phys. Chem.* **93**, 7057 (1989).

<sup>14</sup>J. D. Andrade, L. M. Smith, and D. E. Gregonis, in *Surface and Interfacial Aspects of Biomedical Polymers*, edited by J. D. Andrade, (Plenum, New York & London, 1985), Vol. 1, p. 249.

<sup>15</sup>K. L. Johnson, K. Kendall, and A. D. Roberts, *Proc. R. Soc. London Ser. A* **324**, 301 (1971).

<sup>16</sup>H. M. Pollock, M. Barquins, and D. Maugis, *Appl. Phys. Lett.* **33**, 798 (1978); M. Barquins, and D. Maugis, *J. Mec. Theor. Appl.* **1**, 331 (1982).

<sup>17</sup>J. N. Israelachvili, *Intermolecular and Surface Forces* (Academic, New York, 1985).

<sup>18</sup>R. G. Horn, J. N. Israelachvili, and F. Pribac, *J. Colloid Interface Sci.* **115**, 480 (1987).

<sup>19</sup>J. N. Israelachvili, and G. E. Adams, *J. Chem. Soc. Faraday Trans. 1* **74**, 975 (1978); J. N. Israelachvili, and P. M. McGuiggan, *J. Mater. Res.* **5**, 2223 (1990).

- <sup>20</sup>W. A. Zisman, *Ind. Eng. Chem.* **55**, 19 (1963); F. M. Fowkes, *Ind. Eng. Chem.* **56**, 40 (1964); W. A. Zisman, and H. W. Fox, *J. Colloid Sci.* **7**, 428 (1952).
- <sup>21</sup>P. McGuiggan and J. Israelachvili, *J. Mater. Res.* **5**, 2232 (1990).
- <sup>22</sup>R. G. Horn, *J. Amer. Ceram. Soc.* **73**, 1117 (1990).
- <sup>23</sup>J. Israelachvili and P. McGuiggan, *Science* **241**, 795 (1988).
- <sup>24</sup>D. Henderson and M. Lozada-Cassou, *J. Colloid Interface Sci.* **114**, 180 (1986).
- <sup>25</sup>J. Israelachvili, A. Homola, and P. McGuiggan, *Science* **240**, 189 (1988).
- <sup>26</sup>M. Gee, P. McGuiggan, J. Israelachvili, and A. Homola, *J. Chem. Phys.* **93**, 1895 (1990).
- <sup>27</sup>A. M. Homola, H. V. Nguyen, and G. Hadzioannou, *J. Chem. Phys.* **94**, 2346 (1991).
- <sup>28</sup>M. Schoen, C. Rhykerd, D. Diestler, and J. Cushman, *Science* **245**, 1223 (1989).
- <sup>29</sup>P. Thompson and M. Robbins, *Science* **250**, 792 (1990).
- <sup>30</sup>U. Landman, W. D. Luedtke, N. A. Burnham, and R. J. Colton, *Science* **248**, 454 (1990).
- <sup>31</sup>A. M. Homola, J. N. Israelachvili, M. L. Gee, and P. M. McGuiggan, *J. Tribology* **111**, 675 (1989); A. M. Homola, J. N. Israelachvili, P. M. McGuiggan, and M. L. Gee, *Wear* **136**, 65 (1990).

# Emergence of atomic-level structural information for ordered metal-solution interfaces: Some recent contributions from *in situ* infrared spectroscopy and scanning tunneling microscopy

Xiaoping Gao, Si-Chung Chang,<sup>a)</sup> Xudong Jiang, Antoinette Hamelin,<sup>b)</sup> and Michael J. Weaver<sup>c)</sup>

Department of Chemistry, Purdue University, West Lafayette, Indiana 47907-1393

(Received 31 October 1991; accepted 17 February 1992)

The utilization of infrared reflection-absorption spectroscopy (IRAS) and scanning tunneling microscopy (STM) for extracting atomic-resolution information for ordered metal-solution interfaces in a related (and relatable) fashion to metal-ultrahigh vacuum (UHV) surfaces is illustrated by means of some recent results from our laboratory. Two specific topics are addressed. The first involves the potential-dependent properties of saturated CO adlayers on low-index platinum and rhodium electrodes in aqueous and nonaqueous media. The central role of the surface potential in controlling the CO adlayer structure is discussed on the basis of *in situ* IRAS data, especially in comparison with the properties of corresponding metal-UHV interfaces. The application of *in situ* atomic-resolution STM in tandem with IRAS for elucidating real-space adsorbate structures is noted for saturated CO adlayers on Rh(111) and Rh(110) electrodes. The second topic concerns the application of *in situ* STM to probe potential-induced reconstruction at gold-aqueous interfaces. All three low-index gold surfaces are seen to undergo reconstruction at potentials corresponding to small ( $\sim 10\text{--}15\text{ }\mu\text{C cm}^{-2}$ ) negative electrode charges. The subtle surface relaxation observed for Au(111) is essentially identical to that observed recently by atomic-resolution STM in UHV. The  $(5\times 27)$  and  $(1\times n)$  ( $n = 2,3$ ) symmetries observed for reconstructed Au(100) and (110) electrodes, respectively, are compatible with the structures deduced for the UHV systems by diffraction methods, although the STM data afford greater real-space detail.

## I. INTRODUCTION

As for metal surfaces in ultrahigh vacuum (UHV) environments, a major goal in electrochemical surface science is to elucidate the structural properties of metal-solution interfaces and to relate them to the kinetic, especially catalytic, processes that can occur there. Several factors, however, have conspired these two fundamentally related areas to develop in distinctly different directions. Most obviously, the early emergence of UHV technology itself along with reliable means of both preparing and characterizing ordered monocrystalline metal surfaces in UHV has led to a major and continuing emphasis being placed on the atomic-level structural characterization of such systems. In physical electrochemistry, particular attention was drawn instead to the mercury-aqueous interface. This emphasis resulted not only from the high degree of cleanliness and reproducibility that can be achieved, but also from the detailed thermodynamic analyses that can be undertaken at such liquid-liquid interfaces, yielding accurate surface compositional parameters. As a consequence of the ease by which rate measurements can be made in electrochemical systems by means of faradaic current flow, much attention has also been given to elucidating reaction kinetics at such surfaces and relating them to the interfacial structure.

Given the major advances evident in the structural characterization of metal-UHV surfaces, electrochemists have nevertheless long been motivated by a desire to "bridge the (pressure) gap" between electrochemical and UHV systems, in an experimental as well as conceptual fashion. A

prominent experimental avenue, developed originally by Hubbard *et al.*,<sup>1</sup> involves emerging monocrystalline electrodes from solution under potential control and transferring them into UHV. Such "*ex situ*" procedures have the major virtue of enabling the full range of UHV-based techniques to be harnessed for electrode surface characterization. On the other hand, the approach is limited by the inevitable removal of volatile surface components and other structural changes that can attend solution-UHV electrode transfer. Another insightful approach involves dosing appropriate molecular components of electrochemical interfaces, especially solutes, solvents, and ionizable species, onto the surface held at sufficiently low temperatures in UHV. This "UHV electrochemical modeling" procedure, pioneered by Sass and co-workers,<sup>2</sup> enables the mutual influence of the various components of the so-called "electrochemical double layer" on adsorbate structure to be examined in sequential fashion. In particular, the effect of varying the interfacial ("electrode") potential can be mimicked by monitoring the changes in work function caused by dosing dipolar and ionizable species.

Despite the power of these *ex situ* approaches, it is apparent that the development of molecular- (and atomic-) level techniques applicable to "*in situ*" electrochemical systems, i.e., with the metal surface in solution under potential control, is of great importance. The relative paucity of the latter applications in the past has been due to the inevitable difficulties in accessing the surface by means of probe photons, electrons, etc., in the presence of a macro-

scopic solution phase. An additional impediment has been the lack of reliable procedures for preparing ordered metal surfaces for inspection in an ambient laboratory environment. In the last ten years or so, however, the use of various flame-annealing and related procedures has been shown to yield well-ordered surfaces for several metals of electrochemical importance, including platinum,<sup>3,4</sup> rhodium,<sup>4(b)</sup> gold, and silver.<sup>5</sup> In turn, the emergence of such straightforward methods of preparing ordered metal surfaces in electrochemical environments is giving new impetus to the usage as well as development of *in situ* methods for examining interfacial atomic and molecular structure.

In this article, we summarize and assess some recent activities being pursued in our laboratory along these lines using two such *in situ* approaches: infrared reflection-absorption spectroscopy (IRAS) and scanning tunneling microscopy (STM). While quite different in character, both these techniques share the virtue of being applicable in a similar fashion to both metal-UHV and metal-solution interfaces. As a consequence, they offer so-far unusual, and even unique, opportunities to explore atomic- and molecular-level phenomena at electrochemical surfaces in the same fashion as the detailed structural information which is familiar for related metal-UHV systems. The links thus forged between these two major variants of metal interfaces should therefore be of significance to surface science as a whole.

We restrict attention here to a brief description of selected applications of IRAS and STM, both separately and in tandem, to the elucidation of surface structure at ordered platinum, rhodium, and gold electrodes in aqueous and nonaqueous media. Experimental and other salient details can be found in the references cited. Two specific issues are addressed here. The first involves the potential-dependent properties of saturated CO adlayers on low-index platinum and rhodium, and the second concerns potential-dependent reconstruction on ordered gold. Both these types of examples emphasize the central role played by the applied surface potential in controlling the interfacial structural properties. Besides illustrating how IRAS and STM can provide structural information for metal-solution as well as metal-UHV surfaces at the atomic level, they also offer the prospect that examining the former systems by this means can prove to be of mutual benefit to both research arenas.

## II. POTENTIAL-DEPENDENT INFRARED SPECTRA FOR CO ADLAYERS: COMPARISONS BETWEEN ELECTROCHEMICAL AND UHV SYSTEMS

Carbon monoxide constitutes an adsorbate of archetypal importance in electrochemical as well as UHV surface science. Its significance to the former class of systems arises in part from the common role of CO as an adsorbed poison towards the catalytic electrooxidation of a variety of organic molecules on platinum and other transition-metal electrodes.<sup>6</sup> From a fundamental perspective, adsorbed CO offers some unique attributes as a structure-sensitive model

adsorbate for intercomparing the properties of ordered metal surfaces in electrochemical and UHV environments. Most importantly, the frequency of the C-O infrared stretching vibration ( $\nu_{\text{CO}}$ ) is extremely sensitive to the surface coordination geometry as well as the local chemical and electrostatic environment; as a consequence, IRAS provides an excellent means of exploring the molecular-level adlayer properties.

Following the development of IRAS for examining adsorbates at metal-UHV interfaces,<sup>7</sup> the last decade has seen a substantial growth in the application of this technique to *in situ* electrochemical surfaces.<sup>8</sup> The complications arising from bulk-phase solvent and other interferences can be minimized and even eliminated by the use of thin-layer electrochemical tactics combined with potential-difference spectral techniques.<sup>8</sup> In our laboratory, we have utilized *in situ* IRAS extensively to explore the structural and kinetic properties of CO adlayers on low-index platinum and rhodium electrodes.<sup>9-17</sup> A recent detailed overview article describing several aspects of this work is available.<sup>9</sup> A basic experimental tactic utilized in these studies is the systematic acquisition of infrared spectra as a function of adsorbate coverage  $\theta_{\text{CO}}$  and electrode potential  $E$ . The former can shed light on the roles of adlayer domain formation and solvent and/or hydrogen coadsorption on the adlayer structure; the latter measurements provide direct assessments of the variable influence of the electrostatic double layer.<sup>9</sup>

We will restrict attention here to ordered metal surfaces containing saturated CO adlayers, formed by dosing with solutions containing near-saturated CO concentrations. In this way, we can minimize (or even eliminate) the influence of solvent coadsorption, and examine the effect of varying the potential across the adlayer on the spectral properties. Figure 1 shows a typical sequence of infrared spectra for a saturated CO adlayer on Pt(111) in acetonitrile, taken from Ref. 16(a). The  $E$  values indicated are the electrode potentials [versus aqueous saturated calomel electrode, (SCE)] to which each spectrum refers. Most notably, the  $\nu_{\text{CO}}$  frequencies of both the higher and lower frequency bands, diagnostic of terminal and bridging CO coordination, respectively, upshift progressively as  $E$  is increased. These  $\nu_{\text{CO}} - E$  dependencies have been ascribed either to potential-induced alterations in the metal-CO bonding, or to a first-order Stark effect arising from variations in electrostatic field across the CO adlayer.<sup>18</sup> [In all likelihood, both of these descriptions are incomplete by themselves. Self-consistent treatments, which take into account both surface bonding and field-induced effects, have been described recently in principle.<sup>19</sup>] In addition, Fig. 1 shows that the bridging band undergoes a sharp  $\sim 50 \text{ cm}^{-1}$  frequency upshift positive of  $\sim 0 \text{ V}$  versus SCE (Fig. 1). This discontinuity, together with a concomitant alteration of both the terminal and bridging  $\nu_{\text{CO}} - E$  slopes at this point, are indicative of a potential-induced adlayer structural change at  $0 \text{ V}$  versus SCE.<sup>16(a)</sup>

It is of central interest to relate these potential-dependent spectral properties to the behavior of the corresponding UHV system. A perusal of the electrochemical

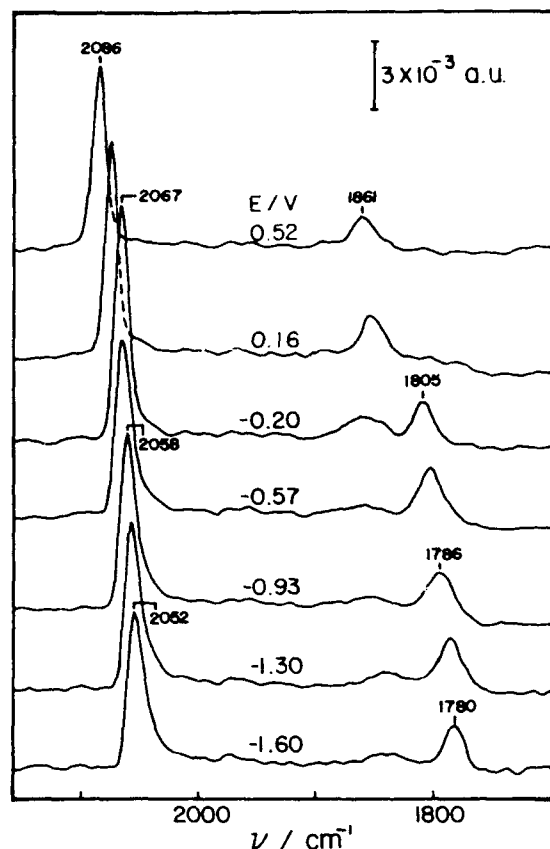


FIG. 1. Sequences of infrared absorbance spectra in the C-O stretching region for CO adlayer on Pt(111) in CO-saturated acetonitrile containing 0.15 M tetrabutylammonium perchlorate, obtained during 2 mV s<sup>-1</sup> positive-going potential sweep from -1.6 V vs SCE. Each spectrum involved acquiring 100 interferometer scans (consuming ~60 s), subtracted from which was a similar set of scans obtained after complete CO electrooxidation, at ~1.0 V. Potentials indicated alongside each spectrum are average values (vs SCE) during the spectral acquisition [see Ref. 16(a) for further details].

infrared spectra at the highest potentials, ~1.0 V versus SCE, indicate a similarity to those obtained for saturated ( $\theta_{\text{CO}} \sim 0.6$ ) CO adlayers on Pt(111) in UHV,<sup>20</sup> in that the intensities of the terminal relative to the bridging band are comparable, and both bands exhibit similar  $\nu_{\text{CO}}$  frequencies (within ~10 cm<sup>-1</sup>) in the two environments.<sup>16(a)</sup>

These similarities, together with related results for other metal/CO adlayer systems, prompt consideration of the potential-dependent nature of such electrochemical surfaces in comparison with metal-UHV systems.<sup>9</sup> The key difference between these two types of metal interfaces is that the metal-solution potential drop  $\phi_s^M$  can be varied continuously by altering the electrode potential  $E$ , whereas the potential drop across metal-vacuum interfaces  $\phi_v^M$  is usually fixed for a given metal and adsorbate composition. Physically, this difference arises from the presence of free charges at electrochemical interfaces, where the excess (or deficiency) of electronic charge accumulated at the metal surface (by virtue of its connection to an external power source) is countered by an equal and opposite ionic charge present, usually as solvated ions at the so-called "outer

Helmholtz plane" (OHP), on the solution side of the interface. (The metal-solution interface can therefore be conceived of as a parallel-plate capacitor.)

At the so-called potential of zero charge  $E_{\text{PZC}}$  this free-charge contribution to  $\phi_s^M$  disappears, at least in the absence of ionic chemisorption as would be anticipated in the presence of saturated CO adlayers. We have obtained approximate estimates of  $E_{\text{PZC}}$  for Pt(111)/CO and other low-index Pt/CO and Rh/CO interfaces in nonaqueous solvents by examining  $\nu_{\text{CO}} - E$  dependencies in electrolytes containing organic cations having different radii.<sup>16</sup> [Note that cations, rather than anions, will accumulate in excess at the OHP in these systems since the electrode potentials accessed lie largely below (i.e., negative of) the  $E_{\text{PZC}}$ .] The different double-layer thicknesses, and hence distinct interfacial potential profiles, thus generated yield dissimilar  $\nu_{\text{CO}} - E$  slopes that should intersect at  $E_{\text{PZC}}$ .<sup>16</sup> This procedure yields relatively high  $E_{\text{PZC}}$  values; for Pt(111)/CO, for example,  $E_{\text{PZC}} \approx 1.0$  V versus SCE [equivalent to 1.25 V versus the normal hydrogen electrode, (NHE)]. The  $\nu_{\text{CO}} - E$  plots are found to be insensitive to the solvent,<sup>13</sup> suggesting that solvent dipole orientation contributes little to the surface potential drop, as might be expected in the presence of a saturated CO adlayer.

On this basis, then, one can surmise that at  $E = E_{\text{PZC}}$  the metal-solution potential drop  $\phi_s^M$  present at, say, Pt(111)/CO electrochemical interfaces will be similar to  $\phi_v^M$  for the corresponding Pt(111)/CO surface in UHV. From the above information, the  $\nu_{\text{CO}}$  frequencies for Pt(111)/CO in the former environment are seen to converge to those in the latter system when  $E \approx E_{\text{PZC}}$ , inferring that a major factor influencing the CO adlayer structure is indeed the average surface potential drop in both cases.<sup>16</sup>

The relation between measured potentials for metal-solution and metal-UHV systems has engendered considerable discussion.<sup>21,22</sup> For the latter interfaces, work-function ( $\Phi_v$ ) measurements provide a direct route to evaluating  $\phi_v^M$ , since  $\Phi_v = e\phi_v^M$ . The assessment of the corresponding metal-solution potential drop  $\phi_s^M$  from electrode potential measurements is less straightforward since the latter are actually potential differences with respect to a reference electrode. The required link with metal-vacuum systems can be made by assessing the so-called "absolute" potential of the reference electrode used,  $E_k(\text{ref})$ .<sup>21</sup> If  $E_k(\text{ref})$  is known, then we can extract  $\phi_s^M$  from the measured electrode potential by using<sup>9</sup>

$$\phi_s^M = E + E_k(\text{ref}) - \chi_s, \quad (1)$$

where  $\chi_s$  is the surface potential of the solution-vacuum interface.<sup>21</sup> (This quantity is commonly estimated to be small, so that  $|\chi_s| \lesssim 0.1 - 0.2$  V.)

There is some controversy regarding the appropriate values of  $E_k(\text{ref})$ , usually considered for the normal hydrogen electrode (NHE). While thermodynamic arguments have led to a value of about 4.45 V for  $E_k(\text{ref})$  of the NHE,<sup>21</sup> higher estimates, 4.7–4.8 V, have been obtained from work-function measurements for electrodes transferred into UHV<sup>22,23</sup> and by other means.<sup>24</sup> Using an average value  $E_k(\text{ref}) = 4.6 \pm 0.2$  V and given that  $E_{\text{PZC}}$



for the Pt(111)/CO electrochemical interface (in acetonitrile) is about 1.25 V versus NHE (*vide supra*), if  $\chi_s$  is neglected we deduce from Eq. (1) that the metal-solution potential drop at  $E_{PZC}$  is  $\phi_s^M \approx 5.9$  V. Interestingly, the latter value is essentially equal to the potential drop at the Pt(111)/CO-vacuum interface  $\phi_s^M$  as extracted from work-function measurements.<sup>11(b),25</sup> This identity deduced between  $\phi_s^M$  for the *uncharged* electrochemical system and  $\phi_s^M$  for the corresponding (necessarily uncharged) metal-UHV interface further supports the major role played by the surface potential drop in controlling the adlayer properties.

It is appropriate to comment further on the potential-induced changes in the CO adlayer properties observed at transition-metal electrochemical interfaces in comparison with the metal-UHV systems. Under most circumstances, the electrode potential ranges accessible in electrochemical environments lie well ( $\sim 1$ – $2$  V) below  $E_{PZC}$ , i.e., correspond to negative electrode charges. This is especially the case in aqueous media, where adsorbed CO electrooxidation to form CO<sub>2</sub> typically occurs at low potentials. Nevertheless, most IRAS studies of this type in our laboratory as well as elsewhere have utilized aqueous, and especially acidic aqueous, media. There are several reasons for this choice, including the use of surface pretreatment procedures that utilize aqueous solutions, and the observation of voltammetric features in such media that have proved to be diagnostic of the surface order.<sup>3,4</sup>

A notable feature of the CO adlayer structures on low-index platinum and especially rhodium electrodes is the sensitivity of the CO binding geometries to the electrode potential.<sup>9,10</sup> Decreasing the potential (so to increase the negative charge density) tends to favor increasingly bridging versus atop CO coordination.<sup>9,10</sup> The effect can be understood qualitatively in terms of the increased degree of  $d\pi - 2\pi^*$  metal-ligand backbonding that occurs as the metal charge becomes more negative.<sup>9,10,17</sup> In addition, the CO coordination geometry is sensitive to both the nature of the metal surface and its crystallographic orientation.<sup>9,10</sup> These latter effects by themselves are well known from studies of the corresponding metal-UHV interfaces. Significantly, different surface-dependent CO binding geometries, however, can be obtained in electrochemical environments due to the additional influence of the applied potential.<sup>9,10</sup>

Theoretical understanding of these trends has so far been pursued largely on a qualitative level. The molecular orbital atom superposition and electron delocalization molecular orbital (ASED-MO<sup>26</sup>) method of Anderson, involving potential-induced shifts in the surface valence-band energy,<sup>8(a)</sup> has been used with some success to describe CO site occupancies on Pt and Pd surfaces,<sup>27</sup> and to account for the marked differences in potential-dependent CO binding geometries observed on Rh(111) versus Rh(100).<sup>17</sup> In addition, the ASED-MO model can account semiquantitatively for the observed<sup>9,10,15</sup> propensity for atop versus bridging coordination on (111) planes for Pt-group metals in the sequence Ir > Pt > Rh > Pd.<sup>28</sup> While the ASED-MO method does therefore appear to provide a useful semi-

empirical means of describing potential-dependent surface bonding, as noted above it ignores the influence of electrostatic field on the adsorbate, presuming tacitly that the surface potential drop falls entirely *between* the metal and the adsorbate molecule; it also does not consider explicitly the surface charge density. A more self-consistent picture of potential-dependent surface binding, taking these combined factors into account,<sup>19</sup> will hopefully be forthcoming.

### III. STM AND IRAS AS COMBINED PROBES OF ADLAYER STRUCTURE: CO ON Rh(111) AND Rh(110) ELECTRODES

While IRAS can yield detailed insight into the coordination geometry of CO and other suitable adsorbates, it lacks the spatial information required to deduce real-space adlayer structures. In UHV environments, such information is commonly provided by low-energy electron diffraction (LEED). In a number of cases, the required spatial structural arrangement of the adlayer with respect to the underlying substrate has been deduced from the LEED adlayer symmetry in combination with site occupancies as obtained from vibrational spectra.<sup>29</sup> Such tactics are inapplicable to *in situ* electrochemical interfaces, where LEED usually cannot be employed. However, the recent emergence of STM as a *truly* atomic-resolution structural probe applicable to metal-solution,<sup>30,31</sup> as well as to other metal (and semiconductor), interfaces is beginning to change this situation. Indeed, in suitable cases atomic-resolution STM offers a detailed assessment of the real-space adlayer structure, rather than merely an assignment of the unit-cell symmetry as is commonly extracted from LEED measurements. (The deduction of the real-space adlayer arrangement within the unit cell requires dynamical LEED analyses, the execution of which is usually not unambiguous.)

A difficulty with STM, however, is that at the present stage of technique development the interpretation of atomic-resolution images is often not clearcut. Apart from the need for near-optimal tunneling conditions so to obtain the desired spatial resolution, the surface electronic properties that determine the observed images are incompletely understood. For these reasons, together with the need to match the adlayer structure with that of the underlying substrate (i.e., determine adsorbate surface binding sites), it is desirable to couple STM with an independent *in situ* structural probe, such as IRAS.

We have chosen for initial study in this regard saturated CO adlayers on low-index rhodium-aqueous interfaces. Pertinent results are summarized here for Rh(111) and (110); original STM data are shown for the latter surface since they are unavailable elsewhere. As already mentioned, significantly potential-dependent CO structures are often deduced from IRAS, arising from the increased propensity for bridging versus terminal coordination as the electrode potential is decreased. For Rh(111) in aqueous 0.1 M NaClO<sub>4</sub>, in particular, a relatively sharp, yet reversible, structural transition from primarily terminal to bridging CO coordination is observed as the potential is lowered below  $\sim -0.1$  to  $-0.2$  V versus SCE.<sup>10(a)</sup>

The extraction of detailed adlayer structures from a comparison between the corresponding potential-dependent IRAS and STM data for Rh(111)/CO is outlined in Ref. 32. Briefly, at potentials above where adsorbed CO electrooxidation proceeds ( $\sim 0.3$  V), well-defined STM images of the Rh(111) substrate are obtained, consisting specifically of image "spots" (tunneling maxima) spaced in a hexagonal array 2.7 Å apart. At lower potentials, where the close-packed CO adlayers are present, markedly different STM images were obtained that reflect the structure of the adlayer rather than the underlying substrate.

Significantly, two distinct images are obtained over the same potential regions where the two CO adlayer structures, as deduced by IRAS, are present. At potentials above  $\sim -0.1$  V versus SCE, a structure having  $(2 \times 2)$ -3CO symmetry is discerned. The CO coverage thus deduced,  $\theta_{\text{CO}} = 0.75$ , is in agreement with the value determined from voltammetry and infrared spectrophotometry. Of the three distinguishable STM spots within the  $(2 \times 2)$  unit cell, two are noticeably "brighter" (i.e., induce greater tunneling current). The corresponding IRAS data show the presence of two-thirds of the adsorbate ( $\theta_{\text{CO}} = 0.5$ ) present in atop (or near-atop) sites, with one-third ( $\theta_{\text{CO}} = 0.25$ ) in a bridging geometry (as deduced by  $\nu_{\text{CO}}$  bands at 2025–2045 and 1800–1820  $\text{cm}^{-1}$ , respectively). On this basis, then, the brighter and weaker STM spots are attributed to tunneling via atop and bridging CO's, respectively; this conclusion is also consistent with the intuitive prediction of greater tunneling current (at constant tip-surface separation) via the atop adsorbate. A very similar  $(2 \times 2)$  structure for the Rh(111)/CO ( $\theta_{\text{CO}} = 0.75$ ) surface in UHV was deduced earlier on the basis of dynamical LEED measurements.<sup>33</sup> The occurrence of such similar adlayer structures at the electrochemical interface at higher potentials with the corresponding UHV system is in harmony with the important role of surface potential in determining adlayer structure, outlined above.

At potentials below  $-0.2$  V, markedly different STM images, having  $(3 \times 3)$  rect-4CO symmetry ( $\theta_{\text{CO}} = 0.67$ ), are obtained. Matching these results again with the corresponding IRAS data, only a single CO in the unit cell is identified as atop, two of the three remaining CO's being present in asymmetric bridging sites (appearing as a prominent  $\nu_{\text{CO}}$  band at 1885–1900  $\text{cm}^{-1}$ ). Both the high- and low-potential adlayer structures appear to represent a compromise between the energetic preferences for CO binding, favoring atop and bridging CO coordination, respectively, and the surface stereochemical constraints necessary to reach the observed high packing densities [cf. Ref. 20(b)].

In contrast to Rh(111), saturated CO adlayers on Rh(110) display no sharp potential-dependent changes in binding geometry as deduced from IRAS. Thus over the potential range from  $-0.25$  to  $0.25$  V versus SCE in  $0.1$  M  $\text{HClO}_4$ , both atop and bridging  $\nu_{\text{CO}}$  features are observed (at 2020–2040 and 1890 to 1910  $\text{cm}^{-1}$ , respectively) with comparable integrated intensities, even though the latter binding mode is favored increasingly towards lower potentials.<sup>10(a)</sup> Comparison with the corresponding

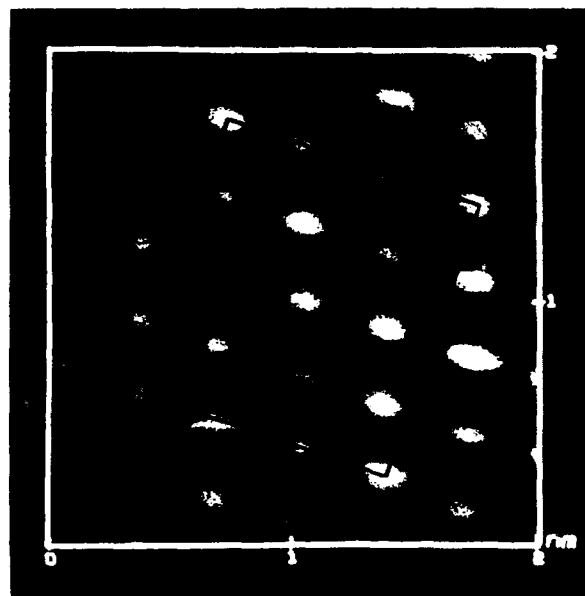


Fig. 2. Midly FT-filtered top-view STM image of  $(4 \times 3)$ -12CO structure obtained for Rh(110) in CO-saturated aqueous  $0.1$  M  $\text{HClO}_4$  at  $-0.2$  V vs SCE. Rectangle shown refers to unit cell as depicted in Fig. 3. Image was obtained in "constant-height" mode. Tunneling conditions: bias voltage  $V_b = 4$  mV, set-point current  $i_s = 20$  nA.

Pt(110) system illustrates the anticipated greater propensity for bridging versus atop CO coordination on rhodium; while the saturated CO coverage is essentially unity on both surfaces, Pt(110) displays almost entirely terminal coordination.<sup>10(a),12(c)</sup>

A typical atomic-resolution STM image for Rh(110) in CO-saturated  $0.1$  M  $\text{HClO}_4$  (at  $-0.2$  V versus SCE) is displayed in Fig. 2. [See the figure caption along with Ref. 32 for STM procedural details. The Rh(110) crystal, 9 mm diam and 2 mm thick, was pretreated by a flame-annealing/iodine coating procedure as in Ref. 13(a) (cf. Ref. 4)]. The image is seen to consist of strings of individually resolved spots (i.e., regions of higher tunneling current in a direction  $\sim 20^\circ$  to the  $x$  axis). These rows correspond closely to the  $[1\bar{1}0]$  direction as discerned from x-ray back diffraction. Comparable images were obtained over the potential range from  $-0.25$  to  $0.1$  V versus SCE. Several properties of the STM images (as seen in Fig. 2) enable the CO adlayer symmetry to be deduced. First, the distances between spots along the  $[1\bar{1}0]$  direction, 3.5 Å, and across these rows in the  $[001]$  direction, 2.75 Å, both differ from those expected (and observed) for the  $(1 \times 1)$  Rh(110) surface,<sup>34</sup> 2.7 and 3.8 Å, respectively.<sup>35</sup> [The  $x$  and  $y$  distances evaluated by the STM piezoelectric drivers are calibrated by examining substrate images for well-defined surfaces, such as Au(111) and Rh(111), and are reliable to  $\sim \pm 10\%$ .] Second, instead of the spots in adjacent rows being lined up in the  $[001]$  direction, as for the substrate atoms or for a  $(1 \times 1)$  commensurate adlayer ( $\theta_{\text{CO}} = 1.0$ ), they are seen to form parallel lines running at  $\sim 75^\circ$  to the  $[1\bar{1}0]$  direction (Fig. 2).

These two pieces of information both indicate that an

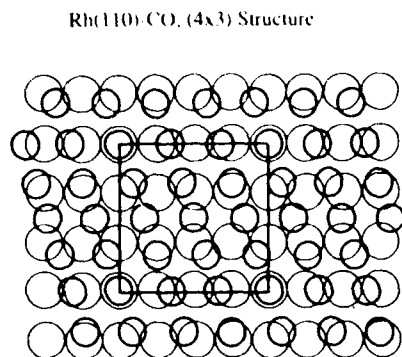


FIG. 3. Proposed top-view ball model for (4×3)-12CO adlayer structure on Rh(110). The top-layer rhodium atoms are depicted as the larger circles, with smaller circles representing position of individual CO adsorbate molecules as deduced from STM image in Fig. 2 (see text for details).

adlayer (rather than a substrate) image is obtained for the Rh(110)/CO ( $\theta_{\text{co}} = 1$ ) surface, which is not commensurate in simple fashion with the metal lattice. Nevertheless, a definite symmetry of the adlayer with respect to the substrate can be confirmed from the mild yet discernable intensity pattern in the STM spots, whereby every third spot along the  $[1\bar{1}0]$  rows tends to be more intense. Assuming, as before, that such spots are associated with CO bound to symmetric atop sites leads to the suggested "ball-model" adlayer structure shown in Fig. 3. (The smaller and larger circles in Fig. 3 depict the CO adsorbate, and Rh surface atoms, respectively.) The (4×3)-12CO structure depicted matches well with the STM images (see the corresponding unit cell superimposed on Fig. 2), and has the correct CO coverage ( $\theta_{\text{co}} = 1.0$ ).

Careful inspection of Fig. 3 reveals that besides the single symmetric atop CO (located on the corners of the unit cell as drawn), most of the remaining CO's are situated in asymmetric atop or bridging sites. This structure might appear to be in disagreement with the corresponding IRAS data which, as noted above, consists of only two discrete  $\nu_{\text{co}}$  bands diagnostic of terminal and bridging coordination geometries.<sup>10(a)</sup> While the infrared spectra certainly cannot confirm the STM-deduced adlayer structure, the two data sets are, however, not inconsistent. Thus the terminal  $\nu_{\text{co}}$  frequency is expected to be insensitive to displacement away from symmetrical atop sites, and distributions of nearby CO's in similar, yet distinct, sites can appear as single relatively narrow  $\nu_{\text{co}}$  bands as a result of intensity transfer effects.<sup>20</sup> At least qualitatively, then, the appearance of a pair of broad, relatively asymmetric,  $\nu_{\text{co}}$  bands in the infrared spectra, nominally associated with atop and bridging configuration,<sup>10(a)</sup> is in reasonable harmony with the real-space adlayer structure as deduced from STM.

As for the Rh(111) surface, the structure of saturated CO adlayers on Rh(110) appears to result from adsorbate packing considerations intertwined with site-specific binding energies. A similarly complex (2×4) structure for saturated CO on Rh(100) in aqueous 0.1 M HClO<sub>4</sub> has also been deduced from STM,<sup>36</sup> reflecting a combination of

atop and bridge-bound adsorbate as seen by IRAS.<sup>10(a),13(b)</sup> It would be of great interest to pursue STM measurements for these and other CO adlayer systems in related UHV environments. It is nonetheless appropriate to point out an important (perhaps obvious) limitation of such STM measurements: the extraction of such real-space atomic structures requires that the adlayer is extremely immobile. Adsorbate motion of only several angstroms on the long ( $\geq 10^{-1}$  s) time scale required to obtain at least a portion of the STM x-y scan should seriously "blur" the resulting image. The compressed CO adlayers are presumably sufficiently immobile to satisfy this requirement.

#### IV. POTENTIAL-DEPENDENT SURFACE RECONSTRUCTION AS PROBED BY ATOMIC-RESOLUTION STM

This article has so far concentrated on one specific, albeit important, topic: the structural properties of CO adlayers on transition-metal electrodes. As already noted, STM also offers considerable promise for elucidating the atomic structure of ordered metal surfaces in the absence of chemisorbed adlayers.<sup>30</sup> While low-index rhodium surfaces usually display simple bulk-terminated [i.e., (1×1)] surface structures even in the absence of chemisorption, many other metal surfaces are known to reconstruct to form markedly different atomic rearrangements.<sup>37</sup> An interesting example is gold, especially so since emersion of low-index gold electrodes from solution into UHV, followed by LEED and related characterization, have indicated the presence of potential-dependent surface reconstruction, triggered at lower electrode potentials.<sup>38</sup> We have recently utilized *in situ* STM to explore in detail the electrode potential-induced reconstruction of both ordered low- and higher-index gold surfaces in aqueous solution.<sup>39-42</sup> The primary findings, particularly as they relate to the behavior of the corresponding gold-UHV interfaces, are summarized briefly here.

The Au(111)-UHV surface is unique among face-centered-cubic (fcc) metals in undergoing a subtle, yet significant, reconstruction as deduced originally by diffraction techniques,<sup>43</sup> and latterly in remarkable detail by atomic-resolution STM.<sup>44,45</sup> The ( $\sqrt{3} \times 22$ ) reconstruction features a periodic alteration from fcc to hexagonal-close-packed (hcp) stacking, yielding parallel pairs of mild corrugations along one of the  $[11\bar{2}]$  directions, i.e., at an angle midway between a pair of intersecting close-packed atomic rows. Intriguingly, an essentially identical reconstruction pattern is observed by STM at the Au(111)-aqueous 0.1 M HClO<sub>4</sub> interface at potentials below  $\sim -0.1$  V versus SCE, i.e., at small negative electrode charge densities ( $\sim -10$  to  $-15$   $\mu\text{C cm}^{-2}$ ).<sup>40</sup> Moreover, most of the longer-range superstructures occurring in the UHV system are also observed in the *in situ* electrochemical environment. An interesting difference, however, is that an essentially unreconstructed Au(111) surface is obtained at  $E_{\text{pzc}}$  (0.25 V versus SCE),<sup>40</sup> even though the Au(111)-UHV surface is also necessarily uncharged (*vide supra*). This difference may well be due to the influence of the interfacial water, or conceivably to adsorbed perchlorate anions.

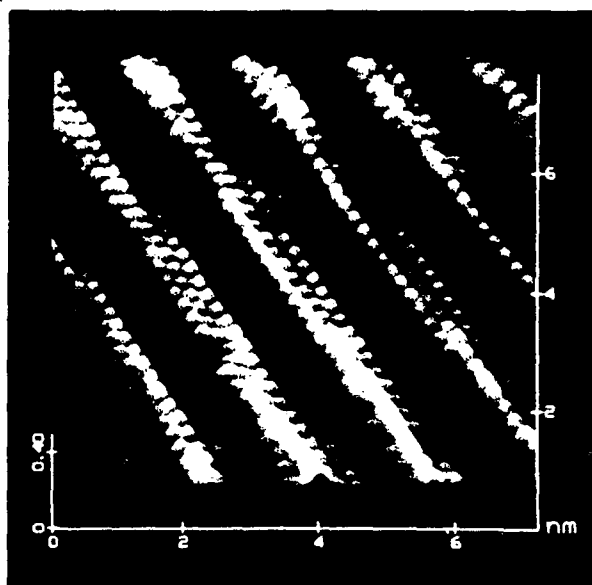


FIG. 4. Height-shaded STM image for reconstructed Au(100) surface in aqueous 0.1 M HClO<sub>4</sub> at  $-0.4$  V vs SCE. Image was obtained in "constant-current" mode. Tunneling conditions:  $V_b = 10$  mV,  $I_t = 20$  nA. (See Ref. 39 for other details.)

Both Au(100) and (110) in aqueous 0.1 M HClO<sub>4</sub> are also largely unreconstructed at  $E_{PZC}$ , yet undergo marked reconstruction at somewhat (0.2–0.3 V) lower potentials.<sup>39,41</sup> Figure 4 shows a representative height-shaded STM image, viewed 30° off the surface normal, obtained for Au(100) at  $-0.3$  V versus SCE (see Ref. 39 for details). Evident are corrugated strings of atoms which form in a given  $[0\bar{1}1]$  and  $[01\bar{1}]$  direction along the previously square-planar  $(1 \times 1)$  lattice. A buckled quasi-hexagonal arrangement is formed, featuring six atoms packed across each corrugation, replacing five atoms in the  $(1 \times 1)$  structure. In addition, large ordered domains exhibit a regular longer-range periodicity along the row direction, featuring undulations of the gold strings (see Fig. 4). These 14-atom periodic transitions (between structures I and II as described in Ref. 39) yield a mild compression along the row direction, so that 28 atoms are present in place of 27 for the unreconstructed surface. The net  $(5 \times 27)$  symmetry designation of the Au(100) reconstruction is compatible with earlier detailed diffraction analyses for clean Au(100) in UHV,<sup>43,46</sup> although the latter *reciprocal-space* techniques cannot diagnose such structures with confidence. [We discuss the assignment of this structure in detail elsewhere.<sup>39(b)</sup>] In keeping with the substantial (24%) increase in forming the  $(5 \times 27)$  structure from the  $(1 \times 1)$  square-planar lattice, the reconstruction dynamics are slow, requiring  $\sim 10$  min for completion at  $-0.3$  to  $-0.4$  V. The STM images also indicate that the additional gold atoms diffuse from terrace and other domain edges.

Figure 5 is an illustrative height-shaded STM image, again viewed 30° off the surface normal, for Au(110) in 0.1 M HClO<sub>4</sub> at  $-0.3$  V versus SCE. (See Ref. 41 for details.)

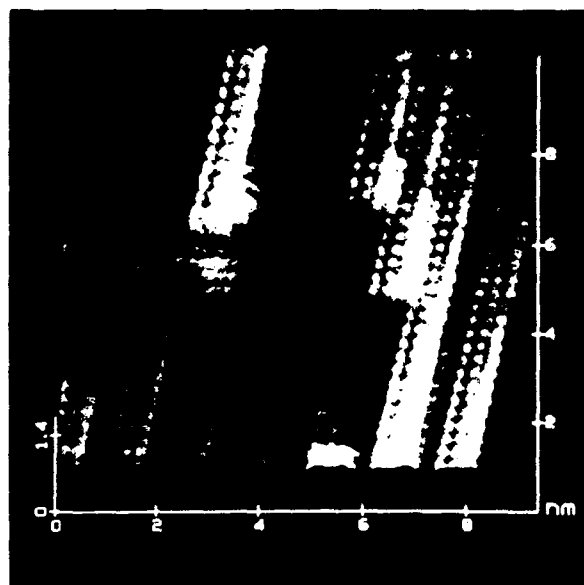


FIG. 5. Height-shaded STM image of reconstructed Au(110) surface in aqueous 0.1 M HClO<sub>4</sub> at  $-0.3$  V vs SCE, showing  $(1 \times 2)$  and  $(1 \times 3)$  regions. Image was obtained in constant-current mode. Tunneling conditions:  $V_b = 5$  mV,  $I_t = 25$  nA.

This image shows the characteristic feature of the Au(110) reconstruction: stacked sets of parallel ribbon segments, running along the  $[1\bar{1}0]$  crystallographic direction. Each ribbon consists of a trio of three parallel rows of gold atoms. The spacing between these ribbons is mostly  $(4.0 \times n)$  Å, where  $n = 2$  or 3, i.e., corresponding to  $(1 \times 2)$  or  $(1 \times 3)$  symmetries, respectively. The former symmetry corresponds to the "missing-row" reconstruction commonly proposed for clean Au(110) in UHV.<sup>47</sup> However, detailed examination of the  $(1 \times 2)$  STM images indicates that some "surface relaxation" occurs, involving both the top and underlying gold atoms so to form a significant asymmetric structure involving pairing of second-layer atoms.<sup>41</sup>

The  $(1 \times 3)$  regions, exemplified in the bottom left-hand segment of the image in Fig. 5, appear as separated ribbons overlaid on the underlying substrate. In this sense, the resulting structures can be viewed as forming "added-," rather than "missing-," row domains. The concerted motion of atoms required to form (or remove) such reconstructions appear to involve migration both across and along the rows. The small and rather irregular domain sizes observed typically on reconstructed Au(110) suggest that only short-range atomic motion is required. Consistent with this last feature is the observation that the potential-induced structural changes are surprisingly rapid as well as near reversible, the reconstruction being lifted largely within  $\sim 2$  s upon stepping the potential from  $-0.3$  to 0 V versus SCE, and reappearing on the same timescale when the potential is returned to  $-0.3$  V.<sup>41</sup>

As for Au(111), both Au(100) and (110) form stable  $(1 \times 1)$  structures in the aqueous electrochemical environment at  $E_{PZC}$ , whereas the corresponding clean surfaces in

UHV are reconstructed. Nevertheless, the role of negative surface electronic charge density in triggering reconstruction is in harmony with some theoretical predictions for low-index noble metal surfaces.<sup>48</sup>

Most recently, we have examined potential-dependent structures of higher-index, especially stepped, gold surfaces, such as Au(210), (533), (311), and (221) in 0.1 M HClO<sub>4</sub>. Perhaps surprisingly, these surfaces undergo only mild reconstruction, occurring again at negative electrode charges, that involves slight relaxation of the atoms forming (or adjacent to) the monoatomic steps. These results are described in detail elsewhere<sup>42</sup>; they offer significant implications for the interpretation of surface crystallographic effects on electrocatalytic processes.<sup>49</sup>

While the foregoing is necessarily an incomplete summary, focusing only on recent results from our own laboratory, it is now evident that both IRAS and STM can provide molecular- and atomic-level structural information for ordered metal-solution interfaces at a level of detail (and understanding) which is on a par with the well-established applications of these techniques to metal-UHV systems. While experimental inquiries for electrochemical interfaces along these general lines have been pursued for some time by means of *ex situ* emersion procedures,<sup>1</sup> the development of such *in situ* techniques offers a significant new dimension in electrochemical surface characterization. Together, then, this expanding family of experimental methods should encourage an increasing commonality of understanding in electrochemical and ultrahigh vacuum surface science.

## ACKNOWLEDGMENTS

This work is supported by the National Science Foundation and the Office of Naval Research.

This article was presented at the 38th National Symposium of the American Vacuum Society Topical Conference, Surface Science at the Solid-Liquid Interface (TC1).

<sup>41</sup>Present address: Dow Chemical Co., Midland, MI 48674.

<sup>42</sup>Permanent address: Laboratoire d'Electrochimie Interfaciale du C.N.R.S., 1, Place A. Briand, 92195, Meudon, France.

<sup>43</sup>Author to whom correspondence should be addressed.

<sup>1</sup>For example: A. T. Hubbard, *Chem. Rev.* **88**, 633 (1988).

<sup>2</sup>For example: J. K. Sass and K. Bange, *ACS Symp. Ser.* **378**, 54 (1988).

<sup>3</sup>(a) J. Clavilier, R. Faure, G. Guinet, and R. Durand, *J. Electroanal. Chem.* **107**, 205 (1980); (b) Also see: J. Clavilier, *ACS Symp. Ser.* **378**, 202 (1988).

<sup>4</sup>(a) D. Zurawski, L. Rice, M. Hourani, and A. Wieckowski, *J. Electroanal. Chem.* **230**, 221 (1987); (b) M. Hourani and A. Wieckowski, *ibid.* **227**, 259 (1987).

<sup>5</sup>A. Hamelin, in *Modern Aspects of Electrochemistry*, edited by B. E. Conway, R. E. White, and J. O'M. Bockris (Plenum, New York, 1986), Vol. 16 Chap. 1.

<sup>6</sup>For example: L.-W. H. Leung and M. J. Weaver, *Langmuir* **6**, 323 (1990).

<sup>7</sup>For example: A. M. Bradshaw and E. Schweizer, in *Spectroscopy of Surfaces*, *Advances in Spectroscopy*, edited by R. J. H. Clark and R. E. Hester (Wiley, New York, 1988), Vol. 16, p. 413.

<sup>8</sup>(a) A. Bewick and S. Pons, in *Advances in Infrared and Raman Spectroscopy*, edited by R. J. H. Clark and R. E. Hester (Wiley, New York, 1985), Vol. 12, Chap. 1; (b) P. Christensen and A. Hamnett, in *Comprehensive Chemical Kinetics*, edited by R. G. Compton and A. Hamnett (Elsevier, Amsterdam, 1989), Vol. 29, Chap. 1.

<sup>9</sup>For an overview: S.-C. Chang, and M. J. Weaver, *J. Phys. Chem.* **95**, 5391 (1991).

<sup>10</sup>(a) S.-C. Chang, and M. J. Weaver, *Surf. Sci.* **238**, 142 (1990); (b) S.-C. Chang, J. D. Roth, Y. Ho, and M. J. Weaver, *J. Electron Spectrosc. Relat. Phenom.* **54/55**, 1185 (1990).

<sup>11</sup>(a) L.-W. H. Leung, A. Wieckowski, and M. J. Weaver, *J. Phys. Chem.* **92**, 6985 (1988); (b) S.-C. Chang, L.-W. H. Leung, and M. J. Weaver, *ibid.* **93**, 5341 (1989).

<sup>12</sup>(a) S.-C. Chang, and M. J. Weaver, *J. Chem. Phys.* **92**, 4582 (1990); (b) **94**, 5095 (1990); (c) *Surf. Sci.* **230**, 222 (1990); (d) J. D. Roth, S.-C. Chang, and M. J. Weaver, *J. Electroanal. Chem.* **288**, 255 (1990); (e) S.-C. Chang, J. D. Roth, and M. J. Weaver, *Surf. Sci.* **244**, 113 (1991).

<sup>13</sup>(a) L.-W. H. Leung, S.-C. Chang, and M. J. Weaver, *J. Chem. Phys.* **90**, 7426 (1989); (b) S.-C. Chang and M. J. Weaver, *J. Electroanal. Chem.* **285**, 263 (1990).

<sup>14</sup>S.-C. Chang and M. J. Weaver, *Surf. Sci.* **241**, 11 (1991).

<sup>15</sup>X. Jiang, S.-C. Chang, and M. J. Weaver, *J. Phys. Chem.* **95**, 7453 (1991).

<sup>16</sup>(a) S.-C. Chang, X. Jiang, J. D. Roth, and M. J. Weaver, *J. Phys. Chem.* **95**, 5378 (1991); (b) X. Jiang and M. J. Weaver, *Surf. Sci.* (in press).

<sup>17</sup>S.-C. Chang, A. B. Anderson, and M. J. Weaver, *J. Phys. Chem.* (in press).

<sup>18</sup>(a) A. B. Anderson, *J. Electroanal. Chem.* **280**, 37 (1990); (b) D. K. Lambert, *J. Chem. Phys.* **89**, 3847 (1988), and previous references cited therein.

<sup>19</sup>H. J. Kreuzer, in *Chemistry and Physics of Solid Surface VIII*, *Springer Series in Surface Science*, edited by R. Vanselow and R. Howe (Springer, Berlin, 1990), Vol. 22.

<sup>20</sup>For example: (a) E. Schweizer, B. N. J. Persson, M. Tushaus, D. Hoge, and A. M. Bradshaw, *Surf. Sci.* **213**, 49 (1989); (b) B. N. J. Persson, M. Tushaus, and A. M. Bradshaw, *J. Chem. Phys.* **92**, 5034 (1990).

<sup>21</sup>S. Trasatti, *J. Electroanal. Chem.* **150**, 1 (1983).

<sup>22</sup>For a brief overview: W. N. Hansen and G. J. Hansen, *ACS Symp. Ser.* **378**, 166 (1988).

<sup>23</sup>R. Kötz, H. Neff, and K. Müller, *J. Electroanal. Chem.* **215**, 331 (1986).

<sup>24</sup>R. Gomer and G. Tryson, *J. Chem. Phys.* **66**, 4413 (1977).

<sup>25</sup>A slightly (0.2 eV) higher work function for CO-covered Pt(111) has recently been deduced by means of photoemission measurements: H. H. Rotermund, S. Jakubith, S. Kubala, A. Von Oertzen, and G. Ertl, *J. Electron Spectrosc. Related Phenom.* **52**, 811 (1990).

<sup>26</sup>ASED-MO = "atom superposition and electron delocalization molecular orbital" method [Ref. 18(a)].

<sup>27</sup>(a) A. B. Anderson and M. K. Awad, *J. Am. Chem. Soc.* **107**, 7854 (1985); (b) S. P. Mehandru and A. B. Anderson, *J. Phys. Chem.* **93**, 2044 (1989).

<sup>28</sup>S.-C. Chang, A. B. Anderson, and M. J. Weaver (unpublished results).

<sup>29</sup>(a) J. P. Biberian and M. A. Van Hove, *Surf. Sci.* **138**, 361 (1984); (b) **118**, 443 (1982).

<sup>30</sup>O. M. Magnussen, J. Hotlos, R. J. Nichols, D. M. Kolb, and R. J. Behm, *Phys. Rev. Lett.* **64**, 2729 (1990).

<sup>31</sup>S.-L. Yau, C. M. Vitus, and B. C. Schardt, *J. Am. Chem. Soc.* **112**, 3677 (1990).

<sup>32</sup>S.-L. Yau, X. Gao, S.-C. Chang, B. C. Schardt, and M. J. Weaver, *J. Am. Chem. Soc.* **113**, 6049 (1991).

<sup>33</sup>M. A. Van Hove, R. J. Koestner, J. C. Frost, and G. A. Somorjai, *Surf. Sci.* **129**, 482 (1983).

<sup>34</sup>Unlike Pt(110), even clean Rh(110) does not appear to undergo surface reconstruction. (Ref. 35).

<sup>35</sup>For example: (a) M. Bowker, Q. Guo, and R. Joyner, *Surf. Sci.* **253**, 33 (1991); (b) K. Lehnberger, W. Nichtl-Pecher, W. Oed, K. Heinz, and K. Müller, *ibid.* **217**, 511 (1989).

<sup>36</sup>C. Vitus, Ph.D. thesis, Purdue University, 1991.

<sup>37</sup>For example: G. A. Somorjai and M. A. Van Hove, *Prog. Surf. Sci.* **30**, 201 (1989).

<sup>38</sup>(a) M. S. Zei, G. Lehmppfuhl, and D. M. Kolb, *Surf. Sci.* **221**, 23 (1989); (b) D. M. Kolb and J. Schneider, *Electrochim. Acta* **31**, 929 (1986).

<sup>39</sup>(a) X. Gao, A. Hamelin, and M. J. Weaver, *Phys. Rev. Lett.* **67**, 618 (1991); (b) X. Gao, A. Hamelin, and M. J. Weaver, *Phys. Rev. B* (in press); (c) A. Hamelin, X. Gao, and M. J. Weaver, *J. Electroanal. Chem.* **323**, 361 (1992).

- <sup>40</sup>X. Gao, A. Hamelin, and M. J. Weaver, *J. Chem. Phys.* **95**, 6993 (1991).
- <sup>41</sup>X. Gao, A. Hamelin, and M. J. Weaver, *Phys. Rev. B* **44**, 10983 (1991).
- <sup>42</sup>X. Gao, A. Hamelin, and M. J. Weaver, *Surf. Sci.* (in press).
- <sup>43</sup>M. A. Van Hove, R. J. Koestner, P. C. Stair, J. P. Biberian, L. Kesmodel, I. Bartos, and G. Somorjai, *Surf. Sci.* **103**, 189 (1981).
- <sup>44</sup>C. Wöll, S. Chiang, R. J. Wilson, and P. H. Lippel, *Phys. Rev. B* **39**, 7988 (1989).
- <sup>45</sup>J. V. Barth, H. Brune, G. Ertl, and R. J. Behm, *Phys. Rev. B* **42**, 9307 (1990).
- <sup>46</sup>K. H. Rieder, T. Engel, R. H. Swendsen, and M. Manninen, *Surf. Sci.* **127**, 223 (1983).
- <sup>47</sup>For example: E. Vlieg, I. K. Robinson, and K. Kern, *Surf. Sci.* **233**, 248 (1990).
- <sup>48</sup>(a) K.-M. Ho and K. P. Bohnen, *Phys. Rev. Lett.* **59**, 1833 (1987).  
(b) V. Heine and L. D. Marks, *Surf. Sci.* **165**, 65 (1986).
- <sup>49</sup>A. Hamelin, Y. Ho, S.-C. Chang, X. Gao, and M. J. Weaver, *Langmuir* **8**, 975 (1992).

# Photon emission at metal/solution interface induced by electron injection from solvated electrons

Kei Murakoshi and Kohei Uosaki

Physical Chemistry Laboratory, Department of Chemistry, Faculty of Science, Hokkaido University, Sapporo 060, Japan

(Received 3 October 1991; accepted 30 December 1991)

Light emission from metal, induced by electron injection from solvated electrons, was observed in an electrochemical system. The efficiency of emitted light increases drastically as electrode potential becomes positive. The high energy threshold of the spectrum increases as the electrode potential becomes positive by 1 eV/V. The peak energy also shifts positively as the electrode potential becomes positive, although the degree of the shift is much smaller. Various processes are considered as a possible mechanism for a photon emission. From the qualitative comparison of the results at platinum and gold electrode, the contribution of the inverse photoemission process to the bulk band states at the light emission process in the electrochemical system is suggested. The feasibility of applying this phenomenon to a novel spectroscopy is discussed.

## I. INTRODUCTION

Although many important processes take place at solid/solution interfaces, e.g., electrochemical reaction, corrosion, and crystal growth, the understanding of these processes is still very immature. To fully understand how these processes proceed, one needs to know the electronic and morphological structures of solid surfaces and adsorbed molecules, i.e., reactants, intermediates, and products. Thus, the development of novel techniques to obtain the structural information of the solids and adsorbed molecules *in situ* is one of the most important subjects in the field of surface physical chemistry during the last decade. While *in situ* vibrational spectroscopic techniques provide the information of structures of adsorbed molecules<sup>1</sup> and morphological structures of solid surfaces can be determined by an *in situ* electrochemical scanning tunneling microscope with atomic resolution,<sup>2</sup> determination of surface electronic structure *in situ* is still very difficult in electrochemical systems. Although surface electronic states can be evaluated in ultrahigh vacuum by various techniques, e.g., ultraviolet photoemission spectroscopy (UPS)<sup>3</sup> and inverse photoemission spectroscopy (IPS),<sup>4</sup> they are not suitable for an *in situ* investigation of solids in solution.

McIntyre and Sass proposed a new technique which may be able to determine the electronic structure of electrode.<sup>5</sup> They observed light emission from a metal when highly energetic chemical species exist in solution. They considered that light is emitted as a result of radiative relaxation of energetic electrons injected from an electron donor in solution, e.g., an organic anion radical, to empty electronic states in a metal, i.e., inverse photoemission (IP) process, and, therefore, the spectrum of emitted light reflects the electronic structure of the metal. Ouyang and Bard confirmed the observation and supported this mechanism. They concluded that the relaxation is mainly to Schockley-type surface state.<sup>6</sup>

The quantitative analysis of the observed spectrum is, however, not easy because of the complexity both in the

experimental procedure and in the interpretation. In the emission experiment proposed by McIntyre and Sass, the electrode potential is first pulsed to a very negative potential to generate the organic anion radical which acts as the electron injecting species, then it is pulsed to a positive potential so that the electron is injected from the anion radical to the metal.<sup>5</sup> Usually this process is repeated many times to improve the *S/N* ratio. During the potential pulsing, decomposition of solvent, supporting electrolyte, added organic compound and/or impurities may take place. Decomposition of these species results in electrogenerated chemiluminescence (ECL) which interferes the emission from metal. The decomposed species sometimes polymerize and deposit on the electrode surface<sup>7</sup> and, therefore, reproducibility of the experiment becomes low. Furthermore, a large potential modulation causes reconstruction and roughing of the surface which also lowers the reproducibility. Thus, a new experimental procedure should be developed.

The interpretation of the results is not satisfactory either. Although it has been considered that IP is the only cause of the photon emission in an electrochemical system, the origin and nature of the states which participate to the radiation process are not clear. One reason for the difficulties of the quantitative analysis is the complex scattering process of the energetic electrons in the metal. Light emission from the metal induced by electron injection with excess energies of a few eV has been observed also at metal-insulator-metal (MIM), tunneling junction (TJ),<sup>8</sup> and scanning tunneling microscope (STM) systems.<sup>9</sup> A totally different model is proposed for the light emission at these systems. In these cases, it is considered that the tunneling electron excites a certain surface plasmon mode that decays radiatively.<sup>8,9</sup> Thus, it seems to be necessary to evaluate the various contributions to the light emission process in electrochemical systems to analyze the emitted photon spectrum.

In this work, we have used chemically generated solvated electrons as electron injecting species so that the potential of the electrode is always kept at relatively posi-

tive potential region and decomposition of chemical species can be avoided during the emission measurement. We examined the origin of emitted light and discussed the feasibility of applying this method to determine electronic structure at the electrode/solution interface as a novel spectroscopy.

## II. EXPERIMENTAL

Reagent grade hexamethylphosphoric triamide (HMPA: Wako Pure Chemicals Co. Ltd.) and sodium perchlorate (Aldrich Chemicals Co.) were used as solvent and supporting electrolyte, respectively. They were purified by usual manners<sup>10</sup> and dehydrated in a vacuum. The electrolyte solution was prepared under a pure  $N_2$  (99.999%) atmosphere. Solvated electrons were generated by dissolving sodium metal (Wako Pure Chemicals Co. Ltd.) in 0.2 M  $NaClO_4$ /HMPA solution. The prepared solution showed blue color with an absorption maximum at 770 nm which proves the formation of solvated electrons.<sup>11</sup> Solvated electrons generated in this manner lasted for more than several hours at room temperature.

Metal electrodes (Au and Pt) were prepared on clean glass by vacuum deposition using a pure metal wire (99.99%) as a source in  $10^{-6}$  Torr vacuum. The temperature of the glass substrate during Au deposition was controlled by a hot-plate controller (Chino Co., DB-01-3) at 300 °C. The deposition rate and the thickness of the film were measured with a quartz crystal thickness monitor (ULVAC Co., CRTM-1000). Deposition rate (0.1 nm/s for Au and 0.01 nm/s for Pt) was controlled by changing the current passed through the tungsten wire around which metal wire was wound. Surface smoothness of the films was examined by scanning tunneling microscope (STM; Digital Instruments Co., NanoScope I).

Emission experiments were performed with a flow-type thin layer spectroelectrochemical cell made of Teflon.<sup>12</sup> The separation between the UV-quartz optical window and the working electrode was set to 100  $\mu m$  with a Teflon spacer to minimize the absorption of emitted light by the electrolyte solution itself. The electrolyte solution was transferred from the supply flask to the thin layer compartment of the cell through a Teflon tube by positive  $N_2$  pressure with constant flow rate so that solvated electrons around the metal electrode were not depleted. The potential of the working electrode was referred to the Ag/0.01 M  $AgNO_3$  reference electrode. No electrochemical reactions due to residual moisture or other impurities were detected within the potential region examined in the present study (−3.4–0 V).

Light intensity was monitored with a photomultiplier tube (PMT: Hamamatsu Photonics Co. Ltd., R636) and a photon counter (NF Electronics, LI-574). Spectra of emitted light from metal electrode were obtained by using an imaging spectrograph (Jobin Yvon, CP-200) and a multi-channel detector (Hamamatsu Photonics Co. Ltd., IMD-C3330) with an image intensifier.<sup>13</sup> Light emission measurements were carried out while the potential of the working electrode was either kept constant or swept be-

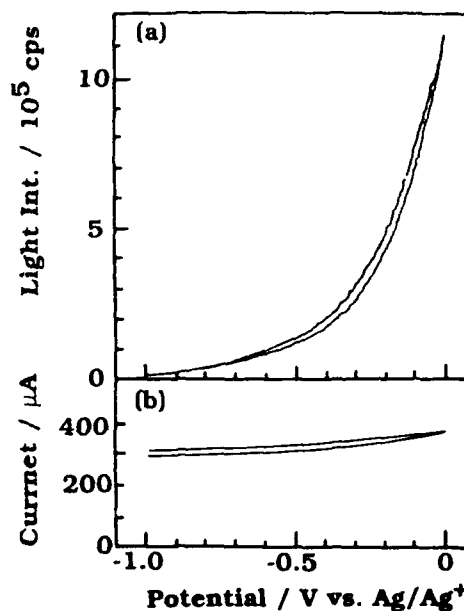


FIG. 1. Potential dependence of (a) emission intensity and (b) oxidation current at Au electrode in 0.2 M  $NaClO_4$ /HMPA containing solvated electrons. Scan rate: 20 mV/s.

tween −1.0 and 0 V. The positive potential limit (0 V) was chosen to avoid decomposition of the solvent.

All the measurements were carried out at room temperature.

## III. RESULTS

The intensity of emitted light from Au and oxidation current were recorded simultaneously as a function of electrode potential and typical results are shown in Fig. 1. Although the oxidation current increases only slightly as potential  $U_w$  becomes positive, light intensity increases significantly. This means that the quantum efficiency of this process changes depending on electrode potential and is estimated as  $10^{-8}$  at 0 V and  $10^{-9}$  at −1.0 V.<sup>14</sup> The intensity of emitted light and anodic current did not change with time as long as electrode potential was kept constant.

Typical spectra of emitted light from Au are shown in Fig. 2. It is clearly seen that both the high energy threshold  $E_{th}$ <sup>15</sup> and the peak energy  $E_p$  of the spectra increase as  $U_w$  becomes more positive. Figure 3 shows the potential dependence of  $E_{th}$  and  $E_p$ .  $E_{th}$  shifts linearly with  $U_w$  by 1 eV/V. The  $E_{th}$  is almost equal to the maximum energy of injected electron  $E_{inj}$  which is given by the energy difference between the Fermi level of the metal and the highest electronic energy level of solvated electrons in solution, i.e.,  $E_{th}/e = E_{inj}/e = -(U^0 - U_w)$ , where  $U^0$  is the redox potential of solvated electron.<sup>16,17</sup> The potential dependence of  $E_p$  is smaller than that of  $E_{th}$  and the shift is ~0.2 eV/V. Thus, the shape of the spectrum is also affected by the electrode potential (Fig. 2).

Photon emission was also observed at Pt electrode, although the intensity was much weaker. A typical spectrum is shown in Fig. 2. The potential dependence of the spectra



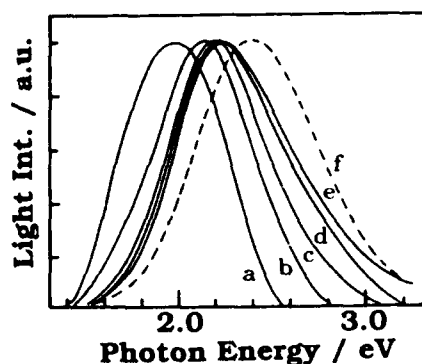


FIG. 2. Normalized spectra of emitted light from Au [(a)–(e); —] and Pt [(f); - - -] electrodes in 0.2 M NaClO<sub>4</sub>/HMPA containing solvated electrons. The electrode potential was kept at (a) -0.8 V, (b) -0.6 V, (c) -0.4 V, (d) -0.2 V, (e) 0 V, and (f) 0 V. The emission peak intensities are normalized to that of the spectrum (e). The enlargement factors are (a) 15.3, (b) 4.4, (c) 1.5, (d) 1.2, and (f) 1.1, respectively.

at Pt has a tendency similar to that at Au as  $E_{th}$  shifts by 1 eV/V and  $E_p$  shifts to higher energy as electrode potential becomes positive. The  $E_p$ , however, is higher than that at Au by 0.1–0.2 eV at a given potential when  $U_w$  is more positive than -0.2 V as shown in Fig. 3. When the  $U_w$  is very negative, i.e.,  $E_{inj}$  is very small, Spectra of Pt is very weak and it is very difficult to determine  $E_p$  and  $E_{th}$ . Therefore, only the values obtained at more positive potential than -0.7 V were shown in Fig. 3.

#### IV. DISCUSSION

There are various possibilities for the origin of the light emission at metal/electrolyte interfaces. The first possibility is the emission from chemical species in solution, e.g., ECL in which case the shape of spectrum is unique for a given system and should have no potential dependence.<sup>18</sup> The linear relation between  $E_{th}$  and  $U_w$  mentioned above

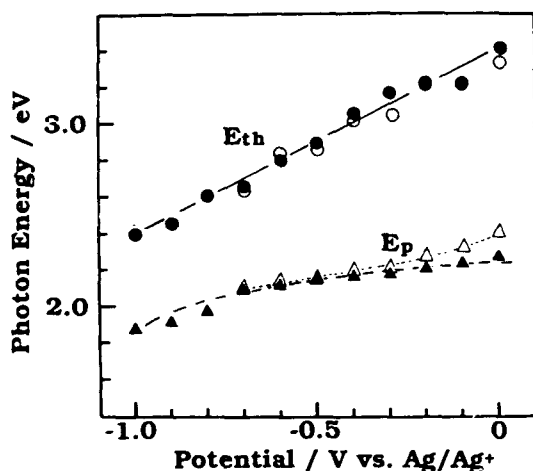


FIG. 3. Potential dependence of the high energy threshold  $E_{th}$  and the peak energy position  $E_p$  of the spectra at Au (●, ▲) and Pt (○, △) electrodes.

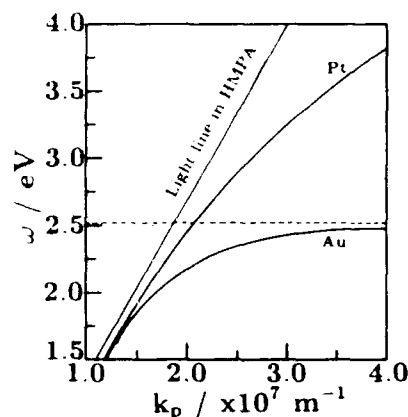


FIG. 4. Dispersion curves of surface plasmon at metal/HMPA interface

excludes this possibility. Thus, it is certain that the light emission is from metal electrode induced by injected electrons.

The second possibility is a surface plasmon excitation decay process which is considered as the most important photon emission process in TJ and STM systems.<sup>8,9</sup> At these tunneling junctions with a bias voltage of 2–5 V, injected electrons induce photon emission as they excite surface plasmon which decays radiatively. Surface plasmon is generally nonradiative but it becomes radiative when translational invariance along the surface is broken by roughness or irregularities at TJ<sup>8</sup> or the presence of the microscope tip at STM.<sup>19</sup> STM measurement showed that the surface of the electrode used here had relatively flat terrace of lateral dimension of a few tens–100 nm which is a reasonable size for photons to couple with the surface plasmon mode around 2–3 eV.<sup>20</sup> The total external quantum efficiency at TJ calculated by using the theory of Laks and Mills increases exponentially as bias voltage becomes larger.<sup>21</sup> Similarly, the emission efficiency at STM system is enhanced as tip-sample voltage increases.<sup>9</sup> In the present system, the quantum efficiency also increases drastically as  $U_w$  becomes positive, i.e.,  $E_{inj}$  becomes larger. From the above considerations, the electromagnetic resonance at the metal surface seems to contribute for the photon emission process at the electrochemical system. Energy range of emitted photon can be estimated by the dispersion of surface plasmon at the metal/HMPA interface. The dispersion curves of Au and Pt in HMPA as well as light line in HMPA were calculated by using the tabulated dielectric constant  $\epsilon_m$  and plotted in Fig. 4.<sup>22</sup> Although the surface plasmon dispersion for Pt is drawn in Fig. 4, the resonance at Pt/HMPA interface is rather broad and strongly damped due to relatively large imaginary component of the dielectric constant of Pt.<sup>23</sup> The maximum of surface plasmon energy of Au is determined as  $\omega$  for  $k_p \rightarrow \infty$  and is indicated in Fig. 4 by dotted line. The surface plasmon excitation decay process can produce a spectrum of only photons with the energy lower than the maximum surface plasmon energy. The cut off energy at Au/HMPA interface is  $\sim 2.5$  eV as shown in Fig. 4 and, therefore, the maximum energy of emitted photon is expected to 2.5 eV.

However, the energy of emitted photons from Au always extends right up to  $E_{inj}$  which can be much larger than 2.5 eV in some case. Furthermore, the photon emission was also observed at Pt electrode despite of the fact that the electromagnetic effect of surface plasmon does not operate due to the strong damping as mentioned before. Thus, the surface plasmon excitation decay process may be involved in the photon emission process but could not be the major contribution.

The other possible mechanism for the light emission process in this system is the charge transfer reaction inverse photoemission (CTIP) process proposed by McIntyre and Sass.<sup>5</sup> In this process, some of energetic electrons, injected from radical species in solution, relax radiately to unoccupied bulk or surface states at lower energies of the metal. Importance of surface states in CTIP process was suggested by Ouyang and Bard<sup>6</sup> and present authors.<sup>17</sup> Electroreflectance (ER) spectroscopy study showed that the surface states of Au(111) are partly occupied at the potential of zero charge (pzc) in aqueous media ( $-0.16$  V versus  $Ag/Ag^+$ <sup>24</sup>) and become unoccupied only when the electrode is biased sufficiently positive.<sup>25</sup> The potential region examined in this study is relatively negative and it is reasonable to think that the surface states of Au are occupied and cannot contribute to the relaxation process. Furthermore, the surface state of Pt(111) is known to locate at higher energy than that of Au.<sup>26</sup> Thus, if the spectrum of emitted light reflects the distribution of surface states, photons emitted from Pt should have smaller energy than that of Au at a given potential. However  $E_p$  at Pt is almost the same as that at Au in the relatively negative potential region and shows more contribution of photons of higher energy in more positive potential region. These results suggest that the unoccupied electronic states of Pt to which injected electron relax are located at lower energy than that of Au contrary to the expectation. It seems, therefore, that the emitted photon spectrum reflects the relaxation of injected electrons to the bulk band states of metal rather than the surface states.

Large potential dependence of the emission intensity at the present system shown in Fig. 1 can be explained by considering the energy dependence of the radiative relaxation probabilities of electron in the spontaneous emission processes. It is known the probability becomes higher as the energy difference between the states is larger.<sup>27</sup> This means that the emission efficiency should be higher as  $E_{inj}$  becomes larger.

The above considerations suggest that the IP process to the bulk band states is the major contribution to the light emission from the metal in the present system. The spectrum reflects the density of the unoccupied states just above Fermi level and the relaxation probability of each transition. The spectrum of emitted light also contains the information of the electron transfer process, since the distribution of the injected electron energy was perturbed dur-

ing the electron transfer process at an interface. More quantitative analysis of the spectra is under way to investigate these contributions.

## ACKNOWLEDGMENT

This work was supported by a Grant-in-Aid for Scientific Research of the Ministry of Education, Science and Culture, Japan (02453001).

This article was presented at the 38th National Symposium of the American Vacuum Society Topical Conference, Surface Science at the Solid-Liquid Interface (TC1).

<sup>1</sup>*Spectroelectrochemistry*, edited by J. Gale (Plenum, New York, 1988).

<sup>2</sup>O. M. Magnussen, J. Hotlos, R. J. Nichols, D. M. Kolb, and R. J. Behm, *Phys. Rev. Lett.* **64**, 2929 (1990).

<sup>3</sup>J. B. Pendry, *Surf. Sci.* **57**, 679 (1976).

<sup>4</sup>N. V. Smith and D. P. Woodruff, *Prog. Surf. Sci.* **21**, 295 (1986).

<sup>5</sup>R. McIntyre and J. K. Sass, *Phys. Rev. Lett.* **56**, 651 (1986); *J. Electroanal. Chem.* **196**, 199 (1985); R. McIntyre, D. K. Roe, J. K. Sass, and W. Storck, *J. Electroanal. Chem.* **228**, 293 (1987); R. McIntyre, D. K. Roe, J. K. Sass, and H. Gerischer, in *Electrochemical Surface Science*, edited by M. P. Soriaga, ACS Symposium Series 378 (American Chemical Society, Washington, DC, 1988), p. 233.

<sup>6</sup>J. Ouyang and A. J. Bard, *J. Phys. Chem.* **91**, 4058 (1987); **92**, 5201 (1988).

<sup>7</sup>J. Ouyang and A. J. Bard, *J. Electroanal. Chem.* **222**, 331 (1987).

<sup>8</sup>J. Lambe and S. L. McCarthy, *Phys. Rev. Lett.* **37**, 923 (1976).

<sup>9</sup>J. H. Coombs, J. K. Gimzewski, B. Reihl, J. K. Sass, and R. R. Schlitter, *J. Microsc.* **152**, 325 (1988); J. K. Gimzewski, J. K. Sass, R. R. Schlitter, and J. Schott, *Europhys. Lett.* **8**, 435 (1989).

<sup>10</sup>D. D. Perrin, W. L. F. Armarego, and D. R. Perrin, in *Purification of Laboratory Chemicals*, 2nd ed. (Pergamon, New York, 1981).

<sup>11</sup>J. M. Brooks and R. R. Dewald, *J. Phys. Chem.* **72**, 2655 (1968).

<sup>12</sup>K. Murakoshi and K. Uosaki, *J. Electroanal. Chem.* **308**, 351 (1991).

<sup>13</sup>This system covers over a photon energy range of 1.4–3.5 eV. The resolution was  $\sim 4$  nm and the spectral response was calibrated by a tungsten-halogen lamp.

<sup>14</sup>The quantum efficiency of this process is estimated by assuming that  $\sim 80\%$  of photons are transmitted through electrolyte solution and quartz window, and the counting efficiency of the PMT is  $\sim 10\%$ .

<sup>15</sup>The high energy threshold  $E_{th}$  was determined somewhat arbitrarily by extrapolating the high energy portion of the spectrum to abscissa (energy axis).

<sup>16</sup>From this relation,  $U^0$  of solvated electrons is estimated as  $-3.4$  V vs  $Ag/Ag^+$  (Ref. 12).

<sup>17</sup>K. Uosaki, K. Murakoshi, and H. Kita, *Chem. Lett.* 1159 (1990); *J. Phys. Chem.* **95**, 779 (1991).

<sup>18</sup>L. R. Faulkner, in *Methods in Enzymology*, edited by M. A. DeLuca (Academic, New York, 1978), Vol. 57, p. 455.

<sup>19</sup>P. Johansson, R. Monreal, and P. Apell, *Phys. Rev. B* **42**, 9210 (1990).

<sup>20</sup>D. L. Mills, M. Weber, and B. Laks, in *Tunneling Spectroscopy*, edited by P. K. Hansma (Plenum, New York, 1982), p. 140.

<sup>21</sup>J. Kirtley, T. N. Theis, and J. C. Tsang, *Phys. Rev. B* **24**, 5650 (1981), and references therein.

<sup>22</sup>The dielectric response function of HMPA ( $\epsilon_r$ ) is  $\sim 2.2$  (Ref. 23). The horizontal axis is the component of the wave vector parallel to the surface  $k_p$  given by  $k_p = (\omega/c)(1/\epsilon_m + 1/\epsilon_r)^{-1/2}$ .

<sup>23</sup>H. Ueba, *Surf. Sci.* **129**, L267 (1983).

<sup>24</sup>F. Silva, M. J. Sottomayor, and A. Hamelin, *J. Electroanal. Chem.* **294**, 239 (1990).

<sup>25</sup>S. H. Liu, C. Hinnen, C. N. V. Huong, N. R. D. Tacconi, and K. M. Ho, *J. Electroanal. Chem.* **176**, 325 (1984).

<sup>26</sup>G. Larsson and P. O. Nilsson, *Phys. Lett. A* **85**, 393 (1981).

<sup>27</sup>H. Eyring, L. J. Walter, and G. E. Kimball, in *Quantum Chemistry* (Wiley, New York, 1944), p. 114.

# Comparison of Cu(111) in aqueous electrolytes and in ultrahigh vacuum: An optical second harmonic generation study

E. K. L. Wong, K. A. Friedrich, J. M. Robinson,<sup>a)</sup> R. A. Bradley, and G. L. Richmond  
Chemical Physics Institute, University of Oregon, Eugene, Oregon 97403

(Received 1 October 1991; accepted 30 December 1991)

The rotational anisotropy of the second harmonic intensity has been used to provide information about the structural and electronic properties of a Cu(111) electrode surface in 0.01 M NaClO<sub>4</sub>. The experiments have involved measurement of the changes in the second harmonic (SH) intensity and relative phase of the SH response as the surface is biased at various potentials. Complementary measurements of the SH response from Cu(111) examined in ultrahigh vacuum (UHV) have also been performed and indicate that when this surface is in solution, it has very different optical (electronic) properties from the native surface at all applied potentials studied. Dosing of the sample in UHV with oxygen provides evidence for the existence of oxygen containing species on the surface in the electrochemical environment despite rigorous exclusion of molecular oxygen during both the surface preparation and the optical measurements. These studies demonstrate the utility of making comparative measurements of the surface in different environments, for which the SH technique is ideally suited.

## I. INTRODUCTION

Surface second harmonic generation (SSHG) has attracted considerable attention as a versatile and very sensitive optical probe of surfaces.<sup>1</sup> As with other surface optical methods, second harmonic generation (SHG) is applicable to any interface accessible by light and is therefore attractive as a probe of interfaces existing between two dense media. Second harmonic generation is particularly useful in such an application due to its inherent surface sensitivity which results from the dipole-forbidden character of the second harmonic (SH) response in the bulk of a medium with inversion symmetry. When a pulsed laser source is used as a probe, one has the added capability of monitoring temporal behavior over a wide range of time scales.<sup>2</sup>

Surface SHG has been applied in numerous studies of the electrolyte/metal interface in which these above attributes of the technique have been exploited.<sup>3</sup> Very recent studies employed an additional advantage of the technique, which is the ability to make comparative SH measurements of metal surface properties in ultrahigh vacuum (UHV) and in solution.<sup>4,5</sup> In the past, it has been difficult for electrochemists to use the valuable and extensive data base that exists regarding electronic and geometrical structure of surfaces studied in UHV for drawing conclusions about the properties of these same surfaces immersed in a solution. Transfer experiments have been the most informative in providing information about geometrical structure in the electrochemical environment.<sup>6-8</sup> These experiments have involved the study of the surface in UHV by such techniques as low-energy electron diffraction (LEED) after controlled emersion of the electrode and transfer into a vacuum chamber. The complicating factor in the comparative analysis is the sometimes questionable assumption that the transfer process itself has not perturbed the surface properties as they originally existed in solution. In the determination of the electronic properties of the electrode surface, comparative studies have been difficult since con-

ventionally used electrochemical methods such as electroreflectance, or UHV compatible techniques such as photoemission and inverse photoemission, are only applicable in a single environment. In this laboratory, our recent focus has been to apply SHG to both environments as a means of tying together the results of numerous previous studies made in a single environment.

In this paper we report the results of our comparative studies of Cu(111) surfaces *in situ* and in UHV. The *in situ* experiments have involved measurement of the rotational anisotropy in the SH response from a Cu(111) electrode examined over whole potential region within the limits of hydrogen evolution and copper dissolution. The optical response is found to be highly potential dependent throughout this region, in correspondence with features in the cyclic voltammograms. The potential induced changes in the magnitude and phase of the second harmonic response derived from the rotational anisotropy data and related phase measurements have then been compared with the SH measurements of this surface in UHV, where the structural and reactive properties of the surface can be more carefully controlled. We compare these results and additional related studies of metal overlayer deposition with previous electrochemical and SH measurements of Cu(111) in which parallel UHV experiments were not performed. The results demonstrate that such comparative measurements provide important new information about the surface structural and reactive properties in solution.

## II. THEORY

Under the electric dipole approximation, the second order response vanishes in the bulk of centrosymmetric media and is allowed only at the interface, such as the electrode/electrolyte junction, where the inversion symmetry is broken. The surface allowed dipole contribution can be written as<sup>9</sup>:

$$P^{(2)}(2\omega) = \chi^{(2)}:E(\omega)E(\omega), \quad (1)$$

where  $\chi^{(2)}$  is the second order susceptibility tensor of third rank reflecting the optical and symmetry properties of the surface layer. The variation in the SH intensity as a function of azimuthal angle reflects the overall symmetry of the surface. A crystalline (111) surface of  $C_{3v}$  symmetry yields the following angular dependence for  $p$ -polarized SH radiation if excited by a  $p$ -polarized pump beam at frequency  $\omega$ <sup>10</sup>:

$$I(2\omega)_{p/p} \propto |a^{(\infty)} + c^{(3)} \cos(3\phi)|^2, \quad (2)$$

where  $a^{(\infty)}$  and  $c^{(3)}$  are referred to as the isotropic and anisotropic coefficients, respectively. For metals, the rotational coefficients are comprised of surface susceptibility elements  $\chi_{ijk}^{(2)}$  and higher order bulk susceptibility elements scaled by the appropriate fresnel factors at  $\omega$  and  $2\omega$ . The observed rotational anisotropy, described by  $c^{(3)}$  arises from the in-plane polarization, whereas  $a^{(\infty)}$  contains the surface tensor elements responsible for the out-of-plane response. Best fits of the data to Eq. (2) yield the ratio of  $c^{(3)}/a^{(\infty)}$ . Since both the susceptibilities and fresnel factors can have both real and imaginary parts, this ratio has both a magnitude and phases. The measured phase angle in the ratio represents the difference in phase between the factors within  $a^{(\infty)}$  and  $c^{(3)}$ .

The SH experiments consist of measuring the variation in SH intensity as the crystal is rotated 360° azimuthally. To selectively monitor continuous changes in the in-plane ( $c^{(3)}$ ) and the out-of-plane ( $a^{(\infty)}$ ) contributions, it is necessary to fix the azimuthal angle at  $\phi = 30^\circ$  under specific polarization conditions. At this angle the isotropic contribution ( $a^{(\infty)}$ ) is obtained under  $p$ -polarized excitation with  $p$ -polarized SH intensity, whereas the anisotropic contribution ( $c^{(3)}$ ) involves measuring the  $s$ -polarized SH intensity with  $p$ -polarized excitation.

A more explicit understanding of the changes in the phase during surface alteration can be obtained by interference measurements in which the SH reflectance is measured relative to a reference SH field from a quartz crystal. The measurements are performed under geometrical and optical conditions that isolate the isotropic and anisotropic contributions. Other studies from this laboratory have shown that the magnitude and phase of the ratio derived from the anisotropy data is extremely sensitive to changes in the electronic properties of the surface as it is chemically altered.<sup>11</sup>

### III. EXPERIMENTAL APPROACH

A conventional reflective optical geometry was used and the details were previously published.<sup>3</sup> Measurements were made using the 10 ns 1064 nm pulses from a Nd-YAG laser operating at 10 Hz. The incident angle between the excitation beam and the electrode surface normal was 32° for the solution experiment and 45° for the UHV measurements. All experiments were repeated several times to check the reproducibility. To avoid damage to the surface the incident laser energy density was under 3 mJ/pulse. Laue back reflection indicated that the 99.999% Cu crystal was oriented within 1° of the (111) plane.

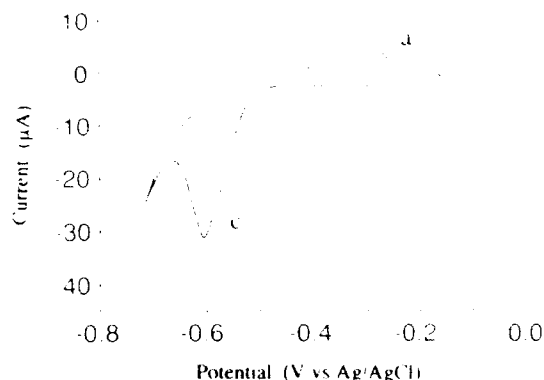


FIG. 1. Cyclic voltammogram of Cu(111) in 0.01 M NaClO<sub>4</sub> (pH 4) at a scan rate of 20 mV s<sup>-1</sup>.

The phase measurements of the anisotropic and isotropic contributions are made using an interference technique.<sup>12</sup> The experiment consists of measuring the interference between the SH light from the sample at a fixed azimuthal angle and that from a quartz crystal reference which is translated in the beam path.

For the electrochemical experiments, the crystal was mounted on a rotatable Kel-F shaft within the spectroelectrochemical cell. The azimuthal angle ( $\phi$ ) of rotation of the crystal is defined as the angle between the  $[2\bar{1}1]$  direction and the projection of the incident wave vector parallel to the surface. The Ag/AgCl reference electrode was used in the standard three electrode geometry and all potentials are reported relative to this reference electrode. The standard electropolishing procedure consisted of three steps.<sup>13</sup> The crystal is first immersed in orthophosphoric acid at  $E = 0.76$  V versus Ag/AgCl, then washed in dilute sulfuric acid, and finally the crystal is polarized to  $-0.56$  V versus Ag/AgCl in 0.5 M NaF. The electrochemical polishing and transfer of the copper electrodes to the spectroelectrochemical cell is performed under an inert atmosphere to minimize oxide formation and throughout the course of the experiments, the solutions were continuously purged with oxygen free nitrogen.

For the vacuum experiments the crystal was cleaned by sputtering and annealing procedures in a chamber with a base pressure of  $3.5 \times 10^{-10}$  Torr and the quality of the sample was checked with Auger and LEED. The electropolishing preparation of the crystal for the UHV measurements consisted only of the "etching" step in orthophosphoric acid. The O<sub>2</sub> dosing experiments were performed at room temperature by exposing the crystal to a background pressure of  $1 \times 10^{-6}$  Torr of oxygen.

### IV. RESULTS AND DISCUSSION

Figure 1 shows a cyclic voltammogram (CV) of Cu(111) in 0.01 M NaClO<sub>4</sub> (pH 4). The CV reveals two clearly distinguishable anodic (a) peak and cathodic (c) peaks corresponding to a charge of approximately 150  $\mu\text{C}/\text{cm}^2$ . We find that the area under these peaks and their relatively large potential difference between the anodic and

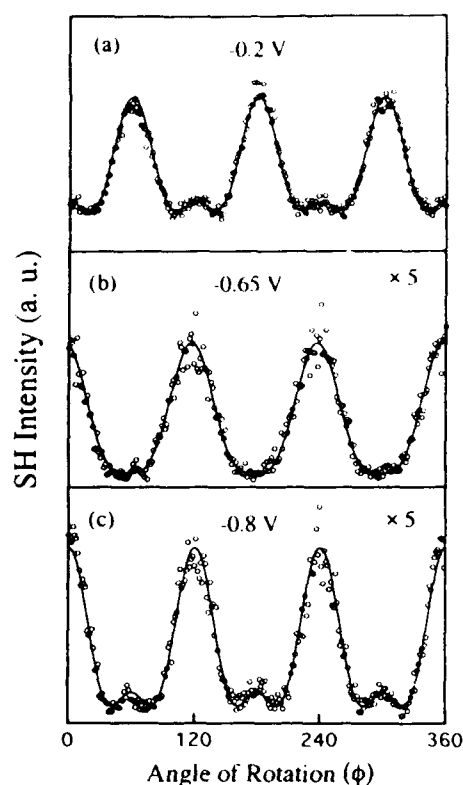


FIG. 2. SH rotational anisotropies from a Cu(111) electrode immersed in 0.01 M NaClO<sub>4</sub> at pH 4. *p*-polarized 1064 nm excitation and *p*-polarized SH was used at the following fixed potentials: (a)  $-0.20$  V vs Ag/AgCl, (b)  $-0.65$  V vs Ag/AgCl, (c)  $-0.80$  V vs Ag/AgCl. The data is shown with open circles and the theoretical fit using Eq. (2) with solid lines.

cathodic processes is dependent on scan rate. All of our observations are consistent with previous cyclic voltammograms of Cu(111) of Vilche and Juettner<sup>14</sup> in which the features in the CV were associated with the formation (anodic) and reduction (cathodic) of an oxygen-containing surface film. The potential region of this oxygen containing layer and the kinetic characteristics of its formation was found to be dependent on pH and electrolyte solution in a complex manner. The existence of this layer was invoked by the authors to explain the remarkably irregular behavior of the lead deposition on Cu(111) previously reported by Bewick *et al.*<sup>15</sup> and Siegenthaler *et al.*<sup>16</sup>

Figure 2 displays the SH rotational anisotropies for Cu(111) in 0.01 NaClO<sub>4</sub> (pH 4) measured at three different potentials. Both the fundamental incident light and the outgoing SH response are *p* polarized. All the data show a threefold pattern consistent with the  $C_{3v}$  symmetry of the surface. In Fig. 2(a), the measurement was made at  $-0.20$  V versus Ag/AgCl, near the potential of zero charge (PZC).<sup>17</sup> At this potential, minimal perturbation of the surface electronic properties by the presence of the solution double layer is expected. A fit of the data to Eq. (2) yields a ratio of the phenomenological constants of  $c^{(3)}/a^{(\infty)} = 0.9e^{i121^\circ}$ . This value is different than the ratio of  $0.5e^{i180^\circ}$  reported for Cu(111) at the PZC by Shannon *et al.*<sup>18</sup> We attribute this discrepancy to differences in the

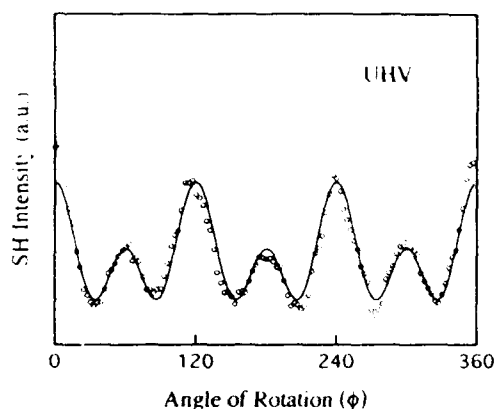


FIG. 3. SH rotational anisotropy from clean Cu(111) in UHV at  $3.5 \times 10^{-10}$  Torr, under *p*-polarized excitation at 1064 nm. The open circles represent the *p*-polarized SH data and theoretical fits using Eq. (2) are indicated with a solid line.

surface preparations and surface quality as will be discussed in more detail later.

Figures 2(b) and 2(c) show the rotational anisotropies measured under the same optical conditions at  $-0.65$  and  $-0.80$  V, respectively. The most striking result is the relatively large change in intensity and phase angle as the potential is varied. The ratios vary from  $0.77e^{i32^\circ}$  at  $-0.65$  V, to  $1.33e^{i44^\circ}$  at  $-0.80$  V. These changes in the SH response show a direct correlation with the two redox peaks visible in the cyclic voltammogram (Fig. 1). This correlation was verified by a series of detailed experiments in which the pH of the solution was varied. We found that the two redox peaks were shifted to more negative potentials as the pH was increased. SH patterns like that in Figs. 2(b) and 2(c) were observed at applied potentials in exact correspondence with shifted CV peaks.

For comparison with the Cu(111) electrode response in solution, we have performed SH rotational anisotropy measurements of a sputtered and vacuum annealed Cu(111) surface in UHV. As reported in a recent preliminary publication<sup>5</sup> and examined in more detail in this study, the response from this crystal in UHV is distinctly different than can be obtained at any potential in solution. Figure 3 shows the results in UHV for the same optical input and output polarizations as shown in Fig. 2. The threefold rotational anisotropy of Cu(111) in UHV was first reported by Tom and Aumiller using a different optical geometry.<sup>19</sup> We determine the ratio  $c^{(3)}/a^{(\infty)}$  to be equal to  $1.2e^{i77^\circ}$ . The most significant difference between the vacuum and solution data is in the phase angle. The closest agreement is observed from the reduced surface at negative potentials, where both the magnitude and the phase angle approach the value of the UHV measurement.

It is interesting to compare these results with similar UHV/solution measurements performed on Ag(111) under both nonresonant conditions, where a 1064 nm excitation beam was used,<sup>4</sup> and resonant conditions, where visible excitation was employed.<sup>20</sup> For the electrochemical studies in which the Ag(111) surface was biased at the PZC, the SH response in solution under both resonant and

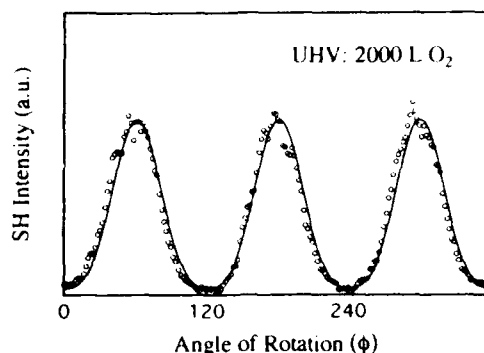


FIG. 4. SH rotational anisotropy from Cu(111) after exposure to 2000 L of  $O_2$ . Under  $p$ -polarized excitation shown are the  $p$ -polarized SH data (open circles) and theoretical fits (solid lines) to Eq. (2).

nonresonant conditions is nearly identical in magnitude and phase angle with the response in UHV. Similarly, the analogous measurements for Au(111) in UHV and in solution indicate that the surface properties of Au(111) in solution are minimally perturbed near the PZC.<sup>21</sup> Based on the conclusions from these studies of Ag(111) and Au(111), we conclude that the difference in the response for Cu(111) in solution and in UHV can not simply be attributed to the presence of the static field in solution or to the double layer structure. Therefore, the different anisotropic response from Cu(111) in solution relative to that in UHV can only be explained by the presence of an adsorbed species which significantly alters the electronic properties of the surface in solution.

The most likely surface species responsible for these observations is some form of oxygen physically or chemically bound to the surface. Previous cyclic voltammetry studies have suggested that oxygen containing species might be present on the surface of copper at the more positive potentials.<sup>14</sup> To check this supposition, we dosed the clean Cu(111) surface in UHV with increasing exposures of oxygen. The resulting oxygen dosed surface gives a SH response which can be more closely correlated to the Cu(111) electrode response at  $-0.2$  V than to the clean surface data. When the surface is dosed with  $O_2$ , the initial intensity maximum at  $\phi = 0$  progressively decreases to a minimum. As the dosing proceeds, the rotational anisotropy is described by an increasing phase angle. At an exposure of 900 L of  $O_2$ , the SH pattern is similar to that obtained in solution at  $-0.2$  V. Figure 4 shows the saturated SH response from Cu(111) with 2000 L of  $O_2$ . When the data is fit to Eq. (2), the value obtained for  $c^{(3)}/a^{(\infty)}$  is  $0.8e^{i194^\circ}$ . This pattern and its fit are also very similar to the angular dependence of SH intensity obtained previously by Tom and Aumiller<sup>19</sup> for Cu(111) under ambient condition. In our experiment, we can not distinguish the form of the oxygen species which exists at the surface. However, we can conclude from the UHV data that the presence of oxygen, even at low exposures, can cause significant perturbations in the electronic properties of the surface.

To try to obtain a more fundamental understanding of how the presence of oxygen can alter the SH response and

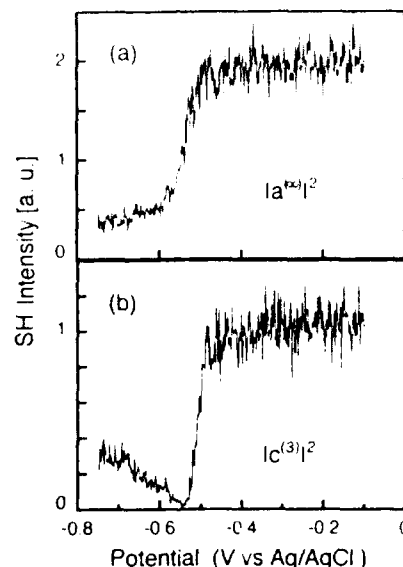


FIG. 5. Potential dependence of isotropic and anisotropic intensities from a Cu(111) electrode immersed in 0.01 M  $NaClO_4$  at pH 4 at  $\phi = 30^\circ$ .  $(c^{(3)})^2$  is measured for  $p$ -polarized fundamental and  $s$ -polarized SH radiation, and  $(a^{(\infty)})^2$  is measured under  $p$ -polarized input and  $p$ -output conditions.

corresponding electronic properties of the surface we have performed experiments which measure the potential dependence of the intensity of the isotropic  $a^{(\infty)}$  and anisotropic  $c^{(3)}$  response, respectively, over the entire potential range. These terms were isolated under specific optical and geometrical conditions described earlier. We find a strong potential dependence in both coefficients as shown in Figs. 5(a) and 5(b) for a cathodic scan, progressively reducing the surface. Both measurements show a relatively high intensity at potentials where the oxide layer is stable ( $-0.1$  to  $-0.5$  V  $pH = 4$ ) and exhibit a strong decrease at potentials (negative from  $-0.5$  V) where the electroreduction of the oxide layer takes place. We attribute these relatively large magnitudes in the oxide layer region of the in-plane and out-of-plane contributions to a resonant effect. As the surface oxide is formed, the SH fields can resonantly couple to optical transitions of the surface oxide (direct band gaps of 2.17 eV for  $Cu_2O$  and 1.5 eV for  $CuO$  have been reported<sup>22</sup>), leading to an overall enhancement in SH intensity.

An interesting feature of the potential dependence of the anisotropic response in Fig. 5(b) is that at the onset of the surface reduction this contribution actually becomes zero such that the overall response of the surface at this potential is only isotropic. Since the surface geometrical structure still possesses  $C_{3v}$  symmetry, the vanishing contribution from the anisotropic term can be understood by the destructive interference of two or more separate in-plane contributions (one from the native surface and other from the oxide layer or from the unknown bulk anisotropies).

To provide additional support for our conclusions we have also measured the potential dependence of the phase of the isotropic and anisotropic SH responses. As demon-

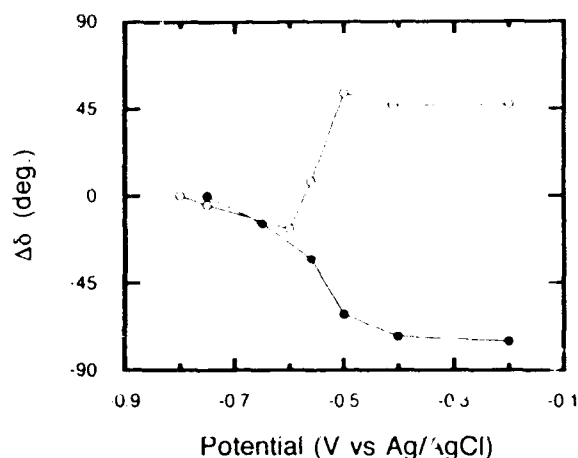


FIG. 6. Change in the relative phase for the isotropic (full circles) and anisotropic (open circles) susceptibilities as a function of potential from a Cu(111) electrode immersed in 0.01 M NaClO<sub>4</sub> at pH 4. The relative phase at  $-0.80$  V vs Ag/AgCl is taken as a reference value.

strated in previous studies by Koos *et al.* for underpotential deposition (UPD) of thallium on Au(111),<sup>12</sup> phase measurements such as these can provide very valuable additional information to complement the intensity measurements. Merely obtaining phase information from fits to the rotational anisotropy measurements is not sufficient to describe the nonlinear optical response since changes in the ratio  $c^{(3)}/a^{(\infty)}$  are relative, and in some cases can be deceptive (e.g., if the phase of  $c^{(3)}$  and  $a^{(\infty)}$  change by the same amount, no apparent change in phase angle upon surface modification is observed). Figure 6 shows the changes in relative phase of the isotropic (full circles) and anisotropic (open circles) response in solution as a function of potential. The phase at the most negative potential was taken as the reference point because the rotational pattern at negative potentials correlates best to that of the clean surface in UHV. Consistent with the intensity data are the dramatic changes in the phase angle of both  $a^{(\infty)}$  and the  $c^{(3)}$  from  $-0.3$  to  $-0.6$  V. With the formation of the oxide layer in this potential region, the phase of  $a^{(\infty)}$  is advanced steadily, exhibiting a maximum phase change of  $75^\circ$ . In contrast, the anisotropic  $c^{(3)}$  term shows a retardation in phase of  $47^\circ$  when the oxide is formed. Upon oxygen exposure in vacuum corresponding to that in Fig. 3, the phase in the isotropic component is also advanced ( $104^\circ$ ) whereas the anisotropic contribution does not change within our experimental uncertainty of  $10^\circ$ . The different behavior of the phase of the  $c^{(3)}$  term suggests that the oxidation processes which take place on the electrode surface and the UHV surface are not the same. This is not surprising as oxygen is known to form a disordered oxygen-copper layer upon saturation adsorption and under certain conditions to go subsurface in UHV.<sup>23</sup> In contrast, in solution a variety of O-containing species are possible (e.g., CuOH, Cu<sub>2</sub>O, or CuO).<sup>24</sup>

As noted above, a previous study of Cu(111) from Shannon *et al.*<sup>18</sup> indicated a somewhat different SH behavior which is now understandable in light of these UHV/

solution comparative studies. The former study was conducted without the aid of complementary UHV experiments described here. In these early studies, the rotational anisotropy near the PZC ( $-0.20$  V) has a much larger phase angle suggestive of a more substantial oxide layer on the surface as in Fig. 4. No potential dependence of the SH response was reported in these earlier studies between  $-0.70$  and  $-0.20$  V because a more negative potential needs to be applied in order to remove the oxide layer at the higher pH value of 6. We believe that we have been able to minimize the presence of oxides formed during surface preparation by more refined polishing techniques and more rigorous attention to oxygen exclusion during surface preparation and sample mounting.

It is interesting to note that in the earlier study of Shannon *et al.*<sup>18</sup> in which the UPD of thallium on Cu(111) was also examined, the SH response indicated that the thallium deposited on the surface in a highly disordered manner. This conclusion came from the highly irregular and non-periodic nature of the rotational anisotropy upon deposition of a monolayer of thallium. We have recently repeated the UPD studies of Shannon *et al.* using our refined preparation procedures. We find that whereas the intensity and phase angle changes upon deposition of one and two monolayers, the SH pattern retains its regular form and the anisotropic contribution does not change significantly after depositing the first monolayer. Koos *et al.* found that structural information can be extracted from the change of the anisotropic SH response upon underpotential deposition.<sup>25</sup> A commensurate overlayer had no strong affect on the electronic properties, whereas incommensurate overlayers induced a strong perturbation of the anisotropic response. Therefore our results are more suggestive of ordered overlayer formation. Although a oxygen containing species is still present in our current studies as suggested by the UHV work, possibly formed during surface preparation, it does not appear to be an important factor in disrupting the overlayer deposition process as strongly as reported in the earlier study. One of the most interesting results from this series of studies with regards to the applicability of SHG to studying structural aspects of UPD is that SH rotational anisotropy is able to distinguish between what appears to be disordered growth for the surface of poorer quality and a more ordered structure in the current study. Details of these SHG studies of the UPD of thallium on Cu(111) and the deposition kinetics will be explored in a later paper.

## V. SUMMARY

The angular dependence of the second harmonic intensity has been measured for a Cu(111) electrode in 0.01 M NaClO<sub>4</sub> at different potentials. Changes in the SH response are observed which correlate with surface reactions seen in the cyclic voltammograms. Comparison with measurements on a clean surface in UHV shows that the Cu(111) surface in solution is very different from that in UHV, as differences in the magnitude and phase angle of the ratio  $c^{(3)}/a^{(\infty)}$  are obvious at all potentials. Dosing the surface with O<sub>2</sub> resulted in SH patterns which are described by an

increasing phase angle. Since the phase angle is similarly large for the SH response of the Cu(111) electrodes at positive potentials and considering that the most likely adsorbate in solution is oxygen, we conclude that at positive potentials and throughout most of the double layer charging region an oxygen containing surface species is present, in agreement with earlier electrochemical measurements. This study demonstrates the importance of being able to perform comparative measurements between UHV and solution with the same technique, since the UHV measurements were critical to the interpretation of the optical properties and gave insight into the chemical properties of Cu(111) in an electrolytic environment.

## ACKNOWLEDGMENTS

The authors gratefully acknowledge the financial support from the Office of Naval Research for the solution studies, and the Donors of the Petroleum Research Fund of the American Chemical Society (24180-AC5-C) for the vacuum measurements.

This article was presented at the 38th National Symposium of the American Vacuum Society Topical Conference, Surface Science at the Solid-Liquid Interface (TC1).

<sup>1</sup>Present address: Chemical and Laser Science Division, Los Alamos National Laboratory, Los Alamos, New Mexico 87545.

<sup>2</sup>G. L. Richmond, J. M. Robinson, and V. L. Shannon, *Prog. Surf. Sci.* **28**, 1 (1988); G. L. Richmond in *Second Harmonic Generation/Sum Frequency Generation at Surfaces*, edited by G. L. Richmond (Elsevier, Amsterdam, 1992), Chap. 5.

<sup>3</sup>H. W. K. Tom, G. D. Aumiller, and C. H. Brito-Cruz, *Phys. Rev. Lett.* **60**, 1438 (1988); J. M. Robinson and G. L. Richmond, *Electrochim. Acta* **34**, 1639 (1989).

<sup>4</sup>G. L. Richmond, *Electroanalytical Chemistry*, edited by A. J. Bard Marcel (Dekker, New York, 1991), Vol. 17, *Advances in Electrochem-*

*ical Science and Engineering*, edited by H. Gerischer and C. W. Tobias (VCH, New York, 1991).

<sup>5</sup>R. A. Bradley, S. Areka, R. Georgiadis, J. M. Robinson, S. D. Kevan, and G. L. Richmond, *Chem. Phys. Lett.* **168**, 468 (1990).

<sup>6</sup>R. A. Bradley, K. A. Friedrich, F. K. L. Wong, and G. L. Richmond, *J. Electroanal. Chem.* **309**, 319 (1991).

<sup>7</sup>A. T. Hubbard et al., *J. Electroanal. Chem.* **168**, 43 (1984).

<sup>8</sup>P. N. Ross, *J. Vac. Sci. Technol. A* **5**, 948 (1987).

<sup>9</sup>D. M. Kolb, *J. Vac. Sci. Technol. A* **4**, 1294 (1986).

<sup>10</sup>Y. R. Shen, *The Principles of Nonlinear Optics* (Wiley, New York, 1984).

<sup>11</sup>H. W. K. Tom, Ph.D. dissertation, University of California, Berkeley, 1984; J. E. Sipe, D. J. Moss, and H. M. van Driel, *Phys. Rev. B* **35**, 1129 (1987).

<sup>12</sup>R. Georgiadis and G. L. Richmond, *J. Phys. Chem.* **95**, 2895 (1990); R. Georgiadis, G. A. Neff, and G. L. Richmond, *J. Chem. Phys.* **92**, 4623 (1990).

<sup>13</sup>D. A. Koos and G. L. Richmond, *J. Chem. Phys.* **93**, 869 (1990).

<sup>14</sup>W. J. McG. Tegart, *The Electrolytic and Chemical Polishing of Metals in Research and Industry* (Pergamon, New York, 1959).

<sup>15</sup>J. R. Vilche and K. Jüttner, *Electrochim. Acta* **32**, 1567 (1987).

<sup>16</sup>A. Bewick, J. Jovicevic, and B. Thomas, *Faraday Symp. Chem. Soc.* **12**, 24 (1977).

<sup>17</sup>H. Siegenthaler and K. Jüttner, *J. Electroanal. Chem.* **163**, 327 (1984).

<sup>18</sup>A. Hameiri, T. Vitanov, E. Sevastyanov, and A. Popov, *J. Electroanal. Chem.* **145**, 225 (1983).

<sup>19</sup>V. L. Shannon, D. A. Koos, S. A. Kellar, P. Huifang, and G. L. Richmond, *J. Phys. Chem.* **93**, 6434 (1989).

<sup>20</sup>H. W. K. Tom and G. D. Aumiller, *Phys. Rev. B* **33**, 8818 (1986).

<sup>21</sup>R. A. Bradley, R. Georgiadis, S. D. Kevan, and G. L. Richmond, *J. Vac. Sci. Technol. A* **10**, 2996 (1992).

<sup>22</sup>K. A. Friedrich, E. K. L. Wong, R. A. Bradley, and G. L. Richmond (to be published).

<sup>23</sup>C. G. Riobing and A. Roos, *Handbook of Optical Constants of Solids II*, edited by E. D. Palik (Academic, Boston, 1991).

<sup>24</sup>H. Niebur, *Surf. Sci.* **130**, 41 (1983).

<sup>25</sup>M. R. Gennero de Chialvo, J. O. Zerbino, S. L. Marchiano, and A. J. Arvia, *J. Appl. Electrochem.* **16**, 517 (1986).

<sup>26</sup>D. A. Koos and G. L. Richmond, *J. Chem. Phys.* (in press).

<sup>27</sup>J. M. Robinson, E. K. L. Wong, and G. L. Richmond (in preparation).



# X-ray photoelectron spectroscopy study on the electrical double layer at an $\text{Al}_2\text{O}_3$ -Al interface

Hideo Sambe and David E. Ramaker

Chemistry Department, George Washington University, Washington, DC 20052

(Received 7 October 1991; accepted 6 January 1992)

Upon oxidation of a clean Al surface, an electrical double layer (EDL) is formed at the Al- $\text{Al}_2\text{O}_3$  interface. This EDL is investigated using x-ray photoelectron spectroscopy data available in the literature. The EDL strength, measured as a potential difference across the EDL, depends on the Al surface and the oxidation process. The polarity of the EDL is however invariably the same: the  $\text{Al}_2\text{O}_3$  side of the Al- $\text{Al}_2\text{O}_3$  interface is always positively charged. The reduction of the Al work function upon oxidation is attributed to this EDL. The asymmetry in the potential barrier shape formed in Al- $\text{Al}_2\text{O}_3$ -Al sandwiches is also attributed to a strong EDL at the electrode-film interface and a weaker EDL at the interface between the counter electrode and the film.

## I. INTRODUCTION

When a pure aluminum metal is oxidized in dry  $\text{O}_2$  at room temperature, an amorphous  $\text{Al}_2\text{O}_3$  film of about 30 Å is formed on its surface.<sup>1</sup> At the Al- $\text{Al}_2\text{O}_3$  interface, as well as at any other phase boundaries, an electrical double layer (EDL) is expected to develop.<sup>2</sup> This EDL produces a potential difference (PD) across the interface and modifies the work function of Al. However, measurement of the Al work function with an oxidized Al surface generally involves not only the Al- $\text{Al}_2\text{O}_3$  interface but also the  $\text{Al}_2\text{O}_3$ -vacuum interface. In this article, we use x-ray photoelectron spectroscopy (XPS) to investigate the PD produced across an Al- $\text{Al}_2\text{O}_3$  interface. Our XPS study, unlike the work-function measurements, can separate out the effects of the Al- $\text{Al}_2\text{O}_3$  interface from those of the  $\text{Al}_2\text{O}_3$ -vacuum interface.

The Al- $\text{Al}_2\text{O}_3$  system is chosen, simply because rather accurate XPS data are available for the aluminum-oxygen compounds.<sup>3,4</sup> We first present our model and later verify it with experimental results available in the literature.

## II. THEORETICAL BACKGROUND

### A. General features of XPS for oxidized Al

In XPS measurements on an oxidized Al metal, an electron-energy analyzer generally faces the oxide surface as shown in Fig. 1. The oxide ( $\text{Al}_2\text{O}_3$ ) film is generally so thin ( $\approx 30$  Å) that electrons originating from the metal portion, as well as those from the oxide portion, can reach the analyzer. Consequently, two peaks appear both in the Al 2*p* photoelectron spectrum and in the Al *KLL* Auger spectrum. These two peaks arise from Al atoms located in the oxide and metal portions of the sample. One can easily identify the origin (metal or oxide) of these peaks based on the expected chemical shifts for Al ( $\text{Al}^0$ ) and  $\text{Al}_2\text{O}_3$  ( $\text{Al}^{+3}$ ) and on the dependence of the relative intensity of the two peaks with change in the  $\text{Al}_2\text{O}_3$ -film thickness. Figure 2 shows two such peaks in the Al 2*p* photoelectron spectra. The  $\text{Al}^{+3}$  binding energies in the figure are aligned for comparison.

We denote the electron kinetic energies (KE) of the two peaks in the Al *KLL* Auger spectrum as  $\text{KE}(\text{Auger}, \text{Al}^0)$  and  $\text{KE}(\text{Auger}, \text{Al}^{+3})$  and those in the Al 2*p* photoelectron spectrum as  $\text{KE}(\text{photo}, \text{Al}^0)$  and  $\text{KE}(\text{photo}, \text{Al}^{+3})$ .  $\text{KE}(\text{Auger})$  denotes the energy of the most intense  $\text{KL}_{23}\text{L}_{23}$  transition for an Al atom and hence does not depend on the incident x-ray energy. On the other hand,  $\text{KE}(\text{photo})$  depends on the incident x-ray energy. However, the binding energies (BE) of the Al 2*p* electrons,

$$\text{BE}(\text{Al}^0) = h\nu - \text{KE}(\text{photo}, \text{Al}^0), \quad (1)$$

$$\text{BE}(\text{Al}^{+3}) = h\nu - \text{KE}(\text{photo}, \text{Al}^{+3}), \quad (2)$$

are independent of the incident x-ray energy  $h\nu$ . In short, XPS measurements for an oxidized Al metal provide four physically significant energies:  $\text{KE}(\text{Auger}, \text{Al}^0)$ ,  $\text{KE}(\text{Auger}, \text{Al}^{+3})$ ,  $\text{BE}(\text{Al}^0)$ , and  $\text{BE}(\text{Al}^{+3})$ . We employ, however, an alternative set of four independent energies defined by

$$E(\text{Al}^0) \equiv \text{KE}(\text{Auger}, \text{Al}^0) + \text{BE}(\text{Al}^0), \quad (3)$$

$$E(\text{Al}^{+3}) \equiv \text{KE}(\text{Auger}, \text{Al}^{+3}) + \text{BE}(\text{Al}^{+3}), \quad (4)$$

$$E(\text{M/O}) \equiv \text{BE}(\text{Al}^{+3}) - \text{BE}(\text{Al}^0), \quad (5)$$

$$E(\text{O/V}) \equiv \text{BE}(\text{Al}^{+3}). \quad (6)$$

These energy parameters are more useful because, except for  $E(\text{O/V})$ , they eliminate the static-charge referencing problem.  $E(\text{Al}^{+3})$  and  $E(\text{Al}^0)$  are nothing but the modified Auger parameters (MAP) introduced by Wagner<sup>3</sup> and are independent of the interfacial potentials.  $E(\text{M/O})$  depends on only the metal-oxide interfacial potentials, as explained below.

Electrons originating from the metal portion must cross the M/O (metal-oxide) and O/V (oxide-vacuum) interfaces to reach the electron-energy analyzer (see Fig. 1), and consequently experience the potential differences (PD) across these interfaces denoted as  $\text{PD}(\text{M/O})$  and  $\text{PD}(\text{O/V})$ . These PDs enter in both  $\text{KE}(\text{Auger}, \text{Al}^0)$  and  $\text{BE}(\text{Al}^0)$ , since their electrons originate from the metal portion ( $\text{Al}^0$ ). However, because of Eq. (1), the PDs in

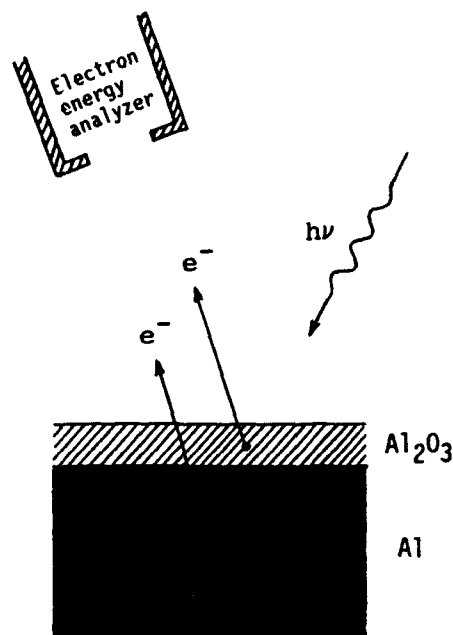


FIG. 1. Configuration of sample and electron detector for typical XPS measurements on oxidized Al. The electron detector faces the oxidized surface of Al. As a result, electrons originating from the metal portion must cross the two (M/O and O/V) interfaces in order to enter the detector, while those from the oxide portion cross only the O/V interface on their way to the detector.

$\text{KE}(\text{Auger}, \text{Al}^0)$  and  $\text{BE}(\text{Al}^0)$  enter with opposite signs. Therefore, a sum of these energies, that is  $E(\text{Al}^0)$ , is independent of both  $\text{PD}(\text{M/O})$  and  $\text{PD}(\text{O/V})$ .

Electrons originating from the oxide portion ( $\text{Al}^{+3}$ ), on the other hand, cross only the O/V interface on the way to the electron-energy analyzer and hence experience only  $\text{PD}(\text{O/V})$ . This  $\text{PD}(\text{O/V})$  also enters in  $\text{KE}(\text{Auger}, \text{Al}^{+3})$  and  $\text{BE}(\text{Al}^{+3})$  with opposite signs, so that  $E(\text{Al}^{+3})$  is similarly independent of both  $\text{PD}(\text{M/O})$  and  $\text{PD}(\text{O/V})$ .

$E(\text{M/O})$  is defined as an energy difference between  $\text{BE}(\text{Al}^{+3})$  and  $\text{BE}(\text{Al}^0)$ . Since  $\text{PD}(\text{O/V})$  enters in  $\text{BE}(\text{Al}^{+3})$  and  $\text{BE}(\text{Al}^0)$  with the same sign, the  $\text{PD}(\text{O/V})$  contributions cancel in  $E(\text{M/O})$  and consequently  $E(\text{M/O})$  does not depend on  $\text{PD}(\text{O/V})$ . In other words,  $E(\text{M/O})$  depends only on  $\text{PD}(\text{M/O})$ . The  $\text{PD}(\text{M/O})$  is expected to be stable and reproducible, while  $\text{PD}(\text{O/V})$  is harder to obtain reproducibly because of adventitious surface contamination.

## B. Theoretical model

Let us first consider an imaginary  $\text{Al}_2\text{O}_3$ -Al system. Suppose that a thin  $\gamma\text{-Al}_2\text{O}_3$  film is made separately and then brought into contact with a clean Al surface. In this case, electron migration across the  $\text{Al}_2\text{O}_3$ -Al interface will not take place, since the Fermi level of the Al metal is situated inside the forbidden band gap of the insulator  $\text{Al}_2\text{O}_3$ , well away (more than 2 eV) from the top of the valence band (VB) and the bottom of the conduction band (CB). The electron energy diagram for this  $\text{Al}_2\text{O}_3$ -Al sys-

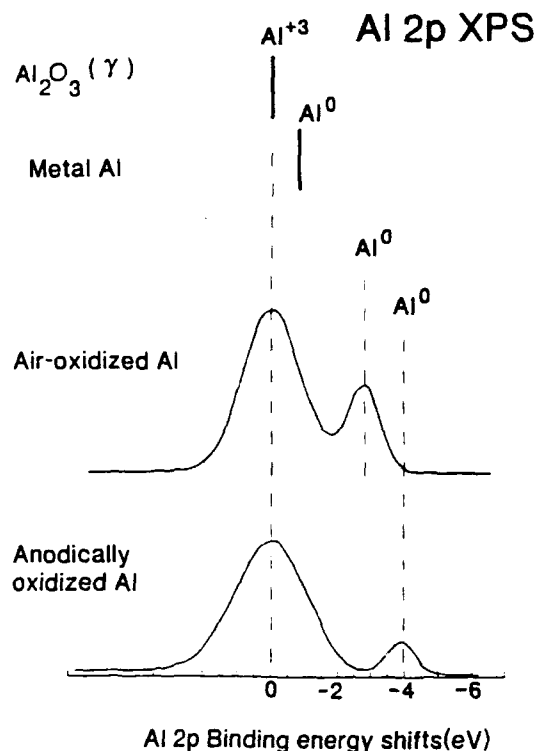


FIG. 2. Al 2p photoelectron spectra for air-oxidized Al and anodically oxidized Al obtained from Ref. 6. The  $\text{Al}^0$  and  $\text{Al}^{+3}$  peaks have been attributed to electrons originating from the metal ( $\text{Al}^0$ ) and the oxide ( $\text{Al}^{+3}$ ) portions of the samples. Also included is the Al 2p binding energy of isolated Al metal relative to that of isolated  $\text{Al}_2\text{O}_3$  ( $\gamma$ ), which are taken from Ref. 3. The  $\text{Al}^{+3}$  binding energies are aligned for comparison.

tem is nothing but energy diagrams for the isolated  $\gamma\text{-Al}_2\text{O}_3$  and elemental Al, where the vacuum level between them disappears, as shown in Fig. 3(a). Note that, in the figure, the vacuum level (VL) for  $\text{Al}_2\text{O}_3$  is equal to that for Al. We use this imaginary  $\text{Al}_2\text{O}_3$ -Al system as a reference system.

Now, we consider a more realistic  $\text{Al}_2\text{O}_3$ -Al system: A thin  $\text{Al}_2\text{O}_3$  film is grown on a clean Al surface by exposing it to dry  $\text{O}_2$  at room temperature. It is known that the oxide film formed in this way is an amorphous  $\gamma\text{-Al}_2\text{O}_3$  and almost homogeneous throughout except at the phase boundaries.<sup>5</sup> The main difference between this  $\text{Al}_2\text{O}_3$ -Al system and the reference system described above is therefore the phase boundaries. It is quite reasonable that the asymmetric forces, which are always present at phase boundaries, are adjusted in the process of the  $\text{Al}_2\text{O}_3$  film formation. Adjustment at a phase boundary normally results in the formation of an EDL at the phase boundary and hence a PD across the phase boundary.<sup>2</sup> Consequently all of the electronic energy levels of  $\text{Al}_2\text{O}_3$  shift uniformly in comparison with those levels of  $\text{Al}_2\text{O}_3$  in the reference system (a), as shown in Fig. 3(b) where the uniform shift is denoted as  $\text{PD}(\text{M/O})$ . The work function of Al metal also changes by  $\text{PD}(\text{M/O}) + \text{PD}(\text{O/V})$ , where  $\text{PD}(\text{O/V})$  is due to the EDL at the O/V interface.

XPS measurements on our reference  $\text{Al}_2\text{O}_3$ -Al system would give  $E(\text{M/O})$  as  $\text{BE}(\gamma\text{-Al}_2\text{O}_3) - \text{BE}(\text{element Al})$ ,

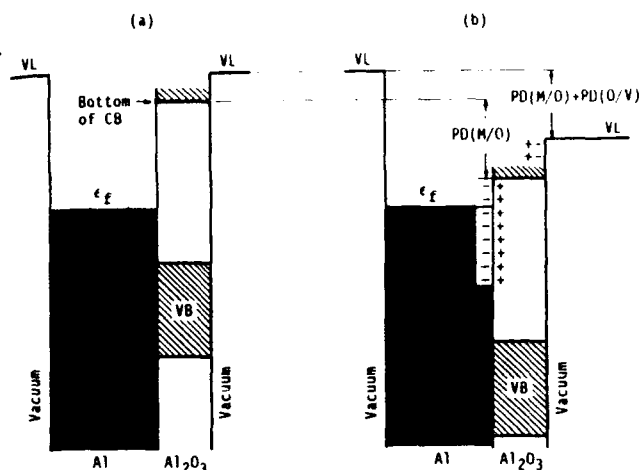


FIG. 3. Simplified electron potential energy diagrams for two distinct  $\text{Al}_2\text{O}_3$ -Al systems: For (a), the  $\text{Al}_2\text{O}_3$  film is made separately and then brought into contact with a clean Al surface; the  $\text{Al}_2\text{O}_3$  film for (b) is formed on the Al surface by exposing to  $\text{O}_2$  gas. Only in case (b) does an electrical double layer develop at the phase boundaries, especially strongly at the M/O boundary.

where  $\text{BE}(\gamma\text{-Al}_2\text{O}_3)$  and  $\text{BE}(\text{element Al})$  are the Al 2p binding energies for the isolated  $\gamma\text{-Al}_2\text{O}_3$  compound and isolated elemental Al, respectively. On the other hand, XPS measurements on the  $\text{Al}_2\text{O}_3$ -Al sample represented by Fig. 3(b) will yield the  $E(\text{M/O})$  energy parameter to be

$$E(\text{M/O}) = \text{BE}(\gamma\text{-Al}_2\text{O}_3) - \text{BE}(\text{element Al}) - \text{PD}(\text{M/O}), \quad (7)$$

provided that the XPS chemical states of the  $\text{Al}_2\text{O}_3$  film and the Al substrate are still those of the isolated  $\gamma\text{-Al}_2\text{O}_3$  and element Al. From this equation, we obtain

$$\text{PD}(\text{M/O}) = \text{BE}(\gamma\text{-Al}_2\text{O}_3) - \text{BE}(\text{element Al}) - E(\text{M/O}). \quad (8)$$

The sign of  $\text{PD}(\text{M/O})$  is chosen to be negative when the electronic levels of  $\text{Al}_2\text{O}_3$  are lowered relative to the Fermi level of Al. The EDL at the M/O interface shown in Fig. 3(b) therefore gives a negative  $\text{PD}(\text{M/O})$  and the EDL at the O/V interface gives a positive  $\text{PD}(\text{O/V})$ .

The interfaces of an Al- $\text{Al}_2\text{O}_3$ -Al sandwich are closely related to those of the previous two  $\text{Al}_2\text{O}_3$ -Al systems. In a sandwich, an ultrathin  $\text{Al}_2\text{O}_3$  film is grown on an aluminum metal ( $\text{Al}'$ ) by exposing its surface to  $\text{O}_2$  and then another aluminum metal ( $\text{Al}''$ ) is deposited on the already grown  $\text{Al}_2\text{O}_3$  film. Therefore, the  $\text{Al}'$ - $\text{Al}_2\text{O}_3$  interface will be almost identical to the Al- $\text{Al}_2\text{O}_3$  interface represented by Fig. 3(b), while the  $\text{Al}_2\text{O}_3$ - $\text{Al}''$  interface will be similar to the  $\text{Al}_2\text{O}_3$ -Al interface of the reference system [Fig. 3(a)]. Figure 4(a) shows a simplified electron-potential-energy diagram for the  $\text{Al}'$ - $\text{Al}_2\text{O}_3$ - $\text{Al}''$  sandwich. In this diagram, the effect of the EDL at the  $\text{Al}_2\text{O}_3$ - $\text{Al}''$  interface is neglected in comparison with that at the  $\text{Al}'$ - $\text{Al}_2\text{O}_3$  interface. All electron energy levels of  $\text{Al}_2\text{O}_3$  and  $\text{Al}''$  and

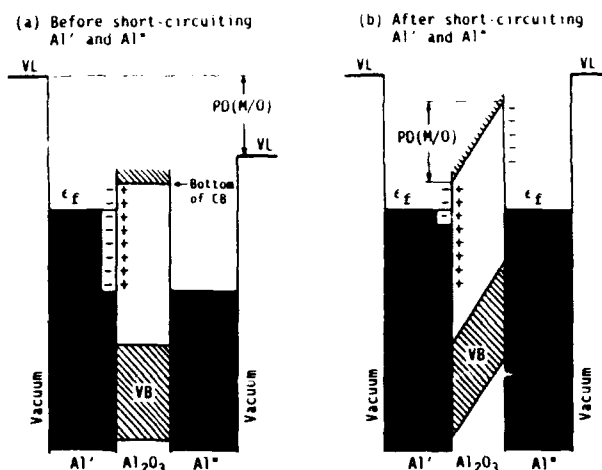


FIG. 4. Simplified electron potential energy diagrams for an Al- $\text{Al}_2\text{O}_3$ -Al sandwich. The  $\text{Al}_2\text{O}_3$  film is grown on an aluminum substrate  $\text{Al}'$  by exposing to  $\text{O}_2$  gas, and then another aluminum  $\text{Al}''$  film is deposited on the already grown  $\text{Al}_2\text{O}_3$  film. The  $\text{Al}'$  and  $\text{Al}''$  electrodes of the sandwich is open in (a), but short circuited in (b).

also the vacuum level connected to the  $\text{Al}''$  metal are lowered uniformly by  $\text{PD}(\text{M/O})$  due to the EDL at the  $\text{Al}'$ - $\text{Al}_2\text{O}_3$  interface. When the  $\text{Al}'$  and  $\text{Al}''$  electrodes of the sandwich [Fig. 4(a)] are short circuited, electrons flow from  $\text{Al}'$  to  $\text{Al}''$  until the Fermi levels of these two metals coincide with each other. As a result, positive charge is left behind at the  $\text{Al}'$ - $\text{Al}_2\text{O}_3$  interface and excessive electrons are built up on the  $\text{Al}''$  surface at the  $\text{Al}''$ - $\text{Al}_2\text{O}_3$  interface. This pair of positive and negative charges produces a trapezoidal potential barrier between the two Al metals, as shown in Fig. 4(b). Thus, the asymmetry of the potential barrier can originate from a strong double layer at the  $\text{Al}'$ - $\text{Al}_2\text{O}_3$  interface. In short, there is a close connection between the potential barrier shape of the Al- $\text{Al}_2\text{O}_3$ -Al sandwich and the EDL strengths at the two phase boundaries.

### III. EXPERIMENTAL RESULTS

#### A. Modified Auger parameters $E(\text{Al}^{+3})$ and $E(\text{Al}^0)$

Wagner conducted a comprehensive survey on Auger and photoelectron energies published up to 1982 and compiled these energies and also the modified Auger parameters in Ref. 3. The claimed accuracy of the data for aluminum-oxygen compounds is around  $\pm 0.1$  eV.<sup>4</sup> Table I lists the modified Auger parameters (MAP) obtained from Refs. 3 and 4 for Al metal and  $\text{Al}_2\text{O}_3$  oxides. For easier comparison, the MAP minus 1460 eV are listed.

Oxidized Al, which is denoted as  $\text{Al}_2\text{O}_3/\text{Al}$  in Table I, exhibits two MAPs, since it has two (metal and oxide) phases. The  $E(\text{Al}^0)$  of the oxidized Al agrees with the MAPs of pure Al (see Table I), indicating that the metal portion of the  $\text{Al}_2\text{O}_3/\text{Al}$  was not altered significantly by oxidation as far as XPS can detect. Further, the  $E(\text{Al}^{+3})$  of oxidized Al is equal to the MAP of pure  $\gamma\text{-Al}_2\text{O}_3$ , which differs substantially from the MAPs of other  $\text{Al}_2\text{O}_3$  com-

TABLE I. The modified Auger parameters (MAP) obtained from Ref. 3 for Al metal and Al<sub>2</sub>O<sub>3</sub> compounds. For easier comparison, the MAP (in eV) minus 1460 eV are listed.

Compound	$E(\text{Al}^{+3}) - 1460 \text{ eV}$	$E(\text{Al}^0) - 1460 \text{ eV}$
Al <sub>2</sub> O <sub>3</sub> /Al	1.6	6.3*
Al <sub>2</sub> O <sub>3</sub> /Al	1.6	6.2*
Al <sub>2</sub> O <sub>3</sub> ( $\gamma$ )	1.6	...
Al <sub>2</sub> O <sub>3</sub> ( $\alpha$ )	2.1	...
Al <sub>2</sub> O <sub>3</sub> sapphire	2.0	...
Al <sub>2</sub> O <sub>3</sub> sapphire <sup>b</sup>	2.0	...
Al <sub>2</sub> O <sub>3</sub> (undefined)	1.9	...
Al	...	6.1
Al	...	6.1
Al	...	6.2

\*Calculated from the MAP difference and the  $E(\text{Al}^{+3})$  value.

<sup>b</sup>Heated in vacuum at 450 °C.

pounds, as seen in Table I. This confirms that an oxide film on Al is indeed a  $\gamma$ -like alumina as found previously.<sup>5</sup> Furthermore, this agreement also confirms that  $E(\text{Al}^{+3})$  and  $E(\text{Al}^0)$  are indeed independent of the interfacial potentials.

## B. $E(\text{M/O})$ and $\text{PD}(\text{M/O})$

Table II lists some of the observed  $E(\text{M/O})$ , which is defined as the energy difference between the two Al 2p peaks [see Eq. (5)]. Figure 2 shows the XPS spectra for the first and the last data entries in Table II, revealing the energy changes. Also shown in the figure is the Al 2p binding energy of the isolated Al metal relative to that of the isolated  $\gamma$ -Al<sub>2</sub>O<sub>3</sub> compound. The Al<sup>+</sup><sup>3</sup> binding energies are aligned for comparison. Table II reveals that the  $E(\text{M/O})$  values depend on the oxidation conditions. Later we will show that  $E(\text{M/O})$  also depends on the Al surface indices (i.e., surface on which the Al<sub>2</sub>O<sub>3</sub> film grows). For the XPS measurements referenced in Table II, the Al surfaces were not well characterized. To separate out these two effects, we need more systematic measurements on well defined Al surfaces and specific oxidation conditions.

The  $E(\text{M/O})$  value depends not only on  $\text{PD}(\text{M/O})$  but also on the XPS chemical states of the Al<sub>2</sub>O<sub>3</sub> film and the Al metal. Changes in the XPS chemical states can be monitored by measuring the MAPs. But unfortunately no such monitoring has been carried out except for the first case in Table II, which shows that the XPS chemical states of the Al<sub>2</sub>O<sub>3</sub> films and the Al substrate are those of pure  $\gamma$ -Al<sub>2</sub>O<sub>3</sub>

TABLE II. Observed  $E(\text{M/O})$  values for Al<sub>2</sub>O<sub>3</sub> films grown on an Al surface under various oxidation conditions.

Oxidation conditions	$E(\text{M/O})$ (in eV)	$-\text{PD}(\text{M/O})^a$ (in eV)	Ref.
Air, at room temperature	2.7	1.9	6
O <sub>2</sub> , at room temperature	2.7	1.9	1
O <sub>2</sub> , at 700 °C for 16 min	3.2	2.4	8
O <sub>2</sub> , at 700 °C for 42 min	3.6	2.8	8
Anodic	3.4	2.6	7
Anodic, in Na <sub>2</sub> SO <sub>4</sub>	4.0	3.2	6

<sup>a</sup>Calculated from Eq. (8) with  $\text{BE}(\gamma\text{-Al}_2\text{O}_3) - \text{BE}(\text{pure Al}) = 0.8 \text{ eV}$  obtained from Ref. 3.

and elemental Al as detected by XPS. Furthermore it is known that the anodic films formed on Al are also  $\gamma$ -like Al<sub>2</sub>O<sub>3</sub>.<sup>5</sup> Based on these facts, we speculate that the XPS chemical state changes of the Al<sub>2</sub>O<sub>3</sub> and the Al substrate contribute less than 0.5 eV to the  $E(\text{M/O})$  value, which is the largest XPS chemical state change observed among the Al<sub>2</sub>O<sub>3</sub> compounds (see Table I).

The  $\text{PD}(\text{M/O})$ 's in Table II are calculated from Eq. (8) with  $\text{BE}(\gamma\text{-Al}_2\text{O}_3) - \text{BE}(\text{element Al}) = 0.8 \text{ eV}$ , which are evaluated with the data from Ref. 3. Here we have assumed that the XPS chemical states of the Al<sub>2</sub>O<sub>3</sub> film and the Al substrate are the same as those of  $\gamma$ -Al<sub>2</sub>O<sub>3</sub> and elemental Al. The error in  $\text{PD}(\text{M/O})$  due to this assumption could be as large as 0.5 eV as discussed in the previous paragraph. The sign of  $\text{PD}(\text{M/O})$  is, however, invariably negative for all cases in Table II. This means that the polarity of the EDL is always the polarity shown in Fig. 3(b), namely, an excess positive charge on the Al<sub>2</sub>O<sub>3</sub> surface and the induced counter electron charge on the Al surface.

## C. Magnitude of $\text{PD}(\text{O/V})$

Now, we attempt to estimate the magnitude of  $\text{PD}(\text{O/V})$  due to an EDL at the O/V interface. The difference between  $\text{BE}(\text{Al}^{+3})$  of the Al<sub>2</sub>O<sub>3</sub> film and  $\text{BE}(\gamma\text{-Al}_2\text{O}_3)$  of the isolated  $\gamma$ -Al<sub>2</sub>O<sub>3</sub> should give  $\text{PD}(\text{O/V})$ , provided that the following conditions are met: (a) the static-charge-referencing problem for these two measurements do not introduce errors and (b) not only the XPS chemical state but also the surface conditions of the Al<sub>2</sub>O<sub>3</sub> are the same as those of the isolated  $\gamma$ -Al<sub>2</sub>O<sub>3</sub>. Assuming that the data cited in Ref. 3 satisfy these conditions, we obtain  $\text{PD}(\text{O/V}) = +0.4 \text{ eV}$ . Although the error in  $\text{PD}(\text{O/V})$  could be as large as  $\pm 0.5 \text{ eV}$ , we may conclude that the magnitude of  $\text{PD}(\text{O/V})$  is substantially smaller than that of  $\text{PD}(\text{M/O})$ .

## D. Work function change

The work function changes ( $\Delta\phi$ ) of the three Al surfaces (111), (110), and (100) upon oxidation with a high oxygen exposure ( $> 400 \text{ L}$ ) are about  $-0.2$ ,  $-0.8$ , and  $-1.3 \text{ eV}$ , respectively.<sup>9,10</sup> In our model, the work function change of the oxidized Al is given by

$$\Delta\phi = \text{PD}(\text{M/O}) + \text{PD}(\text{O/V}), \quad (9)$$

as can be seen in Fig. 3(b). From XPS data, we have deduced a large negative value for  $\text{PD}(\text{M/O})$  and a small value for  $\text{PD}(\text{O/V})$ . Therefore we expect a negative  $\Delta\phi$  for all cases agreeing with the above observations. Conversely, we may state that the work function change is mainly due to the formation of an EDL at the Al-Al<sub>2</sub>O<sub>3</sub> interface. This statement implies that the EDL strength depends on the Al surface on which the Al<sub>2</sub>O<sub>3</sub> film grows. This is, we think, quite reasonable.

## E. Potential barrier shape for Al-Al<sub>2</sub>O<sub>3</sub>-Al sandwich

The composition of the Al-Al<sub>2</sub>O<sub>3</sub>-Al sandwich suggests a symmetric potential barrier shape. However, experiments consistently show an asymmetric potential barrier of ap-

proximately the trapezoidal barrier shape as shown in Fig. 4(b).<sup>11-13</sup> The barrier height  $\phi_1$  at the  $\text{Al}'\text{-Al}_2\text{O}_3$  interface is always found to be lower than the barrier height  $\phi_2$  at the  $\text{Al}_2\text{O}_3\text{-Al}''$  interface,<sup>11-13</sup> as indicated in Fig. 4(b). The observed value for  $\phi_2 - \phi_1$ , however, varies from 0.4 eV (Ref. 11) to 1.9 eV (Ref. 12) and other measurements<sup>13</sup> fall between these two values. In our model described in Sec. II B, we have

$$\phi_2 - \phi_1 \approx -PD(M/O), \quad (10)$$

neglecting the effect of the weaker EDL at the  $\text{Al}_2\text{O}_3\text{-Al}''$  interface. Since  $PD(M/O)$  was always found to be negative from the analysis of the XPS data, we expect  $\phi_2 - \phi_1 > 0$  for all cases as observed. Conversely, the main cause of the asymmetric barrier shape for  $\text{Al-Al}_2\text{O}_3\text{-Al}$  sandwiches can be attributed to a strong EDL formed at the  $\text{Al-Al}_2\text{O}_3$  interface by oxidation.

#### IV. SUMMARY

XPS data, work function changes, and potential barrier shapes all consistently reveal that a strong EDL is formed at the  $\text{Al-Al}_2\text{O}_3$  interface upon oxidation of a clean Al surface. The EDL strength depends on the Al surface indices and the oxidation conditions. The polarity of the EDL is always found as such: a positively charged  $\text{Al}_2\text{O}_3$  interface surface and the counter electrons in the Al metal.

In a larger sense, this work has demonstrated for the first time that XPS can be used to investigate the interfacial potential induced between an ultrathin film and its substrate. The photoelectron-binding-energy (or Auger-line-energy) difference of a selected atom of the film and another selected atom of the substrate directly depends on

this interfacial potential. If the modified Auger parameters of the film and the substrate are unchanged, a change in the energy difference equals a change in the interfacial potential. The advantage of utilizing these (photoelectron or Auger) energy differences is that they are independent of the surface conditions of the thin film.

#### ACKNOWLEDGMENTS

This work was supported by the U.S. Office of Naval Research. The authors acknowledge Xiaowei Jin's assistance in preparing Fig. 2.

This article was presented at the 38th National Symposium of the American Vacuum Society Topical Conference, Surface Science at the Solid-Liquid Interface (TC1).

<sup>1</sup>A. Barrie, *Chem. Phys. Lett.* **19**, 109 (1973).

<sup>2</sup>J. O'M. Bockris and A. K. N. Reddy, *Modern Electrochemistry* (Plenum, New York, 1970), Chap. 7.

<sup>3</sup>C. D. Wagner, in *Practical Surface Analysis by Auger and X-ray Photoelectron Spectroscopy*, edited by D. Briggs and M. P. Seah (Wiley, Chichester, 1983), p. 477.

<sup>4</sup>C. D. Wagner *et al.*, *J. Vac. Sci. Technol.* **21**, 933 (1982).

<sup>5</sup>A. Despic and V. P. Parkhutik, in *Modern Aspects of Electrochemistry No. 20*, edited by J. O'M. Bockris, R. E. White, and B. E. Conway (Plenum, New York, 1989), Chap. 6.

<sup>6</sup>G. D. Davis, W. C. Moshier, T. L. Fritz, and G. O. Cote, *J. Electrochem. Soc.* **137**, 422 (1990).

<sup>7</sup>A. C. Miller cited by B. R. Strohmeyer, *Appl. Surf. Sci.* **40**, 249 (1989).

<sup>8</sup>C. Ocal, B. Basurco, and S. Ferrer, *Surf. Sci.* **157**, 233 (1985).

<sup>9</sup>R. Michel *et al.*, *Surf. Sci.* **95**, 309 (1980).

<sup>10</sup>P. Hofmann, W. Wyrobisch, and A. M. Bradshaw, *Surf. Sci.* **80**, 344 (1979).

<sup>11</sup>A. Braunstein, M. Braunstein, G. S. Picus, and C. A. Mead, *Phys. Rev. Lett.* **14**, 219 (1965); A. I. Braunstein, M. Braunstein, and G. S. Picus, *ibid.* **15**, 956 (1965).

<sup>12</sup>K. W. Shepard, *J. Appl. Phys.* **36**, 796 (1965).

<sup>13</sup>T. E. Hartman, *J. Appl. Phys.* **35**, 3283 (1964).

# Observation of electronic structure at the metal/electrolyte and metal/vacuum interface by second-harmonic generation

R. A. Bradley and R. Georgiadis

*Department of Chemistry, University of Oregon, Eugene, Oregon 97403*

S. D. Kevan

*Department of Physics, University of Oregon, Eugene, Oregon 97403*

G. L. Richmond

*Department of Chemistry, University of Oregon, Eugene, Oregon 97403*

(Received 1 October 1991; accepted 11 May 1992)

The detailed frequency dependence of second-harmonic generation (SHG) from Ag(111) is remarkably similar for the metal/electrolyte and metal/vacuum interface. In both environments, resonant enhancement of the SHG is observed which is attributed to optical transitions at the metal surface consistent with the surface electronic band structure.

## I. INTRODUCTION

Determination of the electronic structure of metal surfaces under ultrahigh-vacuum (UHV) conditions has been an active area of both experimental and theoretical research over the past two decades. Because of these efforts, there is a vast data base that describes the electronic bands and states that exist at a wide range of surfaces, how these relate to the bulk band structure, how they are affected by the presence of adsorbates, and how they might influence the chemical and structural stability of the surface. Unfortunately, due to the incompatibility of the experimental techniques used in these studies to more reactive conditions, such as a metal in an electrolyte, characterization of the electronic structure of metals outside of UHV is nearly nonexistent. Techniques such as electroreflectance have been useful, but since analogous measurements in the UHV environment are not possible, assignments of surface electronic structure based merely on the optical reflectance of the surface are subject to some uncertainty. Such questions arise in particular when surface states are invoked in the electrochemical studies. In UHV, one means of verification of a surface state detected by various electron spectroscopy techniques is to watch its disappearance as an adsorbate is introduced to the surface. The fact that water adsorbed on Ag(111) at 110 K has been shown to quench surface states in UHV (Ref. 1) raises the question of whether surface states in the electrochemical environment may also be quenched.

What is clearly needed to provide an understanding of the electronic structure of metal electrode surfaces is a technique that is not only surface specific but is also one that can transcend the problem of incompatibility with various environments and draw on information available for metal surfaces characterized in vacuum. Our approach has been to use optical second-harmonic generation (SHG) to achieve such a goal.<sup>2</sup> In addition to being surface specific and compatible to vacuum, ambient, and solution conditions, as in any spectroscopy, one can take advantage of optical resonance effects to locate surface structure and the effect of the environment on such electronic properties. At this time, due to the youth of the field relative to tech-

niques such as photoemission, much of the current experimental work is of an exploratory nature. In addition, nearly all theoretical efforts that might aid the progress rely upon hydrodynamic and free-electron models which cannot address resonant effects due to electronic band structure. Critical to progress in the experimental area is the ability to make wavelength-dependent measurements of the SH response from these surfaces in solution and compare the results with complementary UHV SH measurements which can be correlated with what is known about these surfaces in UHV.

A particular surface that has been of interest to our laboratory is Ag(111).<sup>3-8</sup> Over the years there have been a number of electroreflectance studies which have attempted to probe the electronic structure of this metal in solution, involving measurements of the linear reflectivity of the surface as a function of surface charge, wavelength, and optical polarization. The early studies in this area have described the observed potential dependence in the reflectance with a free-electron model.<sup>9</sup> Later studies which showed polarization anisotropy in the linear response attributed the potential-dependent observations to electro-modulation of surface states at the Ag(110) electrode surface.<sup>10,11</sup> Silver surfaces in solution<sup>12</sup> and in UHV (Ref. 13) have also been the focus of several theoretical efforts aimed at developing a model describing its nonlinear optical response. Recent studies from this laboratory which show that the SH response with incident infrared wavelengths varies with azimuthal rotation of the crystal calls into question the validity of any interpretation of this metal as exhibiting free-electron behavior. Other studies from this laboratory<sup>5,6,14</sup> and Furtak<sup>15</sup> have shown that the SH response from the metal examined in solution varies as the incident or SH photons can energetically couple to the electronic structure of the metal.

This paper reports the first detailed frequency-dependent measurements of the SH response from a Ag(111) surface examined in both the electrochemical environment and in UHV. We have chosen incident wavelengths in the region between 1064 and 532 nm with particular focus on 660–620 nm where it was previously

shown that the SH response exhibits dramatic variations in the rotational anisotropy with wavelength and also exhibits extreme sensitivity to the applied potential.<sup>6</sup> The frequency dependence of the SH response in UHV shows the sensitivity of SHG to the electronic structure, in qualitative agreement with results previously reported by Giesen *et al.*<sup>16</sup> The analogous frequency-dependent measurement obtained in the electrochemical environment provides information about the electronic structure in the presence of electrolyte and applied potential. More important, the results demonstrate that the nonlinear optical properties of the surface biased at the potential of zero charge are nearly identical to the clean surface in UHV, suggesting that the water does not strongly perturb the surface electronic structure.

## II. EXPERIMENT

For the optical measurements at 1064 and 532 nm excitation, the fundamental or second-harmonic output from a 10 Hz Nd:YAG laser producing 10 ns pulse was used. The output of a Nd:YAG pumped-dye laser (Spectraphysics, PDL-3) was employed for other visible wavelengths. The angle of incidence for all experiments described here is fixed at 45°, but for the electrochemical experiments the dispersion of water yields an effective angle of 32°. A high-extinction-coefficient broadband polarizing beamsplitting cube selects the polarization of the light striking the metal surface and of the SH generated at the surface. For the dye laser experiments, a portion of the incident light was split off from the main beam and directed into a 1-mm-long quartz cell containing a suspension of potassium dihydrogen phosphate (KDP) powder in decahydronaphthalene.<sup>17</sup> The transmitted SH light served as a reference to normalize for the quadratic dependence of SHG and to correct for intensity variations in the dye laser gain curve. Appropriate filters and a monochromator separate the second-harmonic signal (or reference) from the specularly reflected (or transmitted) fundamental light. The output of each monochromator is detected by a photomultiplier tube using a fast preamplifier with gated electronics.

For both experiments, the 99.999% pure Ag(111) crystal (Monocrystals, Cleveland, OH) was oriented within 1° by Laue x-ray diffraction. For the UHV experiments, the surface was chemomechanically polished with chromic acid before insertion into UHV. After successive cycles of sputtering and annealing, the Ag(111) surface was found free of impurities by Auger spectroscopy and exhibited a low-energy electron diffraction (LEED) pattern characteristic of a well-ordered (1×1) surface. These experiments were performed in a chamber with a base pressure of  $3 \times 10^{-10}$  Torr and equipped with a manipulator capable of 360° azimuthal sample rotation and standard surface preparation techniques. Before each experiment, the surface was sputtered and annealed to 400 °C. For the solution experiments, the mechanically polished surface was maintained under an inert O<sub>2</sub>-free atmosphere throughout the electrochemical polishing and subsequent transfer into the electrochemical cell. The electrochemical polishing was employed to remove the remaining damage layer after me-

chanical polishing to a bright, specular surface. All solutions were prepared from high-purity salts and nanopure water, and the electrolyte was continuously purged with O<sub>2</sub>-free N<sub>2</sub> throughout the electrochemical experiments to avoid oxide formation. The electrochemical cell design has been described previously.<sup>4</sup> The electrochemical potential was restricted within the limits of solvent reduction and surface oxidation to avoid surface charge-transfer reactions, as evidenced by a featureless cyclic voltammogram for all experiments.

## III. THEORY

The SH measurements in this work were measured with *p*-polarized incident light and either *p*- or *s*-polarized second-harmonic light. Theoretical fits to the rotational anisotropy are from a phenomenological theory of optical second-harmonic generation from cubic media given by Tom<sup>18</sup> and Sipe, Moss, and Van Driel.<sup>19</sup> In such media, bulk SH is forbidden under the electric dipole approximation, with surface sensitivity of SHG for Ag derived from inversion symmetry breaking at the metal surface. The second-harmonic intensity  $I(2\omega)$  is described by

$$I_{p,p}(2\omega) \propto |a^{(\infty)} + c^{(3)} \cos(3\phi)|^2, \quad (1)$$

$$I_{p,s}(2\omega) \propto |b^{(3)} \sin(3\phi)|^2, \quad (2)$$

where the subscripts refer to the polarizations of the fundamental and SH light, respectively. The azimuthal angle  $\phi$  is defined as the angle between the  $2\bar{1}\bar{1}$  direction and the projection of the incident wave vector parallel to the surface. The complex coefficients  $a^{(\infty)}$ ,  $b^{(3)}$ , and  $c^{(3)}$  contain surface dipole susceptibility elements  $\chi_{ijk}$ , higher-order bulk susceptibility terms  $\gamma$  and  $\zeta$ , and appropriate fresnel factors. The selected polarization conditions are useful for probing electronic structure. For example, with *p*-input and *s*-output polarization (*p,s*), and an azimuthal angle of 30°, the in-plane response contained in the parameter  $b^{(3)}$  is isolated. This anisotropic, or in-plane response arises from the susceptibility elements  $\chi_{xxx}$  and  $\zeta$ , which are contained in both  $b^{(3)}$  and  $c^{(3)}$ . For *p* input and output the observed intensity modulation with azimuthal rotation, or rotational anisotropy, arises from the interference between the anisotropic and isotropic terms. A fit to Eq. (2) yields the ratio  $c^{(3)}/a^{(\infty)}$ , which contains a magnitude and a phase angle reflecting this interference under the experimental conditions. In general, not only the susceptibility elements but the fresnel coefficients will influence this interference. Therefore, rotational anisotropy under these polarization conditions is very sensitive to relative changes in both magnitude and phase of either the isotropic or anisotropic contributions. With the azimuthal angle set at  $\phi = 30^\circ$  for this polarization combination, one can isolate the contribution from the  $a^{(\infty)}$  term, referred to as the isotropic coefficient since the susceptibilities contained therein do not vary with azimuthal angle and describe the out-of-plane response.

## Ag(111)

in UHV

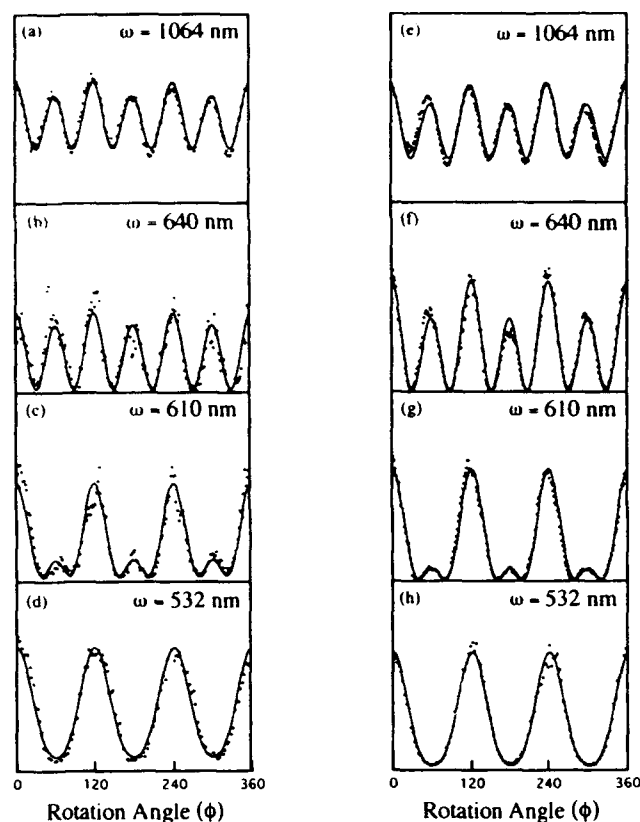
0.1 M NaClO<sub>4</sub>  
at the PZC

FIG. 1. SH rotational anisotropy from Ag(111) under *p*-polarized excitation at the wavelength indicated: (a)–(d) in UHV at  $3 \times 10^{-10}$  Torr; and (e)–(h) in aqueous electrolyte at the PZC. The open circles represent the *p*-polarized SH data and theoretical fits using Eq. (2) are indicated with a solid line. See Table I for fitting parameters.

## IV. RESULTS

Figures 1(a)–1(d) show the rotational anisotropy for *p* input and output polarizations from a clean Ag(111) crystal in UHV at a series of excitation wavelengths. For these experiments, the crystal was clean and well ordered as verified by Auger spectroscopy and LEED. As the incident photon energy increases, the progressive change in the anisotropies is best described by the change in the phase angle of  $c^{(3)}/a^{(\infty)}$ , the difference in phase between the in-plane and out-of-plane response. The fitting parameters for each excitation wavelength are given in Table I. This is the first study in UHV to demonstrate the sensitivity of these SH anisotropy measurements to wavelength. The overall change in pattern and associated phase angle can be attributed to increased coupling of the harmonic field to surface electronic transitions near 3.9 eV. Although normalized intensity measurements have not been made over this entire spectral region, the relative phase change is consistent with a progression to nonresonant from resonant conditions. A future paper will address this in more detail.<sup>7</sup> Previous wavelength-dependent SH measurements have only involved intensity measurements, ignoring this very

TABLE I. Wavelength dependence of the rotational anisotropy from Ag(111) in UHV and in solution, held at the PZC; fitting parameters are from Eq. (1).

SH photon energy (eV)	$\lambda_{exc}$ (nm)	$c^{(3)}/a^{(\infty)}$	
		Solution	UHV
2.33	1064	$1.2 e^{i80^\circ}$	$1.2 e^{i85^\circ}$
3.875	640	$5.4 e^{i57^\circ}$	$3.95 e^{i81^\circ}$
4.065	610	$1.85 e^{i18^\circ}$	$1.74 e^{i42^\circ}$
4.66	532	0.6	0.7

important additional phase information which can identify resonant coupling. We find that this additional sensitivity to resonance phenomena which the phase data provides, either directly through interference measurements or indirectly through anisotropy data, is particularly valuable when studying a broad wavelength range where intensity normalization for different dye ranges can be difficult. One does however have to be somewhat cautious in overinterpretation of the phase difference between  $c^{(3)}$  and  $a^{(\infty)}$  since both terms may change phase with wavelength. More valuable and explicit phase information can be garnered from direct phase measurements using an interference method.<sup>20</sup> Nevertheless, for Ag(111) the phase angle varies with wavelength in a well-behaved manner and converges to  $\pi/2$  at wavelengths longer than 1064 nm.<sup>7</sup>

Figures 1(e)–1(h) show an equally dramatic variation in the rotational anisotropy for *p* input and output polarizations from an Ag(111) crystal in 0.1 M NaClO<sub>4</sub> electrolyte at the same excitation wavelengths. For the electrochemical experiments, the electrode was held at the potential of zero charge (PZC) to minimize the effect of the dc field across the electrochemical interface. At fixed excitation wavelength the data can be fit well by the functional form given in Eq. (1). The fitting parameters for each excitation wavelength are also given in Table I for comparison with the UHV data. One might assume that this striking similarity draws into question the sensitivity of SHG to surface properties. However, the PZC is a very special condition and when the electrode is biased to either side of the PZC, the SH response changes dramatically.<sup>6</sup> At the longer wavelengths, the magnitude of the isotropic contribution changes with potential whereas at shorter wavelengths both the isotropic and anisotropic terms change in magnitude and phase with potential.

Rotational anisotropy data collected in these experiments for additional wavelengths (not shown) indicate that the most dramatic changes in anisotropy occur between  $\omega = 640$  nm and  $\omega = 610$  nm. To explore this behavior in more detail we have measured the wavelength dependence in solution and in UHV in this region. Figure 2 shows the explicit wavelength dependence of the SH intensity from Ag(111) in UHV for *p*-input and *s*-output (*p,s*) polarization from  $2\omega = 307$  nm to  $2\omega = 330$  nm. The normalized intensity shows a peak at  $2\omega = 325$  nm (3.82 eV), with a full width at half-maximum (FWHM) of 9 nm (100 meV). For the experiments in this spectral region, the greatest intensity is observed for the (*p,s*) polarization con-



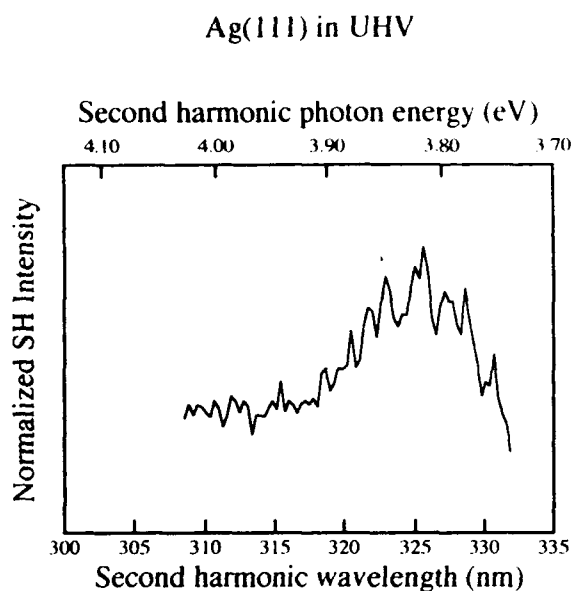


FIG. 2. Normalized SH intensity of the in-plane or anisotropic response from Ag(111) in UHV under  $p$ -polarized input and  $s$ -polarized output as a function of the second-harmonic photon wavelength in nm (lower axis) and energy in eV (upper axis).

dition (data shown), but under  $(p,p)$  polarization the intensity is significantly smaller, close to the detection limits. This is in contrast with the response at 1064 nm, where the  $p$ -output polarization dominates. As the  $(p,s)$  polarization condition probes the  $\chi_{xxx}$  and  $\zeta$  susceptibilities, these terms dominate the total SH response in this spectral region.

Our results can be compared with the previous studies of Giesen *et al.*<sup>16</sup> in which the frequency dependence of the SH intensity from Ag(111) in UHV was measured between  $\omega = 620$  nm and  $\omega = 665$  nm ( $2\omega = 4$ –3.73 eV) and the results correlated with two-photon photoemission measurements. Their two-photon photoemission measurements showed a sharp resonance feature at 3.84 eV, which was only observed for photons having an  $E_z$  component of the electromagnetic field. They assigned this feature to a transition from an occupied crystal-induced surface state  $A$  of mostly  $p_z$  character at  $\bar{\Gamma}$  to an unoccupied ( $n = 1$ ) image potential state  $I$ . In their SH measurements, they defined the input polarization but did not define the output polarizations. For both  $p$ - and  $s$ -input polarizations they observed a feature at  $2\omega = 3.85$  eV ( $2\omega = 322$  nm), which was assigned to the  $A$ - $I$  transition. They also reported a shoulder in the SH intensity toward lower energy near 3.70 eV ( $2\omega = 335$  nm) which was attributed to a surface plasmon at 3.6 eV. Although we also find a feature at 3.82 eV ( $2\omega = 325$  nm), the SH intensity is largest for input and output photons with  $E_x$  polarization. However, there is no evidence of the "surface-plasmon" shoulder in our spectra.

To investigate the impact of the presence of the electrolyte on the peak which we observe near 3.82 eV, direct comparative measurements were made in solution. Figure 3 shows the explicit wavelength dependence of the SH intensity from a Ag(111) electrode for  $p$ -input and  $s$ -output polarization from  $\omega = 614$  nm to  $\omega = 660$  nm. The elec-

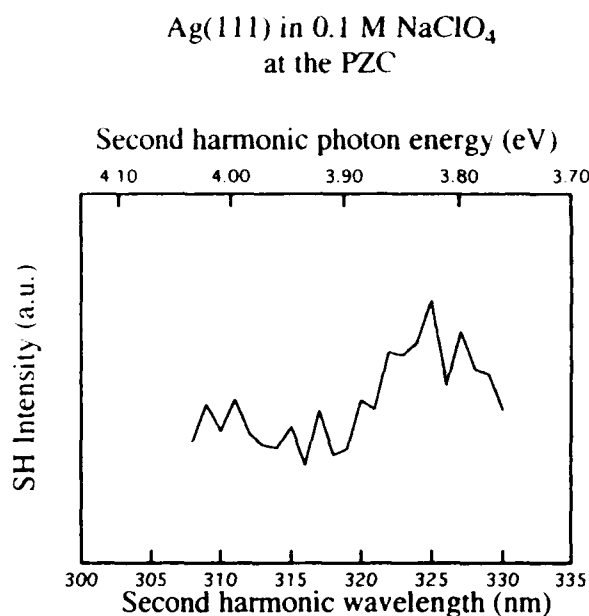


FIG. 3. Normalized SH intensity of the in-plane or anisotropic response from a Ag(111) electrode under  $p$ -polarized input and  $s$ -polarized output as a function of the second-harmonic photon wavelength in nm (lower axis) and energy in eV (upper axis). The Ag(111) electrode was immersed in 0.25 M Na<sub>2</sub>SO<sub>4</sub> and the electrode potential was held near the PZC,  $-0.7$  V vs Ag/AgCl.

trode was in 0.1 M NaClO<sub>4</sub> electrolyte and the applied potential was held at the PZC to minimize the influence of the electrochemical double layer on the SH response. In these experiments, the signal-to-noise ratio is somewhat lower than our UHV data, but the feature at  $\omega = 650$  nm ( $2\omega = 3.82$  eV) is clearly evident in the SH response. Although normalized intensity values for the UHV and electrochemical measurements are not directly comparable due to power-density differences, the qualitative agreement between the spectra is striking. In the electrochemical environment we find the intensity of this peak sensitive to applied potential with little change in the spectral energy.

Previously, Schneider, Franke, and Kolb<sup>21</sup> reported two features at 3.5 and 4.0 eV in electroreflectance measurements of Ag(111) in solution. They attributed the 3.5 eV feature to the  $A$ - $I$  transition, the intensity of which varies with electrode potential without noticeable shift in its energetic position. They assigned a broad feature near 4.0 eV with a similar potential dependence to transition from  $A$  to the unoccupied bulk  $sp$  band edge. To assign the observed features, the authors invoked inverse photoemission measurements performed in UHV (Ref. 22) which placed the energetic position of  $A$  at 400 meV above the Fermi level. In addition, critical to assignment of both transitions is the presumption that the state  $A$  is 400 meV above the Fermi level at the PZC, and that it becomes occupied upon negative bias of the electrode, where it can be observed as the initial state. The authors assign the final state  $I$  of this transition based on Giesen *et al.*'s two-photon photoemission measurements<sup>16</sup> by requiring that state  $A$  have a width of at least 400 meV.

Our results are the first to show the strong correlation of

both the rotational anisotropies and detailed frequency dependence of the SH response from Ag(111) in UHV and in solution at the PZC. Furthermore, our results show that the *A-I* transition assigned by Giesen *et al.* for Ag(111) in UHV to be at 3.84 eV is energetically unaltered and persists in the presence of the solution at the PZC. Therefore, our results imply the surface state *A* is occupied at the PZC, as well as in UHV. This is supported by angle-resolved photoemission measurements<sup>23</sup> on Ag(111) in UHV which identified the surface state *A* to be 120 meV below the Fermi level at  $\bar{\Gamma}$  with the natural linewidth estimated to be less than 50 meV. In addition to the *A-I* assignment, another possible explanation for the observed peak at 3.82 eV is a transition from *A* to the bulk *sp* band. Both assignments are consistent with our electrochemical measurements which show that the applied potential alters the intensity of the transition, consistent with change in occupation of *A* with potential as assumed in the previous study. In addition, the striking similarity in the anisotropy and intensity measurements between the Ag(111) surface in solution at the PZC and in UHV is completely inconsistent with arguments requiring in the state *A* be unoccupied at the PZC. This critical assumption in the previous electrochemical study was the basis for the assignment of a feature near 3.4 eV to the *A-I* transition. Further comparative studies at this lower-energy region are currently in progress as are studies to make a more definitive assignment of the transitions near 3.8 eV.

## V. CONCLUSIONS

This study demonstrates the value of SH rotational anisotropy measurements in identifying surface electronic structure for metals as well the importance of direct comparative measurements for correlating electronic properties in solution with the known electronic properties of metals in UHV. The detailed wavelength dependence measurements show a resonant transition at 3.8 eV. The trend observed in the relative phase (obtained by fitting the rotational anisotropies) is consistent with the existence of a resonance condition. More importantly for the electrochemical community and the study of Ag electronic structure in solution, our results reveal the striking similarity in the nonlinear optical response from Ag in UHV and solution, when the Ag electrode is held at the PZC. We are

currently investigating the potential dependence as well as extending the wavelength region of our comparative measurements.

## ACKNOWLEDGMENTS

The authors wish to thank Andreas Friedrich for scientific discussions pertaining to the manuscript. Financial support from the Army Research Office (DAAL 03-89-K-0051), for the UHV measurements, and the NSF (CHE-8801348 and CHE-9022538) for the electrochemical measurements, is gratefully acknowledged.

This article was presented at the 38th National Symposium of the American Vacuum Society Topical Conference, Surface Science at the Solid-Liquid Interface (TC1).

- <sup>1</sup>B. Reihl, K. H. Frank, and R. R. Schlittler, *Phys. Rev. B* **30**, 7328 (1984).
- <sup>2</sup>G. L. Richmond, J. M. Robinson, and V. L. Shannon, *Prog. Surf. Sci.* **28**, 1 (1988).
- <sup>3</sup>V. L. Shannon, D. A. Koos, and G. L. Richmond, *J. Phys. Chem.* **91**, 5548 (1987).
- <sup>4</sup>D. A. Koos, V. L. Shannon, and G. L. Richmond, *J. Phys. Chem.* **94**, 2091 (1990).
- <sup>5</sup>R. A. Georgiadis, G. A. Neff, and G. L. Richmond, *J. Chem. Phys.* **92**, 4623 (1990).
- <sup>6</sup>R. Georgiadis and G. L. Richmond, *J. Phys. Chem.* **95**, 2895 (1991).
- <sup>7</sup>E. K. L. Wong, K. A. Friedrich, and G. L. Richmond, *Chem. Phys. Lett.* (to be published).
- <sup>8</sup>D. A. Koos, V. L. Shannon, and G. L. Richmond (unpublished).
- <sup>9</sup>J. D. E. McIntyre, *Advances in Electrochemistry and Electrochemical Engineering* (Wiley, New York, 1973).
- <sup>10</sup>T. E. Furtak and D. W. Lynch, *Phys. Rev. Lett.* **35**, 960 (1975).
- <sup>11</sup>K.-M. Ho, C. L. Fu, S. H. Liu, D. M. Kolb, and G. J. Piazza, *Electroanal. Chem.* **150**, 235 (1983).
- <sup>12</sup>P. Guyot-Sionnest, A. Tadjeddine, and A. Liebsch, *Phys. Rev. Lett.* **64**, 1678 (1990).
- <sup>13</sup>A. Liebsch, *Phys. Rev. Lett.* **61**, 1233 (1988).
- <sup>14</sup>R. A. Bradley, S. Arekote, J. M. Robinson, R. Georgiadis, S. D. Kevan, and G. L. Richmond, *Chem. Phys. Lett.* **168**, 468 (1990).
- <sup>15</sup>T. E. Furtak, L. J. Simpson, and Y. Tang, *Bull. Am. Phys. Soc.* **35**, 218 (1990).
- <sup>16</sup>K. Giesen, *Phys. Scr.* **35**, 578 (1987).
- <sup>17</sup>R. D. Jones and P. R. Callis, *J. Appl. Phys.* **64**, 4301 (1988).
- <sup>18</sup>H. W. K. Tom, Ph.D. thesis, University of California, Berkeley, 1984.
- <sup>19</sup>J. E. Sipe, D. J. Moss, and H. M. Van Driel, *Phys. Rev. B* **35**, 1129 (1987).
- <sup>20</sup>R. Superfine, J. Y. Huang, and Y. R. Shen, *Opt. Lett.* (to be published).
- <sup>21</sup>J. Schneider, C. Franke, and D. M. Kolb, *Surf. Sci.* **198**, 277 (1988).
- <sup>22</sup>B. Reihl, K. H. Frank, and A. Otto, *Z. Phys. B* **62**, 473 (1986).
- <sup>23</sup>S. D. Kevan and R. H. Gaylord, *Phys. Rev. B* **36**, 5809 (1987).

# Electrochemical and *in situ* atomic force microscopy and scanning tunneling microscopy investigations of titanium in oxalic acid solution

Gilbert M. Brown

Chemistry Division, Oak Ridge National Laboratory, Oak Ridge, Tennessee 37831

T. Thundat, D. P. Allison, and R. J. Warmack

Health and Safety Research Division, Oak Ridge National Laboratory, Oak Ridge, Tennessee 37831

(Received 1 November 1991; accepted 7 January 1992)

The growth of an oxide film and the dissolution of the metal were studied by atomic force microscopy (AFM) and scanning tunneling microscopy (STM) for titanium electrodes which had been pretreated by a chemical polishing procedure. Images were obtained with a gas-solid interface and under an aqueous solution containing 0.1 M oxalic acid. The electrochemical polarization of titanium in 0.1 M oxalic acid is qualitatively the same as observed in chloride or sulfate medium, and the dissolution reaction in oxalic acid appears to follow the same monolayer coverage mechanism as in the other media. The titanium specimen is polycrystalline and the presence of grain boundaries between individual crystallites is observed by AFM. *In situ* microscopy indicates that both the rate of growth of oxide and the dissolution of the metal are dependent on the crystallographic face of the titanium. AFM and STM show that the growth of titanium (IV) oxide or hydrous oxide has the appearance of hemispherical domes which grow together to form peaks on the surface. Dissolution of the metal in the active region occurs first in areas between the peaks where the oxide is thin, and later the oxide coverage of the small peaks appears to coalesce to a smaller number of large peaks.

## I. INTRODUCTION

Scanning tunneling microscopy (STM) and atomic force microscopy (AFM) can both be carried out with the substrate of interest covered with an electrolyte solution. These microscopies allow the topography of the surface to be observed with the substrate under potentiostatic control. STM has been demonstrated to give atomic resolution with a number of substrates in air, in a vacuum, and under a layer of solution. Nanometer resolution has been routinely demonstrated for many materials by STM and also by AFM. The application of STM has been referred to as "a natural for electrochemistry."<sup>1</sup> The same certainly holds true for AFM. The latter has the advantage that the polarization current of the tip, faradaic current at the tip, and local changes in the electric field that occur with STM are not a problem with AFM. In general, AFM suffers from the disadvantage of lower resolution than STM due to convolution of the tip geometry with that of features on the substrate. These microscopies are powerful methods for studying electrochemical processes in which the surface is undergoing change such as in electrodeposition or dissolution. Very early in the application of STM to electrochemical problems the deposition of one metal on another has attracted attention.<sup>2-5</sup> The application of STM to the dissolution of a surface, such as in corrosion, is beginning to attract attention.<sup>6-9</sup>

Titanium is a structural material of some importance, and it is used in applications which require either a lightweight material or a corrosion resistant material. Thus, a study of the electrochemical properties of titanium is important. The electrochemistry of titanium is also important since this metal is a model<sup>10</sup> for materials such as stainless steel and other alloys which exist in an active and a passive

state. The passive state of titanium is characterized by a surface which is covered by an insoluble oxide film ( $\text{TiO}_2$ ). In the active state titanium metal is oxidized to form  $\text{Ti(III)}$  ions in solution. The potential region of the active-passive transition is of particular importance since the activation of a passive surface and the passivation of an active surface are believed to be the important factors in localized corrosion phenomenon such as crevice corrosion, pitting, and stress-corrosion cracking, etc.<sup>10</sup>

We report an electrochemical and an *in situ* imaging study of chemically polished, polycrystalline titanium in an aqueous 0.1 M oxalic acid solution. The chemical polishing procedure differentially etches different crystal faces of titanium, and well-defined single crystallites of Ti are observed by AFM in air. STM and AFM images of Ti with the substrate-solution interface under potentiostatic control were observed in the passive, active, and the active-passive transition potential regions. STM images of electropolished titanium surfaces have previously been reported,<sup>11</sup> but this appears to be the first report of *in situ* images of a titanium surface.

## II. EXPERIMENTAL PROCEDURES

Sodium chloride (Fisher, analytical reagent grade), hydrochloric acid (Baker, Ultrex grade), and oxalic acid (Mallinckrodt, analytical reagent grade) were used without further purification. House line distilled water was further purified by passage through a Barnstead Nanopure II apparatus. The titanium electrodes used in this study were fabricated from polycrystalline, zone-refined rods (Materials Research Corporation, Marz grade). Samples for electrochemical polarization measurements used a 12.7 mm long section of 6.4 mm diam rod which had been internally

threaded. Samples were held on the end of a glass holder with a threaded stainless steel rod, and the titanium to holder seal was made leak tight with a teflon washer. The other planar surface of the specimen was sealed with a teflon washer and Kel-F nut so that only the cylindrical surface was exposed to solution. Samples of titanium for STM and AFM investigation were cut with a diamond saw from 12.7 mm diam stock. Samples were pretreated by a chemical polishing or etching procedure which results in a surface with a relatively bright finish. The Ti specimens were dipped for a few seconds in a 1:1:1 (volume) mixture of lactic acid, concentrated nitric acid, and hydrofluoric acid. After a momentary induction period, the ensuing reaction was extremely vigorous, and it was quenched by flooding the sample with water.

Electrochemical measurements were made using an instrument consisting of a PAR model 173 potentiostat, a PAR model 175 programmer, and a pair of Keithley model 177 digital multimeters. The current and potential were recorded by feeding the current and electrometer outputs of the potentiostat to the multimeters. The analog outputs of the multimeters were displayed on a strip chart recorder to determine when the current had reached a stationary state ( $di/dt = 0$ ). The value was then read from the multimeter. The electrochemical cell for the polarization measurements was constructed of glass and teflon and had separate compartments for the reference, test, and auxiliary electrodes, separated by ungreaed precision ground glass stopcocks. The reference and test compartments were jacketed and maintained at 25 °C with a circulating water bath. The cell solutions were continuously purged with Ar to maintain anaerobic conditions. The reference electrode was either a saturated calomel electrode (SCE) or a saturated calomel electrode with the fill solution replaced with saturated NaCl (NaSCE).

STM and AFM measurements were recorded using a Digital Instruments Nanoscope II instrument. The STM head had a built in potentiostat which was used for potential control and potential measurement in combined STM-electrochemical experiments. Images were taken in the constant current mode at a tunneling current of approximately 1 nA using cut Pt-Ir tips insulated with Apiezon black wax (The faradiac current for these tips was less than 1 nA.) The electrodes for *in situ* electrochemical measurements consisted of a Pt loop auxiliary electrode and a silver wire quasireference electrode (Ag QRE). The latter was contained within a glass capillary tube which had been drawn to a very fine tip to serve as the solution-reference electrode junction. The potential of this electrode versus NaSCE is +20 mV at 25 °C. The surface of freshly chemically polished titanium is completely "wet" by aqueous solutions, and a thin film of stopcock grease was painted on the edges of the 12.7 mm Ti disk so that several drops of solution would be held on the surface. The Pt loop auxiliary electrode was pressed to the top of the pool of solution, and the reference electrode and STM tip were placed inside the loop. The STM head was covered with a bell jar, and the solution degassed by passing a stream of nitrogen through the bell jar. The Digital Instruments Nanoscope

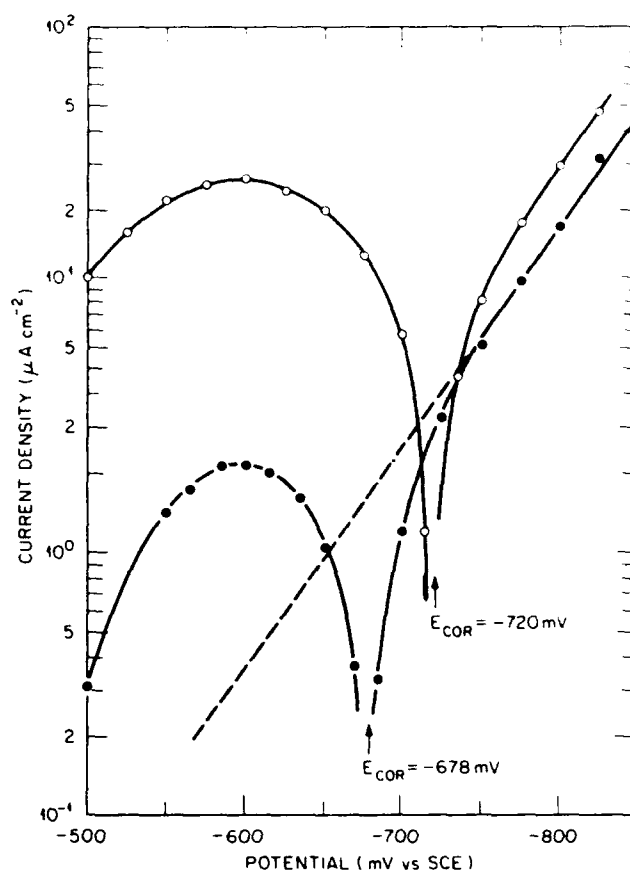


FIG. 1. Plot of  $\log I$  vs  $E$  showing the stationary state polarization of titanium in 0.1 M HCl with the ionic strength adjusted to 1.0 M with NaCl (pH 0.9). Closed circles, chloride alone. Open circles,  $1 \times 10^{-2}$  M oxalate added.

AFM solution cell was used for *in situ* AFM measurements. In the AFM measurements, potential control and measurements were made with a Bank Wenking Model POS 70 potentiostat. The reference electrode was configured in the cell by drilling a hole in a 5 ml plastic syringe near the lure tip. The Ag wire in a capillary was glued in the hole with RTV silicon rubber silastic. Degassed oxalic acid solution was drawn into the syringe and then injected into the solution cell via one of the lure joint syringe fittings and left in place. The auxiliary electrode was the small Pt wire cantilever clip which is a part of the Digital Instruments Nanoscope liquid cell.

### III. RESULTS AND DISCUSSION

#### A. Electrochemistry of titanium

The stationary state polarization of titanium in 0.1 M HCl with the ionic strength adjusted to 1.0 M with NaCl (pH = 0.9) is shown in Fig. 1 as a plot of the logarithm of the current density ( $I$ ) versus potential ( $E$ ). Also shown in Fig. 1 is the polarization behavior with the addition of  $1 \times 10^{-2}$  M oxalate ion. The anodic dissolution current in the presence of the oxalate ion is greater than in the solution containing only chloride anions, and this is taken as evidence that oxalate promotes the dissolution of titanium

more than does chloride ion. The plot of  $\log I$  versus  $E$  shows cathodic and anodic branches (anodic processes occur at potentials positive of  $E_{\text{cor}}$ ). This presentation allows the cathodic branch (due to  $\text{H}_2$  evolution) to be extrapolated back to the potential region of the anodic branch so that the anodic current can be corrected for the partial cathodic process. This also allows an estimate of the current at the open circuit potential (or corrosion potential) at which the net current is zero. In the anodic branch the stationary state current increases to a maximum, and then decreases as the titanium surface becomes passivated. In the active region the current increases with increasing potential, and the dissolution product is  $\text{Ti(III)}$ . The potential region in which the current reaches a maximum and then begins to decrease defines the active-passive transition region. Kelly<sup>10</sup> has proposed a comprehensive mechanism to explain the steady state polarization of titanium in the active and active-passive transition potential regions. The mechanism assumes the surface is covered with a monolayer of low valent species. At stationary state the surface is primarily covered with  $\text{Ti(II)}$  and  $\text{Ti(IV)}$  species with  $\text{Ti(III)}$  present as an intermediate. At the potential of the current maxima the coverage of  $\text{Ti(II)}$  and  $\text{Ti(IV)}$  are approximately 2/3 and 1/3, respectively. As the potential becomes more anodic, the fraction of  $\text{Ti(IV)}$  increases, and the  $\text{Ti(IV)}$  species is responsible for the passivation of the surface. In the passive state, a layer of  $\text{TiO}_2$  or a hydrous  $\text{Ti(IV)}$  oxide is formed on the surface.

A medium containing 0.1 M oxalic acid was chosen for an *in situ* study of the dissolution of titanium by STM and AFM. The oxalate concentration is sufficient to ensure that the dissolution reaction will occur at a high enough rate that the traces of oxygen in the solutions would not passivate the surface. On the other hand the corrosive constituent is not volatile and will not corrode the components of the STM head or the AFM cantilever. Furthermore, the ionic strength is not so high that it interferes with the maintenance of a stable tunneling current between the tip and the substrate. The anodic branch of the stationary state polarization of titanium in 0.1 M oxalic acid is shown in Fig. 2. The shape of the polarization curve and the potentials of the current maximum and the corrosion potential are similar to that observed in chloride medium, and we assume that the mechanism derived for chloride and sulfate solutions is operative in this medium also. The time to reach stationary state appears to be longer for the chemically polished samples, employed in the 0.1 M oxalic acid solution for STM-AFM investigation, than for mechanically polished samples employed in the chloride containing solutions. In general, freshly polished titanium electrodes, treated by either a mechanical or chemical procedure, take at least 24 h to come to a reproducible stationary state current at  $E_{\text{max}}$  and a reproducible open circuit or corrosion potential.

## B. AFM images of titanium with a gas-solid interface

The AFM images of the titanium surface recorded with a stream of dry nitrogen maintained through the protective bell jar are shown in Fig. 3. The surface was freshly treated

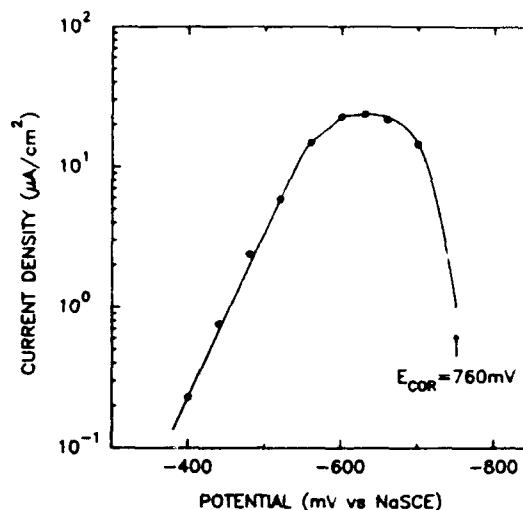


FIG. 2. Plot of  $\log I$  vs  $E$  showing the stationary state polarization of titanium in 0.1 M oxalic acid solution.

with the chemical polish, rinsed with water, rinsed with 95% ethanol, and air dried. The sample is polycrystalline, and the presence of individual randomly oriented crystallites is shown by the relatively sharp lines which separate them. The chemical polishing process removes material from different crystallographic faces at varying rates, and this results in the relatively faceted appearance of the surface in the micrograph of Fig. 3(a). The chemical polishing process apparently leads to the formation of shallow pits on the surface, and two such pits are shown in the upper left and lower right hand corners of Fig. 3(a). These pits are about 2  $\mu\text{m}$  in diameter and have a depth of approximately 0.5  $\mu\text{m}$ . At high magnification the surface has relatively large areas which are flat but covered with hemispherical domes having an average height of 4 nm above the background as shown in Fig. 3(b). Approximately 4 h after the images in Fig. 3 were recorded, the surface was reimaged and found to be approximately the same except that the density of domes had increased. The roughness was judged by determining the standard deviation of all points from the best fit plane in a 5  $\mu\text{m}$  by 5  $\mu\text{m}$  area. After 4 h the standard deviation was 9.5 nm compared to the initial value of 8.7 nm. We attribute these hemispherical domes to the formation of islands of  $\text{Ti(IV)}$  oxide or hydrous oxide since titanium is known to be a very active metal which will react with adventitious oxygen and water vapor.

AFM images of other freshly polished titanium surfaces showed relatively smooth open areas surrounded by large, circular peaks (100 nm height and diameter), some of which had the appearance of multiple, overlapping peaks. The image of these flat open areas showed the appearance of small domelike structures similar to those shown in Fig. 3(b) after standing in air for two days. These dome-like structures did not grow on the peaks which were present following the initial chemical polish. We could not obtain a stable STM image of the surface after two days in air. Presumably the oxide layer had become so thick that a

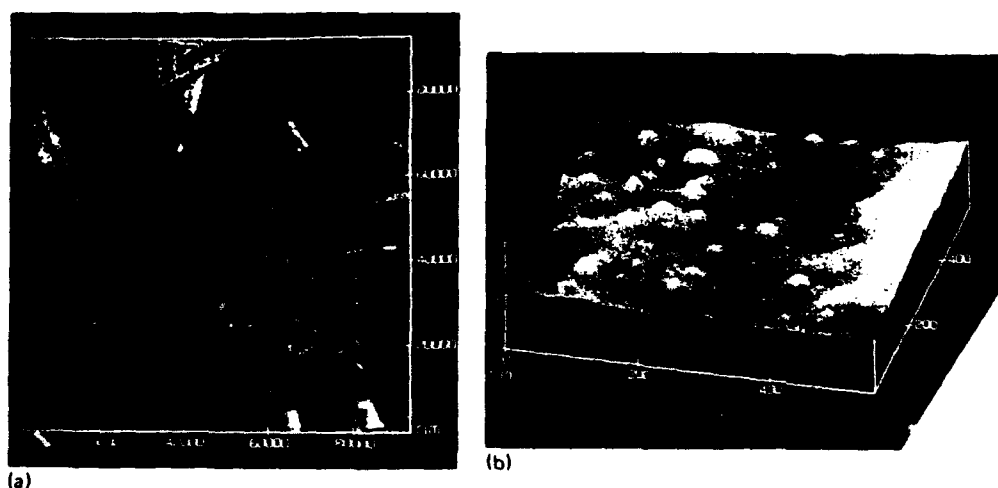


FIG. 3. AFM images of freshly polished titanium in a nitrogen atmosphere. Large area scan (a) shows the presence of grain boundaries between crystallites of titanium. The grey scale corresponds to height changes with a black to white range of 858 nm. (b) A surface view image ( $500 \times 500 \text{ nm}^2$ ) shows nodules or domes of  $\text{Ti(IV)}$  oxide on the surface.

stable tunneling current could not be established.

A titanium disc was freshly polished, and then allowed to stand overnight at an active potential in 0.1 M oxalic acid. During this time the current at  $E_{\text{max}}$  and the open circuit potential approached the stationary state values. Simultaneously the bright metallic finish was reduced to a matte grey appearance. The electrode was removed from the solution, rinsed with water and ethanol, and air dried. The surface was sufficiently roughened by this procedure that a stable AFM image could not be made. It is apparent that the microscopy cannot be determined under the same conditions used for the kinetic studies of the dissolution reaction at stationary state.

### C. *In situ* AFM and STM images of titanium

The rate of formation of the spherical domelike structures on the surface of titanium is greatly accelerated in the presence of an electrolyte solution. Figure 4 shows AFM

images of titanium covered with a solution containing 0.1 M oxalic acid. The potential was monitored while these images were recorded, and the surface was in the passive region due to the presence of an air-formed oxide film initially present on the polished surface. Although the solution was degassed, the oxygen concentration was high enough to keep the surface passive and to promote the growth of the oxide film. A distinctive feature showing the junction between several individual crystallites is shown in the topview image of Fig. 4(a). A magnification of the area indicated by the arrow in Fig. 4(a) is shown in the surface view image of Fig. 4(b). Compared to Fig. 3, the density of the domelike structures shows a dramatic increase, and in the highest density areas most of the structures have grown together. It is also apparent that the rate of oxide formation is different for different crystal faces. Each face appears to have a different density of oxide peaks in Fig. 4(b) which appears to be the junction of three different crystal

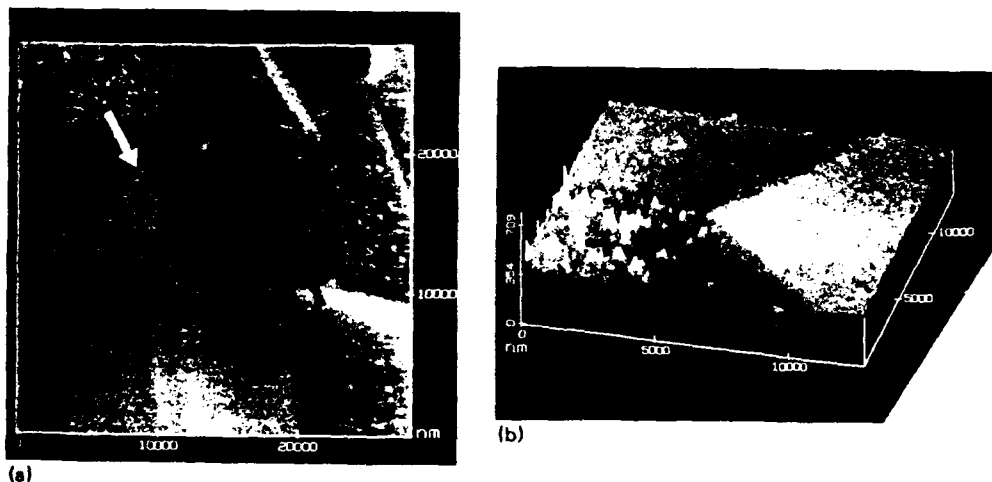


FIG. 4. AFM images of titanium under 0.1 M oxalic acid at a passive potential ( $-250 \text{ mV}$  vs Ag QRE). (a) Topview image showing a characteristic junction of several crystallites. The grey scale corresponds to height changes with a black to white range of 1256 nm. (b) Surface view image showing that the growth of oxide on titanium occurs at different rates for different crystallographic faces.

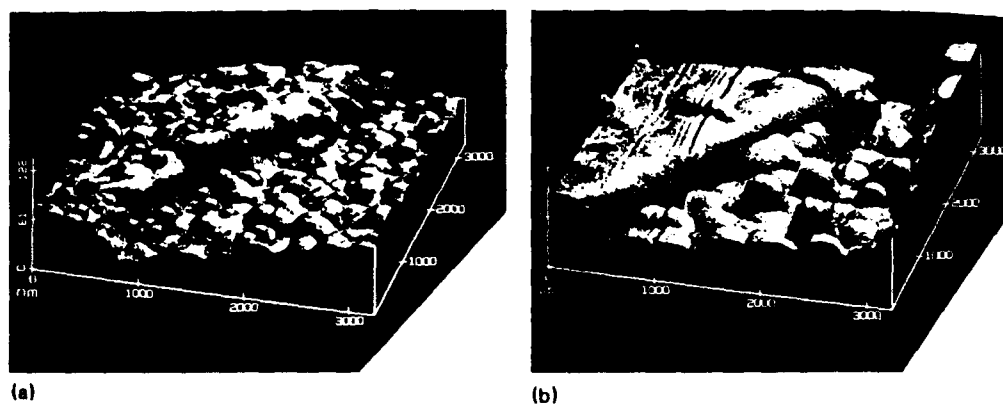


FIG. 5. Surface view AFM images of titanium under 0.1 M oxalic acid solution. (a) Image recorded immediately after passive surface was activated by holding potential at  $-750$  mV vs Ag QRE. (b) Image recorded after potential adjusted to  $-600$  mV vs Ag to increase dissolution rate. The shading in the images has been enhanced by artificial illumination.

faces. The standard deviation of all points from the best fit plane of each individual crystal region was used to judge the roughness of the three distinct areas. The lower left face in Fig. 4(b) has a standard deviation of 51 nm while the upper left is 29 nm, and the right-hand side has a standard deviation of 16 nm from the best fit plane. Images were obtained of titanium by both AFM and STM as the surface activated. Figure 5(a) is an AFM image of the surface view of active titanium showing the boundary between two crystallites. An image was first obtained at a passive potential ( $-250$  mV versus Ag QRE), and the potential was set with the potentiostat to a value near the open circuit active potential ( $-750$  mV versus Ag QRE). The potential was held at this value until the current switched from net cathodic to net anodic, and then the potential of the surface versus the reference electrode was monitored to be certain that the surface remained active. The initial image of the immediately activated surface [Fig. 5(a)] was very close to that of the passive surface. Roughness was determined on each side of the boundary; the lower or front surface in Fig. 5(a) appears to be slightly rougher than the back or upper area as judged by the standard deviation from the best fit plane through these individual areas. The area shown in the lower or front surface had a standard deviation which increased from 8 to 10 nm following activation. Line profiles across the boundary show no significant change immediately after activation as judged by the height difference between these two crystallite faces. The titanium surface was allowed to stand at an active potential for approximately one hour, and during this time the same crystallite boundary was repeatedly imaged. The standard deviation of all of the points in a section of the forward or lower face from the best fit plane was measured to assess the increase in roughness with time. The value increased from the initially measured value of 9 to 11 nm followed by 15 nm. The potential was then set at a value near the stationary state current maximum so that the surface would dissolve at its maximum rate. The AFM image after a short reaction period is shown in Fig. 5(b). Line profiles across the boundary show that the height difference between the two crystallites has not

changed significantly. Furthermore the diameter of the domelike structures is roughly the same but the height of the structures has increased and the number density appears to have decreased. The standard deviation roughness parameter for the forward area has increased to a value of about 25 nm. The upper or back structure appears to be dissolving more uniformly than the lower or forward area. The height of the remaining structures on the lower or forward area of Fig. 5(b) is roughly the same as that of the plateau of the rear or upper area.

*In situ* STM images of the passive surface of titanium under 0.1 M oxalic acid solution are similar to the AFM images previously discussed. Figure 6 is a STM image obtained with the potential held at  $-250$  mV versus Ag QRE. The surface has the appearance of nodules or dome-like structures of relatively uniform size with a density such that some of the nodules or dome-like structures have begun to grow together. However, STM images in the active region showed streaks due to exaggerated or unstable

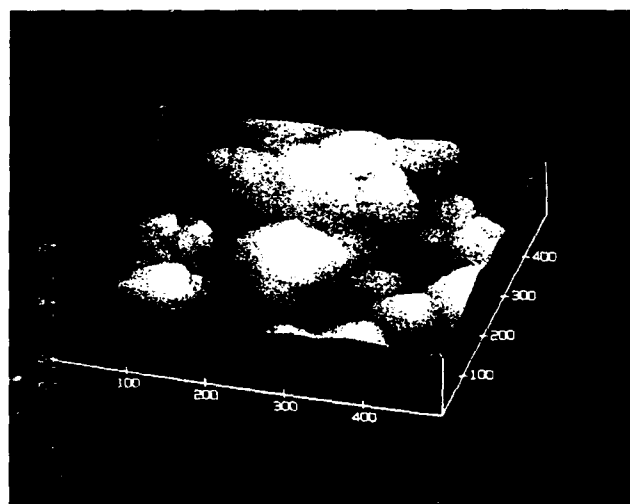


FIG. 6. Surface view STM image of titanium under 0.1 M oxalic acid solution at a passive potential ( $-250$  mV vs Ag QRE).

tip motion. Streaks were not observed with passive state images. These streaks appeared to occur after the tip passed over certain high features on the surface, and we speculate that the presence of an oxide on these features may interfere with the maintenance of a stable tunneling current. The STM images in the active state qualitatively showed the same result as the AFM images. The dense, uniform layer of domelike structures that was present in the passive state begins to disappear in the active state and is replaced with a smaller density of larger structures. The area around some of the domelike structures appears to be disappearing, and the structures have the appearance of being undercut.

#### IV. CONCLUSIONS

The stationary state polarization curve for titanium in 0.1 M oxalic acid suggests that the mechanism for the dissolution of titanium is the same in this medium as it is in chloride or sulfate media. Although the polarization and imaging experiments could not be made under identical conditions, the gross features of the polarization behavior of titanium do not appear to change a great deal from initial immersion in solution to stationary state. The AFM and STM images presented above indicate that neither the growth of an oxide film on titanium nor the dissolution of the metal in 0.1 M oxalic acid are occurring uniformly. Both the growth and dissolution reactions occur at different rates on different crystallographic faces of a polycrystalline sample. In the experiments reported in this article, AFM had more utility than STM for *in situ* imaging because of the streaking problems when titanium is in the active state. The activation of a passive titanium surface involves reduction and or dissolution of the Ti(IV) film. The *in situ* images show very little change immediately after the surface is activated. This suggests that small areas

between domes of Ti(IV) oxide become the active areas but the majority of the surface is still covered with the film. With time the domelike structures coalesce to a smaller number of peaks as a portion of the original Ti(IV) film is undercut. The long time required for the current to reach a stationary state may reflect the long time period required for the thicker islands of oxide to dissolve.

#### ACKNOWLEDGMENTS

Research sponsored by the Exploratory Studies Program of Oak Ridge National Laboratory and by the Office of Health and Environmental Research, U.S. Department of Energy under Contract No. DE-AC05-84OR21400 with Martin Marietta Energy Systems, Inc.

This article was presented at the 38th National Symposium of the American Vacuum Society Topical Conference, Surface Science at the Solid-Liquid Interface (TC1).

<sup>1</sup>R. Sonnenfeld, J. Schneir, and P. K. Hansma, *Modern Aspects Electrochem.* **21**, 1 (1990).

<sup>2</sup>M. P. Green, K. J. Hanson, R. Carr, and I. Lindau, *J. Electrochem. Soc.* **137**, 3493 (1990).

<sup>3</sup>R. Christoph, H. Siegenthaler, H. Rohrer, and H. Wiese, *Electrochem. Acta* **34**, 1011 (1989).

<sup>4</sup>O. M. Magnussen, J. Hotlos, R. J. Nichols, D. M. Kolb, and R. J. Behm, *Phys. Rev. Lett.* **64**, 2929 (1990).

<sup>5</sup>M. J. Armstrong and R. H. Muller, *J. Electrochem. Soc.* **136**, 584 (1989).

<sup>6</sup>F.-R. Fan and A. J. Bard, *J. Electrochem. Soc.* **136**, 166 (1989).

<sup>7</sup>O. Lev, F.-R. Fan, and A. J. Bard, *J. Electrochem. Soc.* **135**, 783 (1988).

<sup>8</sup>I. Sekine, T. Hayakawa, T. Negishi, and M. Yuasa, *J. Electrochem. Soc.* **137**, 3029 (1990).

<sup>9</sup>R. C. Bhardwaj, A. Gonzalez-Martin, and J. O'M. Bockris, *J. Electrochem. Soc.* **138**, 1901 (1991).

<sup>10</sup>E. J. Kelly, *Modern Aspects Electrochem.* **14**, 319 (1982).

<sup>11</sup>M. Jobin, R. Emch, F. Zenhausern, S. Steinemann, and P. Descouts, *J. Vac. Sci. Technol. B* **9**, 1263 (1991).



# Influence of adsorbed and implanted sulfur on the corrosion of iron in calcium nitrate at 60 °C

D. R. Baer, C. F. Windisch, Jr., T. F. Soran, R. H. Jones, and M. H. Engelhard  
*Pacific Northwest Laboratory, Richland, Washington 99352*

(Received 7 November 1991; accepted 2 March 1992)

The influence of S on the anodic corrosion of Fe in a 55 wt %  $\text{Ca}(\text{NO}_3)_2$  solution at 60 °C has been examined using both electrochemical and surface analysis methods. Pure Fe, S-implanted Fe, and Fe with S adsorbed on the surface have been studied. The presence of S, in sufficient amounts, was found to accelerate the corrosion of Fe at 750 mV. For S layers adsorbed on the Fe surface this threshold amount was approximately 1 monolayer. The effect of S was to thicken the oxide layer that formed on the metal and the S remained within the film in a nonoxidized form. These results are consistent with an observed rapid stress corrosion crack growth in the nitrate solution for Fe with S at grain boundaries.

## I. INTRODUCTION

Measurable amounts of S or P at grain boundaries help cause very rapid (up to  $10^{-2}$  mm/s) intergranular stress corrosion cracking (IGSCC) of Fe at passive potentials at 60 °C in  $\text{Ca}(\text{NO}_3)_2$  solution.<sup>1</sup> This cracking results from the combined effects of local grain-boundary and crack chemistry and the presence of applied stress. To help understand the influence of local chemistry, both qualitative and quantitative information about the effects of S and P on the corrosion of Fe are needed. The qualitative information concerns what happens to P and S when present near the metal surface. For example, do S and P change chemical state during metal dissolution? Do they remain at the surface? Do they slow the rate of passivation or alter the passive current density? Quantitative data (e.g., about relationships between contaminant concentration and metal dissolution currents) provide critical information for an analytical model of crack growth rates. This paper reports recent measurements on the effects of adsorbed and implanted S on the corrosion of Fe in the nitrate solution. Similar studies of P in  $\text{Fe}^{2+}$  and earlier work on P and S in Ni (Refs. 1–5) have been reported.

For some metal-impurity systems, the localized corrosion of contaminated grain boundaries causes IGSCC. However, current knowledge is insufficient to predict cracking for a new alloy-contaminant system. It is even difficult to predict the rate of cracking for a system where cracking is known to occur. In the effort to gain a more complete understanding of IGSCC, research was undertaken which combines crack growth rate measurements for well-defined systems, electrochemical and surface science measurements of surface chemistry and reactivity, and mathematical modeling of crack growth kinetics. The electrochemical and surface chemistry measurements use flat surfaces of metal alloys, ion-implanted metal, and adsorbate covered metal to simulate the chemistry occurring at a crack tip. Data from these studies provide important mechanistic and numerical input into the modeling effort. Work performed to date has provided an understanding of

the different effects of P and S in Ni (Ref. 3) and now accurately predict rates of crack growth as a function of load for the Ni–P system.<sup>6</sup>

The ability of S to influence the properties of metal surfaces has been well established. Various forms of S enhance high-temperature corrosion,<sup>7</sup> poison catalytic reactions, enhance hydrogen embrittlement,<sup>8</sup> and contribute to pitting of metals.<sup>9</sup> The study reported here has been directed toward understanding IGSCC, but the results will have implications in some of these other areas.

The experimental procedure involves preparation of a specimen with a known amount of surface or near-surface contaminant, moving the specimen from the vacuum chamber to a corrosion cell for electrochemical testing, and then reinserting the specimen into the vacuum chamber for additional testing, cleaning, or other sample preparation. This process is aided by a specially designed transfer system that removes a sample and holder from a standard manipulator and inserts them into a cell exposing the prepared surface to the electrolyte.

The relationship between the current experiments, which “simulate” metal grain boundaries, and IGSCC occurs both by the qualitative examination of the data in relation to the crack growth experiments and by the inclusion of qualitative and quantitative information into the mathematical model of crack growth. The simulation experiments start with solution and potential conditions similar to those in which the crack growth experiments were conducted. However, solution resistance in the crack can alter the potential at the crack tip, and chemical reactions that occur along the crack wall and the tip can change the pH of the solution in the crack. Because the solution pH and potential at the crack tip are not readily known, data at the applied potential and for “bulk” solution concentrations are collected first (as reported here) to provide input for the model. Additional data (at other potentials or for altered electrolyte concentrations) are gathered as needed, depending upon results of the model calculations and questions that arise from them.

Data reported here concern relationships between S

concentrations and Fe dissolution. In particular, the passivation behavior of Fe at 750 mV [saturated calomel electrode (SCE)] has been measured in relation to S on (or near) the surface. Although both S and P cause rapid cracking of Fe in the nitrate solution, the electrochemical and surface behaviors of the two elements on Fe have significant differences.

## II. EXPERIMENT

The experimental setup used for these experiments has been described in previous publications<sup>1,2,10,11</sup> and only critical features will be given here. Potentiodynamic and potential step tests in conjunction with surface preparation and analysis were used to examine the corrosion behavior of pure Fe and Fe-S in nitrogen-sparged 55wt%  $\text{Ca}(\text{NO}_3)_2$  solutions at 60°C. The base material was 99.999% polycrystalline Fe obtained from Johnson Matthey, Inc., and was prepared by sanding and polishing to a 1  $\mu\text{m}$  finish and vacuum annealing to remove surface damage. Some specimens were then implanted with 150 eV S to a dose of  $5 \times 10^{16} \text{ cm}^{-2}$ .

The surface analysis measurements reported in this paper were collected on a Perkin-Elmer Physical-Electronics 560 surface analysis system that had capability for x-ray photoelectron spectroscopy (XPS), Auger electron spectroscopy (AES), and Ar-ion sputtering. The electron energy analyzer for this system is a double-pass cylindrical mirror analyzer (CMA). Nonmonochromatic  $\text{MgK}\alpha$  x rays were used for the XPS measurements. The binding-energy scale was calibrated by adjusting the  $3p$  and  $2p_{3/2}$  photolines for clean copper to appear at  $75.13 \pm 0.02$  and  $932.67 \pm 0.02$  eV, respectively. Auger data were collected using a 3 or 5 kV electron beam with data collected in the EN(E) mode. Both AES and XPS data are quantified using standard sensitivity factors, a surface correction for evaporated layers, and an instrument correction for low-energy AES data. For S and O on Fe, XPS and AES calculations of coverage usually agree to within 10%. The AES sputter depth profiles were produced by Ar-ion bombardment at 5 kV and the rates were calibrated relative to a known thickness of  $\text{SiO}_2$ . The Fe specimens with adsorbed S were prepared by a solid-state electrochemical S doser.

Electrochemical polarization tests were performed using a PAR 273 potentiostat. Potential-step responses were recorded for various times on a computer disk. A three-electrode system was used for all electrochemical measurements. The working electrodes were the Fe or Fe-S specimens under study; a Pt wire was used as the counter electrode; and a saturated calomel electrode (SCE) fitted with a Luggin probe was used as the reference electrode. All potentials reported here are with respect to SCE unless otherwise noted. The specimens were transported to and from the corrosion cell and the spectrometer using a UHV-compatible transfer system evacuated with a turbomolecular pump.

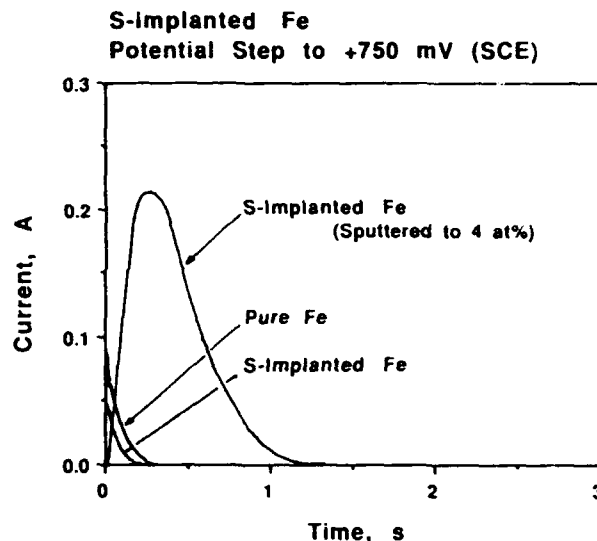


FIG. 1. Plot of anodic current as a function of time, following application of a 750 mV potential, for three specimens: (i) pure Fe; (ii) Fe implanted with S and sputter cleaned; and (iii) Fe implanted with S and sputtered to near the maximum S concentration.

## III. RESULTS

The two types of Fe-S samples used in this study have somewhat different characteristics (for relating to S at grain boundaries). The implanted specimens have lower concentrations of S than often observed at grain boundaries of the Fe ( $\approx 3$  at. % maximum for the implant versus up to 50 at. % at the grain boundary) but have S present both at the solution-metal interface and below the surface (in the  $z$  or depth direction). In contrast, the adsorbed S layers have coverages comparable to that of the grain boundaries, but no supply of S below the surface layer.

### A. S-implanted Fe

The electrochemical current responses for cleaned pure Fe and Fe implanted with S after the potential was stepped from the open-circuit potential ( $\approx -150$  mV) to +750 mV are shown in Fig. 1. For specimens cleaned by a light amount of sputtering (to remove only surface C and O) little difference was observed for the pure Fe and for the S-implanted Fe. Sulfur may even speed the passivation. This behavior of the S-implanted Fe differs significantly from that of P-implanted Fe. Specifically, the S-Fe implanted specimen (with only light sputter cleaning) did not show an enhanced corrosion when compared to clean Fe while the P-implanted Fe showed a significant current transient. A sputter depth profile demonstrated that the S layer was intact in the Fe under the passive film that quickly formed. [This profile is essentially identical to that shown in Fig. 2(c).] In contrast, passivation did not occur until the whole P-implant region had been dissolved away for the Fe-P material.

In order to determine if a higher concentration of S in Fe would cause a current response, part of the surface of an implanted specimen was sputtered to reach the S maximum [Fig. 2(a)]. Insertion of this specimen into the nitrate

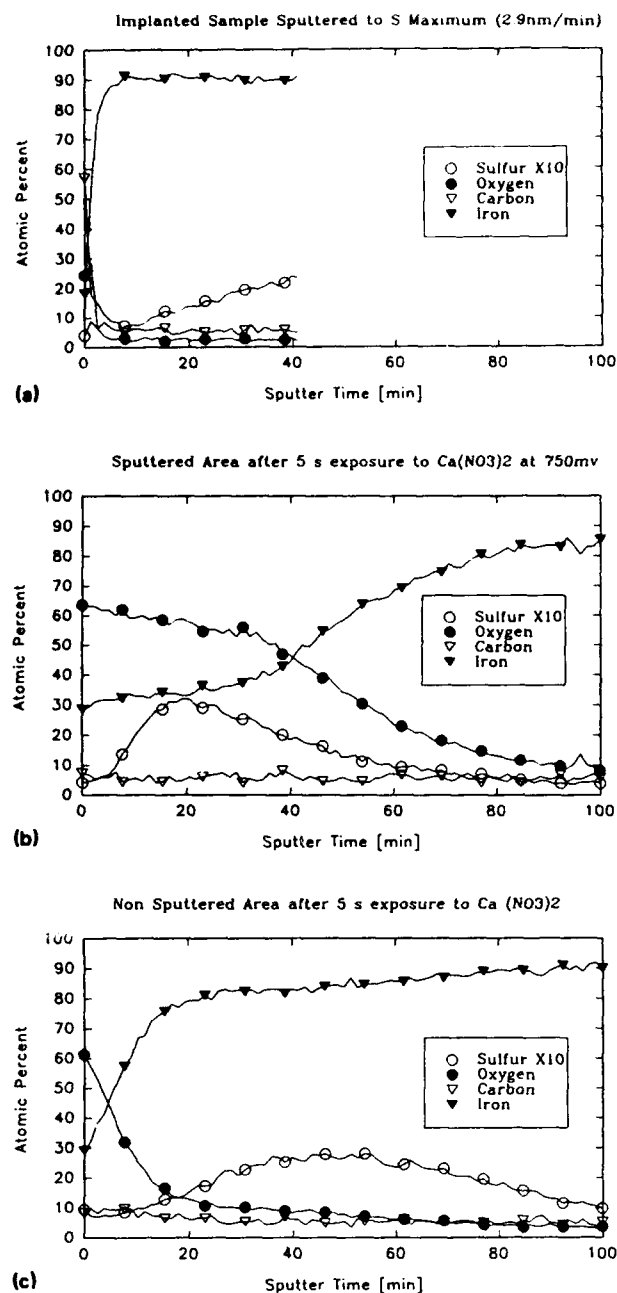


FIG. 2. Auger electron spectroscopy sputter depth profiles showing calculated atomic compositions as a function of sputter time for S-implanted Fe in three different circumstances: (a) as-implanted specimen sputtered until near the maximum concentration of S; (b) film that formed, after 5 s exposure to a 750 mV potential, on an area which had been sputtered to expose the maximum concentration of S; (c) film that formed on an area of the same specimen that had not been sputtered to expose S. The sputter rate for each profile was  $\approx 2.9$  nm/min. Film profile (c) is nearly identical to that produced for specimen (ii) in Fig. 1.

solution and stepping the potential to 750 mV produced the significant current response for the sputtered specimen shown in Fig. 1. The films formed on two different regions of the specimen (sputtered to the S maximum and only cleaned) showed that different thicknesses of reaction occurred in each area. In particular, the film formed in the exposed S region [Fig. 2(b)] was  $\approx 5\times$  thicker than the film formed in the area that had been only cleaned [Fig. 2(c)]. Because the S remained in the film [as shown in Fig.

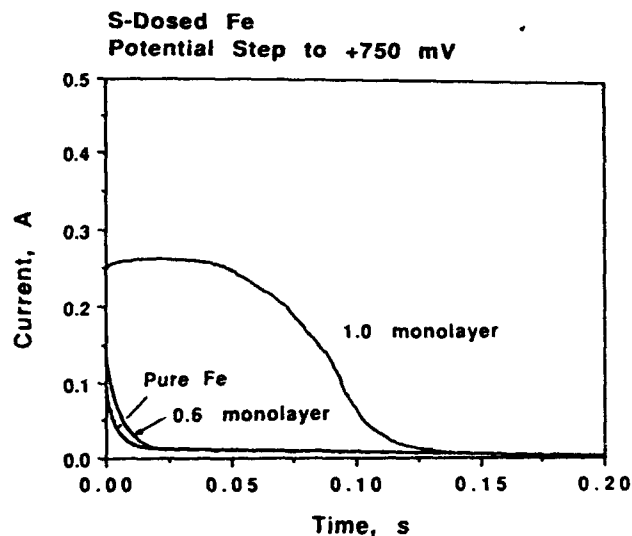


FIG. 3. Plot of anodic current as a function of time following application of 750 mV potential for pure Fe and Fe covered with differing amounts of adsorbed S.

2(b)] and did not appear to be oxidized, the large current spike observed upon jumping the potential to 750 mV can be associated with the oxidation of Fe. It is relatively easy to observe differences between oxidized S (sulfate) and unoxidized S (free S or sulfide) by peak position in XPS ( $\text{BE} \approx 168.5$  eV for sulfate versus  $\approx 161.5$ – $164$  for sulfides and free S)<sup>12–14</sup> or peak shape in AES (Ref. 15) (although beam effects can alter the AES peak shape). Based upon AES and XPS line shapes before and during sputtering, there was no evidence that the S retained in the oxide film had been oxidized.

In summary, two observations can be made from preliminary analysis of these results. First, Fe passivates very quickly in the nitrate solution and the presence of small amounts of S do not change this. Second, larger amounts of S increase the thickness of the passive film and slow the rate of passivation. There appears to be a critical (or threshold) amount of S necessary to observe this effect.

## B. S-dosed specimens

Sputter-cleaned Fe specimens, dosed with differing levels of S, were subjected to potential-step tests as described above. Plots of anodic corrosion current as a function of time for several specimens are shown in Fig. 3. These curves also show a threshold effect. For S coverages below roughly 0.7 monolayer (ML) there was very little difference between S-covered Fe and clean Fe. However, at about 1 ML and above there was a significant increase in dissolution current which lasted for about 0.1 s. As indicated in a summary plot (Fig. 4), once the enhanced current was established there was a relatively slow variation of current density with increased S coverage.

The initial chemistry of the S-adsorbed layer appears to be the same as that observed for S segregated to the Fe surface.<sup>11,16</sup> Photoelectron spectroscopy of films after the exposure to 750 mV indicated that at least some S re-

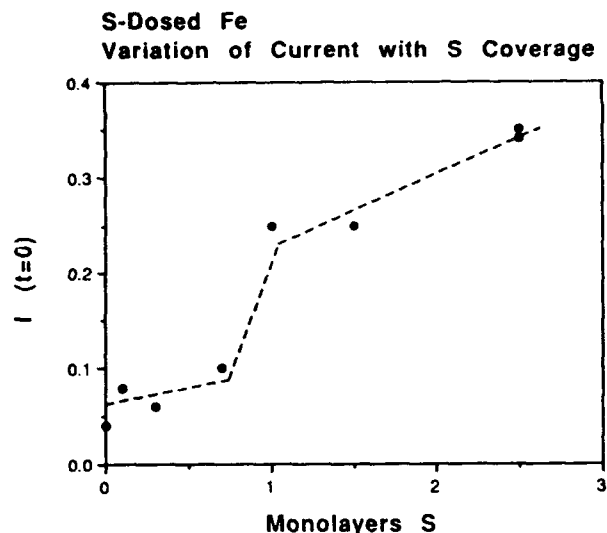


FIG. 4. Variation of amplitude of current transient produced upon the application of 750 mV potential as a function of amount of S adsorbed on an Fe surface.

maintained in the passive film. The film which formed on one specimen, which had been coated with  $\approx 2.7$  ML of S before the potential step test, was examined by XPS and AES sputter profiling. The XPS multiplex data established that a small percentage of the S was oxidized (less than 10% of the S signal was observed at the sulfate binding energy) but that most of the S was still in the film in a nonoxidized form after the test. The total amount of S in the passive film was estimated, using an integration of the AES peak amplitude data as described previously,<sup>10</sup> to be equivalent to 2.8 ML of S. The method is subject to considerable uncertainty, but it is clear that relatively little of the S was lost from the surface during the passive film formation. The oxide that formed over the 2.7 ML of S was  $\approx 11$  nm thick (based upon oxygen signal dropping to 50% of maximum amplitude) while the oxide that formed on clean Fe for similar conditions was  $\approx 4$  nm thick.

#### IV. DISCUSSION

The picture that develops from these tests (including both implant and surface S data) indicates that S, in sufficient concentrations, accelerates the corrosion of Fe in the calcium nitrate solution. However, there appears to be a threshold below which the S has little effect. When the amount of S is above the threshold, the metal rapidly oxidizes until the S is incorporated in the oxide layer and then passivates. Very little of the S was observed to be oxidized during this process.

Although the general summary, stated above, includes both specimen types, it is a qualitative statement and quantitative details of comparison are not yet well established. For example, although a threshold effect has been observed for both surface S and S-implanted specimens, we have not established the relationship between the  $\approx 1$  ML threshold for surface coverage and the  $\approx 2$  at. % threshold for implanted specimens. Similarly, S concentrations above the

threshold for the implanted specimens cause an increased oxide thickness. Although a similar effect (S increases oxide thickness) has been observed for surface S, a relationship between the effects or effectiveness of surface and implanted S has not been established.

There are two differences in the results from the two types of specimens that deserve some comment. First, after exposure to the 750 mV potential, some of the surface S for the 2.7 ML S coverage was oxidized ( $< 10\%$  of the S), while no oxidized S was observed for the implanted specimens after similar treatment. We do not, at this time, consider the relatively small amount of oxidation to be significant and note the possibility of some oxidation of the surface S during the specimen transfer when the specimen was exposed to the electrolyte vapor (before the electrochemical test). Second, the duration of the current spikes due to the presence of S (Figs. 1 and 3) varies with specimen type. We think these differences in time were due to the different physical location of the S for the two specimen types. When S was only at the surface, the duration of the spike was shorter; when the S was spread over  $\approx 100$  nm in depth, the current lasted longer.

The general behavior of S (from the current data) and P (from an earlier study<sup>2</sup>) on Fe have both similar and contrasting trends in the calcite solution. First, both elements cause an increased anodic current at 750 mV. In spite of the increased oxidation current the presence of neither element prevents the formation of a passive film. Both elements increase the time required to form a passive film and alter slightly the composition of the film formed. However, unlike P, which seems to enhance the dissolution of Fe at any concentration, S appears to have a threshold as noted above. Second, although both S and P are incorporated into the films that form at passive potentials, P was observed to be oxidized while there is no spectroscopic evidence of S oxidation. The presence of nonoxidized forms of both elements at the metal surface appears critical to the enhanced corrosion.<sup>2</sup> Whenever the supply of nonoxidized S or P at the interface is depleted, passivation occurs. For adsorbed layers this occurred within 0.2 s while a somewhat longer time was required for the implanted specimen where there was a depth distribution of S. More detailed studies of the length of the current transients are planned.

The behavior observed for S on Fe in calcium nitrate also has both similar and contrasting behavior when compared to that of S on Ni in nitric and sulfuric acids. Although the S was also incorporated in the thin film formed on the Ni, over  $\frac{1}{3}$  of the S was oxidized after exposure to the passive potentials. Very little of the S on Fe was observed to oxidize after exposure to the 750 mV potential. Studies by Marcus and Oudar<sup>17</sup> indicate that there is a threshold effect for S on Ni and Ni-Fe alloys. Above 1 ML, S can block the formation of an oxide and prevent passivation. However, other work suggests that passivation can occur,<sup>4,5</sup> in spite of the S. For Fe it is clear that the effect of S was not to block film formation, but that it enhanced the oxide growth. Vacuum studies have shown that S on the Fe surface increases oxidation.<sup>18</sup> For S-contaminated

grain boundaries, an enhanced local oxidation may contribute to cracking.

The time required to passivate a surface appears to be an important difference between different metals. For example, the presence of several layers of S on Fe was observed to slow passivation compared to pure Fe, but it still occurred within  $\approx 0.10$  s. In contrast, similar tests recently completed for stainless steel indicate that the effect of similar S layers lasts for many seconds.<sup>11</sup>

The rapid oxidation of Fe caused by S is consistent with the existence of stress corrosion cracking for Fe with S-contaminated grain boundaries. The IGSCC cracking of Ni has been effectively modeled using the  $\text{Ni}^{++}$  transport along the length of the crack as the rate-limiting process. Because the cracking of Fe is considerably faster than that which was observed for Ni, it may be that the dissolution of metal and ion transport down the crack do not control the rate of crack growth. This possibility is given some support by initial calculations of the relationships of current and film thickness. Iron passivates more quickly than Ni and forms a thicker passive film. The influence of S appears to be the growth of an even thicker layer. Although more accurate and careful data is needed, both for integrated current and film thickness, initial calculations suggest that the increase in oxide thickness may account for most of the observed charge flow due to the presence of S. If oxide growth can account for most of the observed current, there need be little metal ion transport down the crack in order to facilitate crack growth. Both the relationship between film thickness, adsorbed S, and mechanisms of IGSCC are currently being examined in greater detail.

## ACKNOWLEDGMENTS

The authors would like to thank NORCUS summer students Jennifer Slippert and Matthew Porter for assistance with the data collection. This work was sponsored by the Division of Materials Sciences, Office of Basic Energy

Sciences, U.S. Department of Energy under contract DE-AC06-76RL0 1830 with Battelle Memorial Institute.

This article was presented at the 38th National Symposium of the American Vacuum Society Topical Conference, Surface Science at the Solid-Liquid Interface (TC1).

<sup>1</sup>R. H. Jones, C. F. Windisch, Jr., B. W. Arey, and D. R. Baer, *Corrosion* (Houston) **47**, 542 (1991).

<sup>2</sup>C. F. Windisch, Jr., D. R. Baer, R. H. Jones, and M. H. Engelhard, in *The Application of Surface Analysis Methods to Environmental/Materials Interactions*, edited by D. R. Baer, C. R. Clayton, and G. D. Davis (The Electrochemical Society, Pennington, NJ, 1991).

<sup>3</sup>R. H. Jones, M. J. Danielson, and D. R. Baer, *J. Mater. Energy Syst.* **8** 187 (1986).

<sup>4</sup>D. R. Baer and M. J. Danielson, *J. Vac. Sci. Technol. A* **5**, 1147 (1987).

<sup>5</sup>M. J. Danielson and D. R. Baer, *Corros. Sci.* **29**, 1265 (1989).

<sup>6</sup>E. P. Simonen and R. H. Jones, in *Parkins Symposium on Fundamental Aspects of Stress Corrosion Cracking*, edited by S. M. Bruemmer, (The Minerals, Metals and Materials Society, Warrendale, PA, 1992).

<sup>7</sup>T. T. Hyang, B. Peterson, D. A. Shores, and E. Pfender, *Corros. Sci.* **24**, 167 (1984).

<sup>8</sup>R. H. Jones, S. M. Bruemmer, M. T. Thomas, and D. R. Baer, *Metal. Trans. A* **12**, 1621 (1981).

<sup>9</sup>J. E. Castle and Ruoru Ke, *Corros. Sci.* **30**, 409 (1990).

<sup>10</sup>D. R. Baer and S. M. Lannutti, *J. Vac. Sci. Technol. A* **9**, 1368 (1991).

<sup>11</sup>D. R. Baer, C. R. Windisch, Jr., R. H. Jones, and T. F. Soran, in *Parkins Symposium on Fundamental Aspects of Stress Corrosion Cracking*, edited by S. M. Bruemmer (The Minerals, Metals and Materials Society, Warrendale, PA, 1992).

<sup>12</sup>NIST XPS Data Base, assembled by C. D. Wagner and available from NIST, Gaithersburgh, MD 20899.

<sup>13</sup>C. D. Wagner, in *Practical Surface Analysis*, edited by D. Briggs and M. P. Seah (Wiley, Chichester, 1983), Appendix 4.

<sup>14</sup>C. D. Wagner, W. M. Riggs, L. E. Davis, J. F. Moulder, and G. E. Muilenberg, *Handbook of X-ray Photoelectron Spectroscopy* (Perkin-Elmer, Eden Prairie, MN, 1979).

<sup>15</sup>M. K. Bennett, J. S. Murday, and N. H. Turner, *J. Electron Spectrosc. Relat. Phenom.* **12**, 375 (1977).

<sup>16</sup>H. J. Grabke, in *Chemistry and Physics of Fracture*, NATO ASI Series E: Applied Sciences, No. 130, edited by R. M. Latanision and R. H. Jones (Nijhoff, Dordrecht, 1987), p. 388.

<sup>17</sup>P. Marcus and J. Oudar, in *Chemistry and Physics of Fracture*, NATO ASI Series E: Applied Sciences, No. 130, edited by R. M. Latanision and R. H. Jones (Nijhoff, Dordrecht, 1987), p. 670, and references therein.

<sup>18</sup>M. R. Shanabarger (private communication).

# Copper adlayer formation on Au(111) from sulfuric acid electrolyte

Michael P. Green and Karrie J. Hanson<sup>a)</sup>

AT&T Bell Laboratories, 600 Mountain Ave. Murray Hill, New Jersey 07974

(Received 15 November 1991; accepted 6 January 1992)

We have used *in situ* scanning tunneling microscopy to examine submonolayer Cu deposition from a sulfuric acid electrolyte on Au(111), sampling over large areas of the surface. We describe the growth of three distinct superlattice phases of Cu on the Au(111) surface before the onset of bulk deposition of Cu. In the earliest stages of deposition, during an electrochemical current peak, we observe the rapid growth of a low height phase, with an apparent height of  $0.46 \pm 0.10$  Å. During this time, a second, monolayer-height phase forms as small islands. We identify these phases as the  $(\sqrt{3} \times \sqrt{3})R30^\circ$  and  $(1 \times 1)$  Cu superlattices, respectively. A third phase appears at about 175 mV (versus  $\text{Cu}/\text{Cu}^{+2}$ ), and grows from nucleation points at the top edges of atomic steps and around the small  $(1 \times 1)$  Cu islands. This phase, which we believe is a  $(5 \times 5)$  Cu adlayer, slowly supplants the  $(\sqrt{3} \times \sqrt{3})R30^\circ$  layer.

## I. INTRODUCTION

Recent *in situ* scanning tunneling microscopy (STM),<sup>1</sup> atomic force microscopy (AFM),<sup>2</sup> and x-ray absorption spectroscopy (XAS)<sup>3</sup> studies have considered the underpotential deposition (UPD) of Cu onto Au(111) in sulfate containing electrolytes. In each case the emphasis has been on the atomic arrangement of the Cu adatoms at various stages of the monolayer formation. In this paper we report *in situ* STM studies concentrating on larger substrate areas, and imaging continuously during the layer formation stages. This approach allows consideration of the film growth dynamics.

Using STM, Magnussen *et al.*<sup>1</sup> distinguished two atomic structures during the Cu deposition process. Above the UPD potential region the atomic spacing corresponding to the Au(111) surface (2.88 Å) was poorly resolved; the difficulty in imaging was attributed to adsorption of mobile anions. When the potential was swept negatively into the first of the two Cu UPD peaks, they saw the abrupt onset of a structure compatible with the expected  $(\sqrt{3} \times \sqrt{3})R30^\circ$  superlattice. This  $(\sqrt{3} \times \sqrt{3})$  structure has been described in studies using *ex situ* low-energy electron diffraction (LEED), reflection high-energy electron diffraction (RHEED), and Auger electron spectroscopy (AES).<sup>4</sup> A Cu coverage ( $\Theta$ ) of 0.33 monolayer (ML) relative to the close packed Au(111) substrate was reported. The driving force for the formation of the open  $(\sqrt{3} \times \sqrt{3})$  structure is attributed to either adatom-adatom repulsion due to incomplete discharge of the  $\text{Cu}^{+2}$  ions upon adsorption,<sup>3</sup> or to sulfate coadsorption.<sup>5</sup>

Magnussen *et al.* note that regions of the surface show a second, less well resolved phase which grows slowly, at the expense of the  $(\sqrt{3} \times \sqrt{3})$  phase. A continued reduction of electrode potential, to just negative of the first deposition peak, causes this phase, identified as  $(5 \times 5)$  ( $\Theta = 0.64$ ), to completely cover the surface. A height difference of  $\sim 0.5$  Å is found from the maxima of the  $(\sqrt{3} \times \sqrt{3})$  corrugation to the average  $(5 \times 5)$  level.

The AFM experiments of Manne *et al.*<sup>2</sup> reverse the electrochemical process, and show the atomic structure during the removal of bulk Cu from Au(111). At the potential

where bulk Cu has been plated, they see a hexagonal lattice with atomic spacing of  $2.6 \pm 0.2$  Å, which corresponds to the bulk Cu(111) surface. Upon stripping of the bulk, and passage into the potential region between the two UPD stripping peaks, they see a structure which matches the  $(\sqrt{3} \times \sqrt{3})R30^\circ$  superlattice, in agreement with Magnussen *et al.* for this potential region. In contrast to Magnussen *et al.*, however, the AFM results show no indication of the  $(5 \times 5)$  structure. A continued potential sweep positive of the second UPD peak returns the unreconstructed Au(111) lattice spacing. Orientation of the two phases,  $30 \pm 10^\circ$ , confirms the superstructure assignment. A height difference of  $1.8 \pm 0.5$  Å is quoted between the maxima of the corrugation for the substrate and  $(\sqrt{3} \times \sqrt{3})$  phases.

The *in situ* x-ray absorption spectroscopy (XAS) results of Tadjeddine *et al.*<sup>3</sup> agree in most respects with the STM and AFM results. They noted that at  $\Theta = 0.33$  ML [220 mV versus saturated calomel electrode (SCE)] the initial Cu-Cu distance was 4.88 Å, which perfectly fits the  $(\sqrt{3} \times \sqrt{3})$  superlattice distance. After apparently maintaining the coverage at 0.33 ML for 1 h, however, a second Cu-Cu bond length 3.59 Å, matching the  $(5 \times 5)$  structure, was seen coexisting with the  $(\sqrt{3} \times \sqrt{3})$  spacing. After increasing the coverage to 0.6 ML (150 mV versus SCE), only the  $(5 \times 5)$  spacing was evident. At  $\Theta = 1$  ML (80 mV versus SCE), in the range covered by neither Magnussen *et al.* nor Manne *et al.*, the XAS data revealed that the Cu-Cu spacing equaled that of the Au(111) substrate, suggesting  $(1 \times 1)$  epitaxial adsorption. When the Cu adlayer was stripped to a coverage of 0.6 ML, it was discovered that all three phases,  $(1 \times 1)$ ,  $(5 \times 5)$ , and  $(\sqrt{3} \times \sqrt{3})$ , could exist in equilibrium on the surface. For each of these structures, and at all coverages, there is a Cu-O signal indicating a bond distance of 1.95 Å. Whether this Cu-O bond is due to sulfate or just oxygen is not clear. The experimental arrangement makes the results insensitive to bond orientations perpendicular to the surface, so the signal must be due to oxygen in or near the Cu adlayer plane. This contradicts the results of Melroy *et al.*,<sup>6</sup> who find only a perpendicular Cu-O bond signal.

The only real difference among these three sets of results

lies in the AFM experiments, where only the ( $\sqrt{3} \times \sqrt{3}$ ) phase, and not the ( $5 \times 5$ ), was seen during the stripping cycle. It has been demonstrated, however, by Magnussen *et al.*, that the ( $5 \times 5$ ) superstructure may be induced by very low levels of  $\text{Cl}^-$  contamination, possibly introduced by the SCE reference electrodes used by both Magnussen *et al.* and Tadjeddine *et al.* In the AFM studies by Manne *et al.* in which the ( $5 \times 5$ ) phase was not seen, a Cu wire reference electrode was used. A repeat of the STM experiments<sup>7</sup> in which care was taken to exclude  $\text{Cl}^-$  contamination yielded greatly reduced ( $5 \times 5$ ) growth, restricted mainly to the step edges.

In this paper we use *in situ* STM to investigate the dynamics of the Cu UPD growth and stripping over relatively large regions of the electrode surface to study both the formation and interaction of the UPD phases as well as the relationship between local substrate structure and the overlayer phase growth.

## II. EXPERIMENTAL

Our electrochemical STM and evaporated Au substrates have been described in previous papers.<sup>8,9</sup> The apparatus used here is the same as described, except for the substitution of electrochemically etched Ir tips<sup>10</sup> for cut PtIr. Iridium tips were more stable and more easily electrochemically isolated when coated with nail polish.

We did not perform any electrochemical cleaning of the Au substrates prior to Cu deposition, since oxidation of the Au surface can induce structural rearrangement.<sup>11</sup> Therefore, any airborne contaminants adsorbed onto the Au surface which are insoluble in the electrolyte or are not displaced by sulfate adsorption will remain on the surface during at least the first deposition reaction.

Our electrolyte was 0.05 M  $\text{H}_2\text{SO}_4$  (Alfa "Ultrapure") and 0.01 M CuO ( $5\text{H}_2\text{O}$ ) (Aldrich 99.999 + %) made with Millipore Milli-Q Plus filtered water. No deoxygenation was performed prior to experimentation, nor was  $\text{O}_2$  excluded from the STM chamber. Our reference electrode was a Cu wire (Alfa 99.999%) immersed in the STM cell, and potentials are quoted versus  $\text{Cu}^{+2}/\text{Cu}^0$ . The tunneling tip was maintained at a constant tunneling current (1 nA) and a constant tunneling voltage (+20 mV with respect to the Au working electrode). Although this allows the possibility of electrochemical activity (e.g. Cu or sulfate adsorption) at the tip, it reduces the risk of the tip inducing electrochemistry at the substrate. Furthermore, any changes in tip structure should be evident over the entire image, and should easily be discernible from substrate topographic changes.

## III. RESULTS

We observe three distinct Cu phases in our STM images during deposition and stripping. They are distinguished as regions of similar patterns of growth of a certain average height above the bare Au plane. In this section the three phases are referred to as phase I (the lowest), phase II (approximately half of a monolayer high), and phase III (one monolayer high). We assign these phases to the ( $\sqrt{3}$

TABLE I. Assignment of phases.

	Assignment	Measured height above Au surface	Calculated average height (hard sphere model)
Phase I	( $\sqrt{3} \times \sqrt{3}$ ) $R30^\circ$	$0.46 \pm 0.10$ Å	0.55 Å
Phase II	( $5 \times 5$ )	$1.23 \pm 0.23$ Å	1.19 Å
Phase III	( $1 \times 1$ ) epitaxial	$2.38 \pm 0.28$ Å	1.79 Å
Au step		2.35 Å	

$\times \sqrt{3}$ ), the ( $5 \times 5$ ), and the ( $1 \times 1$ ) Cu overlayer structures, respectively. The height of these phases above the Au substrate and the assignments are summarized in Table I and discussed in the next section.

The first of two deposition sequences is shown in Fig. 1. All images in this paper were taken with an acquisition time of 38 s, scanning from bottom to top. Figure 1 shows the surface during a potential sweep from 500 to 75 mV (2 mV/s) and a hold at 75 mV. Three single atomic steps can be seen on the  $750 \times 750$  Å<sup>2</sup> region of the bare Au surface [Fig. 1(a)]. The Au step height of 2.35 Å was used for height calibration. In Fig. 1(b) phases I and III appear, corresponding with the first current peak [current and potential information for this image are given in Fig. 1(d)]. Phase I deposits initially as patches on the top edge of the steps (arrow A) and in the center of the plane, and then grows rapidly over most regions of the Au surface. [This can be seen more easily in the images from the second deposition sequence, where a close up is included as Fig. 3(a).] At the same time, phase III appears as small islands, 10 to 25 Å in diameter, which nucleate in filaments across the surface of the terraces (arrow B) with no apparent orientation. The potential sweep was halted at 75 mV, and Fig. 1(c), taken during the "hold," shows phase III islands distributed across the surface and aligned in strings. Yet another phase (phase II), with an intermediate height between phases I and III, is visible mostly between and around the phase III islands, giving a web-like appearance (arrow C). Other domains of phase II appear, concentrated at the top edge of the steps. Thus, during this deposition sequence, we find that all three Cu phases exist simultaneously.

Reversing the direction of the potential sweep (75 to 500 mV) strips the Cu overlayer. Images of this process are presented in Fig. 2, with the voltammetry data for Fig. 2(c) shown in Fig. 2(d). Figure 2(a) begins at a potential of 200 mV, midway through the adlayer removal. Between 50 and 175 mV (not shown), phase II was stripped and many of the phase III islands disappeared. Phase I is removed with the main anodic current peak at 243 mV. A zoomed view of a portion of Fig. 2(a) is presented in Fig. 2(c) with enhanced contrast, showing the removal of phase I. From the corresponding electrochemical data [Fig. 2(d)] it can be seen that phase I disappears in the potential window 230–243 mV, and is completely dissolved by the time the current begins to decay. During the remainder of the potential sweep phase III is slowly removed by a process of island dissolution and coalescence. Figure

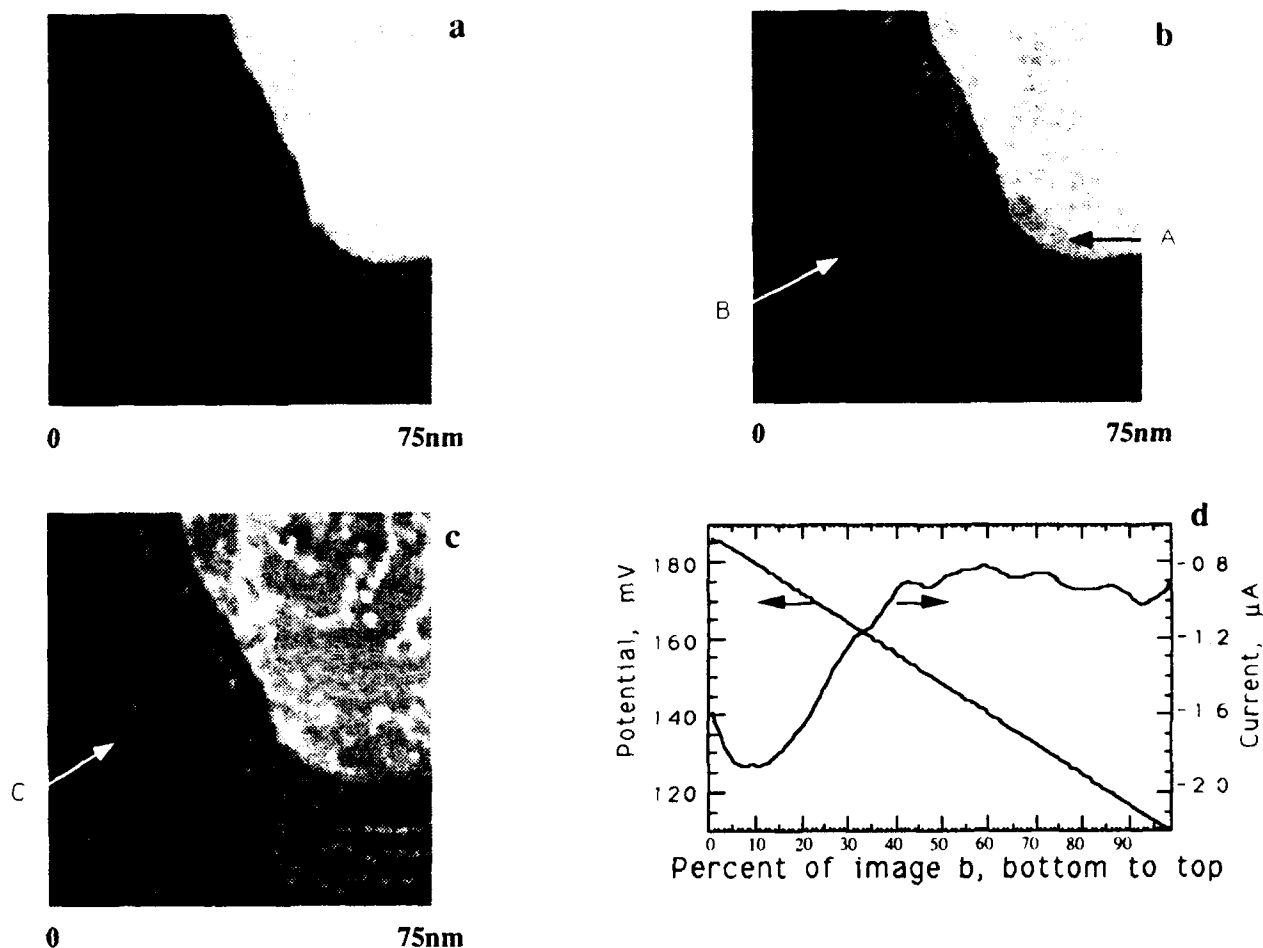


FIG. 1. Initial Cu deposition sequence. Images scanned upwards. (a) Bare Au(111). (b) Formation of phase I layer and phase III islands; potential 190–110 mV vs Cu/Cu<sup>2+</sup>. (c) Weblike phase II domains around phase III islands; potential held at 75 mV. (d) Electrochemical potential and current for image (b).

2(b) shows the Au surface and the few remaining phase III islands at the end of the scan, with the potential held at 500 mV. These islands are relatively stable at this potential but can be removed if the electrode is cycled through the Au oxidation region.

The second deposition is presented in detail in Fig. 3. It consists of a potential sweep from 500 to 30 mV which was interrupted and held at 75, 65, and 50 mV. The deposition of phase I [Fig. 3(a), electrochemical data in Fig. 3(e)] shows the same pattern as on the first sweep, with plating occurring rapidly across the surface (arrow A) at about 200 mV, concomitant with the first UPD current peak. However, unlike the first deposition sequence, phase III island formation does not follow immediately. In the potential range 200–75 mV, as additional Cu is deposited, phases II and III start to appear at the same time. Figure 3(b) (at 75 mV) shows phase III islands scattered across the surface and phase II domains which have grown around and between them. This growth pattern gives the appearance of ribbons which continue to widen and become more distinct as the phase II domains grow slowly outwards to replace phase I [Fig. 3(c), at 65 mV]. The phase II domains finally merge [Fig. 3(d), at 50 mV],

leaving isolated phase I patches, until finally, phase I disappears completely in favor of phase II.

Figure 4 shows the Cu removal from the full phase II coverage, during the potential sweep from 50 to 500 mV with a hold at 150 mV. Figure 4(a) shows the full phase II adlayer before stripping. In Fig. 4(b) pits or holes develop in the layer showing the first stages of the transformation from phase II back to phase I. By comparing the image and the electrochemical data in Fig. 4(d), we see this change occurs just at the point of the first stripping peak (118 mV). When the potential is held at 150 mV [Fig. 4(c)], which is between the two stripping peaks, phase II breaks into domains which are roughly triangular, and do not resemble the pattern of ribbons which we observed during the deposition. A resumption of the potential sweep causes these regions to shrink. Eventually the entire surface is stripped, first of phase II and then, at the main stripping peak (245 mV), of phase I.

#### IV. DISCUSSION

The results presented above showed topographic changes during Cu deposition and stripping on a 750 × 750



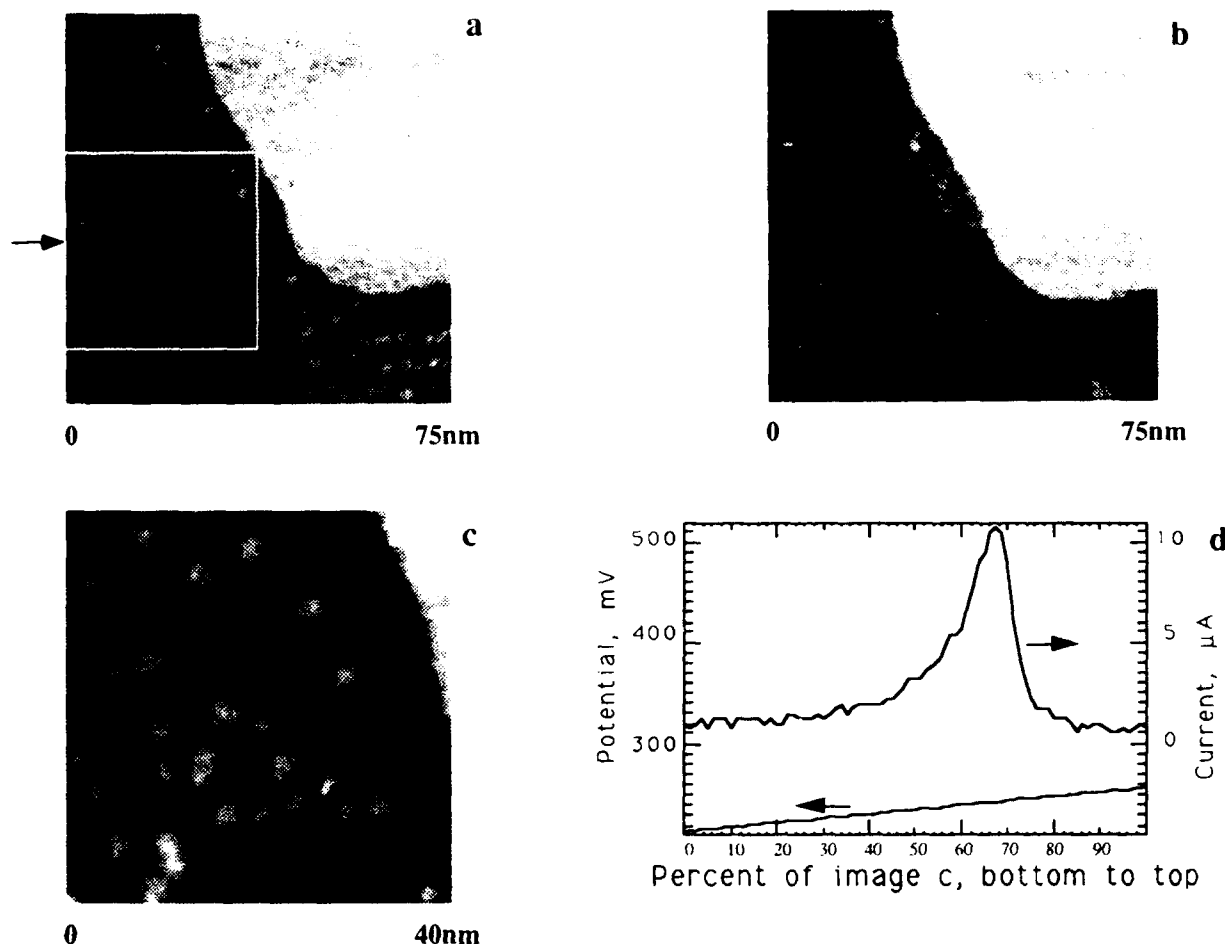


FIG. 2. Removal of first partial Cu adlayer. Images scanned upwards. (a) Before this image phase II is removed, and here a lower number of phase III islands remain. Phase I is removed at arrow, box indicates area reproduced in image (c); potential 200–275 mV. (b) Au substrate with several phase III islands remaining; potential 500 mV. (c) Zoomed view with enhanced contrast of boxed portion of image (a) showing phase I removal at arrow; potential 210–260 mV. (d) Electrochemical current and potential for image (c).

$\text{\AA}^2$  scale. In this range we can distinguish the dynamics of the formation and interconversion of phases, as well as the relationship between the adlayer and topographic features of the substrate. At this scale we cannot determine an atomic lattice spacing for the phases we observe. We therefore rely on comparison of our results with those of previous *in situ* STM, AFM, and XAS studies of this system to assign a structure to the observed phases.

#### A. Phase I: $(\sqrt{3} \times \sqrt{3})R30^\circ$ Cu

During deposition of Cu, the previous STM and XAS results both show the Cu  $(\sqrt{3} \times \sqrt{3})R30^\circ$  superlattice formation concomitant with the first current peak. At this potential, we see the rapid growth of the low-height phase I across the entire surface. Although the hard-sphere model predicts a peak-to-peak (Au maxima to Cu maxima) height difference of  $1.99 \text{ \AA}$  for Cu in threefold-hollow sites for this structure, the average height of the surface with only  $1/3$  of such sites filled is only  $0.54 \text{ \AA}$  above the average level of the Au(111) surface. The apparent  $0.46$

$\pm 0.1 \text{ \AA}$  height of phase I in our images is consistent with the  $(\sqrt{3} \times \sqrt{3})R30^\circ$  Cu superlattice assignment (see Table I).

Of the previously discussed results, only the AFM investigation of Manne *et al.*<sup>2</sup> included a discussion of the height of this adlayer. Their results show a peak-to-peak height of  $1.8 \pm 0.5 \text{ \AA}$ , in reasonable agreement with the hard sphere model. However the transformation from the  $(\sqrt{3} \times \sqrt{3})$  Cu to bare Au(111) atomic lattices did not always correspond with the UPD current peak.<sup>12</sup> In our results the formation and dissolution of phase I were rapid and occurred simultaneously with the current peaks.

#### B. Phase III: $(1 \times 1)$ Cu

During the deposition of phase I (especially on the first cycle), we see the slight codeposition of small islands of phase III, which we have suggested are  $(1 \times 1)$  epitaxial Cu. This behavior has not been previously reported. It is possible that similar islands were never seen in the STM and XAS investigations due to their relative scarcity

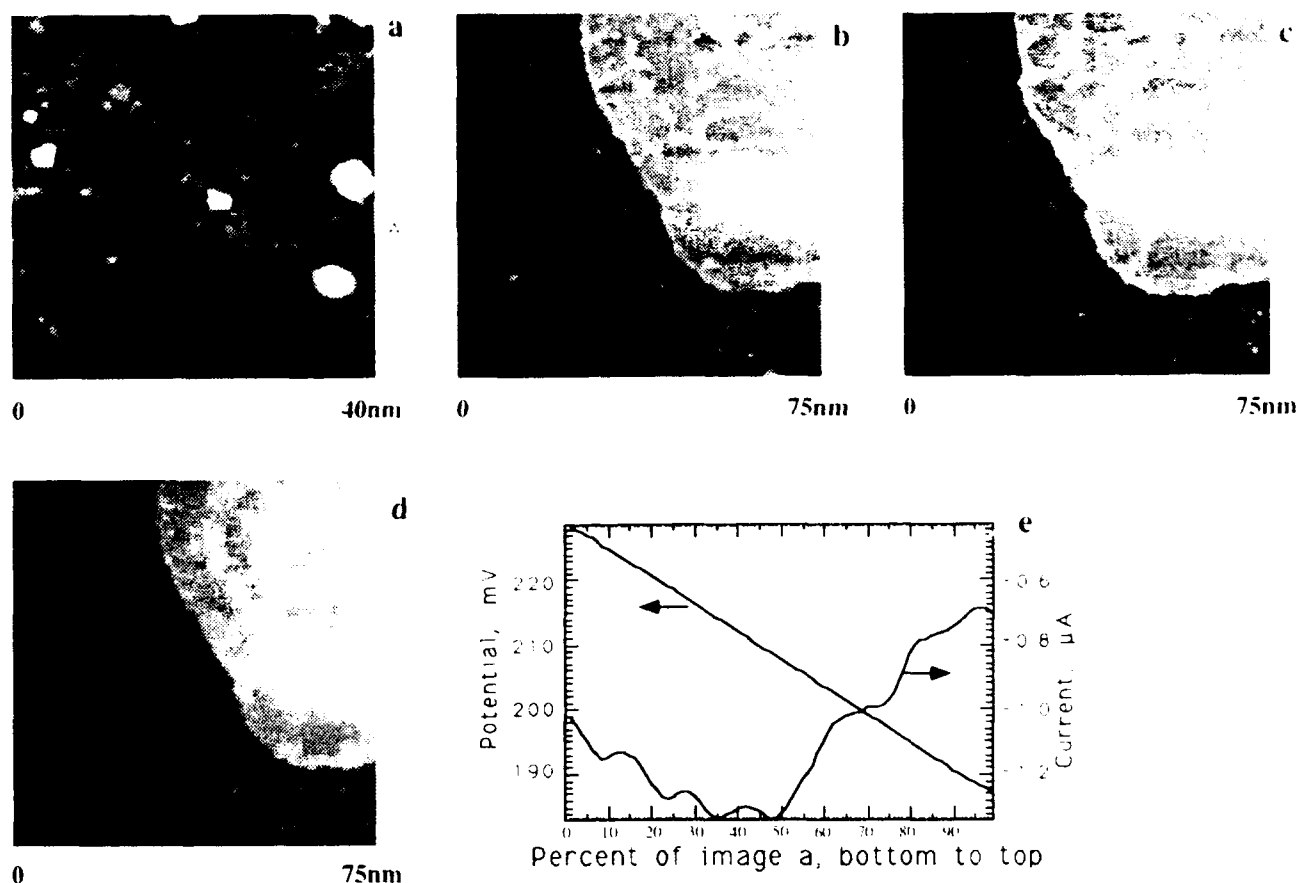


FIG. 3. Second Cu deposition sequence. Images scanned upwards. (a) Zoomed image of the formation of phase I adlayer beginning at arrow, potential 230–188 mV. (b) Initial growth of phase II on top of step edges and around phase III islands; potential 75 mV. (c) Expansion of phase II in "ribbon" domains, potential 65 mV. (d) Continued filling of phase II domains leaving patches of phase I, potential 50 mV. (e) Electrochemical current and potential for image (a).

( $\approx 5\%$ ) on the surface; noticing these islands with atomic-scale STM is complicated by the identical lattice spacing of  $(1 \times 1)$  Cu and the Au(111) substrate. The assignment of a  $(1 \times 1)$  Cu structure for these islands is not straightforward, however, because the measured height of these features above the substrate and above the previously deposited phases is not consistent with the hard sphere model. We can measure the average height of these island structures at three stages of the UPD cycle from three different base-plane heights, that is, from the Au substrate and from the other two Cu phases. (1) From the bare Au substrate (after stripping of the less dense Cu phases), the average  $(1 \times 1)$  island height is found to be  $2.4 \pm 0.3$  Å. (2) From the  $(\sqrt{3} \times \sqrt{3})$  covered plane after the initial Cu deposition, the average  $(1 \times 1)$  island height is  $2.7 \pm 0.4$  Å. (3) From the  $(5 \times 5)$  covered plane, it is  $2.3 \pm 0.3$  Å. These values do not fit the hard sphere model even in their relative magnitudes (see Table I). In fact, the measured height difference of phase III above the Au substrate ( $2.4 \pm 0.3$  Å) is actually smaller than the height above the  $(\sqrt{3} \times \sqrt{3})$ -Cu covered substrate ( $2.7 \pm 0.4$  Å). Several explanations could account for this discrepancy. Tadjeddine *et al.*<sup>3</sup> find that the  $\text{Cu}^{+2}$  ions adsorb with an oxidation state of +1. At some point, however, before the onset of bulk deposition,

this must be reduced to  $\text{Cu}^0$ . If this were to occur in the dense  $(1 \times 1)$  islands at a potential near that of the  $(\sqrt{3} \times \sqrt{3})$  phase formation, the resulting increase in electron density in the adatom layer might cause the Cu  $(1 \times 1)$  phase to appear to grow higher. A second possibility is that the reduction in potential could cause the  $(1 \times 1)$  epitaxial Cu lattice to contract towards its bulk spacing (2.88 to 2.56 Å), thereby forcing Cu atoms out of the threefold hollow sites into an incommensurate structure with a greater average height. Effects of this nature have been seen in x-ray investigations of other UPD systems.<sup>11</sup> The formation of the phase III islands is important, however, since these, in addition to the top of atomic steps, act as nucleation centers for the phase transformation from  $(\sqrt{3} \times \sqrt{3})$  to  $(5 \times 5)$ .

It is surprising, in fact, that any of the phase heights should fit the hard sphere model for Cu alone on the Au surface, since much evidence indicates that Cu does not deposit alone. The XAS data of Tadjeddine *et al.* show oxygen in close proximity to Cu with a Cu–O bond of equal length (1.95 Å) for each of the phases. From a similar experiment, Blum *et al.*<sup>7</sup> suggest that at full coverage, this Cu–O bond results from sulfate coadsorption above each Cu. These results are not entirely consistent with each

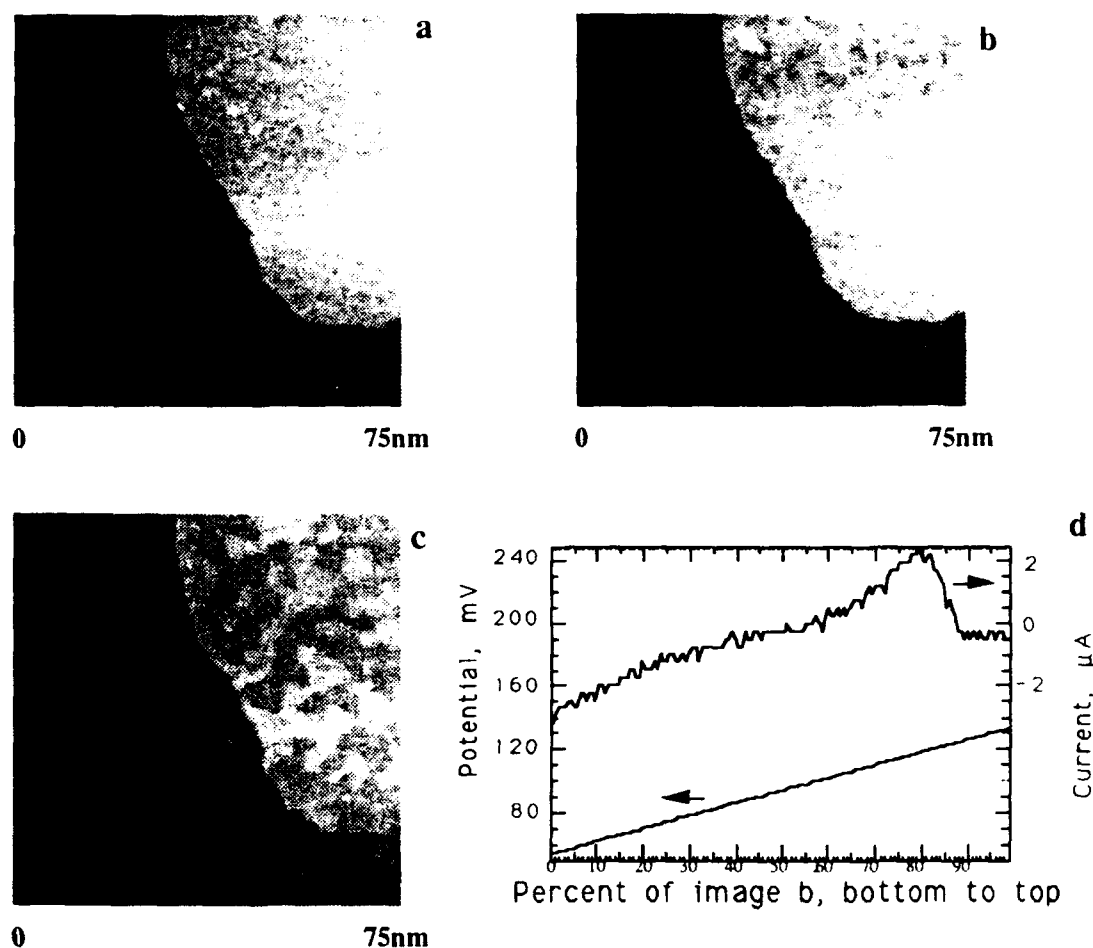


FIG. 4. Stripping of full phase II Cu adlayer. (a) Full phase II coverage; potential 50 mV. (b) Breakup of phase II into phase I domains; potential 55–135 mV. (c) Triangular phase II domains formed during conversion to phase I; potential 150 mV. (d) Electrochemical current and potential for image (b).

other and the exact nature of sulfate coadsorption is unknown, but some coadsorption effect is indicated.

### C. Phase II: ( $5 \times 5$ ) Cu

The Cu ( $5 \times 5$ ) superlattice has an hexagonal arrangement with four Cu atoms overlaying five substrate atoms in each of the lattice directions.<sup>1</sup> Every 14.4 Å (the repeat distance), the Cu atoms return to registry. In the hard sphere model, the average height of this arrangement is 1.19 Å above the bare Au(111) plane, or 0.65 Å above the average ( $\sqrt{3} \times \sqrt{3}$ ) height. We measure the height difference from phase I to phase II to be  $0.77 \pm 0.13$  Å, in agreement with this calculation. Additionally, the slow growth of phase II at the expense of the ( $\sqrt{3} \times \sqrt{3}$ ) phase fits the evidence from STM and XAS experiments.

In addition to the identification, our large-view, time-resolved imaging shows the phase transformation dynamics. The ( $5 \times 5$ ) phase growth starts from nucleation centers at ( $1 \times 1$ ) islands and at the top of atomic terrace steps, and then continues to expand outwards from the established phase boundaries. The initial ribbon or tendril structure may be related to domain boundaries between two different orientations of the ( $\sqrt{3} \times \sqrt{3}$ ) phase. In the

STM investigation of Magnussen *et al.*, the ( $5 \times 5$ ) phase covered the majority of the imaged surface at a potential only several millivolts negative of that necessary to form the initial Cu ( $\sqrt{3} \times \sqrt{3}$ ) adlayer. They were imaging regions of high step density, with terraces no wider than  $\sim 50$  Å. It can be seen from Fig. 3 that because of the enhanced activity at the step edges, one would expect terraces of this width to be sites for the earliest conversion to the ( $5 \times 5$ ) structure.

After the surface became completely covered with the ( $5 \times 5$ ) phase, we continued sweeping the potential negatively, towards the bulk deposition region, but did not see the conversion of the ( $5 \times 5$ ) into the ( $1 \times 1$ ) structure predicted by the XAS results. The only areas of ( $1 \times 1$ ) were those islands which had deposited during the previous phase formations. Correspondingly, we do not see the sharp second UPD current peak associated with this transformation. *In situ* voltammetric data were not included in the STM, AFM, or XAS papers. In our experience, and borne out in the literature, the shape of the current-voltage curve is dependent on many factors and is never exactly repeatable.

Removal of the Cu adlayer shows that the transforma-

tion from the  $(5 \times 5)$  back to the  $(\sqrt{3} \times \sqrt{3})$  structure does not follow a reverse of the sequence for deposition. The initial stripping step, associated with the most negative stripping current peak, is the rapid thinning of small patches of the  $(5 \times 5)$  phase, leaving the  $(\sqrt{3} \times \sqrt{3})$  phase in its place. This is followed by extension of these  $(\sqrt{3} \times \sqrt{3})$  domains with no apparent relationship to the the step edges or the remaining  $(1 \times 1)$  islands.

## V. CONCLUSIONS

*In situ* STM observations of a  $750 \times 750 \text{ \AA}^2$  area of an Au(111) substrate showed three distinct phases forming during the underpotential deposition of Cu from a sulfate containing electrolyte. These phases have been identified as Cu  $(\sqrt{3} \times \sqrt{3})R30^\circ$ ,  $(5 \times 5)$ , and  $(1 \times 1)$  superlattices, in order of apparent thickness. The potential dependence of their appearance on the surface agrees well with voltammetry, x-ray absorption,<sup>3</sup> and atomic resolution STM<sup>1</sup> and AFM.<sup>2</sup> The apparent heights of the  $(\sqrt{3} \times \sqrt{3})$  and  $(5 \times 5)$  phases also agree with those predicted from the hard sphere model. The  $(\sqrt{3} \times \sqrt{3})$  phase nucleates and covers the substrate at the potential of the first deposition peak. Formation of small islands of the  $(1 \times 1)$  phase occurs concurrently. At more negative potentials, regions of the surface transform to the  $(5 \times 5)$  phase, beginning from nucleation centers around the  $(1 \times 1)$  islands and at the top of atomic steps. Growth continues, following a widening filament pattern, until all the  $(\sqrt{3} \times \sqrt{3})$  domains have been converted to the  $(5 \times 5)$  phase. Removal of the Cu progresses by formation (at the first stripping peak) and

expansion of many  $(\sqrt{3} \times \sqrt{3})$  domains within the  $(5 \times 5)$  layer, and eventual removal of the  $(\sqrt{3} \times \sqrt{3})$  phase at the sharp second stripping peak.

This article was presented at the 38th National Symposium of the American Vacuum Society Topical Conference, Surface Science at the Solid-Liquid Interface (TC1).

<sup>†</sup>Author to whom all correspondence should be addressed

<sup>1</sup>O. M. Magnussen, J. Hotlos, R. J. Nichols, D. M. Kolb, and R. J. Behm, *Phys. Rev. Lett.* **64**, 2929 (1990); O. M. Magnussen, J. Hotlos, G. Beitel, D. M. Kolb, and R. J. Behm, *J. Vac. Sci. Technol. B* **9**, 969 (1991); O. M. Magnussen, J. Hotlos, G. Beitel, D. M. Kolb, and R. J. Behm (unpublished).

<sup>2</sup>S. Manne, P. K. Hansma, J. Massie, V. B. Elings, and A. A. Gewirth, *Science* **251**, 183 (1991).

<sup>3</sup>A. Tadjeddine, D. Guay, M. Ladouceur, and G. Tourillon, *Phys. Rev. Lett.* **66**, 2235 (1991).

<sup>4</sup>Y. Nakai, M. S. Zei, D. M. Kolb, and G. Lehmpfuhl, *Ber. Bunsenges. Phys. Chem.* **88**, 340 (1984); M. S. Zei, G. Qiao, G. Lehmpfuhl, and D. M. Kolb, *ibid.* **91**, 349 (1987).

<sup>5</sup>L. Blum, H. D. Abruna, J. White, J. G. Gordon, G. L. Borges, M. G. Samant, and O. R. Melroy, *J. Chem. Phys.* **85**, 6732 (1986).

<sup>6</sup>O. R. Melroy, M. Smaant, J. G. Gordon, L. Blum, J. H. White, M. J. Albarelli, M. McMillan, and H. D. Abruna, *Langmuir* **4**, 728 (1988).

<sup>7</sup>O. M. Magnussen, J. Hotlos, G. Beitel, D. M. Kolb, and R. J. Behm, *J. Vac. Sci. Technol. B* **9**, 969 (1991).

<sup>8</sup>M. P. Green and K. J. Hanson, *Surf. Sci. Lett.* **259**, L749 (1991).

<sup>9</sup>C. E. D. Chidsey, D. N. Loiacono, T. Sleator, and S. Takahara, *Surf. Sci.* **200**, 45 (1988).

<sup>10</sup>D. A. Grigg, P. E. Russel, J. E. Griffith, M. J. Vasile, and E. A. Fitzgerald, *Ultramicroscopy* (to be published).

<sup>11</sup>D. J. Trevor, C. E. D. Chidsey, and D. N. Loiacono, *Phys. Rev. Lett.* **62**, 929 (1989).

<sup>12</sup>A. A. Gewirth (private communication).

<sup>13</sup>M. G. Samant, M. F. Toney, G. L. Borges, L. Blum, and O. R. Melroy, *J. Phys. Chem.* **92**, 220 (1988).

# Surface x-ray diffraction study of the Au(111) electrode in 0.01 M NaCl: Electrochemically induced surface reconstruction

B. M. Ocko, Alan Gibaud,<sup>a)</sup> and Jia Wang

Department of Physics, Brookhaven National Laboratory, Upton, New York 11973

(Received 1 October 1991; accepted 24 February 1992)

The structure of the Au(111) electrode surface in a 0.01 M NaCl electrolyte has been investigated using grazing incident angle x-ray diffraction. The top layer of gold atoms undergoes a reversible phase transition between the  $(1 \times 1)$  bulk termination and a  $(p \times \sqrt{3})$  uniaxial discommensuration (striped) phase on changing the electrode potential. Below a critical potential the stripe separation,  $p = 23$ , is identical to vacuum measurements. At sufficiently positive potentials the surface forms an ideally terminated,  $(1 \times 1)$ , Au(111) surface. Cycling the potential in the reconstructed region improves the reconstructed surface order.

## I. INTRODUCTION

The understanding of surface structure in vacuum has progressed rapidly over the last several decades; many of the developments have been due to techniques involving electron probes. In electrochemistry, electrode surfaces are of fundamental importance, yet, very little is known about their *in situ* structure. In part, this is due to the inability of electrons to penetrate solutions. With the availability of high brightness synchrotron sources surface x-ray diffraction has become a viable method to study *in situ* structure.<sup>1-4</sup>

In vacuum, the Au(111) surface reconstructs to form a uniaxial compressed surface phase.<sup>5-8</sup> Under electrochemical conditions, the surface charge at the Au(111) surface can be varied continuously and reversibly by as much as 0.5 electrons per surface atom. Very little is known about the atomic structure of the Au(111) electrode surface. In this paper we report the results of an x-ray scattering study of the  $(23 \times \sqrt{3})$  reconstruction of the Au(111) electrode surface in 0.01 M NaCl. A full description of the phase behavior and kinetic effects of the Au(111) surface in a variety of salt solutions is reported elsewhere.<sup>9</sup> In order to differentiate the respective roles of surface charge and adsorbates, studies were carried out in 0.1 M solutions of NaF, NaCl, and NaBr as reported in Refs. 9 and 10. The phase transition occurs at an induced surface charge density of  $0.07 \pm 0.02$  e/atom in all three 0.1 M solutions.<sup>9,10</sup>

A current survey of the gold electrode literature can be found in a recent review article.<sup>11</sup> In the following, we review some of the significant studies at the Au(111) face. The possibility that electrochemically induced reconstructions of gold surfaces might exist was proposed by Hamelin based on the hysteresis observed in capacity-potential curves at the same potential where a peak emerged in cyclic voltammograms (current voltage curves).<sup>12,13</sup> *Ex situ* low-energy electron diffraction (LEED) studies by Kolb Schneider have shown that the Au(111) surface, after emersion from an electrochemical cell, forms a  $(23 \times \sqrt{3})$  phase in the negative potential regime.<sup>14</sup> Recent *ex situ* LEED studies by Ross and D'Agostino have confirmed that gold surfaces remain reconstructed after emersion.<sup>15</sup> For the case of the Au(001) surface in HClO<sub>4</sub>, *in situ*

electroreflectance measurements provided further evidence that gold electrodes reconstruct.<sup>14</sup> Second harmonic generation (SHG) measurements at the Au(111) surface<sup>16,17</sup> have demonstrated that the phase transition between the  $(23 \times \sqrt{3})$  and  $(1 \times 1)$  phase can be monitored *in situ* by the additional symmetry pattern in the SHG intensity associated with the uniaxial compressed phase. However, it is difficult to extract detailed structural information from these measurements. Concurrent with the present surface x-ray scattering (SXS) study, *in situ* scanning tunneling microscopy (STM) studies<sup>18,19</sup> in HClO<sub>4</sub> solutions have confirmed the existence of the  $(p \times \sqrt{3})$  reconstruction within the negative potential regime. In the present electrochemical x-ray scattering study, the characteristic stripe separation—averaged over a macroscopic area—versus the applied potential has been measured with a lateral resolution which exceeds the capability of current STM measurements.

Our understanding of the Au(111) surface in vacuum has been obtained from a variety of techniques including LEED,<sup>6,7</sup> transmission electron diffraction (TED),<sup>20</sup> helium scattering,<sup>21</sup> surface x-ray diffraction,<sup>8,22</sup> and from STM.<sup>23,24</sup> The observed diffraction peaks have been interpreted as a rectangular  $(23 \times \sqrt{3})$  unit cell corresponding to a uniaxial compression (4.4%) along the  $\langle 100 \rangle$  direction in hexagonal coordinates (see Sec. II B) as shown in Fig. 1(a). This structure is often referred to as a stripe-domain phase where the stripe separation is proportional to the inverse compressibility. From TED measurements,<sup>20</sup> helium scattering,<sup>21</sup> and from x-ray reflectivity techniques<sup>8</sup> it has been inferred that the surface atoms are arranged in a manner such that the surface stacking sequence changes between ABC to ABA as shown in Fig. 1(a). Recent x-ray scattering<sup>8</sup> and STM studies<sup>23,24</sup> have shown that the discommensuration direction rotates by  $\pm 60^\circ$  to form a regular array of kink dislocations in the discommensuration direction under vacuum conditions. Under electrochemical conditions with STM, similar kinks in the discommensuration direction have been observed at the Au(111) electrode in HClO<sub>4</sub> solutions at negative potentials.<sup>18,19</sup>

In the present study we have characterized the in-plane structure of the Au(111) surface versus potential in 0.01 M NaCl. We have utilized a salt solution instead of the

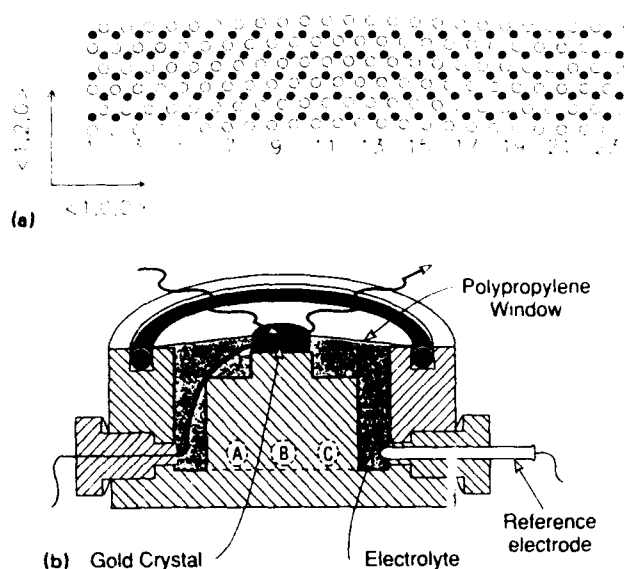


FIG. 1. (a) In-plane hexagonal structure of the Au(111) surface. The solid (filled) circles correspond to atoms in the second (first) layer. Surface atoms in the left and right hand sides of the figure are in undistorted hexagonal sites (ABC stacking sequence) whereas in the center of the figure the atoms are in faulted sites (ABA stacking sequence). (Refs. 21, 22) For 24 surface atoms in place of 23 underlying surface atoms, the compression is  $24/23 - 1 = 4.4\%$  and  $\delta = (\sqrt{3}/2)/23 = 0.038$ . (b) X-ray scattering electrochemical cell. The Au(111) single crystal is held at the top center by a Kel-F clamp. The cell is sealed with a polypropylene window by an o-ring. (A) electrolyte input, (B) counter electrode, (C) electrolyte output. An outer chamber (not shown) is filled with nitrogen gas to prevent diffusion of oxygen through the polypropylene window.

more commonly used acid solutions. Under these conditions we obtain a wider double layer potential range and are able to determine whether cations have any effects on the structure of the Au(111) surface. The latter is not possible in acid solutions since the cation is always a proton. At sufficiently positive potentials the stripe-phase reconstruction vanishes and the diffraction pattern exhibits the symmetry of the underlying lattice. The phase transition is reversible although there are significant hysteresis effects. A comprehensive study of the Au(111) surface in NaF, LiCl, NaCl, KCl, CsCl, and NaBr electrolytes with concentrations ranging between 0.01 and 0.1 M is reported elsewhere.<sup>9</sup>

## II. EXPERIMENTAL TECHNIQUES

### A. Electrochemical and surface preparation

Gold disk electrodes (2 mm by 10 mm diam) were sliced from a common single crystal, and aligned along the nominal (111) direction using a wire spark cutter. These disks were aligned and sanded with the (111) planes oriented within  $0.1^\circ$  of the surface normal axis  $\hat{n}$ . The disks were mechanically polished with 6  $\mu\text{m}$  diamond paste followed by 1  $\mu\text{m}$  alumina powder. Although the surface has a mirror finish, the mechanical polishing creates microscopic surface damage. In order to expose undamaged (111) planes, the samples were electrochemically polished in 1:1:1 (volume) HCl:ethylene glycol:ethanol.<sup>25</sup> The final surface preparation step involved sputtering with argon at

$5 \times 10^{-5}$  Torr at  $800^\circ\text{C}$  using a defocused beam at 2 kV and 2  $\mu\text{A}$  for several hours. The sample was transferred through air to an electrochemical x-ray scattering cell constructed from Kel-F<sup>1</sup> as shown in Fig. 1(b).

A 6  $\mu\text{m}$  polypropylene window covers and seals the cell with a thin capillary electrolyte film between the crystal face and the polypropylene film. An outer chamber was flushed with  $\text{N}_2$  gas to prevent oxygen from diffusing through the polypropylene membrane. The applied potential was referenced to an Ag/AgCl(3 M KCl) electrode connected to the cell through a micro glass frit. Counter electrodes were either gold or platinum wires.

The electrolyte solutions were prepared from superpure NaCl diluted with ultrapure  $\text{H}_2\text{O}$ . The diluted electrolyte solutions were deoxygenated with 99.999%  $\text{N}_2$  gas immediately before filling the cell. After flushing the cell with  $\text{N}_2$  gas, the deoxygenated electrolyte was injected into the cell through a syringe with the control potential turned off. The cell was filled with enough solution to expand the polypropylene window leaving a thick electrolyte layer (several mm) between the face and the window. Cyclic voltammograms were carried out in this geometry to check the electrochemical conditions of the cell. Before carrying out the x-ray scattering measurements the cell was deflated which leaves a thin electrolyte layer which we estimate from the small angle reflectivity measurements to be between 10 and 20  $\mu\text{m}$  thick. In the thin electrolyte layer geometry, the effects of bulk impurities are greatly reduced relative to the thick electrolyte geometry.

Our studies of the Au(111) surface were carried out in a potential range which is referred to the "double layer" region. Within this potential range there are no Faradaic processes and the electrode can be treated as an ideally polarizable interface. We note that the potential region in which this approximation is valid is bounded by hydrogen evolution at negative potentials and gold oxidation processes at positive potentials. In salt solutions (pH about 6), hydrogen evolution occurs below  $-0.8$  V. The high potential limit was 0.8 V.

### B. X-ray techniques

The x-ray scattering measurements reported in this paper were carried out with focused, monochromatic synchrotron radiation at beam line X22B at the National Synchrotron Light Source (NSLS) at Brookhaven National Laboratory. In the four circle geometry the sample orientation is oriented through its Euler angles  $\theta$ ,  $\chi$ , and  $\phi^{26}$  by a spectrometer under computer control. The scattering wave vector magnitude is  $|\mathbf{k}_f - \mathbf{k}_i| = 4\pi/\lambda \sin(2\theta/2)$  where  $\mathbf{k}_i$  and  $\mathbf{k}_f$  correspond to the incident and scattered wave vectors and where  $2\theta$  is the detector angle within the scattering plane. Diffraction measurements are carried out by measuring the scattering intensity along paths in reciprocal space (see below).

Measurements were carried out at an energy corresponding to a wavelength of  $\lambda = 1.54 \text{ \AA}$  at beamline X22B. The scattered intensity is measured with a scintillator detector placed on the  $2\theta$  arm and is normalized to the incident flux. At grazing incidence, i.e., small  $\alpha$ , the incident x

rays illuminate a region of the crystal 0.5 mm wide across the entire crystal face (10 mm). The scattering resolution, in reciprocal space, is primarily determined by the angular acceptance of the scattered radiation and the quality of the mosaic of the Au(111) crystal. The illuminated area of the incident beam does not directly affect the resolution. For the present measurements, the resolution within the scattering plane was determined by an array of equally spaced parallel plates (Soller slits) which provide a  $2\theta$  resolution of  $0.1^\circ$  half-width at half-maximum (HWHM). This corresponds to a longitudinal in-plane resolution in reciprocal space of  $0.007 \text{ \AA}^{-1}$  HWHM at  $\lambda = 1.54 \text{ \AA}$ . The transverse in-plane resolution is limited by the mosaic spread of the crystalline order which is typically  $0.025^\circ$  HWHM. Normal to the scattering plane, the resolution is determined by  $\psi_2$ , which is set by 10 mm detector slits located on the four circle  $2\theta$  arm which is 600 mm from the sample position.

The two principle features of the diffraction pattern from the Au(111) surface in reciprocal space are Bragg reflections and weak streaks of scattering along the surface normal direction.<sup>27-29</sup> In order to describe the scattering wave vector in terms of its components in the surface plane and along  $\hat{n}$  it is convenient to use a hexagonal coordinate system.<sup>8,30,31</sup> The hexagonal reciprocal space position is represented by the vector  $(H,K,L)$  or  $(H,K)$  within the surface plane where

$$a^* = b^* = \frac{4\pi}{\sqrt{3}a} = 2.52 \text{ \AA}^{-1}, \quad c^* = \frac{2\pi}{\sqrt{6}a} = 0.89 \text{ \AA}^{-1}.$$

The nearest-neighbor separation,  $a$ , equals  $2.885 \text{ \AA}$ .

The relationship between the cubic vector,  $(h,k,l)_{\text{cubic}}$ , and the hexagonal vector  $(H,K,L)$  is given by the transformations  $h = -4H/3 - 2K/3 + L/3$ ,  $k = 2H/3 - 2K/3 + L/3$ , and  $l = 2H/3 + 4K/3 + L/3$ . For example,  $(1,1,1)_{\text{cubic}} = (0,0,3)$ ,  $(0,0,2)_{\text{cubic}} = (0,1,2)$ , and  $(0,2,2)_{\text{cubic}} = (1,0,4)$ . The vector  $(H,K,0)$  lies within the surface plane whereas  $(0,0,L)$  is along the surface normal direction.

A principle feature of the Au(111) surface reconstruction (in vacuum) is a uniaxial compression of the top layer of gold atoms by 4.4% as shown in Fig. 1(a). This picture has been inferred from scattering techniques including low-energy electron diffraction (LEED),<sup>6,7</sup> transmission electron diffraction (TED),<sup>20</sup> helium scattering,<sup>21</sup> and surface x-ray diffraction studies.<sup>8</sup> In an x-ray scattering measurement the  $(p \times \sqrt{3})$  reconstruction gives rise to additional rods of scattering. We refer to these rods of scattering as over-layer reflectivity since the scattering originates from the reconstructed "overlayer" (top layer).<sup>8,32</sup> These over-layer reflections (modulation peaks) are arranged in a hexagonal pattern surrounding the integer  $(H,K)$  positions and the magnitude of the modulation wave vector is given by  $\delta a^*$ . Their projection on the surface plane is shown in Fig. 2. These additional reflections originate from the compression of the top layer along the three  $\sqrt{3}$  directions in reciprocal space.

The discommensuration periodicity,  $p$ , is defined as  $\sqrt{3}/(2\delta)$ . For example, if there are 24 surface atoms in place of 23 underlying surface atoms, the compression is  $24/23 - 1$

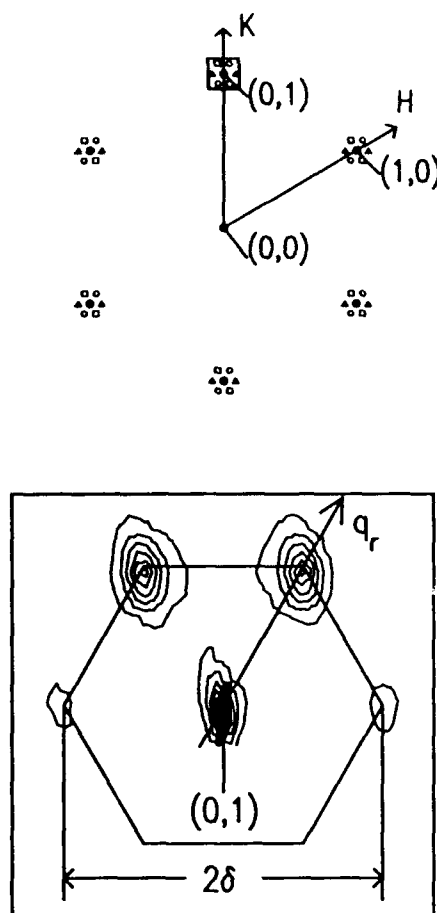


FIG. 2. Top: In-plane diffraction pattern of the Au(111)  $(23 \times \sqrt{3})$  reconstruction in hexagonal coordinates. The solid circles are at the periodicities from the underlying bulk substrate. The open symbols originate from the  $(23 \times \sqrt{3})$  reconstructed phase with three rotational equivalent domains. The axis  $q_r$  is defined to be along the  $\langle 1,1 \rangle$  direction. Bottom: X-ray scattering equal intensity contours in the vicinity of the  $(0,1)$  reflection at  $L = 0.5$  measured in 0.01 M NaCl at  $-0.3 \text{ V}$  vs a saturated Ag/AgCl.

$= 4.4\%$  and  $\delta = \sqrt{3}/2/23 = 0.038$ . In an x-ray scattering experiment in which the intensity is collected over several square mm, all three symmetry equivalent domains are probed. At sufficiently positive applied potentials, in all electrolytes, the scattering from the Au(111) surface does not exhibit the diffraction pattern of a reconstructed surface. Instead, only the integral reflections  $(H,K)$  originating from the substrate are observed.

### III. RESULTS

The in-plane diffraction pattern from the Au(111) surface, obtained within the reconstructed potential regime, is virtually identical in all electrolytes.<sup>9</sup> In the present paper we report the potential dependence of x-ray scattering measurements from the Au(111) surface in 0.01 M NaCl. Below a critical threshold potential, the scattering exhibits the characteristic diffraction pattern of a  $(p \times \sqrt{3})$  striped phase with three rotationally equivalent domains. In the bottom panel of Fig. 2, equal intensity contours are shown in the vicinity of the  $(0,1)$  reflection at  $L = 0.5$  for 0.01 M

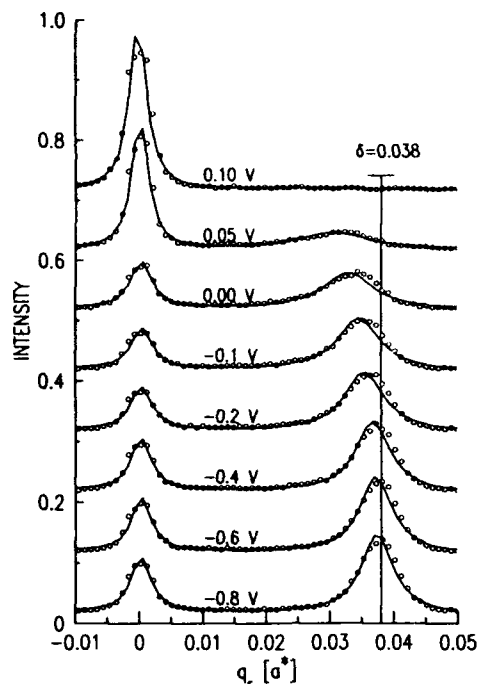


FIG. 3. Representative x-ray scattering scans along the  $q_r$  axis (see Fig. 2) for the Au(111) surface at  $L = 0.2$  in 0.01 M NaCl solution at a series of potentials chosen from scans between 0.1 and  $-0.8$  V in steps of  $-0.05$  V. The solid lines are fits to a Lorentzian line shape described in the text.

NaCl at  $-0.3$  V. Four peaks surrounding the (0,1) reflection are arranged in a hexagonal pattern, where  $\delta = 0.038$  is the length of the hexagon side in dimensionless units.<sup>6,7,20-22</sup> Our electrochemical measurements of the incommensurability are in good agreement with high resolution vacuum measurements at  $T = 300$  K, where  $\delta = 0.0383$ .<sup>6,7,20,21</sup> Figure 2 shows that the two surface reflections at largest wave vector transfer, from the origin, are the most intense and that the two reflections with the smallest wave vector transfer are not observed. These difference can be attributed to the arrangement of atoms in the reconstructed unit cell (structure factor).

We have carried out a detailed study of the potential dependence of the scattering from the Au(111) surface through the (0,1) reflection along the  $\langle 1,1 \rangle$  direction which we label as the  $q_r$  axis in Fig. 2. Along the  $q_r$  axis, the in-plane projection of the scattering wave vector is given by  $(q_r/\sqrt{3}a^*, 1 + q_r/\sqrt{3}a^*)$ . In Fig. 3, we present the measured scattering intensity obtained along the  $q_r$  axis at  $L = 0.2$  at a series of decreasing potentials between 0.1 and  $-0.8$  V with an effective scan rate of 0.5 mV/s. Above 0.10 V the scattering is centered at  $q_r = 0$  (Fig. 3) corresponding to the (0,1) bulk reflection. As the potential is reduced below 0.05 V, the intensity of the reconstruction peaks grows. Concomitantly, the (0,1) reflection decreases in intensity but remains centered at zero. The position of the reconstruction peak moves outward (increasing compression) as the potential is decreased. The maximum scattering intensity at (0,1) is about thirty times the diffuse scattering originating from the electrolyte and window.

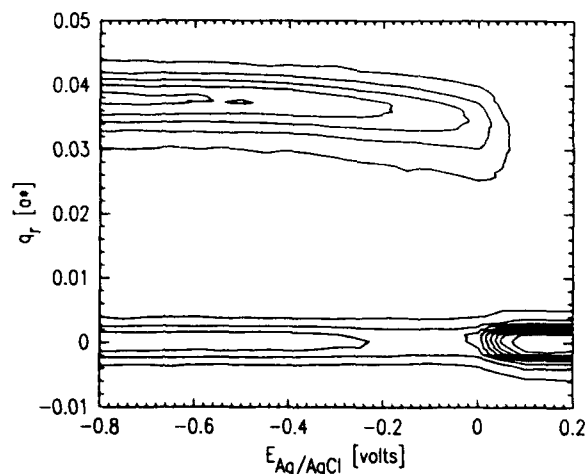


FIG. 4. Equal intensity contours created from the intensity distribution along  $q_r$  starting at a potential of 0.2 V and extending to  $-0.8$  in steps of 0.05 V. The emergence of a broad peak at  $q_r = 0.030a^*$  corresponds to the formation of the reconstructed phase.

An alternative approach for displaying the potential dependence of the surface scattering—shown as a series of displaced curves in Fig. 3—is shown in Fig. 4 as a contour plot. The intensity matrix, used to create the contour plot, was formed by measuring the scattered intensity along  $q_r$  at a series of decreasing potentials starting at a potential of 0.2 V and extending to  $-0.8$  in steps of 0.05 V. It is apparent from Fig. 4 that the reconstructed phases starts to form at 0.05 V as indicated by the emergence of contour lines at  $q_r = 0.030a^*$ . As the potential is further decreased the reconstruction wave vector moves outward to  $q_r = 0.038a^*$  ( $p = 23$ ) and the scattering line shape narrows corresponding to an increased surface order.

To extract additional information from the scattering profiles, we have fit the scattering profiles along  $q_r$  to the sum of two Lorentzians and a small background

$$S(q_r) = \frac{I_0}{1 + q_r^2/\sigma^2} + \frac{I_\delta}{1 + (q_r - \delta)^2/\sigma_\delta^2} + A + Bq_r/a^*. \quad (1)$$

The first term represents the scattering at the substrate (0,1) wave vector, the second term corresponds to the scattering centered at  $(\delta/\sqrt{3}, 1 + \delta/\sqrt{3})$ , and  $A$  and  $B$  are small background parameters. The parameters  $I_0$  and  $I_\delta$  correspond to the peak intensities at  $q_r$  equal to 0 and  $\delta$ , respectively. The Lorentzian profile widths in Eq. (4) are  $\sigma$  and  $\sigma_\delta$ . In reciprocal space, the Lorentzian line shape is derived from a one-dimensional real space atomic model in which the correlation function decays exponentially with a length  $\zeta_\delta = a\sqrt{3}/(4\pi\sigma_\delta)$ . This length is a measure of the distance over which atoms in the reconstructed layer are positionally correlated. The discommensuration periodicity, which we also refer to as the stripe separation,  $L_\delta = pa = a\sqrt{3}/(2\delta)$ .



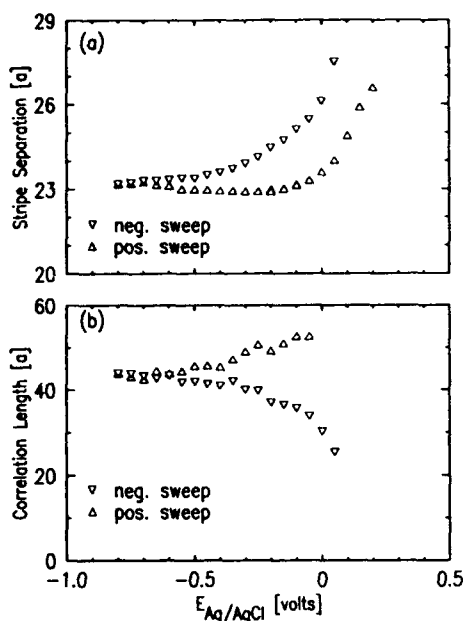


FIG. 5. The stripe separation (a) and correlation length (b) obtained by fitting the data shown in Figs. 3 and 4 to Eq. (1) for the Au(111) surface in 0.01 M NaCl. The triangles and upside down triangles correspond to positive and negative sweep directions, respectively.

In an x-ray scattering measurement, the correlation length of the underlying Au(111) facets can also be determined from the inverse peak widths in reciprocal space. If the surface is composed of terraces (facets) separated from each other by monoatomic steps, the scattering from neighboring facets adds out-of-phase at the (0,1) reflection and the peak width is broadened by this effect. For an exponential facet size distribution, the mean facet size along the  $\langle 1,1 \rangle$  direction  $\zeta$  equals  $a\sqrt{3}/(4\pi\sigma)$ . In the present set of measurements,  $\zeta$  is at least 300 Å and represents a lower bound for the distance between steps. Incorporating finite resolution effects into the analysis increases the effective facet size.

In the fitting procedure the peak position  $\delta$  the widths,  $\sigma$  and  $\sigma_\delta$ , the amplitudes,  $I_0$  and  $I_\delta$ , and the background are varied for the scattering profiles at constant potential. Instrumental resolution effects have not been included in the present analysis since improving the reciprocal space resolution by a factor of ten did not modify the observed scattering linewidths.<sup>33</sup> The scattering in the wings of the peak at  $q_\parallel = 0$  (substrate periodicity) exhibit a  $q_\parallel^{-2}$  fall off. At small  $q_\parallel$ , however, the scattering profiles are not adequately represented by the model. In part, this discrepancy is due to finite substrate mosaic effects which have a Gaussian component that is not included in our Lorentzian model. At  $q_\parallel = 0.038a^*$  (reconstructed periodicity) the scattering is reasonably well represented by the Lorentzian profiles at sufficiently negative potentials.

The stripe separation  $L_\delta$  and the correlation length  $\zeta_\delta$  obtained from fits to Eq. (1) are shown in Figs. 5(a) and 5(b), respectively as a function of the applied potential. The potential cycle originates at 0 V and continues to -0.8 V and then back to 0 V in steps of 0.05 V. After the

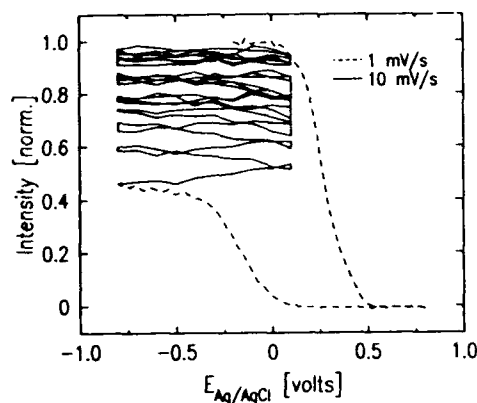


FIG. 6. The effect of surface grooming (see text) at the Au(111) surface in 0.1 M NaF. The data is acquired at fixed scan rates of 1 and 10 mV/s. (see key) at a wave vector  $(0.038/\sqrt{3}, 1 + 0.038/\sqrt{3}, 0.2)$ . At this position the scattered intensity increases as the stripe length  $L_\delta$  approaches 23 and as the correlation length increases. The scattered intensity increases during potential cycles between -0.8 and 0.1 V.

initial signs of the surface reconstruction at 0.05 V, corresponding to the emergence of the modulation peak, there is a continued compression as the potential is decreased, as shown by the inverted triangles in Fig. 5(a). The maximum compression corresponds to a stripe periodicity of 23  $a$ . Changes in the reconstructed surface structure virtually cease below -0.6 V. Further compression and an increase in the correlation length resumes after sweeping the potential positive. The stripe domain correlation length  $\zeta_\delta$  achieves a maximum value of 55  $a$  at -0.1 V. This is at a potential just below where the lifting of reconstruction starts and  $\zeta_\delta$  is always less than  $\zeta$ .

In vacuum, the Au(111) surface forms an ordered array of 60° shifts in the discommensuration direction.<sup>22-24</sup> For the Si(111) surface an ordered array of reconstructed domains with different orientations reduces<sup>22</sup> the strain energy of the underlying substrate. This argument may also apply to the Au(111) surface.<sup>34</sup> These shifts in the discommensuration direction (kinks) for the Au(111) surface are separated by about 80  $a$  at  $T = 300$  K. This new wave vector,  $\sim 2\pi/80a$ , gives rise to additional diffraction spots.<sup>8</sup> At the electrode surface, at all potentials, these additional diffraction spots are absent. Hence, there is no evidence that the kinks form an ordered array. However, the Au(111) electrode surface may form a disordered array of kinks in which the kink spacing is irregular. This observation is consistent with recent *in situ* STM studies of the Au(111) surface in  $\text{HClO}_4$ .<sup>18,19</sup> These studies clearly establish the existence of discommensuration kinks, however, a well ordered array of kinks can not be ascertained from the present STM results.

In 0.01 M NaCl solutions, the correlation length can be increased by cycling the potential in the reconstructed potential region. We refer to the surface state where the maximum compression and correlation length are achieved as the "groomed" surface. The effect of surface grooming on the Au(111) surface is shown in Fig. 6 by recording the scattered intensity while the potential is swept at fixed rates

in both sweep directions. The spectrometer is set to  $(0.038/\sqrt{3}, 1 + 0.038/\sqrt{3}, 0.2)$ . At this position the scattered intensity increases as the stripe length  $L_\delta$  approaches 23 and as the correlation length increases. The effect of surface grooming on the Au(111) surface in 0.1 M NaF is shown in Fig. 6. Similar results have been obtained in 0.01 M NaCl. In Fig. 6, the normalized scattered intensity has been obtained by dividing the scattered intensities by the maximum scattered intensity recorded in the grooming procedure. In the figure, the first potential ramp starts at 0.8 V and stops at  $-0.8$  V at a rate of 1 mV/s. The groomed surface is obtained by repeated potential cycles between 0.8 and 0.1 V at a rate of 10 mV/s. Finally, the potential is swept from  $-0.2$  to 0.8 V at a sweep rate of 1 mV/s. In the first potential ramp the normalized intensity only reaches 45% (dashed line) of the groomed value. During the grooming cycles (solid lines) between  $-0.8$  and 0.1 V the intensity increases substantially. After 20 grooming cycles (1 h) there is no further increase in the intensity at  $(0.038/\sqrt{3}, 1 + 0.038/\sqrt{3}, 0.2)$ . For the studies in 0.01 M NaCl, cycling the potential for several days in the reconstructed potential region did not improve the correlation length beyond 55a. In conjunction with specular reflectivity measurements, which are sensitive to the surface normal structure,<sup>9</sup> we know that the grooming process only involves a rearrangement of the atoms within the surface plane. Finally, the grooming process may facilitate a rearrangement of the discommensuration kinks which leads to a more ordered surface.

Complementary information on the Au(111) surface structure can be obtained by monitoring the potential dependence of the scattering at several positions along the rods of scattering. Different positions in reciprocal space are sensitive to different aspects of the surface structure and likewise the potential dependence varies with reciprocal space position. For instance, scattering with an in-plane wave vector (0,1) couples to the Fourier transform of the atomic density distribution within the surface plane at a wave vector corresponding to the undistorted bulk hexagonal spacing. Also the scattering at the reconstructed position increases with decreasing potential, whereas the scattering at (0,1,0.5) increases when the reconstruction is lifted at positive potentials. These differences have motivated us to present the potential dependence at different reciprocal space positions

Figure 7 displays the potential dependence of the scattering from the Au(111) surface in 0.01 M NaCl at (a)  $(0.038/\sqrt{3}, 1 + 0.038/\sqrt{3}, 0.2)$ , and at (b) (0,1,0.5). Each panel corresponds to a potential cycle starting at 0.6 V to  $-0.8$  V and then back to 0.6 V at a sweep rate of 1.0 mV/s. In the top panel [Fig. 7(a)] the scattering intensity corresponds to the principle  $(23 \times \sqrt{3})$  reconstruction peak. We have subtracted the diffuse background and normalized the intensity to the groomed state. At 0.05 V the intensity at  $(0.038/\sqrt{3}, 1 + 0.038/\sqrt{3}, 0.2)$  starts to increase corresponding to the formation of the reconstructed phase. Note that the maximum scattered intensity is achieved in the positive going potential sweep before the reconstructed

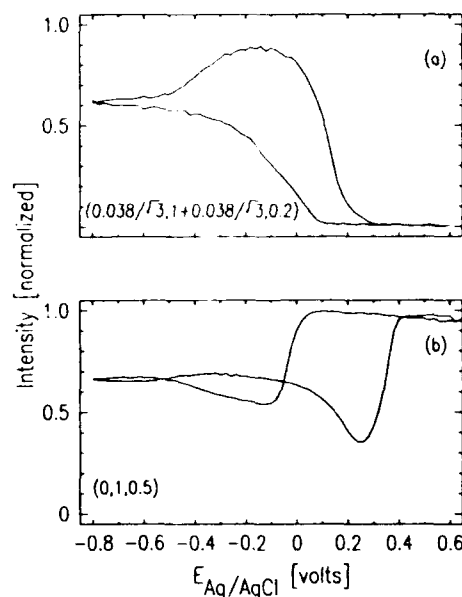


FIG. 7. Potential dependence of the x-ray scattering intensities at (a)  $(0.038/\sqrt{3}, 1 + 0.038/\sqrt{3}, 0.2)$ , and (b) (0,1,0.5) in 0.01 M NaCl solution. Data was acquired at a scan rate of 1 mV/s. In both the negative and positive slow directions as indicated by the arrows in the figures. In all cases the potential cycles start at 0.6 V. The background subtracted intensities are normalized to unity at their maximum values.

phase is lifted. The measured intensity at  $(0.038/\sqrt{3}, 1 + 0.038/\sqrt{3}, 0.2)$  does not always reflect the peak intensity along  $q$ , since  $\delta$  varies with potential as shown in Fig. 3. Despite this fact, the potential dependence at this position does provide a reasonable measure of the reconstructed order parameter. This is because the peak profiles are relatively broad compared to the changes in  $\delta$  with potential.

The scattering at (0,1,0.5) versus the applied potential is shown in Fig. 7(b) where the scattering intensity has been normalized to unity at 0.6 V. This reciprocal space position is exactly halfway between the  $(0,1,\bar{1})$ , and  $(0,1,2)$  Bragg peaks. At these halfway positions, the measured intensities are most sensitive to effects of surface disorder. In the  $(1 \times 1)$  potential region between 0.4 and 0.6 V there is no change in the intensity with potential as shown in Fig. 7(b). As discussed in the context of the nonspecular reflectivity profiles at the Au(111) surface<sup>9</sup> this strongly suggests that the lateral position of the gold atoms in the top atomic layer remains fixed within this potential region. At the lowest potentials the surface is reconstructed and the intensity at (0,1,0.5) falls to about 65% of the  $(1 \times 1)$  value. Comparing the scattering at (0,1,0.5) with the scattering at  $(0.038/\sqrt{3}, 1 + 0.038/\sqrt{3}, 0.2)$  versus potential allows us to draw several interesting conclusions. The sharp break in slope at 0.05 V at  $(0.038/\sqrt{3}, 1 + 0.038/\sqrt{3}, 0.2)$  (negative potential sweep) is clearly correlated with the sharp break in slope at (0,1,0.5) corresponding to the loss of order at the in-plane wave vector (0,1). In the positive sweep direction, the loss of the reconstructed order is nearly complete by 0.25 V, Fig. 7(a), whereas the order at the (0,1) wave vector is not completely restored until 0.40 V. A dip in the scattering

intensity at (0,1,0.5) appears in Fig. 7(b) during both scan directions. In the positive sweep direction this effect is most pronounced and the intensity at 0.25 V falls to 35% of the intensity at 0.6 V. We believe that this dip in the scattering intensity (0.25 V) corresponds to increased surface disorder during the lifting of the reconstructed phase.

#### IV. CONCLUSIONS

In this article we have presented the results of *in situ* structural x-ray scattering studies of the Au(111) electrode surface in 0.01 M NaCl solutions. The top layer of gold atoms undergoes a reversible phase transition between the (1×1) bulk termination and a ( $p \times \sqrt{3}$ ) uniaxial (striped) discommensuration phase on changing the electrode potential. Below a critical potential the stripe separation,  $p = 23$ , is identical to results obtained in vacuum. An ordered array of discommensuration kinks is not observed. At sufficiently positive potentials the striped phase disappears and the surface exhibits the structure of a (1×1) surface.

In a separate paper, a comprehensive x-ray scattering and reflectivity study of the Au(111) surface is reported in a variety of salt electrolytes.<sup>9</sup> The potential dependence of the scattered intensity is a strong function of the electrolyte anion species. However, in all these solutions, the transition between the (1×1) and reconstructed surfaces occurs at a common value of the surface charge. In particular, the reconstruction starts to form and lift at a negative charge of 0.07 electrons per surface gold atom. Additional information on the nature of the reconstruction has been obtained by measuring the transition kinetics after a step change in the potential.

#### ACKNOWLEDGMENTS

The authors thank Hugh Isaacs and Alison Davenport for their assistance. This work has been supported by an exploratory research grant at Brookhaven National Laboratory and by the Division of Materials Research, U. S. Department of Energy, under Contract No. DE-AC02-76CH00016.

This article was presented at the 38th National Symposium of the American Vacuum Society Topical Conference, Surface Science at the Solid-Liquid Interface (TC1).

<sup>4)</sup>University of Maine, U.A. 807, C.N.R.S., Le Mans, France

<sup>1)</sup>M. F. Toney and O. R. Melroy, in *In-Situ Studies of Electrochemical Interfaces*, edited by H. D. Abruna (VCH Verlag Chemical, Berlin, 1991).

- <sup>2</sup>O. R. Melroy, M. F. Toney, G. L. Borges, M. G. Samant, L. Blum, J. B. Kortright, P. N. Ross, and L. Blum, *Phys. Rev. B* **38**, 10962 (1988).
- <sup>3</sup>B. M. Ocko, Jia Wang, Alison Davenport, and Hugh Isaacs, *Phys. Rev. Lett.* **65**, 1466 (1990).
- <sup>4</sup>C. A. Melendres, H. You, V. A. Maroni, Z. Nagy, and W. Yun, *J. Electroanal. Chem.* **297**, 549 (1991).
- <sup>5</sup>M. A. Van Hove, R. J. Koestner, P. C. Stair, J. B. Biberian, L. L. Kesmodel, I. Bartos, and G. A. Somorjai, *Surf. Sci.* **103**, 189 (1981).
- <sup>6</sup>J. Perdureau, J. P. Biberian, and G. E. Rhead, *J. Phys. F* **4**, 1978 (1974).
- <sup>7</sup>D. M. Zehner and J. F. Wendelken, *Proceedings of the Seventh International Vacuum Congress and the Third International Conference on Solid Surfaces*, Vienna, 1977 (F. Berger and Sohne, Vienna, 1977), p. 517.
- <sup>8</sup>A. R. Sandy, S. G. J. Mochrie, D. M. Zehner, K. G. Huang, and D. Gibbs, *Phys. Rev. B* **43**, 4667 (1991).
- <sup>9</sup>J. Wang, B. M. Ocko, A. J. Davenport, and H. S. Isaacs, *Phys. Rev. B* **46** (1992).
- <sup>10</sup>J. Wang, A. J. Davenport, H. S. Isaacs, and B. M. Ocko, *Science* **255**, 1416 (1992).
- <sup>11</sup>D. M. Kolb, in *Frontiers in Electrochemistry*, edited by J. Lipowski and P. N. Ross (VCH, New York, 1991), Vol. 2.
- <sup>12</sup>A. Hamelin, *J. Electroanal. Chem.* **142**, 299 (1982).
- <sup>13</sup>J. P. Bellier and A. Hamelin, *C. R. Acad. Sci.* **280**, 1489 (1975).
- <sup>14</sup>D. M. Kolb and J. Schneider, *Electrochimica Acta* **31**, 929 (1986).
- <sup>15</sup>P. N. Ross, Jr. and A. T. D'Agostino, *Electrochim. Acta* **37**, 615 (1992).
- <sup>16</sup>A. Friedrich, B. Pettinger, D. M. Kolb, G. Lüpke, R. Steinhoff, and G. Marowsky, *Chem. Phys. Lett.* **163**, 123 (1989).
- <sup>17</sup>G. Lüpke, G. Marowsky, R. Steinhoff, A. Friedrich, B. Pettinger, and D. M. Kolb, *Phys. Rev. B* **41**, 6913 (1991).
- <sup>18</sup>N. J. Tao and S. M. Lindsay, *J. Appl. Phys.* **70**, 5143 (1991).
- <sup>19</sup>X. Gao, A. Hamelin, and M. J. Weaver, *J. Chem. Phys.* **95**, 6993 (1991).
- <sup>20</sup>K. Yamazaki, K. Takayamagi, Y. Tanishiro, and K. Yagi, *Surf. Sci.* **199**, 595 (1988).
- <sup>21</sup>U. Harten, A. M. Lahee, J. Peter Toennies, and Ch. Woll, *Phys. Rev. Lett.* **54**, 2619 (1985).
- <sup>22</sup>K. G. Huang, D. Gibbs, D. M. Zehner, A. R. Sandy, and S. G. J. Mochrie, *Phys. Rev. Lett.* **65**, 3317 (1990).
- <sup>23</sup>J. V. Barth, H. Brune, G. Ertl, and R. J. Behm, *Phys. Rev. B* **42**, 9307 (1990).
- <sup>24</sup>D. D. Chambliss and R. J. Wilson, *J. Vac. Sci. Technol. B* **9**, 928 (1991).
- <sup>25</sup>J. L. Whitton and J. A. Davies, *J. Electrochem. Soc.* **111**, 1347 (1964).
- <sup>26</sup>W. R. Busing and H. A. Levy, *Acta. Crystallogr.* **22**, 454 (1967).
- <sup>27</sup>I. K. Robinson, *Phys. Rev. B* **33**, 3830 (1986).
- <sup>28</sup>A. M. Afanas'ev, P. A. Aleksandrov, S. S. Fanchenko, V. A. Chaplanov, and S. S. Yakimov, *Acta. Crystallogr. A* **42**, 116 (1986).
- <sup>29</sup>S. R. Andrews and R. A. Cowley, *J. Phys. C* **18**, 6427 (1985).
- <sup>30</sup>J. Bohr, R. Feidenhans'l, M. Nielsen, M. Toney, R. L. Johnson, and I. K. Robinson, *Phys. Rev. Lett.* **54**, 1275 (1985).
- <sup>31</sup>B. E. Warren, *X-ray Diffraction* (Addison-Wesley, Reading, MA, 1969).
- <sup>32</sup>B. M. Ocko, D. Gibbs, K. G. Huang, D. M. Zehner, and S. G. J. Mochrie, *Phys. Rev. B* **44**, 6429 (1991).
- <sup>33</sup>This was carried out by using a Ge(111) analyzer rather than Soller slits.
- <sup>34</sup>O. L. Alerhand, D. Vanderbilt, R. D. Meade, and J. D. Joannopoulos, *Phys. Rev. Lett.* **61**, 1973 (1988).

# H<sub>2</sub>O adsorption on Ni(s) (111) surfaces: Evidence for a step induced influence on the adsorption geometry

Carsten Benndorf and Carolin Mundt

Department of Physical Chemistry, University of Hamburg, Bundesstrasse 45, D-2000 Hamburg 13, Germany

(Received 21 October 1991; accepted 25 November 1991)

The adsorption of H<sub>2</sub>O on stepped Ni(s) (111) surfaces with nominal (221) and (665) orientation was studied with thermal desorption spectroscopy (TDS), low-energy electron diffraction (LEED), and work function change measurements ( $\Delta\Phi$ ). LEED from both clean surfaces confirmed a (1 $\times$ 1) structure attributed to the presence of (111) terraces and (11 $\bar{1}$ ) steps [Ni(221) = 3(111) terraces + 1(11 $\bar{1}$ ) steps, Ni(665) = 11(111) terraces + 1(11 $\bar{1}$ ) steps]. In TDS experiments on both surfaces desorption states are detected which can be attributed either to terrace or to step sites. The step induced states, which are missing on "flat" Ni(111), are found at higher desorption temperatures compared to the terrace state (denoted as *B* with  $T_m = 175$ –178 K) or to the ice multilayer state (denoted as *A* with  $T_m = 155$ –160 K). The step induced states are related to the desorption of H<sub>2</sub>O monomers adsorbed at step sites (denoted as *C*,  $T_m = 225$  K) or to the recombination of H<sub>2</sub>O dissociation fragments (state *D* and *E* at  $T_m = 260$  and 325 K, respectively). The  $\Delta\Phi$  measurements demonstrate a significant increase of the effective H<sub>2</sub>O dipole moment at step sites, an opposite behavior is found at terrace sites. These data demonstrate that at low H<sub>2</sub>O coverages the steps are first decorated by oriented H<sub>2</sub>O monomers. At higher coverages a bilayer is expanding from the oriented H<sub>2</sub>O monomers at step sites onto the (111) terraces. Due to the presence of "flip-up" and "flop-down" H<sub>2</sub>O dipole orientations the effective dipole moment of the H<sub>2</sub>O bilayer terrace clusters is lowered.

## I. INTRODUCTION

The modification of surfaces is a relevant subject as well in the field of heterogeneous catalysis as for fundamental aspects in surface science. It is well recognized that the adsorption behavior of a perfect single crystal surface can be influenced by the presence of defects as for example steps and kinks. Somorjai and co-workers<sup>1</sup> demonstrated that the dissociation barrier for hydrogen abstraction from adsorbed hydrocarbons may be lowered on stepped surfaces. However, the influence of surface defects (like steps and kinks) on the adsorption energy, the adsorption geometry, and on a possible lowering of a dissociation barrier is not well understood up to now.

From our recent investigations of different adsorption systems, including CO/Ni(s) (111),<sup>2,3</sup> NH<sub>3</sub>/Ni(s) (111),<sup>3</sup> NH<sub>3</sub>/Fe(s) (100),<sup>4</sup> and H<sub>2</sub>O/Ni(s) (111)<sup>5</sup> we concluded, that the influence of steps on the molecule-substrate bond (and therefore also on the intramolecular bond) depends on the nature of the molecule-substrate interaction. In the case of electron donor molecules (as for example NH<sub>3</sub> on Ni or Fe) we observed an increase of the molecule substrate binding energy at step sites with the observation of higher temperature desorption state and the lowering of the barrier for dissociation. In contrast to this behavior, for the CO/Ni(s) (111) system CO can be assumed as an electron acceptor molecule (electron backdonation from the metal into 2 $\pi^*$  CO orbital dominates over the 5 $\sigma$  donation into the metal). For CO/Ni(s) (111) we observed new desorption states at lower desorption temperatures, which are absent on "flat" Ni(111). Further, no hint was found for an increased CO dissociation.<sup>2,3</sup>

In this article we report on H<sub>2</sub>O adsorption experiments on Ni(s) (111) surfaces. The surfaces used in this study, Ni(221) and Ni(665) exhibit the same (111)-step and (11 $\bar{1}$ )-terrace orientation but they differ in the terrace width. For Ni(221) a terrace width of about 3.5 atoms is expected; this value increases to a width of about 11.5 atoms for Ni(665). As expected for an electron donor molecule, H<sub>2</sub>O is bound to the substrate more strongly at step sites. This is in accordance with thermal desorption spectroscopy (TDS) experiments which show a step-induced desorption state at considerably higher desorption temperature ( $\Delta T = 45$  K) on both surfaces. The peak areas for terrace and step induced states evaluated from TDS spectra are in good agreement with expected ratios from terrace widths and step concentrations. The high effective dipole moment associated with H<sub>2</sub>O adsorption at step sites is related to a step-induced ordering of the H<sub>2</sub>O monomers. The negative value of  $\Delta\Phi$  at step sites confirms the bonding of H<sub>2</sub>O to the Ni step sites via the oxygen atom and is consistent with a "step-up" adsorption geometry. Finally, the relatively low contribution of the H<sub>2</sub>O terrace molecules to the work function change is related to the influence of the oriented step molecules on the bilayer cluster configuration (with nearly equal numbers of "flip-up" and "flop-down" dipole orientations<sup>6</sup>).

Some part of the results presented in this paper for the H<sub>2</sub>O/Ni(665) system has been reported recently in Ref. 5. For H<sub>2</sub>O/Ni(221) we will concentrate our present report on the most characteristic TDS and  $\Delta\Phi$  data, a detailed report including also low-energy electron diffraction (LEED) measurements for H<sub>2</sub>O/Ni(221) will be published separately.<sup>7</sup>

## II. EXPERIMENTAL

The ultrahigh vacuum (UHV) system employed in the present study has been described recently in detail elsewhere.<sup>5</sup> In brief, the UHV system allowed base pressures below  $1 \times 10^{-10}$  Torr and was equipped with facilities for LEED, Auger electron spectroscopy (AES) and Ar ion sputtering. The temperature of the Ni(s) (111) crystals could be controlled with liquid nitrogen cooling and resistivity heating between 120 and 1000 K. The temperature was measured with a Ni-Cr/Ni thermocouple spot welded to the periphery of the crystal disc (diam 10–14 mm, 1 mm thick). For thermal desorption experiments the crystal was heated with a rate of 3–5 K/s. The desorption flux was monitored with a quadrupole mass spectrometer (QMS) aligned line-of-sight to the Ni(s) (111) crystal. To improve the signal to noise ratio and to lower the background signal the desorbing flux was focused via a stainless steel tube of 8 mm diam into the entrance of the QMS. Water dosing onto the Ni(s) (111) crystal was achieved with a microcapillary doser system; in this way the pressure during water dosing could be kept in the  $10^{-10}$  Torr range.

Work function change measurements ( $\Delta\Phi$ ) were performed with a vibrating Kelvin probe using a gold plated stainless steel mesh of high transparency as a reference electrode (diam 5 mm). In this report we describe  $\Delta\Phi$  measurements performed during H<sub>2</sub>O desorption. The employed heating rate was the same as for the TDS experiments.

The Ni(s) (111) crystals were prepared in the usual way: alignment by x-ray diffraction technique, cutting by spark erosion, polishing of the elliptical crystal discs with diamond paste, and electrochemical methods. Inside the UHV system, the crystals were cleaned by several cycles of Ar ion sputtering and annealing up to 1000 K. Surface cleanliness and crystallography were checked with AES and LEED, respectively.

## III. RESULTS AND DISCUSSIONS

LEED results from the clean Ni(s) (111) surfaces together with ball models from the "ideal" atomic arrangement of the surfaces are shown in Fig. 1. As a function of electron primary energy, the unit mesh especially for the Ni(221) is not easily identified with LEED due to the strong intensity changes of the (1×1) spots. This is a consequence of the interference from the Ni(221) or Ni(665) unit cell reflexes with the reflexes from the (111) terraces.<sup>8</sup> In the case of the Ni(665) crystal, where the terrace width is relatively large, the LEED pattern can be interpreted as being due to a (111) face-centered-cubic (fcc) surface; the step structure leads to a splitting of the (111) terrace reflexes in directions perpendicular to the step directions. Because the LEED pattern reflects the reciprocal space, the spot splitting  $a^*$  is inverse to the terrace width. Consequently, in the case of the Ni(221) surface, the spot splitting is much larger, therefore the "hexagonal" arrangement of the (111) terrace spots is not so clearly visible for this surface. A straight forward identification is

possible by measuring the ratio of row spacing  $b^*$  to spot splitting  $a^*$  (indicated in Fig. 1). The experimental values of this ratio  $a^*/b^*$  are  $= 2.94 \pm 0.05$  and  $= 7.8 \pm 1.5$  for Ni(221) and Ni(665), respectively. These values are in good agreement with the theoretical values expected for ideal (221) and (665) fcc surface (3.00 and 9.85, respectively<sup>8</sup>).

The step height of the Ni(221) crystal was determined from the intensity variation of the (0,0) and (0,1) LEED reflexes as a function of electron primary energy,<sup>9</sup> giving a value of 0.23 nm. This step height is identical to the distance of Ni(111) planes (0.203 nm) within the error of our evaluation and confirms the existence of steps with one atomic height. Although this procedure was not performed for the Ni(665) crystal separately, we assume here the same one atomic step height. We conclude that our LEED data from both Ni(s) (111) surfaces are consistent with the atomic arrangement expected for the ideal nonreconstructed (221) and (665) fcc surfaces.

Figure 2 summarizes thermal desorption spectra obtained for Ni(221) and Ni(665) for different H<sub>2</sub>O exposures at 150 K. We observe the sequential filling of different adsorption states, denoted as *A* ( $T_m = 155$ –160 K; ice multilayer), *B* ( $T_m = 180$ –175 K; desorption from (111) terraces), *C* ( $T_m = 225$  K; desorption from step sites), *D* and *E* ( $T_m = 260$  and 325 K; recombination of dissociation fragments).

The desorption states *A*, *B*, and *C* are detected on both Ni(s) (111) surfaces at nearly identical temperatures. Desorption states *D* and *E*, which are related to H<sub>2</sub>O dissociation, are observed with significant intensity only on Ni(221). We note, that on the flat Ni(111) surface only two desorption peaks (*A* and *B*) had been observed.<sup>9,10</sup> In accordance with the interpretation for H<sub>2</sub>O/Ni(111) proposed by Madey and Netzer<sup>10</sup> we interpret the desorption state *B* on Ni(s) (111) as due to H<sub>2</sub>O desorption from Ni(111) terraces and state *A* to the desorption from ice multilayers.

The peak temperatures observed on Ni(s) (111) for state *A* and *B* are in good agreement with the values reported for the flat Ni(111) surface. However, in contrast to the behavior of state *B* on Ni(111),<sup>11</sup> which shifts with increasing coverage from 168 to 172 K, we observe on Ni(s) (111) a peak shifting in the opposite direction [from 180 to 175 K on Ni(221)]. This behavior is suggested to be due to an influence of the step structure on the lateral interaction between neighboring H<sub>2</sub>O molecules and will be discussed in more detail below.

In analogy to the results from Madey and Netzer for H<sub>2</sub>O/Ni(111)<sup>10</sup> we assume for Ni(s) (111) that the saturation of state *B* also corresponds to a coverage of  $\Theta = 0.75$  (where  $\Theta = 1$  corresponds to an equal number of adsorbate molecules and Ni(111) substrate atoms, note that this coverage definition is not referred to the unit cells of the Ni(s) (111) surfaces). The desorption states *C*, *D*, and *E* have not been observed on flat Ni(111); they are attributed to molecularly adsorbed H<sub>2</sub>O at step sites (*C*) and/or to the recombination of H<sub>2</sub>O dissociation products (*D* and *E*). These desorption states are assumed to be a

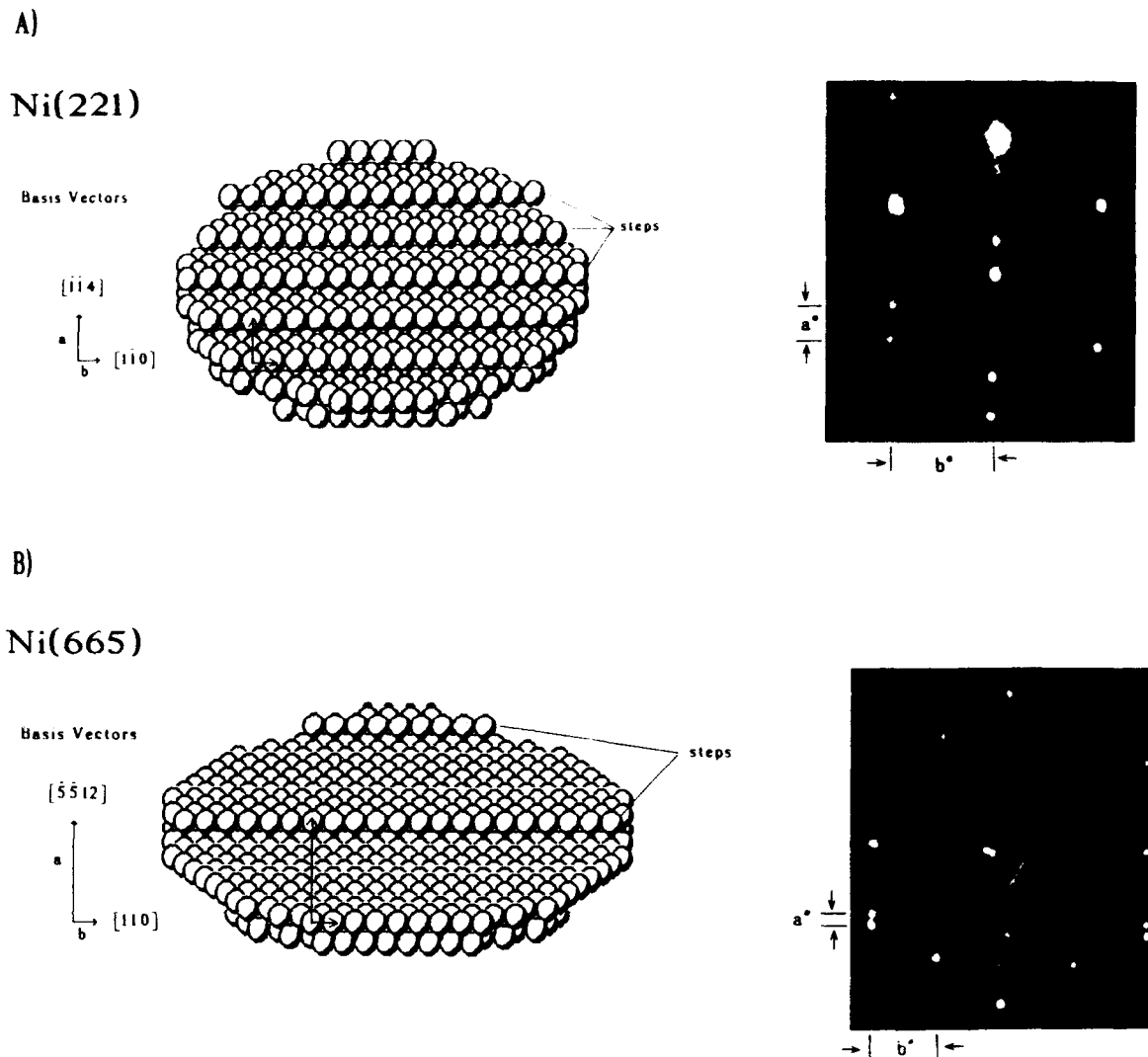


FIG. 1. Ball models and LEED patterns for Ni(s) (111) surfaces. (A) Ni(221) ball model and LEED at  $E_p = 147$  eV (B) Ni(665) ball model and LEED at  $E_p = 240$  eV. Note that the spot splitting  $a^*$  is perpendicular to the step direction  $[11\bar{0}]$

consequence of a dissociation process induced by the presence of steps. The relative coverage evaluated from the TDS peak areas of states  $E - C$  [ $\Theta = 0.33$  for Ni(221) and  $= 0.06$  for Ni(665)] corresponds quite well to the ratio of step to terrace atoms for both surfaces ( $= 0.29$  and  $0.09$ , respectively). Evidence for a partial dissociation of H<sub>2</sub>O on Ni(s) (111) is also found from the evolution of H<sub>2</sub> in the TDS experiments. These results will be discussed in detail elsewhere.<sup>7</sup>

The work function change measured during the H<sub>2</sub>O desorption from Ni(s) (111) are summarized in Fig. 3. Again we note, that the heating rate for the  $\Delta\Phi$  experiment is the same as for the TDS measurements. This allows a direct comparison of  $\Delta\Phi$  changes with the different desorption states.

Figure 3(A) shows the work function change for the Ni(665) surface dosed at 150 K to  $\Theta(\text{H}_2\text{O}) = 0.75$  as a function of crystal temperature (150–400 K). The H<sub>2</sub>O adsorption at 150 K leads to a considerable decrease of  $\Delta\Phi$ .

In the temperature range of 150–200 K we observe a rapid increase of  $\Delta\Phi$  by about 490 meV. This change corresponds to the desorption of H<sub>2</sub>O from (111) terraces (TDS state  $B$ ). A further increase of  $\Delta\Phi$  is observed in the temperature range of 200–250 K by 150 meV, which is attributed to the H<sub>2</sub>O desorption from (111) step sites. Finally, in the temperature range of 250–400 K, where no H<sub>2</sub>O desorption was detected in TDS experiments, a further increase of  $\Delta\Phi$  by 50 meV is observed.

Similar  $\Delta\Phi$  measurements are depicted for H<sub>2</sub>O/Ni(221) in Fig. 3(B). Again, the temperature position of the  $\Delta\Phi$  changes corresponds quite well to the desorption states already detected with TDS. For Ni(221) the H<sub>2</sub>O coverage at 150 K was  $\Theta = 1.1$ . As a consequence, also a small change of  $\Delta\Phi$  by 185 meV is detected in the temperature range of 150–170 K due to the desorption from state  $A$  (ice multilayer). Surprisingly, the  $\Delta\Phi$  change of 120 meV associated with the desorption of state  $B$  [H<sub>2</sub>O from (111) terrace sites, 170–200 K] is much smaller than expected from the relatively high population

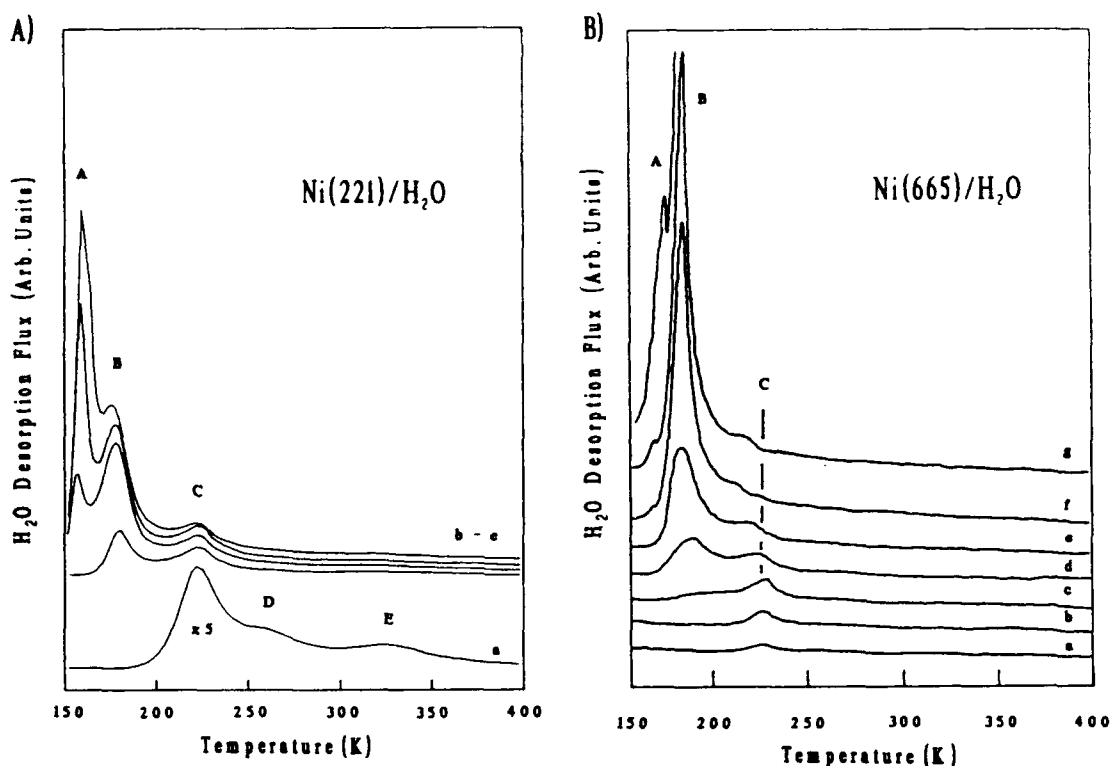


FIG. 2. Thermal desorption spectra for H<sub>2</sub>O/Ni(s) (111). (A) H<sub>2</sub>O/Ni(221); the water coverage for each spectrum is a-e: 0.2; 0.5; 0.85; 1.3 and 1.7. (B) H<sub>2</sub>O/Ni(665); the water coverage for each spectrum is a-g: 0.02; 0.03; 0.06; 0.12; 0.24; 0.48; and 0.8. [ $\Theta = 0.75$  corresponds to a saturated H<sub>2</sub>O bilayer on Ni(111)].

of this state. The saturation coverage of state B is  $\Theta = 0.5$  on Ni(221) and  $= 0.7$  on Ni(665). We conclude that the quantitative changes of  $\Delta\Phi$  in the different adsorption states on Ni(221) and Ni(665) are not a linear function of the population of these states. The low  $\Delta\Phi$  value associated with state B on Ni(221) suggests that the effective H<sub>2</sub>O dipole moment is considerably lowered due to the higher step density (smaller terrace width) of this surface. Further, the desorption state C on Ni(221) is associated with a considerably higher increase of  $\Delta\Phi$  by 610 meV (200–250 K), although the relative coverage of this state is still quite low ( $\Theta = 0.33$  from the peak areas of the sum of desorption states C–E). This corresponds to a high effective H<sub>2</sub>O dipole moment at step sites on Ni(221); a significant  $\Delta\Phi$  change in the C state is also seen on Ni(665).

On both Ni(s) (111) surfaces we detect a further nearly linear increase of  $\Delta\Phi$  in the temperature range of 250–300 K. This change coincides with the observation of the weak desorption peak D [only detected with weak intensity for Ni(221)]. This  $\Delta\Phi$  change is not yet fully understood. However, we have some indication that this change is not mainly due to desorbing H<sub>2</sub>O, but rather due to a reconstruction of the step structure. This leads to irreversible changes of the step structure of the Ni(s) (111) surface, which can be detected in subsequent TDS and  $\Delta\Phi$  measurements.<sup>11</sup> Only the heating of the Ni(s) (111) crystal to higher temperature ( $> 600$  K) restores the original surface.

Finally, in the temperature range of 300–400 K, where with TDS the desorption state E is detected [recombination of OH(ad) to molecular H<sub>2</sub>O and O(ad)] a further small change of  $\Delta\Phi$  is detected on Ni(221).

In summary, we conclude that on the (111) terraces from Ni(s) (111) surfaces the effective H<sub>2</sub>O dipole moment is lowered with decreasing terrace width. The opposite behavior is found for the effective H<sub>2</sub>O dipole moment of H<sub>2</sub>O adsorbed at step sites. Here the effective dipole moment is much higher than on the terrace sites, it increases for decreasing step concentration.

In Fig. 4 we propose a model for the influence of steps on the H<sub>2</sub>O adsorption geometry, which is in accordance with the TDS and  $\Delta\Phi$  data presented above.

Due to the Smoluchowski smoothing effect<sup>12</sup> the electron charge density at the step edges is associated with a dipole field; the step-up edges are positively charged and the step-down notches negatively. Our work function measurements for H<sub>2</sub>O/Ni(s) (111) at low coverage (adsorption state C) suggest that H<sub>2</sub>O is adsorbed on the positively charged step-up adsorption sites. This adsorption geometry together with the proposed H<sub>2</sub>O dipole orientation lowers the coulomb energy between step dipole field and H<sub>2</sub>O dipole. Further, because the H<sub>2</sub>O bonding to transition metal surfaces is associated with an electron donation from the molecule into the substrate, the step-up adsorption sites provide "acid" Ni<sup>δ+</sup> sites which are favoring the electron donation and the increase of the H<sub>2</sub>O–Ni bond strength.<sup>13</sup> In our opinion the increase of the H<sub>2</sub>O–Ni bond strength

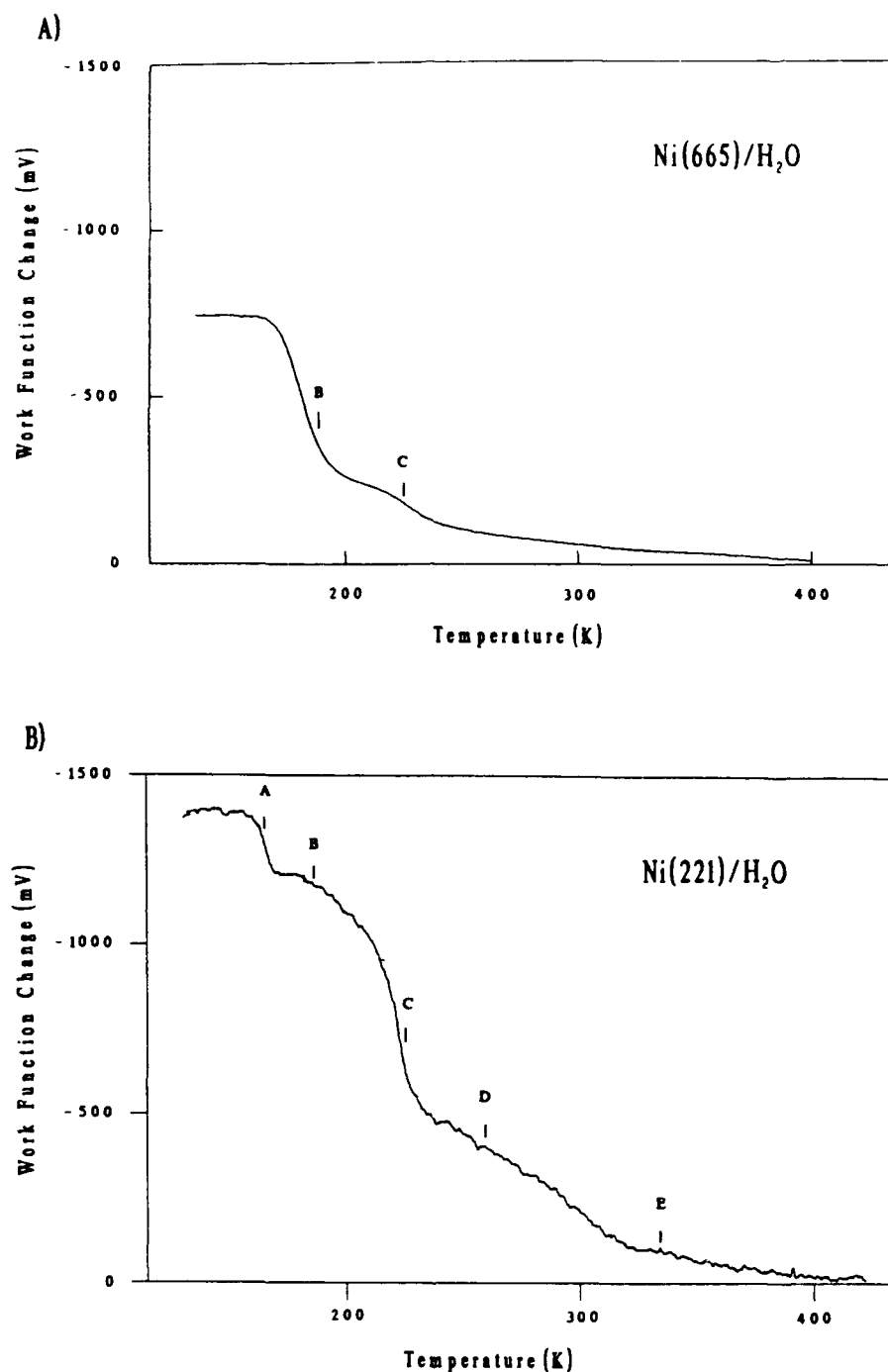


FIG. 3. Work function changes measurements for H<sub>2</sub>O desorption from Ni(s) (111). (A) H<sub>2</sub>O/Ni(665); the water coverage at 150 K was  $\Theta = 0.75$  (B) H<sub>2</sub>O/Ni(221); the water coverage at 150 K was  $\Theta = 1.1$ . Note that the desorption peak temperatures for TDS states A–E are indicated in each figure. The temperature position of state A, B, and C coincide with inflection points of the  $\Delta\Phi$  changes.

and the dipole–dipole (H<sub>2</sub>O dipole with step field) interaction is responsible for a nearly perpendicular orientation of H<sub>2</sub>O in this adsorption state; this adsorption geometry is also responsible for the high effective dipole moment measured with  $\Delta\Phi$ .

Due to the high H<sub>2</sub>O–Ni bond strength, step sites are “decorated” at low coverage by adsorbed water molecules. With increasing H<sub>2</sub>O coverage and the saturation of the step sites we assume the growing of a H<sub>2</sub>O bilayer on the

(111) terraces, starting from H<sub>2</sub>O molecules adsorbed at step sites. This situation is schematically shown in Fig. 4(B). The formation of H<sub>2</sub>O bilayer clusters on transition metal surfaces, in which some water molecules are directly bound via the oxygen atom to the substrate and other “second layer” H<sub>2</sub>O via hydrogen bonding to the “first layer” molecules, is well established in the literature.<sup>14</sup>

To form H<sub>2</sub>O bilayer clusters on Ni(s) (111) starting from step edges, a slight reorientation of the step-edge wa-



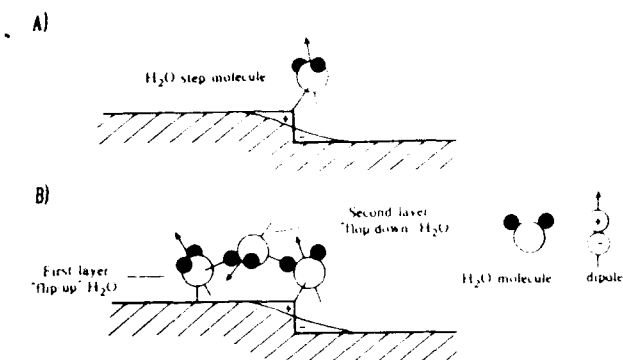


FIG. 4. Model for the H<sub>2</sub>O adsorption geometry on Ni(s) (111) surfaces. (A) Oriented H<sub>2</sub>O monomers at step sites for low H<sub>2</sub>O coverages. (B) After the saturation of step sites, bilayer clusters grow onto the (111) terraces. Due to the presence of second layer flop-down and first layer flip-up orientations, the contribution to  $\Delta\Phi$  changes is low.

ter molecules is necessary [Fig. 4(B)]. After this reorientation the step-edge water molecules are still in a flip-up geometry<sup>6</sup> where the H<sub>2</sub>O dipole is directed away from the Ni(s) (111) surface. The built-up of a bilayer cluster with further "first" and "second" layer molecules requires now an equal number of second layer flop-down (positive end of dipole directed toward the surface) and first layer flip-up molecules. Because the dipole orientations are opposite for flop-down and flip-up molecules, the effective dipole moment (related to work function changes) of H<sub>2</sub>O bilayer clusters on (111) terraces is low. This situation may change with increasing (111)-terrace width. Following Doering and Madey<sup>6</sup> the number of second layer flip-up water molecules is expected to increase for larger bilayer clusters, this configuration would lead to a decrease of  $\Delta\Phi$  (higher effective H<sub>2</sub>O dipole moment).

Finally we want to address the question why the H<sub>2</sub>O dissociation is enhanced on the stepped Ni(s) (111) surfaces. In our adsorption model we assume a step-up adsorption geometry. As mentioned before, due to the presence of acid Ni<sup>δ+</sup> adsorption sites the electron charge transfer from the water molecule to the substrate is increased. This leads on the one hand side to an increase of the H<sub>2</sub>O–Ni and on the other hand to a decrease of the intramolecular H<sub>2</sub>O bond strength. This interpretation is in accordance with quantum-chemical calculations of Stair.<sup>13</sup> To our opinion the weakening of the intramolecular bonds at step sites is responsible for the enhanced H<sub>2</sub>O dissociation on Ni(s) (111).

#### IV. CONCLUSIONS

We briefly summarize the main conclusions which we obtain from our present investigation.

1. LEED investigations of the clean Ni(221) and Ni(665) surfaces confirm an atomic arrangement expected for an ideal nonreconstructed surface; these surfaces exhibit (111) steps of one atomic height and terrace width of 3.5 [Ni(221) or 11.5 (Ni(665))] atoms, respectively

2. Due to the presence of steps, on both surfaces new desorption states at higher desorption temperatures are detected; these states are absent on flat Ni(111). These states are related to oriented H<sub>2</sub>O monomers adsorbed at step-up adsorption sites (C) or to the recombination of dissociation products (D and C). The higher H<sub>2</sub>O–Ni substrate binding energy and the high effective dipole moment of the H<sub>2</sub>O step-up adsorption state is suggested to be due to the coulomb interaction of the H<sub>2</sub>O dipole with the step dipole field. A further contribution to the increase of the H<sub>2</sub>O–Ni binding energy and the lowering of the dissociation barrier is attributed to the enhanced electron donation from H<sub>2</sub>O to the substrate at step sites.

3. The H<sub>2</sub>O orientations within H<sub>2</sub>O bilayer clusters on (111) terrace sites are influenced by the presence of steps. The "decoration" of step sites at low H<sub>2</sub>O coverage by oriented H<sub>2</sub>O monomers leads to the formation of bilayer clusters with nearly equal numbers of second layer flop-down and first layer flip-up molecules [for Ni(221)]. The opposite dipole orientation of flop-down and flip-up H<sub>2</sub>O molecules is believed to be responsible for the relatively low effective H<sub>2</sub>O dipole moment associated with the adsorption on terrace sites.

The present investigation of H<sub>2</sub>O/Ni(s) (111) contributes to the understanding of the role of surface defects (steps) on the adsorption of simple gases. It demonstrates that the presence of steps influences the molecule–substrate binding energy, the molecular orientation and also the barrier for dissociation.

#### ACKNOWLEDGMENT

The financial support of the present investigation by the Deutsche Forschungsgemeinschaft is gratefully acknowledged.

This article was presented at the 38th National Symposium of the American Vacuum Society Topical Conference, Surface Science at the Solid–Liquid Interface (TC1).

<sup>1</sup>S. M. Davis and G. A. Somorjai, in *The Chemical Physics of Solid Surfaces and Heterogeneous Catalysis*, edited by D. A. King and D. A. Woodruff (Elsevier, Amsterdam 1982), Vol. 4, p. 217.

<sup>2</sup>C. Benndorf and L. Meyer, *Surf. Sci.* **251/252**, 872 (1991).

<sup>3</sup>C. Benndorf and L. Meyer, *J. Vac. Sci. Technol. A* **8**, 2677 (1990).

<sup>4</sup>C. Benndorf, T. E. Madey, and A. L. Johnson, *Surf. Sci.* **187**, 434 (1987).

<sup>5</sup>C. Nöbl and C. Benndorf, *Surf. Sci.* **182**, 499 (1987).

<sup>6</sup>D. L. Doering and T. E. Madey, *Surf. Sci.* **123**, 305 (1982).

<sup>7</sup>C. Mundt and C. Benndorf (to be published).

<sup>8</sup>M. A. Van Hove and G. A. Somorjai, *Surf. Sci.* **92**, 485 (1980).

<sup>9</sup>M. Henzler, *Surf. Sci.* **19**, 159 (1970).

<sup>10</sup>T. E. Madey and F. P. Netzer, *Surf. Sci.* **117**, 549 (1982).

<sup>11</sup>R. H. Stulen and P. A. Thiel, *Surf. Sci.* **157**, 99 (1985).

<sup>12</sup>R. Smoluchowski, *Phys. Rev.* **60**, 661 (1941).

<sup>13</sup>P. C. Stair, *J. Am. Chem. Soc.* **104**, 4044 (1982).

<sup>14</sup>P. A. Thiel and T. E. Madey, *Surf. Sci. Rep.* **7**, 211 (1987).

# GaAs deposition on the (100) and (110) planes of gold by electrochemical atomic layer epitaxy: A low-energy electron diffraction, Auger electron spectroscopy, and scanning tunneling microscopy study

Ignacio Villegas and John L. Stickney<sup>a)</sup>

*Department of Chemistry, University of Georgia, Athens, Georgia 30602*

(Received 14 October 1991; accepted 30 December 1991)

Preliminary studies on the deposition of GaAs by electrochemical atomic layer epitaxy (ECALE) were performed. ECALE is based on the alternated underpotential deposition (UPD) of atomic layers of different elements to form a compound. Oxidative UPD of As and reductive UPD of Ga on the low-index planes of gold were studied using Auger electron spectroscopy (AES), low-energy electron diffraction (LEED), scanning tunneling microscopy (STM), and coulometry. AES and LEED were performed in an ultrahigh vacuum (UHV) surface analysis instrument interfaced to an electrochemical cell in an antechamber. This instrument configuration allowed the electrochemical treatment of the samples and their subsequent analysis in UHV without the need to transfer the samples through air. STM was performed under nitrogen at atmospheric pressure. AES and coulometry were used for surface composition analysis while LEED and STM provided structural information. The substrate was a gold single-crystal electrode with three oriented faces, each to a different low-index plane. Oxidative UPD of arsenic was observed only on the (100) and (110) faces. The resulting structures were a  $\text{Au}(100)(2 \times 2)\text{-As}$  at 1/4 coverage and an  $\text{Au}(110)c(2 \times 2)\text{-As}$  at 1/2 coverage. Reductive UPD of Ga was observed on all three faces, although it resulted in disordered layers of Ga oxide upon removal of the substrate from solution, due to partial oxidation of the Ga in contact with water in the absence of potential control. Stoichiometric coverages of Ga and As were obtained on the (100) and (110) surfaces when Ga was underpotentially deposited on the As covered surfaces [ $\text{Au}(100)(2 \times 2)\text{-As}$  at 1/4 coverage and  $\text{Au}(110)c(2 \times 2)\text{-As}$  at 1/2 coverage]. Structures displaying  $(2 \times 2)$  and  $c(2 \times 2)$  LEED patterns were observed on the (100) and (110) faces, respectively.

## I. INTRODUCTION

The preparation of compound semiconductors, II–VI and III–V materials in particular, by electrochemical deposition has been the object of a number of studies during the last twenty years. The development of new, low temperature methods of deposition is an important area of research. Electrochemical deposition represents an alternate methodology to prepare compound semiconductors at room temperature which could avoid interdiffusion problems associated with the high temperatures required in current deposition techniques.<sup>1</sup>

Research in our laboratory is directed towards the development of a method to epitaxially electrodeposit compound semiconductors from aqueous solutions: electrochemical atomic layer epitaxy (ECALE).<sup>2</sup> Previous attempts to electrodeposit compound semiconductors have resulted in polycrystalline deposits. An important example of previous deposition methodology was developed by Kroger *et al.*<sup>3</sup> That method consists of the simultaneous codeposition of both component elements from oxidized species in a single solution. The deposition potential is chosen in order to optimize the stoichiometry of the deposits. Generally, the deposition potential is such that one of the elements is deposited at a rate controlled by mass transfer towards the electrode surface. The other element, present in excess, reacts with the previously deposited element to form the compound. The ECALE methodology is intended

to address problems associated with nucleation and growth. ECALE is based on the alternated electrodeposition of atomic layers of the component elements from two different solutions. Underpotential deposition (UPD) is a surface-limited process where an atomic layer of one element is deposited on a substrate surface composed of a different element at a potential prior to that required for bulk deposition of the first element.<sup>4,5</sup> ECALE takes advantage of this surface-limited process to alternately deposit atomic layers of the desired elements, eliminating three-dimensional nucleation.

Previous studies in our laboratory have concentrated on the ECALE deposition of CdTe.<sup>2,6,7</sup> Preliminary studies involved the UPD of Cd and Te on different polycrystalline substrates (Au, Pt, and Cu) using thin-layer electrochemical cells.<sup>7</sup> Au was selected as the most applicable substrate for subsequent studies of ECALE deposition due to its extended double-layer window which allows the study of UPD with minimum interference from substrate oxidation and hydrogen evolution processes. A fortuitous lattice mismatch of only 3.5% exists between GaAs and twice the Au lattice constant. UPD of Cd and Te on the three low-index planes of gold was studied using Auger electron spectroscopy (AES) and low-energy electron diffraction (LEED).<sup>6,8</sup> The studies described in this manuscript are the continuation of a previous study on the ECALE deposition of GaAs on the three low-index planes of gold.<sup>9</sup>

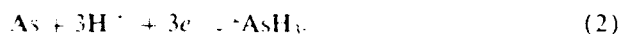
GaAs has been successfully electrodeposited from aqueous solutions<sup>10,11</sup> and from molten salt electrolytes.<sup>12,13</sup> The formation of GaAs was confirmed by x-ray and electron diffraction measurements although the deposits obtained were polycrystalline in each case. The thermodynamic stability of GaAs in aqueous solutions has been addressed in a number of studies. The stability of materials in aqueous solutions are usually evaluated through potential versus pH plots (Pourbaix diagrams). In earlier studies, the stability of GaAs in aqueous solutions was questioned.<sup>10,14</sup> More accurate diagrams have been calculated,<sup>15</sup> and a region of thermodynamic stability between pH 1.3 and pH 13.3 was determined. Our own studies, including calculations which take into consideration a number of concentrations of the different species in solution in contact with the GaAs, indicate the possibility of obtaining stable GaAs deposits in aqueous solutions as long as potential control is maintained.

The electrochemistry of As has been extensively studied and reported in the literature.<sup>16,17</sup> A mechanism has been proposed for the deposition of As on gold, involving three successive one electron transfers and passivation due to the formation of an amorphous layer of As.<sup>17</sup> The electrochemistry of Ga has been studied as well.<sup>18</sup>

Preliminary studies of the ECALE deposition of GaAs were performed using a thin-layer electrochemical cell (TLE) with a polycrystalline gold electrode.<sup>9</sup> Potentials for Ga and As UPD on gold were evaluated. It was determined that Ga UPD occurs 50 mV prior to the hydrogen evolution reaction during the negative scan. Bulk Ga is deposited at potentials more negative than the potential for hydrogen evolution. Arsenic was shown to be reductively deposited from a  $\text{HAsO}_2$  (pH 4) solution between  $-0.3$  and  $-1.5$  V in a three electron transfer according to the reaction



The onset potential for deposition depends on the pH of the solution, shifting towards more negative potentials as the pH increases. It was also found that As coverage reaches a maximum independent of the pH of the solution.<sup>9,16,17,19-23</sup> The potential at which the maximum coverage is reached also shifts towards more negative potentials as the pH of the solution increases. The decrease in As coverage at very negative potentials is due to the reaction



Formation of arsine from As reduction in aqueous solutions has been reported in the literature.<sup>24</sup> The minimum As coverage at negative potentials is about 0.4 As atoms per surface Au atom and is independent of pH for solution pHs higher than 3. For pHs lower than 3, arsine formation is inhibited by depolarization of the electrode potential due to extensive hydrogen evolution. This results in the higher As coverage at potentials below  $-1.0$  V, as the electrode never really attains those highly negative potentials. There are two ways of looking at these results. Deposited arsenic is reduced to arsine at very negative potentials according to reaction (2), leaving behind an atomic layer of As, stabi-

lized by bonding with Au surface atoms. Alternatively,  $\text{HAsO}_2$  can be considered to convert quantitatively to arsine according to the reaction



and an atomic layer of As is deposited by oxidative UPD from arsine.

## II. EXPERIMENTAL

A combination of ultrahigh vacuum (UHV) and ambient pressure surface characterization techniques were used in these studies. The UHV surface analysis instrument included a hemispherical electron analyzer and electron gun for Auger electron spectroscopy (AES) and a set of low-energy electron diffraction (LEED) optics. Electrochemical experiments were performed in an UHV antechamber interfaced to the main analysis chamber. This configuration enables the electrochemical treatment of the samples in an argon atmosphere at ambient pressure and their subsequent analysis in UHV without the need to transport the samples through air. This instrument has been described in detail in previous publications.<sup>9,25</sup> Surface characterization in UHV included AES and LEED, which provided information about the elemental and structural composition of the surfaces, respectively. AES parameters were as follows: 1 mm<sup>2</sup> beam size, 10  $\mu\text{A}$  beam current at 3000 V, 5 min 100–600 eV and 3 min 1000–1300 eV scans.

The gold substrate was a single crystal which had been oriented, using Laue x-ray diffraction, cut and mechanically polished to expose the three low-index planes on three different faces. Electrical connection was made through a gold wire, avoiding the use of other materials which could interfere in the electrochemistry. Surface preparation prior to electrochemical experiments consisted of ion bombardment with 300 V  $\text{Ar}^+$  ions for 1 h and subsequent annealing at 650 °C. The cleanliness and order of the surfaces was monitored using AES and LEED.

A NanoScope II (Digital Instruments) was used in scanning tunneling microscopy (STM) experiments. Electrochemistry and subsequent STM characterization were performed inside a glovebox in a nitrogen atmosphere at ambient pressure. STM tips were prepared by electrochemically etching a tungsten wire in 1.0 M NaOH. The substrate used for STM experiments was a gold single crystal, oriented, cut, and polished to expose the (100) plane on all six sides of a rectangular box.

All solutions used in these studies were prepared with research grade chemicals and pyrolytically triply distilled water.<sup>26</sup> Potentials are reported versus an Ag/AgCl, 1.0 M NaCl reference electrode.

## III. RESULTS AND DISCUSSION

No signals other than those assignable to Au were observed in the Auger spectra of the ion bombarded and annealed surfaces of the gold tricrystal [Fig. 1(a)]. Reconstructions were evident in the LEED patterns for the three surfaces.<sup>27</sup> The voltammogram obtained with the clean Au tricrystal in 1.0 mM  $\text{HAsO}_2$ /1.0 mM  $\text{H}_2\text{SO}_4$  (pH 3.2) is

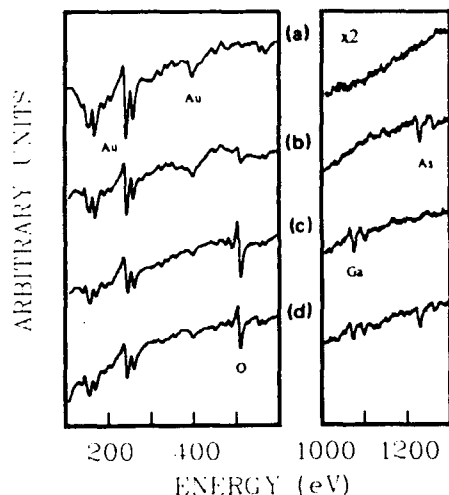


FIG. 1. Auger spectra: (a) Ion bombarded and annealed Au(100). (b) As oxidative UPD on Au(100). (c) Ga reductive UPD on Au(100). (d) Stoichiometric coverage of Ga and As on Au(100).

shown in Fig. 2(a). This voltammogram is analogous to those reported in the literature.<sup>9,17</sup> Oxidative UPD of As on the low-index planes of gold was evaluated as follows. The tricrystal was immersed in a 1.0 mM  $\text{HAsO}_2$ /1.0 mM  $\text{H}_2\text{SO}_4$  (pH 3.2) solution at a series of potentials between  $-1.0$  and  $-1.6$  V for 30 s. The electrode was subsequently emersed (removed) from the  $\text{HAsO}_2$  solution and rinsed three times with 10.0 mM  $\text{H}_2\text{SO}_4$  (pH 1.9) at controlled potential, with the final rinse held for 1 min. Characterization of the surfaces was performed by AES and LEED. Similar procedures were employed using a 10.0

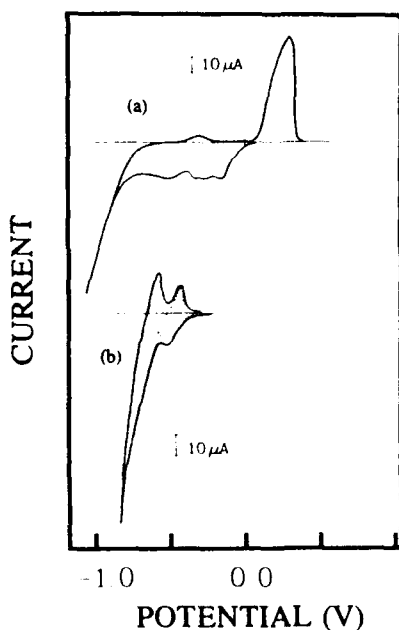


FIG. 2. Cyclic voltammograms of the Au tricrystal: (a) clean in 1.0 mM  $\text{HAsO}_2$ , 1.0 mM  $\text{H}_2\text{SO}_4$  (pH = 3.2) (scan rate = 5 mV/s). (b) clean in 0.5 mM  $\text{Ga}_2(\text{SO}_4)_3$  (pH = 2.7) (scan rate = 5 mV/s).

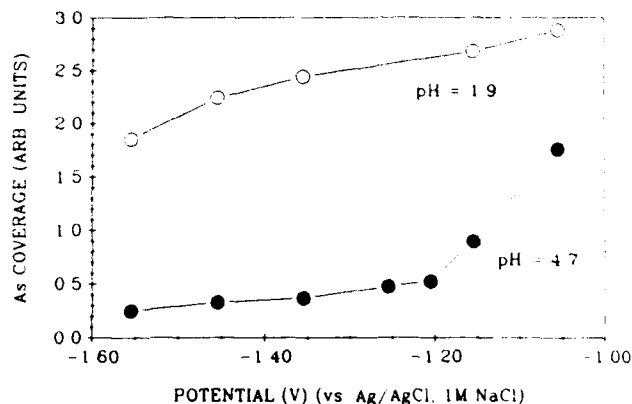
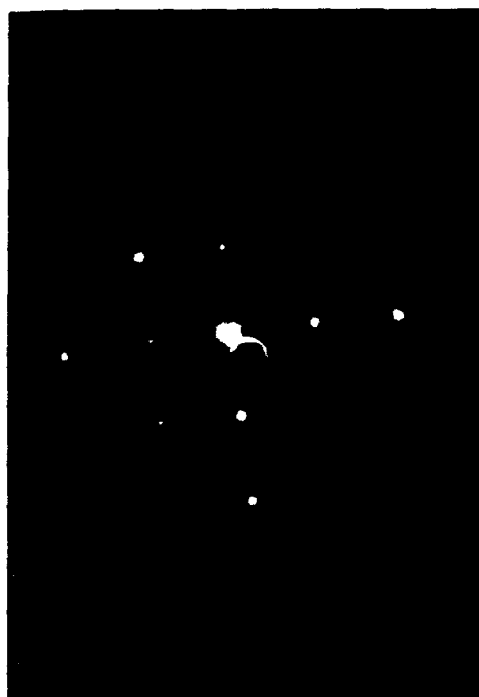


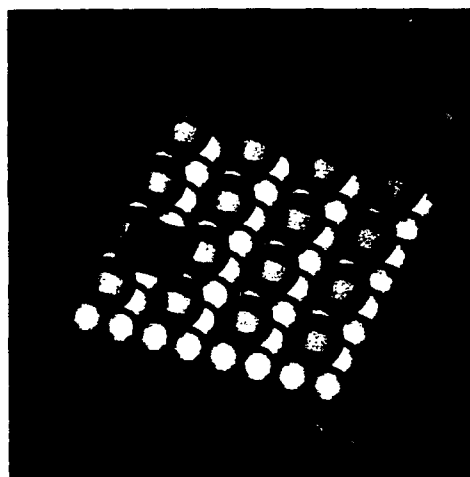
FIG. 3. Total As coverage vs deposition potential and pH on the Au tricrystal.

mM  $\text{Cs}_2\text{SO}_4$  solution, containing a 1.0 mM acetate buffer (pH 4.7) instead of the 10.0 mM  $\text{H}_2\text{SO}_4$ . Emersion from this solution resulted in some excess  $\text{Cs}_2\text{SO}_4$  crystallizing on the surface, which interfered with the As quantitation. For this reason, a final rinse with dilute  $\text{H}_2\text{SO}_4$  was added after emersion from  $\text{Cs}_2\text{SO}_4$ . In each case the initial deposition potential was maintained for all stages where the electrode was in solution. The total As coverage at each potential was determined by subsequent stripping in 10.0 mM  $\text{H}_2\text{SO}_4$ , after the surface characterization had been completed. Coulometric measurements determine the total amount of As deposited on all three faces. Total As coverages as a function of the deposition potential and the pH of the initial reduction solution are presented in Fig. 3. The coverage of As plateaus at 0.4 for potentials between  $-1.2$  and  $-1.5$  V in the pH 4.7 solution. Arsine formation is inhibited by depolarization of the electrode, due to hydrogen evolution in the pH 1.9 solution, resulting in higher As coverages at very negative potentials. These results are analogous to those obtained in studies of oxidative As UPD using TLEs with polycrystalline Au electrodes.<sup>9</sup> Transitions assignable to Au and As were the only observable features in the Auger spectra obtained for the (100) and (110) surfaces at deposition potentials in the plateau region (pH 4.7 solution). A representative spectrum is shown in Fig. 1(b). Auger spectra for the (111) surface displayed only Au transitions, no detectable As signal. For potentials in the plateau region,  $(2 \times 2)$  [Fig. 4(a)] and  $c(2 \times 2)$  [Fig. 5(a)] LEED patterns were obtained for the (100) and (110) surfaces, respectively. Proposed low-coverage structures are shown in Figs. 4(b) and 5(b): an Au(100) $(2 \times 2)$ -As at 1/4 coverage and an Au(110) $c(2 \times 2)$ -As at 1/2 coverage. Higher As coverages resulted only in diffuse LEED patterns for the three low-index planes.

An atomic layer of As was deposited on a six-sided Au(100) crystal (described in the experimental section) by oxidative UPD at  $-1.3$  V at pH 4 according to the procedure described above. The crystal was positioned in the microscope such that rows of atoms in the (100) lattice, the [110] direction, would appear at  $45^\circ \pm 5^\circ$  angles



(a)

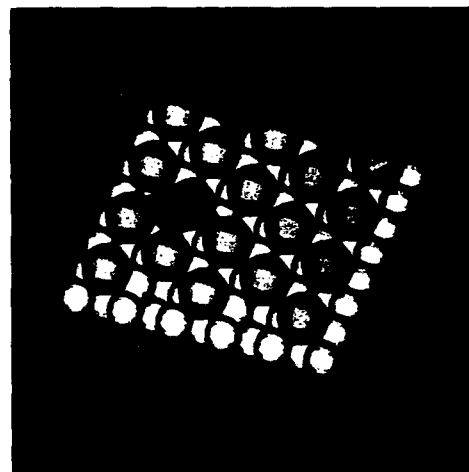


(b)

FIG. 4 (a) Picture of the  $(2 \times 2)$  LEED pattern obtained at  $1/4$  As coverage on Au(100) (beam energy =  $38$  eV). (b) proposed structure for As UPD ( $1/4$  coverage) on Au(100).



(a)



(b)

FIG. 5 (a) Picture of the  $c(2 \times 2)$  LEED pattern obtained at  $1/2$  As coverage on Au(110) (beam energy =  $39$  eV). (b) proposed structure for As UPD ( $1/2$  coverage) on Au(110).

with respect to the horizontal of the instrument's screen. Figure 6 is a picture of the unfiltered image on the instrument's screen showing an Au(100)( $2 \times 2$ )-As structure. The As-As distance corresponds, within experimental error, to twice the Au-Au distance in the (100) lattice. A  $45^\circ$  angle ( $\pm 5^\circ$ ) with respect to the horizontal of the screen is also consistent with a  $(2 \times 2)$  structure. A similar structure has been observed for an Au(100)( $2 \times 2$ )-Te structure at  $1/4$  coverage, reported in this same issue.<sup>28</sup>

Figure 2(d) shows a voltammogram obtained with the Au tricrystal in a  $0.5$  mM  $\text{Ga}_2(\text{SO}_4)_3$  ( $\text{pH } 2.7$ ) solution. In previous studies, it had been determined that the peak at  $-0.5$  V corresponds to the reductive UPD of Ga, while bulk deposition was obscured by hydrogen evolution. The peaks observed during the subsequent positive scan corre-

spond to bulk Ga stripping at  $+0.6$  V and Ga UPD stripping at  $+0.4$  V. Similar Auger spectra were obtained for the three low-index planes emersed from solution just before the Ga UPD stripping peak during the positive scan. Transitions corresponding to Au, Ga, and O were evident in the spectra [Fig. 1(c)]. Completely diffuse LEED patterns were observed for each of the three faces. The presence of oxygen on the surfaces is attributed to partial oxidation of the deposited Ga after emersion and loss of potential control. This is understandable as the electrode remained in contact with a thin layer of solution upon emersion (the emersion layer). Partial oxidation of the Ga in contact with an aqueous solution, without potential control, is consistent with the thermodynamic stability of Ga(0) in the presence of  $\text{H}_2\text{O}$ .<sup>29</sup> Integration of the UPD

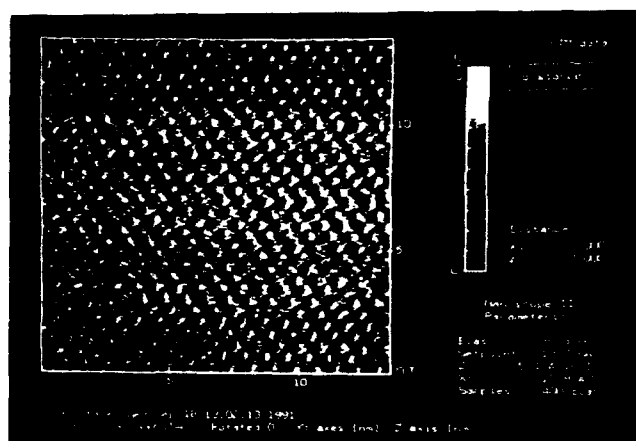


FIG. 6. Unfiltered STM image of the Au(100)(2 $\times$ 2)-As structure.

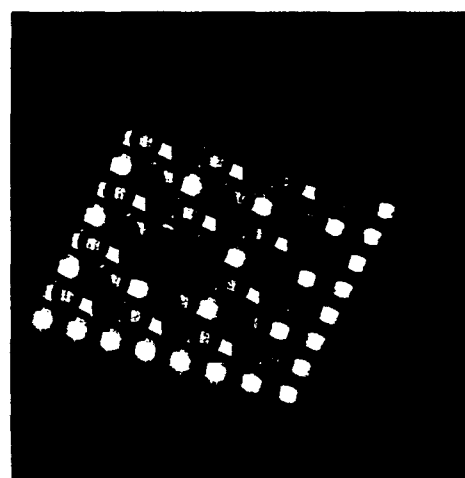
Ga stripping peak resulted in an overall Ga coverage of 0.2–0.3, as long as the electrode was not emersed prior to stripping.

In order to investigate the ECALE deposition of GaAs, the alternated deposition of Ga and As was also investigated. Arsenic was first deposited from a 1.0 mM  $\text{HAsO}_2$ /1.0 mM  $\text{H}_2\text{SO}_4$  (pH 3.2) solution and subsequently reduced in a buffered 10.0 mM  $\text{Cs}_2\text{SO}_4$  (pH 4.7) solution at  $-1.25$  V, according to the procedure described previously. The next step consisted of a series of experiments in which the As-covered surfaces were immersed in a 0.5 mM  $\text{Ga}_2(\text{SO}_4)_3$  (pH 2.7) solution at various potentials between  $-0.96$  and  $-0.40$  V. For Ga deposition potentials between  $-0.71$  and  $-0.56$  V, stoichiometric amounts of Ga, relative to the previously deposited As, were deposited on the (100) and (110) surfaces, as shown by AES [Fig. 1(d)]. Bulk Ga deposition occurred at potentials more negative than  $-0.71$  V while no Ga was deposited at potentials more positive than  $-0.56$  V. Auger transitions for Au, Ga, As, and O are evident in Fig. 1(d). The presence of oxygen on the surface is probably due to partial oxidation of the GaAs upon emersion of the electrode from solution. GaAs in contact with water at open circuit can oxidize to form  $\text{Ga}_2\text{O}_3$  and As.<sup>9</sup>

Stoichiometric coverages of Ga and As resulted in (2 $\times$ 2) [Fig. 7(a)] and  $c(2\times 2)$  [Fig. 8(a)] LEED patterns on the Au(100) and Au(110) surfaces, respectively. Partial oxidation of the Ga, as indicated by AES, accounts for the extra diffuseness observed in the LEED patterns displayed in Figs. 7(a) and 8(a) when compared with the LEED patterns obtained for the As-covered surfaces [Figs. 4(a) and 5(a)]. Partial oxidation of Ga deposited on arsenic-free Au surfaces resulted in completely diffuse LEED patterns. Enhanced stability due to compound formation when Ga is deposited on As-covered Au surfaces is probably responsible for the increased order observed in Figs. 7(a) and 8(a) compared to the studies made sans As. Proposed structures corresponding to monolayers of GaAs on the Au(100) and the Au(110) surfaces are shown in Figs. 7(b) and 8(b). These structures were drawn using the atomic radii of Ga and As.<sup>30</sup> The proposed Au(100)(2



(a)



(b)

FIG. 7. (a) Picture of the (2 $\times$ 2) LEED pattern obtained at stoichiometric coverages of Ga and As on Au(100) (beam energy = 37 eV) (b) proposed structure for stoichiometric coverages of Ga and As on Au(100) (As dark gray, Ga light gray, Au white)

$\times 2$ )-GaAs structure involves stoichiometric coverages of Ga and As and the formation of As dimers on the surface. Dimerization has been reported in the literature, supported by LEED and STM results.<sup>31–35</sup> Stoichiometric coverages of Ga and As on the Au(100) surfaces without dimerization of As would probably result in a  $c(2\times 2)$  LEED pattern, but no signs of this pattern were observed in our studies. The proposed Au(110) $c(2\times 2)$ -GaAs structure, shown in Fig. 8(b), also requires stoichiometric coverages of Ga and As. No dimers are proposed in this case. STM results on GaAs(110) also indicate no dimer formation.<sup>36–38</sup> The (110) surface is more open, permitting both Ga and As bonding to Au surface atoms. The proposed structures resemble truncation of a GaAs crystal

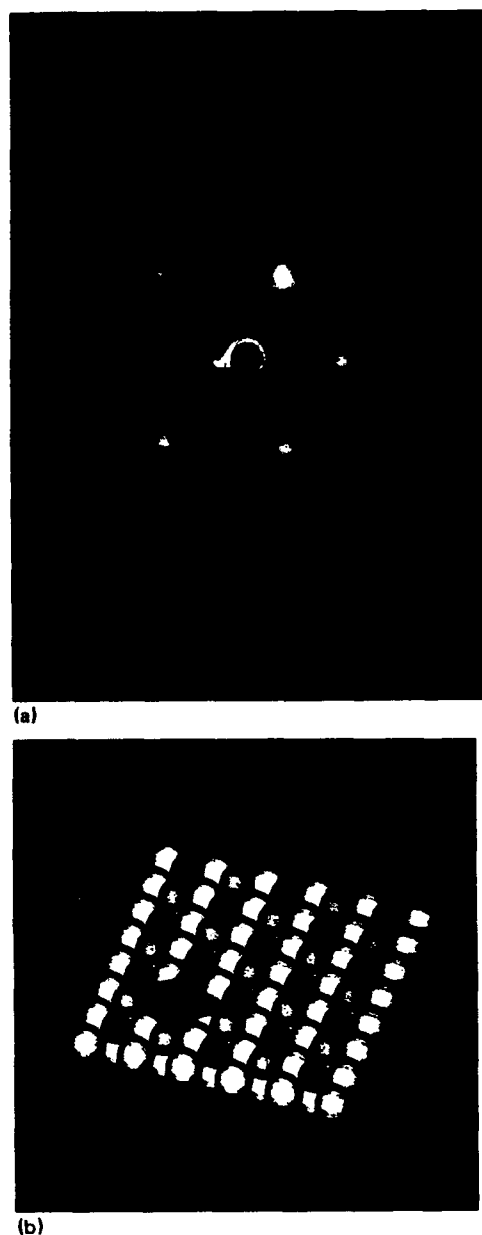


FIG. 8. (a) Picture of the  $c(2 \times 2)$  LEED pattern obtained for stoichiometric coverages of Ga and As on Au(110) (beam energy = 37 eV). (b) proposed structure for stoichiometric coverages of Ga and As on Au(110). (As: dark gray, Ga: light gray, Au: white).

through the (100) and (110) planes, respectively, due to the decent match between the GaAs lattice constant (5.65 Å) and twice the Au lattice constant (5.84 Å). Problems with the lattice match and the critical thickness will occur as the film thickness is increased, and is the topic of further studies.

Potential versus pH plots have been calculated in order to evaluate the stability of GaAs under the conditions to be used for ECALE.<sup>9</sup> According to those plots, a spontaneous reaction may occur between  $H^+$  in solution and GaAs at open circuit. Our calculations showed that GaAs can exist in aqueous solutions as long as the potential is kept within the region of stability. For that reason, successful formation of thicker films of GaAs by the ECALE method will be achieved only if potential control is maintained at all

times. The experimental procedure described above involves emersion of the substrate and loss of potential control after each deposition and rinsing step, resulting in partial oxidation of Ga after it has been deposited. Partial oxidation of the Ga upon emersion of the substrate accounts for the oxygen present in the Auger spectra of the GaAs-covered surfaces. A thin-layer flow cell is being developed in our laboratory, which will enable the exchange of solutions for successive UPD of atomic layers of Ga and As without emersion and loss of potential control.

In conclusion, oxidative UPD of As resulted in ordered layers on the (100) and (110) surfaces of Au. An Au(100)( $2 \times 2$ )-As at 1/4 coverage [Figs. 4(b) and 6] and a Au(110) $c(2 \times 2)$ -As at 1/2 coverage [Fig. 5(b)] are proposed. Reductive UPD of Ga was achieved on the three low-index planes of Au, but resulted a layer of disordered Ga oxide on the three low-index planes of gold after emersion. Successive UPD of atomic layers of As and Ga resulted in ordered structures on the Au(100) and Au(110) surfaces: an Au(100)( $2 \times 2$ )-GaAs [Fig. 7(b)] and an Au(110) $c(2 \times 2)$ -GaAs [Fig. 8(b)]. Proposed structures consist of stoichiometric coverages of Ga and As, and As dimers are proposed to explain the ( $2 \times 2$ ) LEED pattern observed on the (100) surface.<sup>31-35</sup>

## ACKNOWLEDGMENTS

Acknowledgment is made to the Donors of The Petroleum Research Fund, administered by the American Chemical Society, for partial support of this research. Acknowledgment is also given to the National Science Foundation, for partial support of this work under Grant No. DMR-9017431. This work is partially sponsored by the Department of the Navy, office of the Chief of Naval Research, under Grant No. N00014-91-J-1919. I. V. would like to thank INTEVEP S.A. (Caracas, Venezuela) for financial support.

This article was presented at the 38th National Symposium of the American Vacuum Society Topical Conference, Surface Science at the Solid-Liquid Interface (TC1).

<sup>a1</sup> Author to whom correspondence should be addressed.

<sup>1</sup>H. Watanabe, T. Mizutani, and A. Usui, in *Very High Speed Integrated Circuits: Heterostructures*, edited by T. Ikoma, Semiconductors and Semimetals Vol. 30, (Academic, New York, 1990), p. 1.

<sup>2</sup>B. W. Gregory and J. L. Stickney, *J. Electroanal. Chem.* **300**, 543 (1991).

<sup>3</sup>F. A. Kröger, *J. Electrochem. Soc.* **125**, 2028 (1978).

<sup>4</sup>D. M. Kolb, in *Advances in Electrochemistry and Electrochemical Engineering*, edited by H. Gerischer and C. W. Tobias (Wiley, New York, 1978), Vol. 11.

<sup>5</sup>K. Jüttner and W. J. Lorenz, *Z. Phys. Chem. N F* **122**, 163 (1980).

<sup>6</sup>B. W. Gregory, D. W. Suggs, and J. L. Stickney, *J. Electrochem. Soc.* **138**, 1279 (1991).

<sup>7</sup>B. W. Gregory, M. L. Norton, and J. L. Stickney, *J. Electroanal. Chem.* **293**, 85 (1990).

<sup>8</sup>D. W. Suggs and J. L. Stickney, *J. Phys. Chem.* (in press).

<sup>9</sup>I. Villegas and J. L. Stickney, *J. Electrochem. Soc.* (submitted).

<sup>10</sup>S. Chandra and N. Khare, *Semicond. Sci. Technol.* **2**, 214 (1987).

<sup>11</sup>S. Chandra and N. Khare, *Semicond. Sci. Technol.* **2**, 220 (1987).

<sup>12</sup>R. C. De Matter, D. Elwell, and R. S. Feigelson, *J. Cryst. Growth* **43**, 643 (1978).

<sup>13</sup>I. G. Dioum, J. Vedel, and B. Tremillon, *J. Electroanal. Chem.* **139**, 329 (1982).